East European Journal of Physics

East European Journal of Physics

East European Journal of Physics

ORIGINAL PAPERS

East European Journal of Physics

No 3.   2020

STRUCTURE AND CORROSION OF QUASICRYSTALLINE CAST Al–Co–Ni AND Al–Fe–Ni ALLOYS IN AQUEOUS NaCl SOLUTION

Olena V. Sukhova*, Volodymyr A. Polonskyy

Oles Honchar Dnipro National University
72, Haharin Ave., Dnipro, 49010, Ukraine
Corresponding Author: sukhovaya@ukr.net
Received March 23, 2020; revised April 6, 2020; accepted May 30, 2020

In this work the structure and corrosion behavior of quasicrystalline cast $Al_{69}Co_{21}Ni_{10}$ and $Al_{72}Fe_{15}Ni_{13}$ alloys in 5-% sodium chloride solution (pH 6.9–7.1) were investigated. The alloys were cooled at 5 K/s. The structure of the samples was studied by methods of quantitative metallography, X-ray analysis, and scanning electron microscopy. Corrosion properties were determined by potentiodynamic method. Stationary potential values were measured by means of long-term registration of (E,τ)–curves using ПI-50-1 potentiostat and ПР–8 programmer with three-electrode electrolytic cell. A platinum electrode served as counter electrode and silver chloride – as reference electrode. The made investigations confirm the formation of stable quasicrystalline decagonal D-phase in the structure of $Al_{69}Co_{21}Ni_{10}$ and $Al_{72}Fe_{15}Ni_{13}$ alloys. In $Al_{69}Co_{21}Ni_{10}$ alloy, at room temperature D-phase coexists with crystalline $Al_9(Co,Ni)_2$ phase, and in $Al_{72}Fe_{15}Ni_{13}$ alloy – with Al_5FeNi phase. Comparison of Vickers hardness of these phases exhibits the following sequence: $H(D-AlCoNi)>H(D-AlFeNi)>H(Al_5FeNi)>H(Al_9(Co,Ni)_2)$. In 5 % sodium chloride solution, the investigated alloys corrode under electrochemical mechanisms with oxygen depolarization. Compared with $Al_{72}Fe_{15}Ni_{13}$ alloy, $Al_{69}Co_{21}Ni_{10}$ alloy has less negative value of stationary potential (–0,48 V and –0,40 V, respectively), and its electrochemical passivity region extends due to the inhibition of anodic processes. For both alloys, transition to passive state in the saline solution is observed. A corrosion current density, calculated from (E,lgi)-curve, for $Al_{69}Co_{21}Ni_{10}$ alloy amounts to 0.12 mA/cm² and for $Al_{72}Fe_{15}Ni_{13}$ alloy – to 0.14 mA/cm². After immersion in the saline solution for 8 days, pits are revealed on the surface of the alloys in areas, mainly where the phase boundaries and flaws are located. The number and size of pits are smaller on the surface of $Al_{69}Co_{21}Ni_{10}$ alloy as compared with those on the surface of $Al_{72}Fe_{15}Ni_{13}$ alloy. The lower corrosion resistance of $Al_{72}Fe_{15}Ni_{13}$ alloy may be explained by the presence of iron-containing phases in its structure. Based on obtained results, the $Al_{69}Co_{21}Ni_{10}$ alloy has been recommended as coating material for rocket-and-space equipment working in marine climate.
KEYWORDS: decagonal quasicrystals, structure, Vickers hardness, electrochemical polarization, pitting corrosion.

The ternary Al–Co–Ni and Al–Fe–Ni alloys are the most interesting stable quasicrystalline materials having decagonal rotation symmetry [1-8]. Decagonal quasicrystals combine two different types of order, periodicity along the rotational axis and non-periodic order perpendicular to it. This property sets decagonal phases apart from periodic crystals, as well as from icosahedral quasicrystals. The interest also is prompted due to the finding of quasicrystalline phases of the above alloys when they are cast under conventional solidification techniques. Quasicrystals have many attractive properties, such as high hardness, low electrical and thermal conductivities, low surface energy, accompanied by a low coefficient of friction, reasonable oxidation and strong corrosion resistance, and unusual optical properties which have not been observed for crystalline alloys [9-13]. These properties can only be used for technological applications in the form of thin film coatings [14-18] or reinforcement particles in metal matrix composites [19-23] in order to circumvent their intrinsic brittleness. In the course of their operation, Al–Co–Ni and Al–Fe–Ni alloys are often subjected to the action of corrosive media, but very little information is available on how such alloys behave in corrosion media.

For many applications of quasicrystalline coatings, e.g. for equipment of mobile platforms for equatorial launches of loads on specialized Zenit-3SL rockets, corrosion resistance under conditions of marine climate is of utmost importance. Therefore, aim of this paper is to investigate structure of quasicrystalline and crystalline phases observed in the cast Al–Co–Ni and Al–Fe–Ni alloys and compare their corrosion characteristics in aqueous sodium chloride solution.

MATERIALS AND METHODS

The quasicrystalline $Al_{69}Co_{21}Ni_{10}$ and $Al_{72}Fe_{15}Ni_{13}$ alloys were prepared by melting of chemically pure components (<99.99 wt. pct.) in a graphite crucible in a Tamman furnace. The samples were cooled at a rate of 5 K/s. The compositions of the alloys were set close to the compositional range where the decagonal phase had been firstly obtained [2,7]. The average chemical composition of the alloys was studied by atomic absorption spectroscopy method. The relative precision of the measurements was better than ± 1 at. pct. The alloys were examined by *Neophot* light-optical microscope (OM). Quantitative metallography was carried out with structural analyzer *Epiquant*. X-ray diffraction analysis (XRD) was done to identify the existing phases in produced samples on an X-ray diffractometer *ДРОН-УМ* with CuKα source. The local phase compositions were determined in a scanning electron microscope *РЭММА 102-02* by energy-dispersive spectroscopy (EDS) on polished unetched cross-sections.

Corrosion behavior was investigated in 5-% NaCl aqueous solution (pH 6.9–7.1) at the temperature of 293±2 K. Electrochemical measurements were performed using a computer-controlled system including *ПI-50-1* potentiostat and *ПР-8* programmer using three-electrode electrolytic cell. The investigated sample was used as working electrode, a

Olena V. Sukhova, Volodymyr A. Polonskyy

platinum plate – as counter electrode, and silver chloride electrode – as reference electrode. A surface of 1 cm^2 was exposed to the solution for all electrochemical experiments. To avoid contamination of the solution by chloride ions, the reference electrode was in contact with the working electrode through an electrolyte bridge. The Luggin capillary filled with the test solution had a porous ceramic membrane at the end to further delay diffusion of species in the solution. The Luggin capillary tip was placed very close to the electrode surface to minimize the ohmic drop of the solution. Saline solution was freshly prepared from distilled water and pure grade chemicals. The electrolyte was exchanged after each measurement in order to avoid contamination of soluble species. Potentiodynamic measurements were carried out by sweeping the potential in the positive or negative direction with a sweep rate of 1 mV/s until a current limit in the mA range is reached.

Model corrosion tests for 1, 2, 3, 4, 8 days in a 5-% NaCl solution at 293±2 K were carried out with specimens 3.0×0.5 cm in size. The specimens were fully immersed in the saline solution. Testing under these conditions was assumed to be equivalent to a 5-years application in marine atmosphere. The surface morphology was examined using a scanning electron microscope (SEM).

RESULTS AND DISCUSSION

The results of metallographic and XRD analyses of the $Al_{69}Co_{21}Ni_{10}$ alloy are summarized in Fig. 1. Two ternary compounds are found in the structure: the crystalline $Al_9(Co,Ni)_2$ phase and decagonal quasicrystalline (D) phase with the composition $Al_{72}Co_{9.5}Ni_{18.5}$, as EDS measurements show. As the D-phase is observed at room temperature the stability of this phase with respect to decomposition into its neighboring phases is clearly confirmed. The average volume fraction of D-quasicrystals is about 59 vol.% of the total alloy volume [24]. Their sizes range from 50 to 80 μm.

a   b
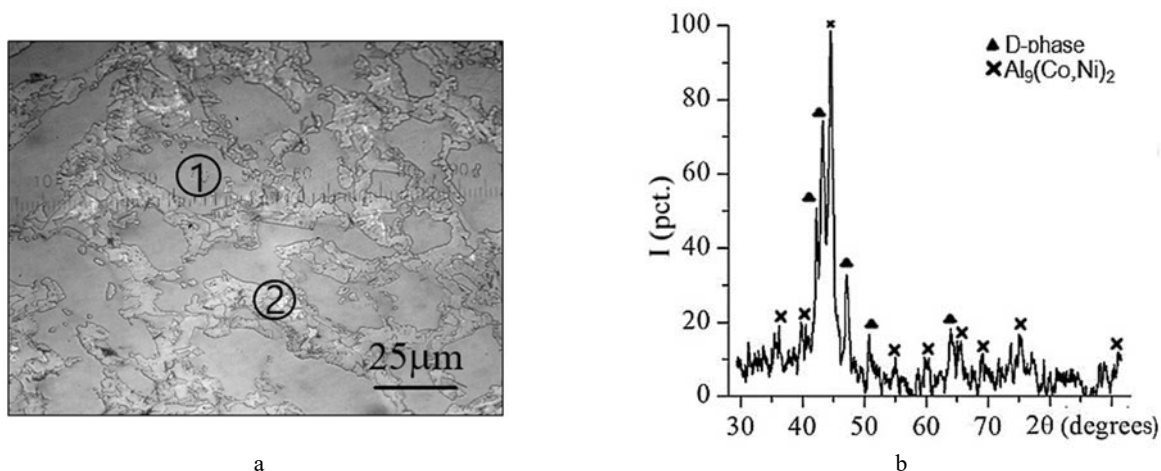
Figure 1. The $Al_{69}Co_{21}Ni_{10}$ alloy: a – OM image, where D-phase (1) and $Al_9(Co,Ni)_2$ (2); b – XRD pattern

The $Al_{72}Fe_{15}Ni_{13}$ alloy exhibits two-phase structure (Fig. 2a). From the XRD, the cast alloy consists of primary Al_5FeNi crystals separated by secondary quasicrystalline decagonal D-phase (Fig. 2b). The estimation of D-phase composition by EDS method gives $Al_{72.5}Ni_{17}Fe_{10.5}$. The volume fraction of D-phase reaches 30 vol. % of a total alloy volume [25].

a   b
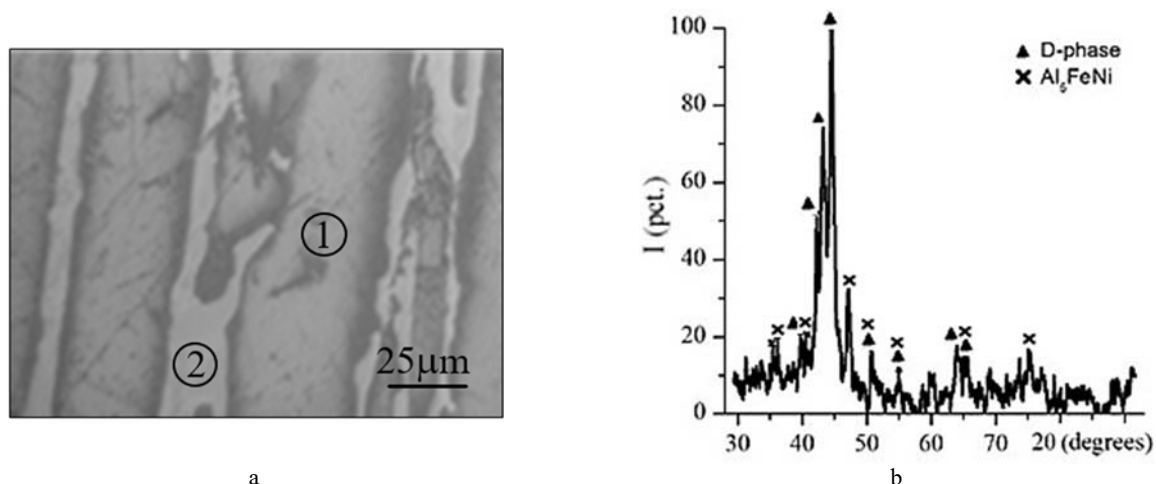
Figure 2. The $Al_{72}Fe_{15}Ni_{13}$ alloy: a – OM image, where Al_5FeNi (1) and D-phase (2); b – XRD pattern

Measurements show that the decagonal D-quasicrystals of $Al_{69}Co_{21}Ni_{10}$ and $Al_{72}Fe_{15}Ni_{13}$ alloys possess a Vickers hardness of about 8.6–10.1 GPa, which is much higher than that for coexisting crystalline phases. Comparison with the intermetallic compounds in the investigated alloys exhibits the following sequence: $H(D-AlCoNi)>H(D-AlFeNi)>H(Al_5FeNi)>H(Al_9(Co,Ni)_2)$.

The studied alloys do not noticeably corrode in 5-% aqueous NaCl solution. Their color and mass do not essentially change. Due to presence of aluminum, both the $Al_{69}Co_{21}Ni_{10}$ and $Al_{72}Fe_{15}Ni_{13}$ alloys exposed to atmosphere after polishing are spontaneously covered with an oxide film. This thin surface film consists predominately of aluminum oxides with also a small contribution of iron, cobalt or nickel oxides. As soon as samples are immersed in 5-% NaCl solution of pH 7.0, the process of the oxide layer stabilization begins. Fig. 3 shows the change of stationary potentials (E_{st}) of $Al_{69}Co_{21}Ni_{10}$ and $Al_{72}Fe_{15}Ni_{13}$ alloys during 45 min. The recorded results reveal that the stationary potentials of the alloys increase very fast towards more positive values during first 300–500 seconds indicating that the major changes in the passive film occur during this time. Afterwards the potential stabilizes reaching a steady value. The result could be attributed to the stabilization of passive oxide film. The stationary potentials amount to –0.48 V and –0.40 V for $Al_{72}Fe_{15}Ni_{13}$ and $Al_{69}Co_{21}Ni_{10}$ alloy, respectively. The $Al_{69}Co_{21}Ni_{10}$ alloy has a slightly nobler potential which indicates more passive state of its surface.
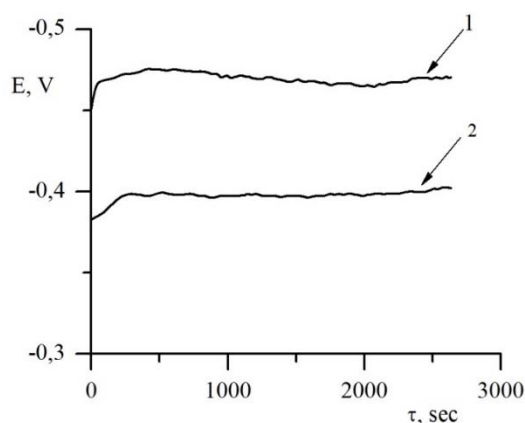
Figure 3. (E,τ)-curves recorded in 5-% NaCl solution (pH=7.0) for $Al_{72}Fe_{15}Ni_{13}$ (1) and $Al_{69}Co_{21}Ni_{10}$ (2) alloys

Fig. 4 illustrates the voltammograms recorded for the $Al_{72}Fe_{15}Ni_{13}$ and $Al_{69}Co_{21}Ni_{10}$ alloys by cyclic potentiodynamic polarization method with periodic sweeping the potential in the opposite directions. As the potential is changed from E_{st} towards more positive values, the anodic current density rises gradually. At potential of ~(–0.3) V, a sharp increase in anodic current is observed which may relate to active dissolution of alloys components. When direction of potential sweep is switched back, the null value of current density is reached at potential of (–0.88) V for the $Al_{72}Fe_{15}Ni_{13}$ alloy (Fig. 4a) and (–0.86) V for the $Al_{69}Co_{21}Ni_{10}$ alloy (Fig. 4b). At potentials more negative than (–1.0) V, a cathodic current density increases which indicates that depolarizer restoration begins. At the next cycle of a potential sweep, the electrochemical passivity regions may be determined. They have close sizes from –1.0 V to –0.5 V for the $Al_{72}Fe_{15}Ni_{13}$ alloy and from –1.0 V to –0.4 V for the $Al_{69}Co_{21}Ni_{10}$ alloy. No active dissolution region is observed, thus indicating that the surface of the alloys is covered with passive oxide layer. This may be explained by the transition of the alloys to passive state due to cobalt and/or nickel present in their composition.
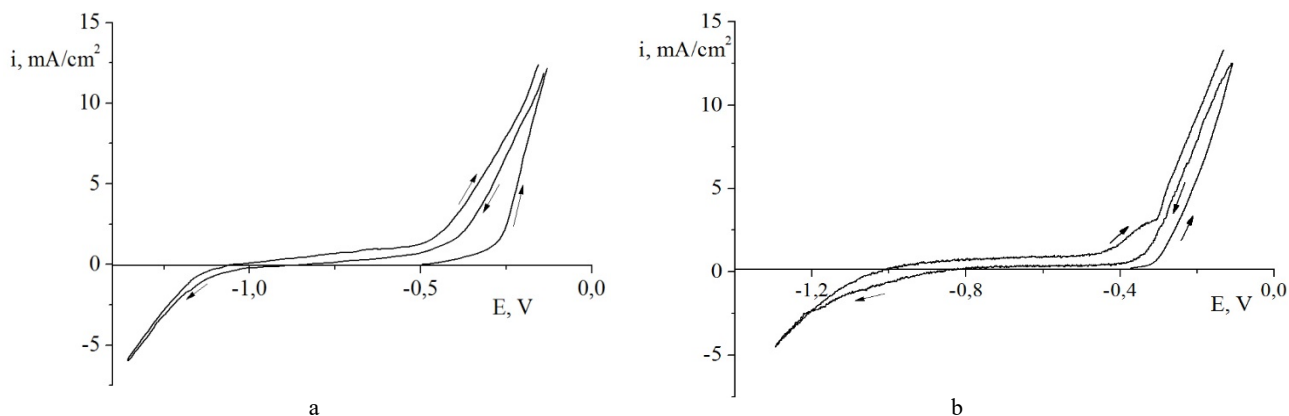
Figure 4. Cyclic voltammogram showing both a positive- and negative-going sweep obtained in 5-% NaCl solution (pH=6.9) for the alloys: a – $Al_{72}Fe_{15}Ni_{13}$; b – $Al_{69}Co_{21}Ni_{10}$.

For both alloys, corrosion in the neutral sodium chloride solution proceeds with oxygen depolarization which gives rise to the close values of the passivity region limit in the negative area of potentials. The extension of electrochemical passivity region towards more positive value of potential for the $Al_{69}Co_{21}Ni_{10}$ alloy may relate to the inhibition of anodic processes. Therefore, the $Al_{72}Fe_{15}Ni_{13}$ alloy has a slightly larger tendency to corrode although the stationary potentials for the investigated alloys follow a similar trend. The (E,lgi)-curves recorded in 5-% NaCl solution are shown in Fig. 5. The intersection point of two plot branches corresponds to a logarithm of corrosion current density (i_{corr}). The value of i_{corr} determined for the $Al_{72}Fe_{15}Ni_{13}$ alloy equals to 0.14 mA/cm² (Fig. 5a), and that for the $Al_{69}Co_{21}Ni_{10}$ alloy is 0.12 mA/cm² (Fig. 5b).

Analysis of the solution left after electrochemical corrosion of the $Al_{69}Co_{21}Ni_{10}$ and $Al_{72}Fe_{15}Ni_{13}$ alloys in the saline media reveals very little Co and/or Ni in solution, implying that the remaining solid surface would be Co- and/or Ni-rich. Hence, the general trend seems to be that the noblest metals remain at the surface during corrosion, while the other components, such as Fe and/or Al, dissolve.
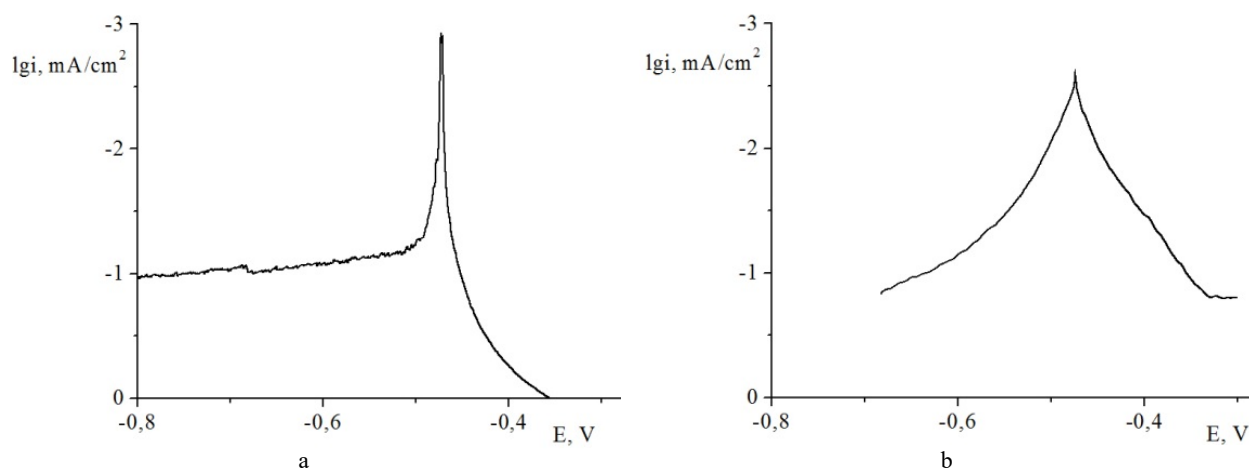
Figure 5. (E,lgi)-curves recorded in 5-% NaCl solution (pH=7.0) for $Al_{72}Fe_{15}Ni_{13}$ (a) and $Al_{69}Co_{21}Ni_{10}$ (b) alloys

After the 8-day immersion test in 5-% NaCl solution, small pits are observed on the surface of the $Al_{72}Fe_{15}Ni_{13}$ alloy (Fig. 6). Pits sites, sized from 5 to 20 μm, are non-uniformly distributed on the surface. The crystalline Al_5FeNi phase and boundaries between the D-phase and Al_5FeNi phase are preferentially dissolved. On the surface of $Al_{69}Co_{21}Ni_{10}$ alloy, pits about 10 μm in size located mainly in the vicinity of defects are revealed as well (Fig. 7). In addition to pitting, preferential dissolution of the interphase boundaries also occurs.
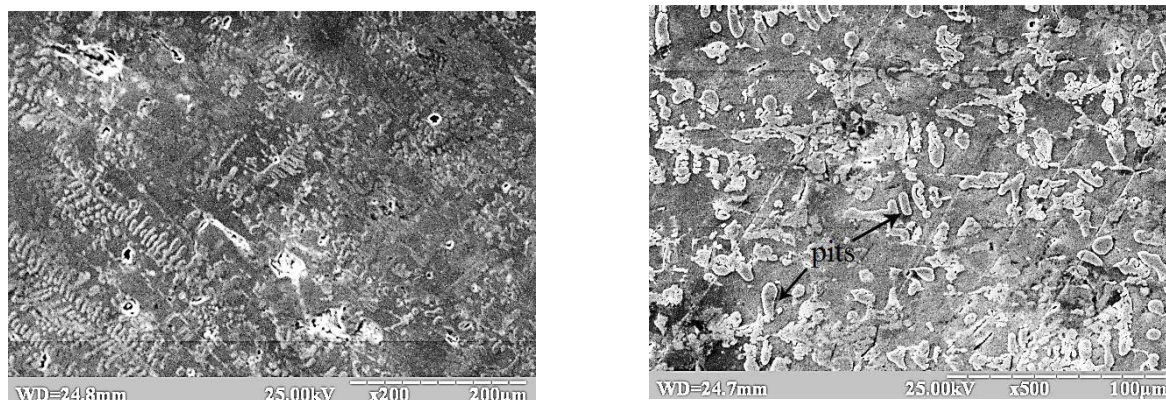
Figure 6. SEM-images of the surface of $Al_{72}Fe_{15}Ni_{13}$ alloy after 8-day immersion test in 5-% NaCl solution (pH=7.0).

Thus, from the electrochemical point of view, the $Al_{69}Co_{21}Ni_{10}$ and $Al_{72}Fe_{15}Ni_{13}$ alloys behave quite similarly in the aqueous sodium chloride solution, but immersion tests show that on the surface of $Al_{72}Fe_{15}Ni_{13}$ alloy visually more pits appear. So, a first order assessment would suggest that the $Al_{72}Fe_{15}Ni_{13}$ alloy has lower resistance to pitting than the $Al_{69}Co_{21}Ni_{10}$ alloy. The reason is that iron-rich phases and their boundaries in the structure of $Al_{72}Fe_{15}Ni_{13}$ alloy are more susceptible to attack by saline solution. The pits on the surface of $Al_{72}Fe_{15}Ni_{13}$ alloy are Ni-rich, apparently forming by dissolution of Al and Fe, and those on the surface of $Al_{69}Co_{21}Ni_{10}$ alloy are Co- and Ni-rich due to preferential dissolution of Al. Corrosion is controlled mainly by chemical composition of the investigated alloys rather than the specific atomic structure of decagonal quasicrystalline D-phase present in their structure.
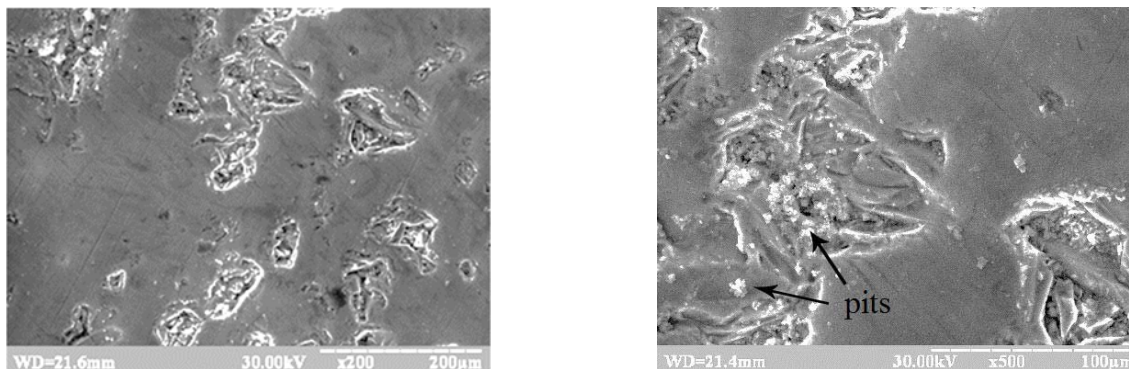
Figure 7. SEM-images of the surface of $Al_{69}Co_{21}Ni_{10}$ alloy after 8-day immersion test in 5-% NaCl solution (pH=7.0).

CONCLUSIONS

The investigations conducted on conventionally solidified $Al_{69}Co_{21}Ni_{10}$ and $Al_{72}Fe_{15}Ni_{13}$ alloys cooled at 5 K/s confirm that both alloys form stable decagonal quasicrystalline D-phase. In $Al_{69}Co_{21}Ni_{10}$ alloy, the primarily solidified phase is D-phase but, in $Al_{72}Fe_{15}Ni_{13}$ alloy, the Al_5FeNi phase. The quasicrystalline D-phase of $Al_{69}Co_{21}Ni_{10}$ alloy coexists with peritectic $Al_9(Co,Ni)_2$ phase. The corrosion of the investigated alloys in 5-% NaCl aqueous solution (pH 6.9-7.0) occurs near the phase boundaries and flawed regions by the electrochemical mechanism. The alloys show an initial stage of dissolution followed by the formation of corrosion layer that blocks further dissolution in the saline solution. The stationary potential for $Al_{69}Co_{21}Ni_{10}$ alloy has more negative value as compared with that for $Al_{72}Fe_{15}Ni_{13}$ alloy. The electrochemical passivity region for $Al_{69}Co_{21}Ni_{10}$ alloy extends due to the inhibition of anodic processes and, therefore, this alloy negligibly corrodes in NaCl solution. As a result, on the surface of the alloy, scarcer and smaller pits are observed. The pits are apparently Ni- or Co-rich, forming by dissolution of Al. The $Al_{72}Fe_{15}Ni_{13}$ alloy has relatively poor corrosion resistance due to preferential dissolution of iron-rich phases in its structure. Therefore, the $Al_{69}Co_{21}Ni_{10}$ alloy shows promise as a coating material to protect rocket-and-space equipment working in marine atmosphere.

ORCID IDs

Olena V. Sukhova, https://orcid.org/0000-0001-8002-0906; **Volodymyr A. Polonskyy,** http://orcid.org/0000-0002-4810-2626

REFERENCES

[1] K. Edagawa, H. Tamaru, S. Yamaguchi, K. Suzuki, and S. Takeuchi, Phys. Rev. B. **50**, 12413 (1994), https://doi.org/10.1103/PhysRevB.50.1213.

[2] A.-P. Tsai, A. Inoue, and T. Masumoto, Mater. Trans. JIM. **30**(2), 150-154 (1989), https://doi.org/10.2320/matertrans1989.30.150.

[3] L. Zhang, Y. Du, H. Xu, C. Tang, H. Chen, and W. Zhang, J. Alloys Comp. **454**, 129-135 (2008), https://doi.org/10.1016/j.jallcom.2006.12.042.

[4] U. Lemmerz, B. Grushko, C. Freiburg, and M. Jansen, Phil. Mag. Lett. **69**(3), 141-146 (2006), https://doi.org/10.1080/09500839408241583.

[5] B. Grushko and K. Urban, Phil. Mag. B. **70**(5), 1063-1075 (2006), https://doi.org/10.1080/01418639408240273.

[6] B. Grushko and T. Velikanova, Computer Coupling of Phase Diagrams and Thermochemistry. **31**, 217-232 (2007), https://doi.org/10.1016/j.calphad.2006.12.002.

[7] R. Wurschum, T. Troev, and B. Grushko, Phys. Rev. B. **52**(9), 6411-6416 (1995), https://doi.org/10.1103/physrevb.52.6411.

[8] Y. Lei, M. Calvo-Dahlborg, J. Dubois, Z. Hei, P. Weisbecker, and C. Dong, J. Non-Cryst. Solids. **330**, 39-49 (2003), https://doi.org/10.1016/jnoncrysol.2003.08.059.

[9] E. Huttunen-Saarivirta, J. Alloys Comp. **363**(1-2), 150-174 (2004), https://doi.org/10.1016/S0925-8388(03)00445-6.

[10] O.V. Sukhova, V.A. Polonskyy, and K.V. Ustinova, Metallofiz. Noveishie Technol. **40**(11), 1475-1487 (2018), https://doi.org/10.15407/mfint.40.11.1475. (in Ukrainian)

[11] O.V. Sukhova, V.A. Polonskyy, and K.V. Ustinova, Mater. Sci. **55**(2), 285-292 (2019), https://doi.org/10.1007/s11003-019-00302-2.

[12] I.M. Spiridonova, E.V. Sukhovaya, V.F. Butenko, A.P. Zhudra, A.I. Litvinenko, and A.I. Belyi, Powder Metallurgy and Metal Ceramics. **32**(2), 139-141 (1993), https://doi.org/10.1007/BF00560039.

[13] O.V. Sukhova, V.A. Polonskyy, and K.V. Ustinova, Voprosy Khimii i Khimicheskoi Technologii. **6**(121), 77-83 (2018), https://doi.org/10.32434/0321-4095-2018-121-6-77-83. (in Ukrainian)

[14] C. Zhou, R. Cai, S. Gong, and H. Xu, Surf. Coat. Technol. **201**, 1718-1723 (2006), https://doi.org/10.1016/j.surfcoat.2006.02.043.

[15] Y. Kang, C. Zhou, S. Gong, and H. Xu, Mater. Sci. Forum. **475-479**, 3355-3358 (2005), https://doi.org/10.4028/www.scientific.net/MSF.475-479.3355.

[16] D.S. Shaitura and A.A. Enaleeva, Crystallography Reports. **52**(6), 945-952 (2007), https://doi.org/10.1134/S1063774507060041.

[17] S.I. Ryabtsev, V.A. Polonskyy, and O.V. Sukhova, Powder Metallurgy and Metal Ceramics. **58**(9-10), 567-575 (2020), https://doi.org/10.1007/s11106-020-00111-2.

[18] I.M. Spyrydonova, O.V. Sukhova, and G.V. Zinkovskij, Metall. Min. Ind. **4**(4), 2-5 (2012). (in Russian)

[19] O.V. Sukhova, Metallofiz. Noveishie Technol. **31**(7), 1001-1012 (2009). (in Ukrainian)

[20] I.M. Spiridonova, E.V. Sukhovaya, S.B. Pilyaeva, and O.G. Bezrukavaya, Metall. Min. Ind. **3**, 58-61 (2002). (in Russian)

[21] G. Laplanche, A. Joulain, and J. Bonneville, J. Alloys Comp. **493**, 453-460 (2010), https://doi.org/10.1016/j.jallcom.2009.12.124.

[22] O.V. Sukhova and K.V. Ustinova, Functional Materials. **26**(3), 495-506 (2019), https://doi.org/10.15407/fm26.03.495.

[23] O.V. Sukhova and Yu.V. Syrovatko, Metallofiz. Noveishie Technol. **33**(Special Issue), 371-378 (2011). (in Russian)

[24] O.V. Sukhova and Yu.V. Syrovatko, Metallofiz. Noveishie Technol. **41**(9), 1171-1185 (2019), https://doi.org/10.15407/mfint.41.09.1171.

[25] O.V. Sukhova, V.A. Polonskyy, and K.V. Ustinova, Physics and Chemistry of Solid State. **18**(2), 222-227 (2017), https://doi.org/10.15330/pcss.18.2.222-227.

СТРУКТУРА ТА КОРОЗІЯ КВАЗІКРИСТАЛІЧНИХ ЛИТИХ СПЛАВІВ Al–Co–Ni ТА Al–Fe–Ni У ВОДНОМУ РОЗЧИНІ NaCl

Олена В. Сухова, Володимир А. Полонський

Дніпровський національний університет імені Олеся Гончара

49010, Україна, м. Дніпро, просп. Гагаріна, 72

В роботі досліджено структуру і особливості корозії квазікристалічних литих сплавів $Al_{69}Co_{21}Ni_{10}$ і $Al_{72}Fe_{15}Ni_{13}$ в 5 % розчині натрій хлориду (pH 6,9-7,1). Швидкість охолодження сплавів складала 5 К/с. Структуру сплавів вивчали методами кількісної металографії, рентгеноструктурного аналізу, растрової електронної мікроскопії. Корозійні властивості досліджували потенціодинамічним методом. Величини стаціонарних потенціалів визначали шляхом довготривалої реєстрації (E,τ)-залежностей за допомогою потенціостата ПІ-50-1 та програматора ПР-8 з використанням триелектродної комірки. Допоміжним електродом слугував платиновий електрод, електродом порівняння – хлоридсрібний. Проведені дослідження підтверджують утворення квазікристалічної декагональної D-фази в структурі сплавів $Al_{69}Co_{21}Ni_{10}$ і $Al_{72}Fe_{15}Ni_{13}$. У сплаві $Al_{69}Co_{21}Ni_{10}$ за кімнатної температури D-фаза співіснує з кристалічною фазою $Al_9(Co,Ni)_2$, а в сплаві $Al_{72}Fe_{15}Ni_{13}$ – з фазою Al_5FeNi. У порядку зростання мікротвердості ці фази можна розташувати в такій послідовності: $H(D-AlCoNi)>H(D-AlFeNi)>H(Al_5FeNi)>H(Al_9(Co,Ni)_2)$. У 5 % розчині натрій хлориду досліджені сплави кородують за електрохімічним механізмом з кисневою деполяризацією. Порівняно зі сплавом $Al_{72}Fe_{15}Ni_{13}$, сплав $Al_{69}Co_{21}Ni_{10}$ має менш від'ємні значення стаціонарного електрохімічного потенціалу (–0,48 В і –0,40 В відповідно), а його зона електрохімічної інертності розширюється за рахунок гальмування анодних процесів. Обидва досліджені сплави переходять у пасивний стан у сольовому розчині. Величина струму корозії, розрахована з (E,lgi)-залежностей, для сплаву $Al_{69}Co_{21}Ni_{10}$ складає 0,12 мА/см^2, а для сплаву $Al_{72}Fe_{15}Ni_{13}$ – 0,14 мА/см^2. Після перебування в сольовому розчині на поверхні сплавів виявлені пітінги переважно в місцях розташування міжфазних границь поділу і дефектів. Кількість та розміри пітінгів на поверхні сплаву $Al_{69}Co_{21}Ni_{10}$ значно менші, ніж на поверхні сплаву $Al_{72}Fe_{15}Ni_{13}$. Більш низьку корозійну тривкість сплаву $Al_{72}Fe_{15}Ni_{13}$ пояснено присутністю в його структурі залізовмісних фаз. Послуговуючись отриманими результатами, для створення покриттів на деталях ракетно-космічної техніки, що працюють в умовах морського клімату, рекомендовано сплав $Al_{69}Co_{21}Ni_{10}$.

КЛЮЧОВІ СЛОВА: декагональні квазікристали, структура, мікротвердість, електрохімічна поляризація, пітінгова корозія.

СТРУКТУРА И КОРРОЗИЯ КВАЗИКРИСТАЛЛИЧЕСКИХ ЛИТЫХ СПЛАВОВ Al–Co–Ni И Al–Fe–Ni В ВОДНОМ РАСТВОРЕ NaCl

Елена В. Сухова, Владимир А. Полонский

Днипровский национальный университет имени Олеся Гончара

49010, Украина, г. Днипро, просп. Гагарина, 72

В работе исследовали структуру и особенности коррозии квазикристаллических литых сплавов $Al_{69}Co_{21}Ni_{10}$ и $Al_{72}Fe_{15}Ni_{13}$ в 5 % растворе хлорида натрия (pH 6,9–7,1). Скорость охлаждения сплавов составляла 5 К/с. Структуру сплавов изучали методами количественной металлографии, рентгеноструктурного анализа, растровой электронной микроскопии. Коррозионные свойства исследовали потенциодинамическим методом. Величины стационарных потенциалов определяли путем длительной регистрации (E,τ)–зависимостей с помощью потенциостата ПИ-50-1 и программатора ПР-8 с использованием трехэлектродной ячейки. Вспомогательным электродом служил платиновый электрод, электродом сравнения – хлоридсеребряный. Проведенные исследования подтверждают образование квазикристаллической декагональной D-фазы в структуре сплавов $Al_{69}Co_{21}Ni_{10}$ и $Al_{72}Fe_{15}Ni_{13}$. В сплаве $Al_{69}Co_{21}Ni_{10}$ при комнатной температуре D-фаза сосуществует с кристаллической фазой $Al_9(Co,Ni)_2$, а в сплаве $Al_{72}Fe_{15}Ni_{13}$ – с фазой Al_5FeNi. В порядке увеличения микротвердости эти фазы можно расположить в такой последовательности: $H(D-AlCoNi)>H(D-AlFeNi)>H(Al_5FeNi)>H(Al_9(Co,Ni)_2)$. В 5 % растворе хлорида натрия исследованные сплавы корродируют по электрохимическому механизму с кислородной деполяризацией. По сравнению со сплавом $Al_{72}Fe_{15}Ni_{13}$, сплав $Al_{69}Co_{21}Ni_{10}$ имеет менее отрицательные значения стационарного потенциала (–0,48 В и –0,40 В соответственно), а его зона электрохимической пассивности расширяется за счет торможения анодных процессов. Оба сплава переходят в пассивное состояние в солевом растворе. Величина тока коррозии, рассчитанная по (E,lgi)–зависимостям, для сплава $Al_{69}Co_{21}Ni_{10}$ составляет 0,12 мА/см^2, а для сплава $Al_{72}Fe_{15}Ni_{13}$ – 0,14 мА/см^2. После пребывания в солевом растворе на поверхности сплавов выявлены питтинги преимущественно в местах расположения межфазных границ и дефектов. На поверхности сплава $Al_{69}Co_{21}Ni_{10}$ питтинги образуются в меньшем количестве и имеют меньшие размеры, чем на поверхности сплава $Al_{72}Fe_{15}Ni_{13}$. Более низкую коррозионную стойкость сплава $Al_{72}Fe_{15}Ni_{13}$ объяснено присутствием в его структуре железосодержащих фаз. С учетом полученных результатов, для создания покрытий на деталях ракетно-космической техники, работающих в условиях морского климата, рекомендован сплав $Al_{69}Co_{21}Ni_{10}$.

КЛЮЧЕВЫЕ СЛОВА: декагональные квазикристаллы, структура, микротвердость, электрохимическая поляризация, питтинговая коррозия.

INVESTIGATION OF EBT3 RADIOCHROMIC FILM RESPONSE IN A HIGH-DOSE RANGE OF 6 MV PHOTON AND 6 MEV ELECTRON BEAMS USING A THREE-COLOR FLATBED SCANNER

Kerem Duruer[a,*], **Durmuş Etiz**[a], **Haluk Yücel**[b]

ᵃEskişehir Osmangazi University Faculty of Medicine Department of Radiation Oncology
26010 Odunpazarı, Eskişehir, Turkey
ᵇAnkara University Institute of Nuclear Sciences
06500 Beşevler, Ankara, Turkey
*Corresponding Author: kduruer@ogu.edu.tr

Radiochromic film dosimetry has been commonly used for determination of dose measurement in radiotherapy for many years because of their high spatial resolution, low energy dependence and its approximate tissue equivalent. Additionally, it has other practical advantages, e.g.it is suitable for therapy range beam qualities, a water resistance material, a relatively insensitive to visible light, and does not need to make bathing process to obtain dose information. They are also independent to dose rate. Hence, they are very useful and practical for clinical applications such as brachytherapy, electron therapy, skin dose measurements and stereotactic radiotherapy. Among them, the dynamic dose range of EBT3 radiochromic films are generally recommended for the dose range of 0.1 to 20 Gy. However, in this study, it is aimed to observe the behavior of EBT3 films in high dose range of up to 90 Gy under the irradiations. For this aim, the net optical densities were obtained with increasing dose values under photon and electron beams by employing three color scanning channels (red-green-blue). Thus, for making calibration curves, it was decided which color channel for EBT3 radiochromic film would be the most suitable one in different dose ranges. In experimental setup, the reference circumstances were first established and dose calibration procedure was carried out in RW3 phantom. Then the irradiated films were cut carefully into 2×2.5 cm² pieces, and they were grouped into 2 as irradiation and control groups. The control group was waited for background, i.e. they are not irradiated. Before the irradiation, two groups of films have been scanned in flatbed scanner for three channels. After that, the irradiation group films were placed to align the exact place of effective point of ionization chamber under the reference condition. Later, they were irradiated one by one to up to 90 Gy with using 6 MV and 6 MeV beam qualities, respectively. Subsequently, both of film groups were again scanned in flatbed scanner for three –color channels. Optical densities and their standard deviations corresponding to the chosen dose values were obtained from the scanned films. Thus, calibration curves were plotted for all three colors channel according to two different beam conditions. The results obtained for 6 MV beam quality showed that if red color channel is selected for 0.9 Gy-7.3 Gy dose range, and green color channel is selected for 7.3 Gy-42.8 Gy dose range, and blue color channel is selected for 42.8 Gy-90.0 Gy dose range, the percentage uncertainty values in the obtained results are minimal. For the 6 MeV beam quality, if red color channel is selected for 0.9 Gy-7.7 Gy dose range, and green color channel is selected for 7.7 Gy-45.3 Gy dose range, and blue color channel is selected for 45.3 Gy-90.0 Gy dose range, the percentage uncertainty values in the obtained results are minimal. In conclusion, the percentage uncertainty values for the obtained results were evaluated for 6 MV photon and 6 MeV electron energies by using different scanning channels of EBT3 radiochromic film. It has been found that measurements having low percentage uncertainty values can be achieved by changing the scanning channel by deciding proper combinations with increasing doses for both energies (6MV photon and 6 MeV electron). The study also shows that EBT3 radiochromic films can be used at lower percentage uncertainty values at doses higher than the recommended dose range values.
KEYWORDS: Radiochromic Film, Uncertainty, High Dose Range, Radiotherapy, Flatbed Scanner

Radiochromic films are very useful two-dimensional (2D) dosimetric systems well known for many advantages, such as high spatial resolution [1-5], low energy dependence at a wide energy range of energies greater than 100 keV [6], approximating tissue equivalence at radiotherapy energies [6], water resistance [4,7,8], relative insensitivity to visible light, which allows the processing and handling of the film in room light [4,9,10], minimal self-spontaneous darkening after film irradiation, thus eliminating the need for any post-irradiation bathing procedure to reveal darkening in contrast to conventional radiography films. Compared with other 2D dosimetric systems, radiochromic films, with their specific suitable properties [2,11], are considered to be highly effective 2D detectors [5]. They provide a highly detailed dose map in a 2D plane and can also be used for a three-dimensional (3D) volumetric analysis when curled or coiled [9]. For almost 30 years (by the mid 1980's) [1], these films have been used for both clinical and research purposes, including brachytherapy, electron therapy, total skin electron therapy, skin dose measurements, whole-body irradiation, stereotactic radiotherapy, dosimetric characterization of proton therapy, and dose verification during cell irradiation in radiobiological experiments [2,3].

Following the launch in 2004 of the EBT GAFChromic film in the medical market, EBT2 GAFChromic film was introduced in 2008. It has the same sensitive layer as in the first version, but the non-homogeneity of the sensitive layer was corrected through the addition of a yellow marker dye. In 2011, the EBT3 GAFChromic film entered the medical market, and this improved version eliminates the artifacts produced by the EBT2 film, such as Newton's rings [5].

Light intensity measurements are conducted to determine the radiochromic film response using transmission, reflection, or both depending on the scanner type and function. Since radiochromic films generally have a wide optical absorption spectrum, the frequency or bandwidth of the light source to be used in the scanner must be specified in

advance [10]. Two main absorption bands lying in 636 ± 3 nm and 585 ± 2 nm have been shown in the optical absorption spectra of EBT, EBT2 and EBT3 radiochromic films, some researchers suggested the presence of a third absorption band with a lower center lying in 560 ± 6 nm [8]. For EBT3 radiochromic films, the manufacturer recommends the use of the red channel for irradiation up to 8 Gy and the green channel for irradiation at doses from 8 to 40 Gy [12,13].

In this study, the commercially available EBT3 GAFChromic[TM] (Ashland Specialty Ingredients, Bridgewater, NJ, USA) was selected as a radiochromic film frequently examined by other researchers [1,2,4,5,13-15]. The manufacturer of this radiochromic film recommends the use of a dose range of 0.01-30 Gy [2]. However, with the use of high doses in radiotherapy (e.g. stereotactic radiosurgery (SRS) and stereotactic body radiation therapy (SBRT)) [16], the use of radiochromic films in these high doses is increasing. It should also be noted that there are few research findings for a higher dose range; for example, from 40 Gy up to 90 Gy [3,17] for radiochromic film irradiations. Thus, the aim of this study was to investigate the response behavior of EBT3 radiochromic films for 6 MV photon and 6 MeV electron beams. For an accurate calibration of the films, the present study covered the dose range recommended by the manufacturer and further higher doses outside this range (90 Gy) for three different scanning channels (red, green, and blue) in a flatbed scanner. For 6 MV photon and 6 MeV electron beams, it is important to determine the optimal scanning channel for a wide dose range by scanning the RGB channels. To do this, the percentage uncertainty values will be calculated from these calibration curves for the comparison and decision for proper scanning channel. This study also aimed at investigating the ideal scanning time for the EBT3 films for different scanning channels in terms of polymerization [2], which continues after irradiation and actually never stops.

MATERIAL AND METHOD

Radiochromic films can be used as reference dosimetric systems and are therefore utilized in absolute dose measurements, as well as in other dosimetric systems (e.g., ion chambers) [2]. The main principle of dose measurements by reference dosimetric systems using films is that they are based on the calibration curve obtained under reference conditions. Thus, the reference dose values must be measured under reference conditions prior to the calibration process. For this purpose, in this study, the TRS 398 protocol [18] was selected as reference measurement conditions.

Calibration of radiochromic film (dosimeter)

The calibration process of the radiochromic films was carried out at 6 MV photon and 6 MeV electron beam qualities using the Elekta Precise model linear accelerator (Elekta AB, Stockholm, Sweden) at the Radiation Oncology Department of Eskişehir Osmangazi University Medical Faculty Hospital. In the calibration process, first, the output (dose) values were measured and calibrated [18]. For this purpose, the experimental setup was established by using 30×30 cm^2 water-equivalent solid phantoms (RW3 Slab Phantom, PTW-Freiburg, Freiburg, Germany). A 0.6 cc PTW Farmer cylindrical ion chamber (PTW-Freiburg, Freiburg, Germany) was utilized for the 6 MV photon beam quality and a 0.02 cc PTW Marcus-type parallel plate ion chamber (PTW-Freiburg, Freiburg, Germany) for the 6 MeV electron beam quality. These ion chambers were calibrated at SSDL (Secondary Standard Laboratory) of the Turkish Atomic Energy Authority. To ensure that the measurements were performed under reference conditions, the effective point of the ion chamber was placed at a depth of 10 cm for the 6 MV photon beam quality and the d_{max} depth (measured with water phantom measurement and the measurement result was 1.2 cm) for the 6 MeV electron beam. A 20 cm solid phantom was placed under the ion chambers at all energies to capture backscatter radiation. With the gantry set to 0^0 angle, the source detector distance was adjusted to 100 cm and the field size to 10×10 cm^2. Before the irradiation process, the electrometer was turned on and allowed to warm up for approximately 20 minutes without any irradiation. Irradiations were performed at 10, 20, 30, 50, 100, 200, 400 and 1000 MU, respectively, and these measurements were repeated three times, in which one monitor unit (MU) equals approximately to the 0.01Gy absorbed dose value.

In this study, at the times when the films were not being irradiated or scanned, they were always stored in dark in a temperature-controlled environment at room temperature. The available EBT3 films from lot number 05171701 was used and they had not expired. The films were handled in accordance with the protocol AAPM Task Group55 [19]. While handling with the films, gloves were always worn to prevent artifact formation on their surfaces during all procedures, such as cutting and placing the films in the scanner. Clean sharp scissors were used to cut the films in order to minimize damage to their layers [10].

The sensitive layer in the radiochromic film changes color when exposed to radiation due to polymerization. The absorption of the measurement light by the film results in the film itself acting as a polarizer. Thus, rotating the film in the scanner would produce different results even in the same region of interest (ROI) [(2)]. In addition, reverse-reading of the irradiation side, which is a problem encountered in the previous-generation EBT2 film (the active layer of EBT2 radiochromic films is not completely centered [2]), is not seen in new-generation EBT3 radiochromic films due to the sensitive layer being located right in the center, allowing for the separation of the irradiation and reading surfaces.

According to the calibration procedure described by Devic et al. [2], the films for which the calibration curves are to be obtained are divided into two groups: those to be irradiated and the non-irradiated control films that are used to eliminate the effect of natural radiation caused by light and radiation in the environment on the measurements. These two batches of films were scanned both before and after the irradiation process. Before scanning, empty scans were performed after waiting for 15 min to warm up the scanner.

The films were cut into rectangles of 2.0×2.5 cm² pieces and placed in the scanner in the same direction. After radiochromic films are irradiated by ionizing radiation, the color components are separated when the films are digitized with white light. When radiochromic films were used, multi-channel scanners would offer good results due to their high sensitivity resulting from their high selectivity to the red channel in the low-dose region and similar sensitivity in high-dose areas for the green and blue channels [15]. In flatbed scanners, the most optimal scanning mode is RGB, resulting in less noise and higher sensitivity; therefore, we chose the 48-bit mode; i.e., 16-bit depth for each color [2]. The scanner used in the research was a multi-channel Epson Expression 11000XL Flatbed scanner (Epson Seiko Corporation, Nagano, Japan).

The films to be irradiated and the control films were placed flat in order to eliminate any rotational effect and at the center of the scanner in the same direction to eliminate any lateral scattering effect [5]. Scanning was performed twice at 72 dPi (dots per inch) scan resolution in the transmission mode and horizontal orientation. Four films were scanned at a time (lateral scanning length of about 10 cm). The results obtained were evaluated by taking the average of the two scans.

During the scanning process, a signal may be generated in the detector even if there is no transmission, which is due to the thermal noise caused by the Charge Coupled Device (CCD) detector [2]. In order to prevent this signal from affecting the measurement results, pieces of thin black cardboard thick enough were used to prevent the passage of scanning light, and these results were recorded as 'background signal' and subtracted from the pixel values of the irradiated and control group films during the calculation.

After performing the pre-irradiation scanning process, the EBT3 radiochromic films were irradiated by dose-calibrated 6 MV photon and 6 MeV electron beam qualities with 0-90 Gy dose range. The small pieces of the films were irradiated one by one under the same geometrical and dosimetric conditions described as the reference conditions, as shown in Figure 1, in which the films are placed in a water-equivalent solid phantom at a depth corresponding to the effective point of an ion chamber. In addition, considering that polymerization continues after irradiation, in order to determine the changes in polymer behavior over time for different scanning channels, one film was irradiated up to 10 Gy at the 6 MV photon energy and scanned immediately after irradiation while the others were scanned at post-irradiation hours 0, 1, 2, 3.5, 4.5, 5.5, 6.5, 7.5, 8.5, 12, 24, 48 and 120. The obtained results were evaluated separately for each channel in terms of the variation in optical density by scanning time. In this procedure, the scanning performed immediately after irradiation was adopted as "reference scanning" for all three channels to evaluate the % differences in other scan times in term of optical density. Here, it should be noted that in accordance with the result obtained from this part of the study, all the remaining scans were carried out approximately 48 hours after irradiation to minimize the effect of radiation-induced continuous polymer behavior [2,10,16,20,21].
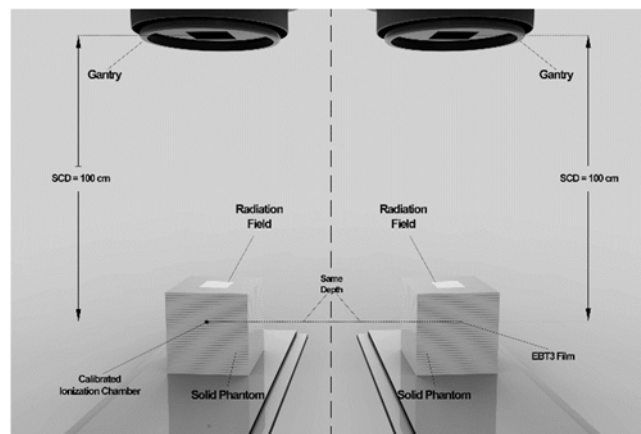
Figure 1. Experimental setup of beam and radiochromic film calibration

The images of the films that were scanned were saved in the "*.tiff "(tagged image file format) format and opened in Image J image-processing software (National Institutes of Health, 1997). Since the beams used in the calibration process are assumed to be homogeneous and most radiochromic films and 2D detector systems slightly deviate from homogeneity by nature; therefore, five ROIs were determined and their pixel values were then combined in weighted averages. The weighted average values were evaluated to achieve more homogeneous results in these measurements. The images of each film were measured individually for the RGB channels. The measurement results were calculated separately using Equations which are described by Devic et al. [2]. The optical density and its standard deviation were determined for each energy, as well as for the three different channels.

RESULTS AND DISCUSSION

Figure 2 shows the percentage change of optical density in the films for the RGB channels with the increasing reading time (i.e., time of scanning). This indicates that the optical densities in the RGB channels were strongly related to the time of scanning when we changed it from 0 to 120 hours under reference irradiation conditions. A remarkable

increase in optical density was observed with the delay in scanning time for all three channels, and after a certain period, the percentage of increase began to gradually decrease. The percentage difference at hour 120 was 6.02% for the red channel, 7.72% for green, and 15.97% for blue. For all three channels, the increase after hour 24 was reduced compared to the increase within the first 24 hours, and the difference between hours 24 and 48 hours was 0.71% for the red channel, 1.24% for green, and 1.72% for blue. The differences in optical density between hours 48 and 120 were 0.83%, 0.56% and 0.26% for the red, green and blue channels, respectively. In particular, there was a remarkable increase in optical density for all three channels within the first 12 hours. Although the results of the 12th hour significantly differed from that of the 24th-hour reading, which is a widely used protocol [2], the results mentioned above support the idea that performing reading after 48 hours of radiation exposure provides more accuracy in the evaluation of the measurement results when EBT3 films are used.
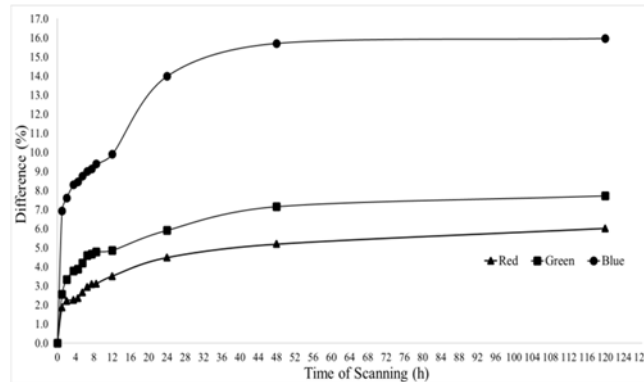
Figure 2. Percentage Difference of Optical Density of EBT3 Radiochromic Film in different scanning channels
when post-irradiation time was selected as reference time

Considering that the differences that occurred within 72 hours from hour 48 to hour 120 was very low for all three channels while the 24-hour differences from hours 24 to 48 were greater compared to the 72-hour differences and that polymerization never stops. From these findings, the optimum scanning time for the EBT3 radiochromic film was determined as 48 hours. In the literature, Borca et al. [17] irradiated EBT3 radiochromic films at different doses from 0.3 Gy to 4 Gy and compared the scan results (in terms of optical density) obtained at different hours from 30 minutes to 6 hours with the 24-hour measurement results. The authors calculated the difference in optical density between the second- and 24th- hour scan results to be less than 2.5%, which was similar 2.48% for the red channel at 10 Gy in our study. In addition, among the three channels, the highest percentage deviation from the reference optical density values obtained immediately after irradiation was observed in the blue channel and the lowest in the red channel. The % difference in optical density for hour 24 was 4.48% for the red channel, 5.91% for the green channel, and 13.99% for the blue channel. From this perspective, if the blue channel is to be used, it is important to wait for 48 hours before reading in order to achieve measurement results with lower uncertainties.
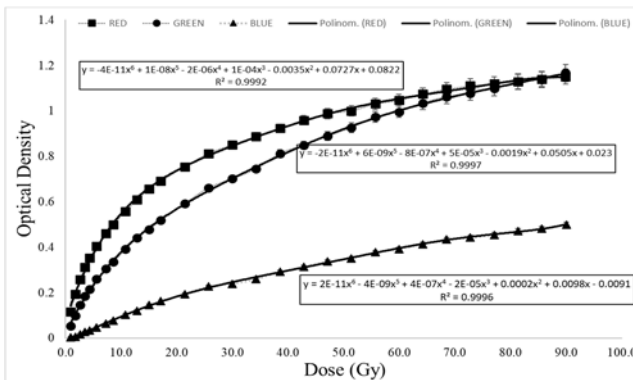
Figure 3. The calibration curves of EBT3 radiochromic film for the three channels at 6 MV photon beam quality
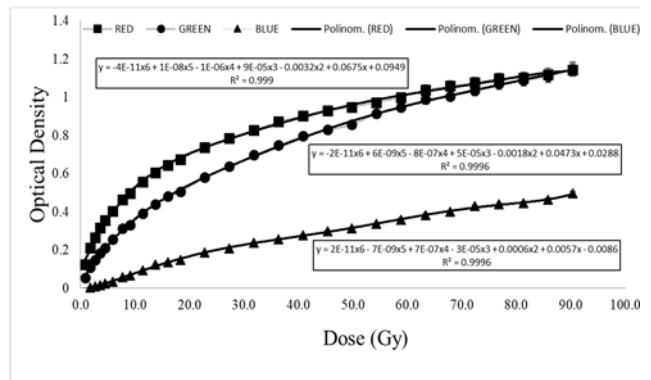
Figure 4. The calibration curves of EBT3 radiochromic film for the three channels at 6 MeV electron beam quality

The calibration curves are shown in Figures 3 and 4 with polynomial fit function for the EBT3 radiochromic film for the three channels at 6 MV photon and 6 MeV electron beam qualities, respectively. The results obtained for the 6 MV photon and 6 MeV electron beam qualities revealed similar trends in the reading values. The curves obtained for the red and green channels showed an increasing tendency in optical density with a greater slope in the low- and medium-dose

regions (up to 20 Gy) while the slope of this increase began to decrease after about 20 Gy, with a considerable decrease seen in the range of about 40-50 Gy. For the blue channel, there was a continuous increase with a lower slope across all dose regions. This behavior of the three channels is consistent with the reported results in the literature [3,17]. We observed that the considerable decrease in the slope after about 40-50 Gy for the red and green channels, but not for the blue channel can be explained by the absorption spectrum of the EBT3 radiochromic film. In these films, the absorption rate is higher for the red and green channels than in the blue channel, in which saturation is only observed after 40-50 Gy, this result explains why there was a remarkable decrease in the rate of increase in optical density in this dose region [3].

The % uncertainty being low in the low-dose region (0-8 Gy) for the red channel, medium-dose region (8-40 Gy) for the green channel, and high-dose region (>40 Gy) for the blue channel at both beam qualities can be explained by the behavior of the EBT3 radiochromic film toward these three colors in the absorption spectrum. Marroquín [8] investigated the absorption spectrum of the EBT3 radiochromic film and observed that the highest absorption occurred in the red region. Therefore, when the low-dose region is examined, the % uncertainty value in the red channel with the highest absorption is expected to be low. Accordingly, in the high-dose region, the uncertainty in the blue channel with an absorption rate lower than the other two-color channels (red-green) would be lower due to not having yet reached saturation. The uncertainty percentages obtained in this study for two different beam qualities were similar to those reported by Marroquín [3] for the 6 MV photon energy up to 120 Gy. Figures 5 and 6 show the % uncertainty values for three channels and Figures 7 and 8 show the most optimal scanning channels for the 6 MV photon and 6 MeV electron beam qualities, which should be used in terms of % uncertainty in a dose region of approximately 90 Gy. According to the graph obtained for the 6 MV photon beam quality, the % uncertainty would be lower for the values acquired using the red channel at doses up to 7.3 Gy, green channel at 7.3 Gy to 42.8 Gy, and blue channel at 42.8 Gy to 90.0 Gy, compared to the cases in which these channels are used at different doses. The graph obtained for the 6 MeV electron energy revealed that the uncertainty rate would be lower if the red channel is used at doses up to 7.7 Gy, green channel at 7.7 Gy to 45.3 Gy, and blue channel at 45.3 Gy to 90.0 Gy. These findings are in agreement with the manufacturer's recommendations and the results reported by Marroquín [3].
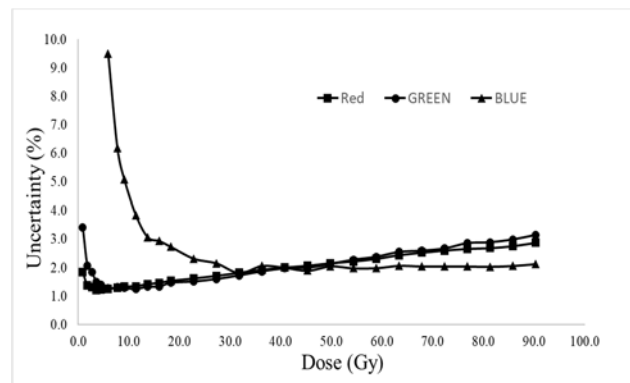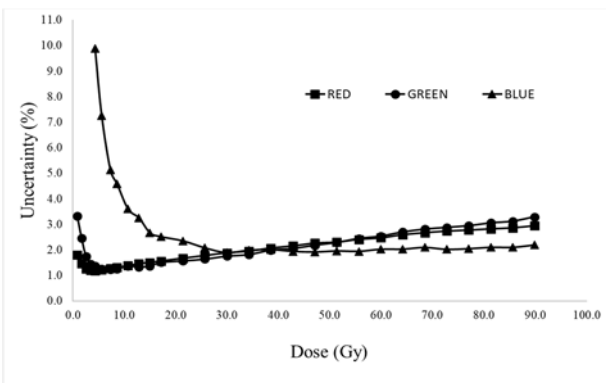
Figure 5. Uncertainty analysis for 6 MV Photon Beam Calibration Curves for all three color channel (It isn't shown in the graph as the uncertainty % of the values for blue channel below 5 Gy was higher than %10)

Figure 6. Uncertainty analysis for 6 MeV Electron Beam Calibration Curves for all three color channel (It isn't shown in the graph as the uncertainty % of the values for blue channel below 6 Gy was higher than %10)
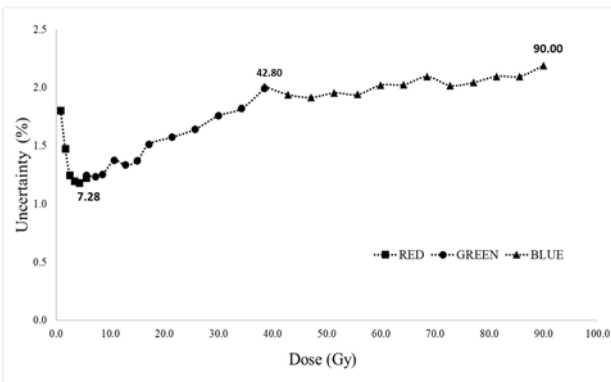
Figure 7. The most optimal scanning channels for the 6 MV photon beam quality, which should be used in terms of % uncertainty in a dose region of 90 Gy
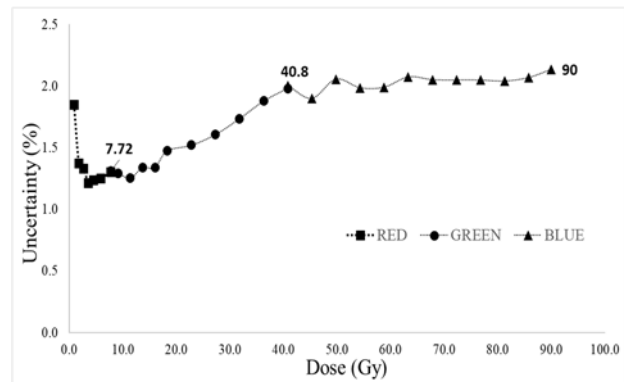
Figure 8. The most optimal scanning channels for the 6 MeV photon beam quality, which should be used in terms of % uncertainty in a dose region of approximately 90 Gy

CONCLUSION

In this study, the calibration curves of EBT3 radiochromic films were obtained using higher dose values of up to 90 Gy for the 6 MV photon and 6 MeV electron beam qualities to determine the best scanning channel at different doses in terms of minimum % uncertainty values for each beam quality. Therefore, this study would be useful for users who will work with EBT3 radiochromic film and multi-channel scanner at doses up to 90 Gy for the 6 MV photon and 6 MeV electron beam qualities. In addition, when EBT3 radiochromic films are used in a multi-channel scanner at either 6 MV photon or 6 MeV electron beam quality, the scanning channel should be selected as red for the dose ranges of conventional radiotherapy applications (3D CRT and IMRT). However, it is clear that the green channel requires even higher doses, such as in SBRT applications, and the blue channel can be used in any application involving a dose higher than about 40 Gy in order to achieve lower % uncertainty values in the measured dose values when using a three-color flatbed scanner.

Also, in the time interval up to 120 hours, the optimal scanning time has been determined in this study. This would be very beneficial for the users in deciding on the optimum scan time when a multi-channel scanner is used because of the polymerization behavior of EBT3 radiochromic films that continues after the irradiation process. The results revealed that for the EBT3 radiochromic film, it would be more appropriate for both higher practicality and accuracy to perform reading at hour 48. In future work, we aim to investigate the response behavior of radiochromic films to beta sources used in brachytherapy using a three-color flatbed scanner.

ORCID IDs
Kerem Duruer, https://orcid.org/0000-0003-2303-4070; **Durmuş Etiz**, https://orcid.org/0000-0003-0793-4941
Haluk Yücel, https://orcid.org/0000-0002-3084-9596

REFERENCES
[1] I.J. Das (Ed), *Radiochromic Film Role and Applications in Radiation Dosimetry*, (CRC Press, Boca Raton, 2017), pp. xiii.
[2] S. Devic, N. Tomic, and D. Lewis, Reference radiochromic film dosimetry: Review of technical aspects, Physica Medica, **32** 541–556 (2016), https://doi.org/10.1016/j.ejmp.2016.02.008.
[3] E.Y. León-Marroquín, J.A. Herrera-González, M.A. Camacho-López, J.E. Villarreal-Barajas, and O.A. García-Garduño, Journal of Applied Clinical Medical Physics, **17**(5), 466-481 (2016), https://dx.doi.org/10.1120%2Fjacmp.v17i5.6262.
[4] L. Marrazzo, M. Zani, S. Pallotta, C. Arilli, M. Casati, A. Compagnucci, C. Talamonti, and M. Bucciolini, Physica Medica **31**, 1035–1042 (2015), https://dx.doi.org/10.1016/j.ejmp.2015.08.010.
[5] L.J. Van Battum, H. Huizenga, R.M. Verdaasdonk, and S. Heukelom, Phys. Med. Biol. **61**, 625–49 (2016), https://doi.org/10.1088/0031-9155/61/2/625.
[6] H. Bekerat, S. Devic, F. DeBlois, K. Singh, A. Sarfehnia, J. Seuntjens, S. Shih, X. Yu, and D. Lewis, Medical Physics, **41**(2), 022101 (2014), https://doi.org/10.1118/1.4860157.
[7] M. Butson, and A. Niroomand-Rad, in: *Radiochromic Film Role and Applications in Radiation Dosimetry*, edited by I.J. Das, (CRC Press, Boca Raton, 2017), pp. 7-28.
[8] E.Y. León-Marroquín, D.J. Mulrow, R. Khan, and A. Darafsheh, Med. Phys. **46**(2), 973-982 (2019), https://doi.org/10.1002/mp.13330.
[9] M. Butson, G. Cho, S. Gill, and D. Pope, in: *Radiochromic Film Role and Applications in Radiation Dosimetry*, edited by I. J. Das, (CRC Press, Boca Raton, 2017), pp. 34-56
[10] S. Devic, Physica Medica, **27**, 122-134 (2011), https://doi.org/10.1016/j.ejmp.2010.10.001.
[11] E.Y. León-Marroquín, M.A. Camacho-López, O.A. García-Garduño, J.A. Herrera-González, J.E. Villarreal-Barajas, R. Gutiérrez-Fuentes, and R. Contreras-Bulnes, Radiation Measurements, **89**, 82-88 (2016), https://doi.org/10.1016/j.radmeas.2016.03.007.
[12] J.E. Villarreal-Barajas, and R.F.H. Khan, Journal of Applied Clinical Medical Physics, **15**(1), 331-338 (2014), https://doi.org/10.1120/jacmp.v15i1.4439.
[13] S.W. Kang, J.B. Chung, K.H. Kim, K.Y. Eom, C. Song, J.W. Lee, W. Cho, and T.S. Suh, Evaluation of Dual-channel Compound Method for EBT3 Film Dosimetry, Progress in Medical Physics, **28**(1), 16-21 (2017), https://doi.org/10.14316/pmp.2017.28.1.16.
[14] S.H. Benedict, K.M. Yenice, D. Followill, J.M. Galvin, W. Hinson, B. Kavanagh, P. Keall, M. Lovelock, S. Meeks, L. Papiez, T. Purdie, R. Sadagopan, M.C. Schell, B. Salter, D.J. Schlesinger, A.S. Shiu, T. Solberg, D.Y. Song, V. Stieber, R. Timmerman, W.A. Tomé, D. Verellen, L. Wang, and F.F. Yin, Medical Physics, **37**(8), 4078-101 (2010), https://doi.org/10.1118/1.3438081.
[15] D. Lewis, A. Micke, X.Yu, and M.F. Chan, Medical Physics, **39**(10), 6339-50 (2012), https://doi.org/10.1118/1.4754797.
[16] T. Yao, L. H. Luthjens, A. Gasparini, and J.M. Warman, Radiation Physics and Chemistry **133**, 37–44 (2017), https://doi.org/10.1016/j.radphyschem.2016.12.006.
[17] V.C. Borca, M. Pasquino, G. Russo, P. Grosso, D. Cante, P. Sciacero, G. Girelli, M.R.L. Porta, and S. Tofani, Journal of Applied Clinical Medical Physics, **14**(2), 158-171 (2012), https://dx.doi.org/10.1120%2Fjacmp.v14i2.4111.
[18] P. Andreo, D.T. Burns, K. Hohlfeld, M.S. Huq, T. Kanai, F. Laitano, V. Smyth, S. Vynckier, *Absorbed Dose Determination In External Beam Radiotherapy: An International Code of Practice For Dosimetry Based On Standards Of Absorbed Dose To Water, International Atomic Energy Agency (IAEA), Technical Reports Series No. 398, IAEA TRS-398*, (2006).
[19] A. Niroomand-Rad, C.R. Blackwell, B.M. Coursey, K.P. Gall, J.M. Galvin, W.L. McLaughlin, A.S. Meigooni, R. Nath, J.E. Rodgers, and C.G. Soares, *Radiochromic film dosimetry: Recommendations of AAPM Radiation Therapy Committee Task Group 55 AAPM TG 55*, (1998).

[20] M. Mathot, S. Sobczak, and M.T. Hoornaert, Physica Medica, **30**, 871-877 (2014), https://doi.org/10.1016/j.ejmp.2014.06.043.

[21] P. Sipila, J. Ojala, S. Kaijaluoto, I. Jokelainen, and A. Kosunen, Journal Of Applied Clinical Medical Physics, **17**(1), 360-373 (2016), https://doi.org/10.1120/jacmp.v17i1.5970.

ДОСЛІДЖЕННЯ РЕАКЦІЇ РАДІОХРОМНОЇ ПЛІВКИ EBT3
ПРИ ВИСОКИХ ДОЗАХ 6 МеВ ФОТОННИХ ТА 6 МеВ ЕЛЕКТРОННИХ ПУЧКІВ
З ВИКОРИСТАННЯМ ТРИКОЛІРНОГО ПЛАНШЕТНОГО СКАНЕРА

Керем Дуруер[a],*, Дурмуш Етіз[a], Халук Юсель[b]

Університет Ескішехір Османгазі, медичний факультет, кафедра радіаційної онкології

26010, Одунпазарі, Эскішехір, Турція

Інститут ядерних наук, Університет Анкари

06500, Бешевлер, Анкара, Турція

Радіохромна плівкова дозиметрія зазвичай використовується для визначення дози в радіотерапії протягом багатьох років через її високого просторову здатність, низьку енергетичну залежність та приблизно тканино-еквівалентна. Крім того, плівкова дозиметрія має й інші практичні переваги, наприклад, підходить для променевих характеристик в терапевтичному діапазоні, водостійка, відносно нечутлива до видимого світла і не вимагає проведення водного процесу для отримання інформації про дозу. Плівки також не залежать від потужності дози. Отже, вони дуже корисні і практичні для клінічних застосувань, таких як брахітерапії, електронної терапія, виміру дози на шкірі і стереотаксичної радіотерапії. Серед іншого динамічний діапазон доз радіохромних плівок EBT3 зазвичай рекомендується в діапазоні доз від 0,1 до 20 Гр. Однак в цьому дослідженні передбачається дослідження поведінки плівок EBT3 при опроміненні в діапазоні високих доз до 90 Гр. З цією метою були отримані кінцеві оптичні щільності при збільшенні значень дози під пучків фотонів і електронів з використанням трьох кольорових каналів при скануванні (червоний-зелений-синій). Таким чином, для побудови калібрувальних кривих було вирішено, який колірний канал для радіохромної плівки EBT3 буде найбільш відповідним до різних діапазонів доз. В експериментальній установці спочатку були встановлені еталонні умови, і процедура калібрування дози проводилася на фантомі RW3. Потім опромінені плівки були акуратно розрізані на шматочки розміром 2×2,5см² і згруповані в 2 групи – опромінення і контролю. Контрольні групи були фоновими, тобто вони не опромінювалися. Перед опроміненням дві групи плівок сканувалися в планшетному сканері для трьох каналів. Після цього плівки групи опромінення розміщали так, щоб вирівняти точне місце ефективної точки іонізаційної камери при стандартних умовах. Пізніше їх опромінювали по одному до 90 Гр з використанням променів 6 МеВ і 6 МеВ відповідно. Згодом обидві групи плівок були знову скановані у трьох-колірному планшетному сканері. Зі скановаих плівок були отримані оптичні щільності і їх стандартні відхилення, які відповідають обраним значенням дози. Таким чином були побудовані калібрувальні криві для всіх трьох кольорових каналів відповідно до двох різних умов опромінення. Результати, отримані для променю 6 МеВ, показали, що якщо канал червоного кольору обраний для діапазону дози 0,9 Гр-7,3 Гр, канал зеленого кольору обраний для діапазону дози 7,3 Гр-42,8 Гр, а канал синього кольору обраний для 42,8 Гр - 90,0 Гр, процентні значення невизначеності в отриманих результатах мінімальні. Для променю 6 МеВ, якщо канал червоного кольору обраний для діапазону дози 0,9 Гр-7,7 Гр, і канал зеленого кольору обраний для діапазону дози 7,7 Гр-45,3 Гр, а канал синього кольору обраний для дози 45, 3 Гр-90,0 Гр, процентні значення невизначеності в отриманих результатах мінімальні. У підсумку, були оцінені значення невизначеності в процентах для отриманих результатів для енергій фотонів 6 МеВ і електронів 6 МеВ з використанням різних каналів сканування радіохромної плівки EBT3. Було виявлено, що вимірювання, які мають низькі значення процентної невизначеності, можуть бути досягнуті зміною каналу сканування шляхом вибору правильних комбінацій зі збільшенням доз для обох енергій (фотонів 6 МеВ і електронів 6 МеВ). Дослідження також показує, що радіохромні плівки EBT3 можуть використовуватися при більш низьких значеннях процентної невизначеності при дозах, що перевищують рекомендовані значення діапазону доз.

КЛЮЧОВІ СЛОВА: радіохромна плівка, невизначеність, висока доза, радіотерапія, планшетний сканер.

ИССЛЕДОВАНИЕ РЕАКЦИИ РАДИОХРОМИЧЕСКОЙ ПЛЕНКИ EBT3
ПРИ ВЫСОКОЙ ДОЗЕ 6 МэВ ФОТОННЫХ И 6 МэВ ЭЛЕКТРОННЫХ ПУЧКОВ
С ИСПОЛЬЗОВАНИЕМ ТРЕХЦВЕТНОГО ПЛОСКОГО СКАНЕРА

Керем Дуруер [a],*, Дурмуш Этиз[a], Халук Юсель[b]

[a]*Университет Эскишехир Османгази, Медицинский факультет, Кафедра радиационной онкологии*

26010, Одунпазари, Эскишехир, Турция

[b]*Институт ядерных наук, Университет Анкары*

06500, Бешевлер, Анкара, Турция

Радиохромная пленочная дозиметрия обычно используется для определения дозы в радиотерапии в течение многих лет из-за ее высокого пространственного разрешения, низкой энергетической зависимости и ее приблизительного тканевого эквивалента. Кроме того, она имеет и другие практические преимущества, например, подходит для лучевых характеристик в терапевтическом диапазоне, водостойкости, относительной нечувствительности к видимому свету и не требует проведения водного процесса для получения информации о дозе. Они также не зависят от мощности дозы. Следовательно, они очень полезны и практична для клинических применений, таких как брахитерапия, электронная терапия, измерение дозы на коже и стереотаксическая радиотерапия. Среди прочего динамический диапазон доз радиохромных пленок EBT3 обычно рекомендуется в диапазоне доз от 0,1 до 20 Гр. Однако в этом исследовании предполагается исследование поведения пленок EBT3 при облучении в диапазоне высоких доз до 90 Гр. Для этой цели были получены конечные оптические плотности при увеличении значений дозы под пучков фотонов и электронов с использованием трех каналов цветного сканирования (красный-зеленый-синий). Таким образом, для построения калибровочных кривых было решено, какой цветовой канал для радиохромной пленки EBT3 будет наиболее подходящим в различных диапазонах доз. В экспериментальной установке сначала были установлены эталонные условия, и процедура калибровки дозы проводилась в фантоме RW3. Затем облученные пленки были аккуратно разрезаны на кусочки размером 2×2,5 см² и сгруппированы в 2 группы облучения и контроля.

Контрольные группы являлись фоновыми, то есть они не облучались. Перед облучением две группы пленок сканировались в планшетном сканере для трех каналов. После этого пленки облучающей группы помещали так, чтобы выровнять точное место эффективной точки ионизационной камеры при стандартных условиях. Позднее их облучали по одному до 90 Гр с использованием лучей 6 МэВ и 6 МэВ соответственно. Впоследствии обе группы пленок были снова отсканированы в планшетном сканере для трехцветных каналов. Из отсканированных пленок были получены оптические плотности и их стандартные отклонения, которые соответствующие выбранным значениям дозы. Таким образом были построены калибровочные кривые для всех трех цветов канала в соответствии с двумя различными условиями луча. Результаты, полученные для луча 6 МэВ, показали, что если канал красного цвета выбран для диапазона дозы 0,9 Гр-7,3 Гр, канал зеленого цвета выбран для диапазона дозы 7,3 Гр-42,8 Гр, а канал синего цвета выбран для 42,8 Гр - 90,0 Гр, процентные значения неопределенности в полученных результатах минимальны. Для луча 6 МэВ, если канал красного цвета выбран для диапазона дозы 0,9 Гр-7,7 Гр, и канал зеленого цвета выбран для диапазона дозы 7,7 Гр-45,3 Гр, а канал синего цвета выбран для дозы 45,3 Гр-90,0 Гр, процентные значения неопределенности в полученных результатах минимальны. В итоге, были оценены значения неопределенности в процентах для полученных результатов для энергий фотонов 6 МэВ и электронов 6 МэВ с использованием различных каналов сканирования радиохромной пленки EBT3. Было обнаружено, что измерения, имеющие низкие значения процентной неопределенности, могут быть достигнуты путем изменения канала сканирования путем выбора правильных комбинаций с увеличением доз для обеих энергий (фотон 6 МэВ и электрон 6 МэВ). Исследование также показывает, что радиохромные пленки EBT3 могут использоваться при более низких значениях процентной неопределенности при дозах, превышающих рекомендуемые значения диапазона доз.
КЛЮЧЕВЫЕ СЛОВА: радиохромная пленка, неопределенность, высокая доза, радиотерапия, планшетный сканер.

ON RELAXATION PROCESSES IN A COMPLETELY IONIZED PLASMA

Alexander I. Sokolovsky[a],*, Sergey A. Sokolovsky[b], Oleh A. Hrinishyn[a]

ªOles Honchar Dnipro National University, Gagarin Ave. 72, Dnipro, Ukraine
ᵇPrydniprovska State Academy of Civil Engineering and Architecture, Chernyshevsky Str. 24a, Dnipro, Ukraine
*Corresponding Author: alexander.i.sokolovsky@gmail.com
Received June 5, 2020; accepted June 30, 2020

Relaxation of the electron energy and momentum densities is investigated in spatially uniform states of completely ionized plasma in the presence of small constant and spatially homogeneous external electric field. The plasma is considered in a generalized Lorentz model which contrary to standard one assumes that ions form an equilibrium system. Following to Lorentz it is neglected by electron-electron and ion-ion interactions. The investigation is based on linear kinetic equation obtained by us early from the Landau kinetic equation. Therefore long-range electron-ion Coulomb interaction is consequentially described. The research of the model is based on spectral theory of the collision integral operator. This operator is symmetric and positively defined one. Its eigenvectors are chosen in the form of symmetric irreducible tensors which describe kinetic modes of the system. The corresponding eigenvalues are relaxation coefficients and define the relaxation times of the system. It is established that scalar and vector eigenfunctions describe evolution of electron energy and momentum densities (vector and scalar system modes). By this way in the present paper exact close set of equations for the densities valid for all times is obtained. Further, it is assumed that their relaxation times are much more than relaxation times of all other modes. In this case there exists a characteristic time such, that at corresponding larger times the evolution of the system is reduced described by asymptotic values of the densities. At the reduced description electron distribution function depends on time only through asymptotic densities and they satisfy a closed set of equations. In our previous paper this result was proved in the absence of an external electric field and exact nonequilibrium distribution function was found. Here it is proved that this reduced description takes also place for small homogeneous external electric field. This can be considered as a justification of the Bogolyubov idea of the functional hypothesis for the relaxation processes in the plasma. The proof is done in the first approximation of the perturbation theory in the field. However, its idea is true in all orders in the field. Electron mobility in the plasma, its conductivity and phenomenon of equilibrium temperature difference of electrons and ions are discussed in exact theory and approximately analyzed. With this end in view, following our previous paper, approximate solution of the spectral problem is discussed by the method of truncated expansion of the eigenfunctions in series of the Sonine polynomials. In one-polynomial approximation it is shown that nonequilibrium electron distribution function at the end of relaxation processes can be approximated by the Maxwell distribution function. This result is a justification of the Lorentz–Landau assumption in their theory of nonequilibrium processes in plasma. The temperature and velocity relaxation coefficients were calculated by us early in one- and two-polynomial approximation.

KEYWORDS: plasma, generalized Lorentz model, relaxation coefficients, collision integral operator, spectral theory, one-polynomial approximations, functional hypothesis.

INTRODUCTION

This paper is devoted to the investigation of relaxation processes in completely ionized plasma. It is meant nonequilibrium processes that can be observed in spatially homogenous states of a system. Near the equilibrium they describe the so-called kinetic modes of the considered system. Taking into account relaxation processes in theory of spatially non-uniform states is the next step after their investigation for spatially uniform nonequilibrium states. From a different point of view taking into account relaxation processes is extension of set of parameters that describe nonequilibrium state (reduced description parameters). This is the main trend in theory of nonequilibrium processes. Some important examples are given by the extended irreversible thermodynamics [1], a theory with nonequilibrium correlations of the standard reduced description parameters as additional independent ones (see, for example, [2]), a theory of nonequilibrium states in the vicinity of the standard ones (see, for example, [3]).

In the present paper plasma is considered in the generalized Lorentz model, in which electron-electron interaction is neglected and the ion subsystem is assumed to be an equilibrium ideal gas. In the standard Lorentz model [4] the ion subsystem is a system of hard spheres in the rest. The generalized Lorentz model is based on the Landau kinetic equation [5] (see also in [6]) and, therefore, takes into account peculiarities of the Coulomb interaction. It was introduced in our paper [7]. The same model is discussed in [8] on the base of the Boltzmann kinetic equation.

In plasma states with different component temperatures their relaxation is observed. For the first time the problem of equalizing the electron and ion component temperatures in plasma was investigated by Landau [5] (the component velocity relaxation is considered analogously in [9]). His research was based on the mentioned kinetic equation [5] and shows that temperature relaxation process is slow one because big difference electron and ion masses. In his investigations (see additional examples in [10]) he assumed without proof that the plasma components quickly become equilibrium and are described by the Maxwell distribution functions. This assumption belongs to Lorentz and was introduced by him in his theory of transport phenomena in metals [4]. Fundamental investigation of the plasma hydrodynamics on the same basis belongs to Braginsky [11]. Similar problem for electron-phonon two-component system was discussed by Bogolyubov and Bogolyubov (Jr.) in their research [12] on the polaron theory. They

considered solution of the kinetic equation for polarons interacting with equilibrium phonon system using the Maxwell distribution with macroscopic velocity as a good approximation for the polaron distribution function.

In fact the mentioned assumption is unfair because the Maxwell distributions for electrons and ions with different temperatures and macroscopic velocities are not solution of kinetic equations for all models of the plasma dynamics. Therefore, the main problem of the theory is to find the main approximation for electron and ion distribution functions of plasma with two component temperatures and velocities. This problem is related to the absence of a small parameter in the theory of relaxation. An approach to solution of this problem was proposed by us with the idea to investigate relaxation processes in the vicinity of standard described nonequilibrium processes (equilibrium states included) [3]. An important example is our investigation of the two-fluid plasma hydrodynamics in the vicinity to one-fluid one [13] (see also a review [14]).

Our previous investigations of nonequilibrium processes in plasma (for example, in [13-15, 16]) are primarily based on the Bogolyubov idea of the functional hypothesis (its consistent and complete discussion see in [6]). According this one plasma component distribution functions $f_{ap}(x,t)$ (a is component number) after some characteristic time τ_0 depend on time only through the asymptotic values $\xi_\mu^{(+)}(x,t)$ of some parameters $\xi_\mu(x,t)$ (μ is parameter number)

$$f_{ap}(x,t)\xrightarrow[t\gg\tau_0]{}f_{ap}^{(+)}(x,t)\,,\qquad \xi_\mu(x,t)\xrightarrow[t\gg\tau_0]{}\xi_\mu^{(+)}(x,t)\,,\qquad f_{ap}^{(+)}(x,t)=f_{ap}(x,\xi^{(+)}(t))\,, \qquad (1)$$

which are called the reduced description parameters. Here $f_{ap}(x,\xi)$ is some functional of the functions $\xi_\mu(x)$. Asymptotic distribution function $f_{ap}^{(+)}(x,t)$ is exact (as well $f_{ap}(x,t)$) solution of kinetic equation which describes evolution of the plasma. Parameters $\xi_\mu^{(+)}(x,t)$ describe states of the plasma and satisfy a closed set of equations of the form

$$\partial_t\xi_\mu^{(+)}(x,t)=L_\mu(x,\xi^{(+)}(t)) \qquad (2)$$

where $L_\mu(x,\xi)$ is some functionals of the functions $\xi_\mu(x)$. The Bogolyubov idea of the functional hypothesis is basis of his method of the reduced description of nonequilibrium systems. In these terms according above discussion the main problem of the relaxation phenomena in plasma investigation is to find the distribution function $f_{ap}(x,\xi)$ in spatially uniform states.

Contrary to our mentioned papers [13-16], which are based on the Bogolyubov method of the reduced description on nonequilibrium states, the present paper develops kinetics of the system through elaborating the spectral theory of the collision integral operator without assumption that relaxation processes are considered at its completion. This is possible because the plasma is considered in the generalized Lorentz model [7] in which kinetic equation for electrons is a linear one and ions form an equilibrium system. In this approach the relaxation phenomena in plasma are discussed for spatially uniform states in our papers [17, 18] and exact distribution function is found in the terms of scalar and vector eigenfunction A_p, $B_p p_n$ of the collision integral operator. These eigenfunction are calculated by the method of truncated expansion in the Sonine polynomial series. The paper [17] discusses this problem for the case of the presence constant small spatially homogeneous external electric field with some simplifying assumptions.

The presented paper provides a consequence investigation of the relaxation processes in plasma at small electric field. Spectral theory of the collision integral operator is discussed in the terms of eigenfunctions that are irreducible tensors.

The paper is constructed as it follows. In the section "Basic equations of the theory" the generalized Lorentz model is formulated following to [7] and basics of spectral theory of the collision integral operator are presented. The section "Evolution of energy and momentum densities of the electron system" discusses dynamics of the densities. The next section "Reduced description of the system by energy and momentum densities" investigates long time evolution of the system and predicts equilibrium state of the system. The section "Approximate calculation of the main quantities of the theory" discusses approximate solution of the spectral problem for the collision integral operator.

BASIC EQUATIONS OF THE THEORY

This paper is devoted to the study of relaxation processes in spatially homogeneous completely ionized plasma in the presence of small external electric field. The plasma is considered in the generalized Lorentz model in which the ion subsystem is assumed to be in equilibrium and in the state of the macroscopic rest with the temperature T_0. The model is based on the Landau kinetic equation [5] and was introduced in our paper [7]. The electron kinetic equation of the model has the form

$$\partial_t f_p(t)=-F_n\frac{\partial f_p(t)}{\partial p_n}+I_p(f_{p'}(t))\,,\qquad (F_n=-eE_n,\qquad \int d^3p f_p(t)=n) \qquad (3)$$

with collision integral given by the formula

$$I_p(\mathrm{f}_{p'}) = \frac{\partial}{\partial p_n}\left[D_{nl}(p)\left(\frac{\partial \mathrm{f}_p}{\partial p_l} + \frac{p_l}{mT_0}\mathrm{f}_p\right)\right]$$

(4)

where function $D_{nl}(p)$ is defined by expressions

$$D_{nl}(p) = 2\pi e^4 z^2 L \int d^3 p' w_{ip'} S_{nl}\left(\frac{p}{m} - \frac{p'}{M}\right), \qquad S_{nl}(u) = (u^2 \delta_{nl} - u_n u_l)/u^3.$$

(5)

Here L is the Coulomb logarithm, $-e$ is charge of an electron, ze is charge of an ion, E_n is homogeneous constant electric field. Hereafter electron and ion equilibrium distribution functions are written as

$$w_p \equiv \frac{n}{(2\pi mT_0)^{3/2}}e^{-\frac{p^2}{2mT_0}}, \quad I_p(w_{p'}) = 0; \qquad w_{ip} \equiv \frac{n_0}{(2\pi M T_0)^{3/2}}e^{-\frac{p^2}{2MT_0}}$$

(6)

(n, n_0 are electron and ion component number of particles densities; m, M are electron and ion masses).

It is convenient to conduct the research of the considered system using the collision integral operator $\hat{K}$ given by the formulas [7]

$$\hat{K}a_p = w_p^{-1}I_p(w_{p'}a_{p'}), \qquad \hat{K}a_p = -\left(\frac{\partial}{\partial p_n} - \frac{p_n}{mT_0}\right)D_{nl}(p)\frac{\partial a_p}{\partial p_l}$$

(7)

(hereafter arbitrary real functions are defined by a_p, b_p, …). In the term of scalar product

$$(a_p, b_p) = \int d^3 p\, w_p a_p b_p = \langle a_p b_p \rangle \qquad (\langle a_p \rangle \equiv \int d^3 p\, w_p a_p)$$

(8)

linear operator $\hat{K}$ is a symmetric and positively defined one. Therefore, its eigenfunctions g_{ip} and eigenvalues λ_i

$$\hat{K}g_{ip} = \lambda_i g_{ip}$$

(9)

have the properties

$$\lambda_i > 0, \qquad (g_i, g_{i'}) \equiv b_i \delta_{ii'}, \qquad \langle g_{ip} \rangle = 0$$

(10)

(b_i are normalization constants). In this paper eigenfunctions g_{ip} are chosen in the form of symmetric irreducible tensors multiplied by a function of the momentum modulus. The simplest of them are given by expressions

$$C(p) = A_p, \quad C_l(p) = B_p p_l, \quad C_{lm}(p) \equiv C_p(p_l p_m - \frac{1}{3}p^2\delta_{lm}), \quad \dots \quad C_{l_1\dots l_s}(p)\dots$$

(11)

Convolution of arbitrary two indices of each tensor $C_{l_1\dots l_s}(p)$ ($s \geq 2$) is equal to zero.

Instead of distribution function f_p it is convenient to introduce new one g_p and rewrite the kinetic equation (3) in its terms

$$\mathrm{f}_p = w_p(1 + g_p), \qquad \partial_t g_p = -F_n \frac{\partial w_p(1 + g_p)}{\partial p_n}w_p^{-1} + \hat{K}g_p$$

(12)

to simplify investigation of the small electric field case. Solution of this equation can be sought, following to our paper [17], in the form of a series in eigenfunctions g_{ip} of the operator $\hat{K}$

$$g_p(t) = \sum_i c_i(t)g_{ip}.$$

(13)

In the absence of the electric field this solution is given by relation

$$g_p^{(0)}(t) = \sum_i c_{i0} g_{ip} e^{-t\lambda_i}, \qquad \lambda_i \equiv 1/\tau_i \tag{14}$$

where the coefficients c_{i0} are defined by initial value of the distribution function $f_p(t=0)$. Each term in this formula describes a relaxation (kinetic) mode of the system (hereafter $a^{(0)}$ denotes contribution to a quantity a in the absence of the electric field). Eigenvalues λ_i are called the relaxation coefficients and define the relaxation times τ_i of the system.

EVOLUTION OF ENERGY AND MOMENTUM DENSITIES OF THE ELECTRON SYSTEM

In this paper relaxation processes are investigated which related to electron subsystem energy ε and momentum π_n densities that are defined by the formulas

$$\varepsilon \equiv \int d^3 p \varepsilon_p f_p = \langle \varepsilon_p g_p \rangle + \varepsilon_0, \qquad \pi_l \equiv \int d^3 p f_p p_l = \langle p_l g_p \rangle \qquad (\varepsilon_p \equiv \frac{p^2}{2m}, \varepsilon_0 \equiv \frac{3}{2} n T_0). \tag{15}$$

In this connection scalar A_p and vector $B_p p_n$ eigenvalues and the corresponding eigenvalues λ_T, λ_u are most important

$$\hat{K} A_p = \lambda_T A_p, \qquad \hat{K} B_p p_n = \lambda_u B_p p_n \qquad (\langle A_p \rangle = 0). \tag{16}$$

To these relations the normalization conditions should be added which for the further convenience are chosen in the form

$$\langle A_p \varepsilon_p \rangle = 3n/2, \quad \langle B_p \varepsilon_p \rangle = 3n/2. \tag{17}$$

According to (13), (16) function g_p can be written in more concrete form

$$g_p = c_T A_p + c_{u_l} B_p p_l + \sum_{i \neq T, u_l} c_i g_{ip} \tag{18}$$

with understandable notations for the coefficients c_i. Now expressions (15) for electron energy ε and momentum π_n densities give

$$\pi_l = c_T \langle p_l A_p \rangle + c_{u_n} \langle p_l B_p p_n \rangle + \sum_{i \neq T, u_l} c_i \langle p_l g_{ip} \rangle, \qquad \varepsilon = \varepsilon_0 + c_T \langle \varepsilon_p A_p \rangle + c_{u_n} \langle \varepsilon_p B_p p_n \rangle + \sum_{i \neq T, u_l} c_i \langle \varepsilon_p g_{ip} \rangle \tag{19}$$

Taking into account the rotational invariance considerations and conditions (17) gives

$$\pi_l = m n c_{u_l}, \qquad \varepsilon = \varepsilon_0 + \frac{3n}{2} c_T \tag{20}$$

because

$$\langle p_l g_{ip} \rangle = 0, \qquad \langle \varepsilon_p g_{ip} \rangle = 0 \quad (i \neq T, u). \tag{21}$$

Note, to explain these identities that tensors $\langle p_l g_{ip} \rangle$ and $\langle \varepsilon_p g_{ip} \rangle$ with $i \neq T, u$ are expressed only through sums of the Kronecker delta of the type δ_{nl} products. Convolution of arbitrary two indices of each irreducible tensor is equal to zero and therefore averages in (21) are equal to zero.

Let us derive time equations for the densities ε, π_n. Kinetic equation (3) and definitions (9), (12), (15), (16), (18) after integration by parts give the next time equations for the momentum density π_l

$$\partial_t \pi_l = n F_l - \langle p_l \hat{K} g_p \rangle = n F_l - c_T \langle p_l \hat{K} A_p \rangle - c_{u_n} \langle p_l \hat{K} B_p p_n \rangle + \sum_{i \neq T, u_l} c_i \langle p_l \hat{K} g_{ip} \rangle =$$
$$= n F_l - c_T \lambda_T \langle p_l A_p \rangle - c_{u_n} \lambda_u \langle p_l B_p p_n \rangle + \sum_{i \neq T, u_l} c_i \lambda_i \langle p_l g_{ip} \rangle, \tag{22}$$

and for the energy density ε

$$\partial_t \varepsilon = \frac{1}{m} \pi_l F_l - \langle \varepsilon_p \hat{K} g_p \rangle = \frac{1}{m} \pi_l F_l - c_T \langle \varepsilon_p \hat{K} A_p \rangle - c_{u_n} \langle \varepsilon_p \hat{K} B_p p_n \rangle + \sum_{i \neq T, u_l} c_i \langle \varepsilon_p \hat{K} g_{ip} \rangle =$$

$$= \frac{1}{m} \pi_l F_l - c_T \lambda_T \langle \varepsilon_p A_p \rangle - c_{u_n} \lambda_u \langle \varepsilon_p B_p p_n \rangle + \sum_{i \neq T, u_l} c_i \lambda_i \langle \varepsilon_p g_{ip} \rangle . \tag{23}$$

are obtained. The rotational invariance considerations, formulas (16), (17), expressions (20) and identities (21) give final form of these equations

$$\partial_t \pi_l = n F_l - \lambda_u \pi_l , \qquad \partial_t \varepsilon = \frac{1}{m} \pi_l F_l - \lambda_T (\varepsilon - \varepsilon_0) . \tag{24}$$

The obtained equations are valid for all times and without assumption that electric field is small.

REDUCED DESCRIPTION STATE OF THE SYSTEM BY ENERGY AND MOMENTUM DENSITIES

Let us discuss state of the system at long times. Here and in our paper [17] it is assumed that characteristic time τ_0 with the property

$$\tau_T, \tau_u \gg \tau_0 \gg \tau_i \qquad (i \neq T, u) \tag{25}$$

exists. Let us prove that at long times the following relation

$$g_p^{(+)}(t) = g_p(\varepsilon^{(+)}(t), \pi^{(+)}(t)) \tag{26}$$

is true, where $g_p^{(+)}(t)$, $\varepsilon^{(+)}(t)$, $\pi_l^{(+)}(t)$ are asymptotic values of the quantities $g_p(t)$, $\varepsilon(t)$, $\pi_l(t)$:

$$\varepsilon(t) \underset{t \gg \tau_0}{=} \varepsilon^{(+)}(t), \qquad \pi_l(t) \underset{t \gg \tau_0}{=} \pi_l^{(+)}(t), \qquad g_p(t) \underset{t \gg \tau_0}{=} g_p^{(+)}(t) \tag{27}$$

and $g_p(\varepsilon, \pi)$ is some function. In the situation described by relations (26), (27) the system would be completely described at $t \gg \tau_0$ by parameters $\varepsilon^{(+)}(t)$, $\pi_l^{(+)}(t)$ because the electron distribution function (12) is expressed at $t \gg \tau_0$ through parameters $\varepsilon^{(+)}(t)$, $\pi_l^{(+)}(t)$

$$f_p(t) \underset{t \gg \tau_0}{=} w_p [1 + g_p(\varepsilon^{(+)}(t), \pi^{(+)}(t))]. \tag{28}$$

Parameters $\varepsilon^{(+)}(t)$, $\pi_l^{(+)}(t)$ according to (22) satisfy exact close equations

$$\partial_t \pi_l^{(+)} = n F_l - \lambda_u \pi_l^{(+)}, \qquad \partial_t \varepsilon^{(+)} = \frac{1}{m} \pi_l F_l - \lambda_T (\varepsilon^{(+)} - \varepsilon_0) \tag{29}$$

According (1), (2), if (26) is true, in the system the reduced description by parameters $\varepsilon^{(+)}(t)$, $\pi_l^{(+)}(t)$ is observed and the statement (26) expresses the Bogolyubov idea of the functional hypothesis.

In our paper [17] under assumption (25) it was proved that in the absence of external electric field function $g_p(\varepsilon, \pi)$ is given by exact expression

$$g_p^{(0)}(\varepsilon, \pi) = (\varepsilon - \varepsilon_0) A_p 2 / 3n + \pi_l B_p p_l / mn . \tag{30}$$

In order to investigate possibility of the reduced description in the presence of electric field let us restrict ourselves by small field. Exact electron distribution function is sought in a series in powers of the field E_l

$$f_p = w_p (1 + g_p), \qquad g_p = g_p^{(0)} + g_p^{(1)} + O(E^2) ; \tag{31}$$

$$g_p^{(0)} = c_T^{(0)} A_p + c_{u_l}^{(0)} B_p p_l, \qquad c_T^{(0)} \equiv c e^{-t\lambda_T}, \qquad c_{u_l}^{(0)} \equiv c_l e^{-t\lambda_u};$$

$$g_p^{(1)} = \sum_i c_i^{(1)} g_{ip} = c_T^{(1)} A_p + c_{u_l}^{(1)} B_p p_l + \sum_{i \neq T,u} c_i^{(1)} g_{ip}$$

where $c_T^{(1)}$, $c_{u_l}^{(1)}$, $c_i^{(1)}$ are functions of time and have to be found. Functions $g_p^{(0)}$, $g_p^{(1)}$ according to (12) satisfy equations

$$\partial_t g_p^{(0)} = -\hat{K} g_p^{(0)}, \qquad \partial_t g_p^{(1)} = -F_l \frac{\partial w_p (1+g_p^{(0)})}{\partial p_l} w_p^{-1} - \hat{K} g_p^{(1)}. \tag{32}$$

First of these equations is due to (16), (31) true. The main contribution $g_p^{(0)}$ to function g_p with arbitrary coefficients c, c_l is chosen in the form (31) that is enough for investigation of the system at $t \gg \tau_0$ because

$$\lambda_i \gg \lambda_T, \lambda_u \quad (i \neq T, u) \tag{33}$$

(see (14), (25)). The second equation (32) with account for normalization condition (10) give set of equations for functions $c_i^{(1)} = (g_p^{(1)} g_{ip}) / b_i$ from (31)

$$\partial_t c_i^{(1)} = F_l (a_{il} e^{-t\lambda_T} + b_{il} e^{-t\lambda_u} + c_{il}) - \lambda_i c_i^{(1)}. \tag{34}$$

Here according to (31) after integration by parts the time independent coefficients a_{il}, b_{il}, c_{il}

$$-\frac{1}{b_i} \int d^3 p \frac{\partial w_p (1+g_p^{(0)})}{\partial p_l} g_{ip} = \frac{1}{b_i} \int d^3 p\, w_p (1+g_p^{(0)}) \frac{\partial g_{ip}}{\partial p_l} = \frac{1}{b_i} \left(\langle \frac{\partial g_{ip}}{\partial p_l} \rangle + \langle g_p^{(0)} \frac{\partial g_{ip}}{\partial p_l} \rangle \right) =$$

$$= a_{il} e^{-t\lambda_T} + b_{il} e^{-t\lambda_u} + c_{il}; \tag{35}$$

$$a_{il} \equiv c \langle A_p \frac{\partial g_{ip}}{\partial p_l} \rangle / b_i, \quad b_{il} \equiv c_m \langle B_p p_m \frac{\partial g_{ip}}{\partial p_l} \rangle / b_i, \quad c_{il} \equiv \langle \frac{\partial g_{ip}}{\partial p_l} \rangle / b_i$$

are introduced (in [17] this expression wrongly assumed to be constant). Solution of equations (34) has the form

$$c_i^{(1)} = c_{i0}^{(1)} e^{-t\lambda_i} + a_{il} F_l (e^{-t\lambda_T} - e^{-t\lambda_i}) / (\lambda_i - \lambda_T) + b_{il} F_l (e^{-t\lambda_u} - e^{-t\lambda_i}) / (\lambda_i - \lambda_u) + c_{il} (1 - e^{-t\lambda_i}) / \lambda_i. \tag{36}$$

Initial conditions $c_{i0}^{(1)} \equiv c_i^{(1)}(t=0)$ for $c_i^{(1)}$ are not related to the external field and further will be replaced by zero. According to (25), (33) expression (36) gives

$$c_i^{(1)} \underset{t \gg \tau_0}{=} a_{il} F_l e^{-t\lambda_T} / (\lambda_i - \lambda_T) + b_{il} F_l e^{-t\lambda_u} / (\lambda_i - \lambda_u) + c_{il} F_l / \lambda_i \qquad (i \neq T, u),$$

$$c_T^{(1)} \underset{t \gg \tau_0}{=} -t a_{Tl} F_l + b_{Tl} F_l (e^{-t\lambda_u} - e^{-t\lambda_T}) / (\lambda_u - \lambda_T) + c_{Tl} F_l (1 - e^{-t\lambda_T}) / \lambda_T, \tag{37}$$

$$c_{u_m}^{(1)} \underset{t \gg \tau_0}{=} a_{u_m l} F_l (e^{-t\lambda_T} - e^{-t\lambda_u}) / (\lambda_T - \lambda_u) - t b_{u_m l} F_l + c_{u_m l} F_l (1 - e^{-t\lambda_T}) / \lambda_u.$$

Entering here coefficients are defined by (35). The rotational invariance considerations give

$$a_{il} \underset{i \neq T,u}{=} c \langle A_p \frac{\partial g_{ip}}{\partial p_l} \rangle / b_i = 0, \quad b_{il} \underset{i \neq T,u}{=} c_m \langle B_p p_m \frac{\partial g_{ip}}{\partial p_l} \rangle / b_i \neq 0, \quad c_{il} \underset{i \neq T,u}{=} \langle \frac{\partial g_{ip}}{\partial p_l} \rangle / b_i = 0;$$

$$a_{Tl} \equiv c \langle A_p \frac{\partial A_p}{\partial p_l} \rangle / b_T = 0, \quad b_{Tl} \equiv c_m \langle B_p p_m \frac{\partial A_p}{\partial p_l} \rangle / b_T \neq 0, \quad c_{Tl} \equiv \langle \frac{\partial A_p}{\partial p_l} \rangle / b_T = 0; \tag{38}$$

$$a_{u_m l} \equiv c \langle A_p \frac{\partial B_p p_m}{\partial p_l} \rangle / b_u \neq 0, \quad b_{u_n l} \equiv c_m \langle B_p p_m \frac{\partial B_p p_n}{\partial p_l} \rangle / b_u = 0, \quad c_{u_n l} \equiv \langle \frac{\partial B_p p_n}{\partial p_l} \rangle / b_u \neq 0$$

(see remark after relations (21)). Therefore, formulas (37) receive the form

$$c_i^{(1)} \underset{t \gg \tau_0}{=} b_{il} F_l e^{-t\lambda_u} / (\lambda_i - \lambda_u) \qquad (i \neq T, u), \qquad c_T^{(1)} \underset{t \gg \tau_0}{=} b_{Tl} F_l (e^{-t\lambda_u} - e^{-t\lambda_T}) / (\lambda_u - \lambda_T),$$

$$c_{u_n}^{(1)} \underset{t \gg \tau_0}{=} a_{u_n l} F_l (e^{-t\lambda_T} - e^{-t\lambda_u}) / (\lambda_T - \lambda_u) + c_{u_n l} F_l (1 - e^{-t\lambda_T}) / \lambda_u. \tag{39}$$

Finally, according to (27), (31) the electron distribution function g_p at long times is given by the formulas

$$g_p^{(+)} = c_T^{(+)} A_p + c_{u_l}^{(+)} B_p p_l + \sum_{i \neq T, u_l} c_i^{(+)} g_{ip};$$

$$c_T^{(+)} \equiv c e^{-t\lambda_T} + b_{Tl} F_l (e^{-t\lambda_u} - e^{-t\lambda_T}) / (\lambda_u - \lambda_T), \qquad c_i^{(+)} \equiv b_{il} F_l e^{-t\lambda_u} / (\lambda_i - \lambda_u), \tag{40}$$

$$c_{u_n}^{(+)} \equiv c_n e^{-t\lambda_u} + a_{u_n l} F_l (e^{-t\lambda_T} - e^{-t\lambda_u}) / (\lambda_T - \lambda_u) + c_{u_n l} F_l (1 - e^{-t\lambda_T}) / \lambda_u$$

with the accuracy up to the first order in the electric field contributions included. It is interesting to note that here secular terms grooving with the time are absents. Relations (37) show that without identities (38) they may be present.

Asymptotic distribution function $g_p^{(+)}$ according (20), (40) takes the form

$$g_p^{(+)} = \frac{2}{3n} (\varepsilon^{(+)} - \varepsilon_0) A_p + \frac{1}{mn} \pi_l^{(+)} B_p p_l + \sum_{i \neq T, u_l} c_i^{(+)} g_{ip}. \tag{41}$$

Also due to (20), (40) asymptotic values of energy and momentum densities are written as

$$\frac{2}{3n} (\varepsilon^{(+)} - \varepsilon_0) = c e^{-t\lambda_T} + b_{Tl} F_l (e^{-t\lambda_u} - e^{-t\lambda_T}) / (\lambda_u - \lambda_T),$$

$$\frac{1}{mn} \pi_n^{(+)} = c_n e^{-t\lambda_u} + a_{u_n l} F_l (e^{-t\lambda_T} - e^{-t\lambda_u}) / (\lambda_T - \lambda_u) + c_{u_n l} F_l (1 - e^{-t\lambda_T}) / \lambda_u. \tag{42}$$

These formulas can be considered as a set of equations for functions $e^{-t\lambda_T}$, $e^{-t\lambda_u}$. These equations are obtained here in the first in the electric field approximation. However, in all approximations relations of this type can by used to express functions $e^{-t\lambda_T}$, $e^{-t\lambda_u}$ through asymptotic densities $\varepsilon^{(+)}$, $\pi_l^{(+)}$. In all approximations in the field coefficients $c_i^{(+)}$ $(i \neq T, u)$ are expressed through exponents $e^{-t\lambda_T}$, $e^{-t\lambda_u}$ and, therefore, always they expressed through densities $\varepsilon^{(+)}$, $\pi_l^{(+)}$. So, in all in the field approximations distribution function $g_p^{(+)}$ is a function of $\varepsilon^{(+)}$, $\pi_l^{(+)}$.

In our case $e^{-t\lambda_u}$ as a function of $\varepsilon^{(+)}$, $\pi_l^{(+)}$ should be substituted in expression for $c_i^{(+)}$ given by (40) and calculated in the main approximation in electric field. Therefore, quantity $e^{-t\lambda_u}$ as a function of $\varepsilon^{(+)}$, $\pi_l^{(+)}$ should be found from (42) only at $F_n = 0$ that gives

$$e^{-t\lambda_u} = \frac{c_n}{c^2 mn} \pi_n^{(+)}, \qquad c_i^{(+)} = F_l \pi_n^{(+)} \frac{b_{il} c_n}{c^2 mn (\lambda_i - \lambda_u)} \qquad (c^2 \equiv c_n c_n) \tag{43}$$

So, asymptotic electron distribution function $g_p(\varepsilon, \pi)$ according (26), (40), (43) has the form

$$g_p(\varepsilon, \pi) = \frac{2}{3n} (\varepsilon - \varepsilon_0) A_p + \frac{1}{mn} \pi_n \left[B_p p_n + F_l \frac{c_n}{c^2} \sum_{i \neq T, u_l} g_{ip} \frac{b_{il}}{\lambda_i - \lambda_u} \right]. \tag{44}$$

In the method of reduced description, elaborated by Bogolyubov, this result with definitions (26), (27) expresses his idea of the functional hypothesis (see general definitions in (1), (2)). It means: after some time τ_0 distribution function $g_p(t)$ depends on time t only trough asymptotic values $\varepsilon^{(+)}(t)$, $\pi_l^{(+)}(t)$ of parameters $\varepsilon(t)$, $\pi_l(t)$ and the

quantities $\varepsilon^{(+)}(t)$, $\pi_l^{(+)}(t)$ satisfy closed set of equations (31). Therefore, in this paper the functional hypothesis is proved in the presence of small electric field. For the case of the absence of the field it was proved in our paper [17].

Reduced description of the system by average densities $\varepsilon^{(+)}(t)$, $\pi_n^{(+)}(t)$ can be discussed in the terms of electron component temperature $T(t)$ and macroscopic velocity $u_n(t)$ defined by formulas

$$\varepsilon^{(+)} = (3nT + mnu^2)/2, \qquad \pi_n^{(+)} = mnu_n. \tag{45}$$

Exact evolution equations (29) gives exact nonlinear dynamic equations describing the system by variables T and u_n

$$\partial_t u_n = -\lambda_u u_n + \frac{1}{m} F_n, \qquad\qquad \partial_t T = -\lambda_T (T - T_0) + (2\lambda_u - \lambda_T) mu^2 / 3 \tag{46}$$

the second of which does not contain the field. The Cauchy problem for these equations can be easily solved. Equilibrium state of the system is described by relations

$$u_n(t) \underset{t \gg \tau_T, \tau_u}{=} u_n^{eq}, \qquad u_n^{eq} = -\nu E_n, \qquad \nu \equiv \frac{e}{m\lambda_u};$$

$$T(t) \underset{t \gg \tau_T, \tau_u}{=} T^{eq}, \qquad T^{eq} = T_0 + \Delta T, \qquad \Delta T \equiv \frac{e^2 (2\lambda_u - \lambda_T)}{3m\lambda_T \lambda_u^2} E^2 \tag{47}$$

($F_n = -eE_n$). Of course, equilibrium quantities u_n^{eq}, T^{eq} coincide with ones u_n^{st}, T^{st} in the steady state of the system. Coefficient ν is called the electron mobility and the developed here theory gives an exact expression for him. Our theory predicts difference ΔT of equilibrium electron and ion temperatures in the presence of external electric field which also is an exact result.

APPROXIMATE CALCULATION OF THE MAIN QUANTITIES OF THE THEORY

Obtained results show that the main next problem is solving of the spectral problem for the collision integral operator $\hat{K}$. In our paper [17] calculation of the eigenfunctions A_p, $B_p p_n$ and corresponding eigenvalues λ_T, λ_u from equations (16), (17) is proposed to conduct by the method of truncated expansion in the Sonine polynomials $S_q^\alpha(x)$ ($q = 0,1,2,...$, α is a real number)

$$A_p = \sum_{q=0}^{\infty} a_q S_q^{1/2}(\beta\varepsilon_p), \qquad B_p = \sum_{q=0}^{\infty} b_q S_q^{3/2}(\beta\varepsilon_p) \qquad (\beta \equiv T_0^{-1}). \tag{48}$$

An example of this approach is given in our paper [19], where relaxation processes in polaron subsystem of semiconductors are investigated on the basis of equations (16), (17) but with different operator $\hat{K}$ and with functions A_p, $B_p p_n$, which describe relaxation processes close to the equilibrium. The choice of polynomials is suggested by normalization condition

$$\langle \varepsilon_p^{\alpha-1/2} S_q^\alpha(\beta\varepsilon_p) S_{q'}^\alpha(\beta\varepsilon_p) \rangle = \frac{n}{\beta^{\alpha-1/2}} \frac{2\Gamma(q+\alpha+1)}{\pi^{1/2} q!} \delta_{qq'} \tag{49}$$

which contains the average with the electron Maxwell distribution w_p (4). Formulas (48), (49) and normalization conditions (17) give first coefficients in expansions (48)

$$a_0 = 0, \quad a_1 = -\beta, \quad b_0 = \beta. \tag{50}$$

In the s-polynomial approximation it is assumed that only s coefficients in (48) are not equal to zero. The convergence rate of this procedure cannot be estimated because the considered spectral problem does not related to a small parameter.

The further calculations are similar to ones in quantum-mechanical perturbation theory. Equations (16) take the form

$$\sum_{q'=1}^{\infty} A_{qq'} a_{q'} = \lambda_T a_q x_q, \qquad\qquad \sum_{q'=0}^{\infty} B_{qq'} b_{q'} = \lambda_u b_q y_q, \tag{51}$$

where $A_{qq'}$, $B_{qq'}$ are matrix elements of the collision integral operator $\hat{K}$ and some coefficients x_q, y_q

$$A_{qq'} = \{S_q^{1/2}(\beta\varepsilon_p), S_{q'}^{1/2}(\beta\varepsilon_p)\}, \qquad B_{qq'} = \{p_l S_q^{3/2}(\beta\varepsilon_p), p_l S_{q'}^{3/2}(\beta\varepsilon_p)\};$$

$$x_q \equiv 2n\frac{\Gamma(q+3/2)}{\pi^{1/2}q!}, \qquad y_q \equiv \frac{4mn}{\beta}\frac{\Gamma(q+5/2)}{\pi^{1/2}q!}$$

(52)

are introduced. Here standard in kinetic theory notation for the matrix elements of the operator $\hat{K}$ is used and related quantities are called the integral brackets

$$\{a_p, b_p\} = \langle a_p \hat{K} b_p\rangle$$

(53)

(according to (8) $\langle a_p b_p\rangle$ is the scalar product of functions a_p, b_p).

In one-polynomial approximation relations (50) - (52) give [7]

$$A_p^{[1]} = -\beta\left(\frac{3}{2} - \beta\varepsilon_p\right), \quad \lambda_T^{[1]} = \frac{2\beta^2}{3n}\{\varepsilon_p, \varepsilon_p\}; \qquad B_p^{[1]} = \beta, \quad \lambda_u^{[1]} = \frac{\beta}{3mn}\{p_l, p_l\}$$

(54)

(a quantity a in s-polynomial approximation is denoted by $a^{[s]}$). Entering here brackets can be calculated exactly [7]

$$\lambda_u^{[1]} = \frac{2^{5/2}\pi^{1/2}e^4 z^2 Ln_0}{3(1+\mu^2)^{1/2}m^{1/2}T_0^{3/2}}, \qquad \lambda_T^{[1]} = \frac{2^{7/2}\pi^{1/2}\mu^2 e^4 z^2 Ln_0}{3(1+\mu^2)^{3/2}m^{1/2}T_0^{3/2}} = \frac{2\mu^2}{1+\mu^2}\lambda_u^{[1]} \qquad (\mu \equiv (m/M)^{1/2})$$

(55)

In paper [13] these values were calculated in the main approximation in the parameter μ which is a small one because

$$\mu \leq (m_e/m_p)^{1/2} \approx 2,34\cdot10^{-2}$$

(56)

(here m_e, m_p are electron and proton masses). As a result our expression for λ_u coincides with one from [13] but our expression for λ_T gives one from [13] after the replacement $n_0 \rightarrow n_0(z+1)$. This result is expected because in [13] the dynamics of ions was more fully taken into account.

Starting from Landau investigation on the temperature relaxation in the completely ionized plasma [5] it is assumed that electron distribution function in spatially uniform states coincides in the main approximation with the Maxwell one (analogous assumption is made in the velocity relaxation theory [9]). In the terms of our consideration it is confirmed only in one-polynomial approximation at small temperature difference $T - T_0$ and small velocity u_n. Really, according to (4), (50) the Maxwell distribution for electron system with temperature T and macroscopic velocity u_n can be rewritten as

$$w_{p-mu}\big|_{T_0 \rightarrow T} = w_p\left[1 + \frac{1}{T_0}\left(\frac{\varepsilon_p}{T_0} - \frac{3}{2}\right)(T - T_0) + \frac{1}{T_0}p_n u_n + \ldots\right] = w_p\left[1 + A_p^{[1]}(T - T_0) + B_p^{[1]}p_n u_u + \ldots\right] =$$

$$= w_p\left[1 + \frac{2}{3n}A_p^{[1]}(\varepsilon - \varepsilon_0) + \frac{1}{mn}B_p^{[1]}p_n\pi_u + \ldots\right]$$

(57)

This expression should be compared with nonequilibrium distribution function given by formulas (12), (30). This remark shows, why Landau relaxation theory [5] gives relaxation coefficient λ_T which coincides with one in one-polynomial approximation $\lambda_T^{[1]}$ from (55) taken in the small μ limit.

Our general expression (47) for the mobility of electron in plasma can be concretize in one-polynomial approximation with the velocity relaxation coefficient λ_u from (55) that in the main in small μ approximation gives

$$\nu = \frac{3T_0^{3/2}}{2^{5/2}\pi^{1/2}e^3 m^{1/2}z^2 Ln_0},$$

(58)

Electron mobility defines electron current j_l of the plasma in the steady state

$$j_l = -neu_l, \qquad u_l^{st} = -\nu E_l \qquad\qquad (59)$$

and therefore gives the plasma conductivity σ

$$j_l^{st} = \sigma E_l, \qquad \sigma = en\nu = \frac{e^2 n}{\lambda_u} \qquad\qquad (60)$$

(see (47)). This formula for σ is exact one. It in the one-polynomial approximation and in the main order in the parameter μ according to expression (58) gives

$$\sigma = \frac{3T_0^{3/2}}{2^{5/2}\pi^{1/2}e^2 m^{1/2} zL} . \qquad\qquad (61)$$

Here the plasma neutrality condition $n_0 z = n$ is taken into account (n, n_0 are electron and ion component densities). Note, that this formula differs by numerical coefficient from one obtained for the Lorentz plasma in [10] where approximate expression for the collision integral of the form

$$I_p(f) = -\nu(p)\delta f_p, \qquad \nu(p) \equiv \frac{4\pi z e^4 n m L}{p^3} \qquad (f_p \equiv w_p + \delta f_p, \;\; I_p(w) = 0) \qquad\qquad (62)$$

is used.

Our formula (47) gives exact expression for the electron and ion component temperature difference in equilibrium or steady state of the plasma. In one-polynomial approximation (55) for relaxation coefficients λ_T, λ_u it can be expressed through the electron mobility ν by the formula

$$\Delta T = \frac{m\nu^2}{3} E^2 . \qquad\qquad (63)$$

This formula was derived also in [8] but without control of its accuracy.

DISCUSSION

In the present paper the investigation of completely ionized plasma based on our generalization of the Lorentz model is conducted in the presence of constant and spatially uniform electric field. The generalization is based on the Landau kinetic equation and takes into account features of the Coulomb interaction. Contrary to Lorentz it is assumed that ions form equilibrium system. Kinetic equation for the model is linear one and for investigation of nonequilibrium processes a spectral theory of the collision integral operator is used. This operator is rotationally invariant, symmetric and positively defined one. Therefore quantum-mechanical approaches for approximate investigation of nonequilibrium processes in the system are applied here. Eigenfunctions of the collision integral operator describe kinetic modes of the system. In the paper irreducible symmetric tensors as eigenfunction of this operator are used. This very simplifies using rotationally invariance ideas in the calculations. On this base it is proved that energy and momentum densities of the electrons ε, π_n are described only by scalar A_p and vector $B_p p_n$ eigenfunctions correspondently. Moreover, this allows proving that for the mentioned densities exact closed linear evolution equations are valid which are true for all times.

Relaxation processes in the electron component can be described instead of densities ε, π_n by corresponding temperature T and macroscopic velocity u_n. The obtained exact evolution equation for the velocity is a linear one but exact evolution equation for the temperature is quadratic in the velocity. These equations contain the temperature and velocity relaxation coefficients λ_T, λ_u as eigenvalues of the collision integral operator corresponding to eigenfunctions A_p, $B_p p_n$. In these terms steady (equilibrium) states of the system are discussed and exact expressions for the electron mobility and conductivity are obtained. The equilibrium phenomenon of electron T and ion T_0 temperature difference is predicted and is described by an exact expression. This effect was discussed in the literature early [8] but with an indefinite accuracy.

Important part of the paper discusses long time behavior of the plasma in the presence of a small constant and spatially uniform electric field. A characteristic time τ_0 is introduced so, that at $t \gg \tau_0$ only vector and scalar modes of the system evolve. The mentioned exact relaxation equations are also true for the asymptotic values $\varepsilon^{(+)}$, $\pi_n^{(+)}$ of the quantities ε, π_n. At these times electron distribution function is investigated. In the straightforward perturbation theory

in electric field it is shown that this function at $t >> \tau_0$ (asymptotic distribution function) depends on time only through the quantities $\varepsilon^{(+)}$, $\pi_n^{(+)}$. This result expresses the Bogolyubov idea of the functional hypothesis that is basis of his method of reduced description of nonequilibrium states.

Further discussion of relaxation phenomena in the system needs of approximate expressions for the relaxation coefficients as eigenvalues of the collision integral operator and corresponding eigenfunctions. However, the related spectral problem can be solved only approximately. With this end in view in the paper the method of truncated expansion in the Sonine polynomials is used. As a result, relaxation coefficients are written in the one-polynomial approximation but exactly in small electron-to-ion mass ratio μ^2. Details of these calculations with consideration of the two-polynomial approximation are discussed in our paper [18]. These results show that commonly used the Maxwell distribution function with electron component temperature and velocity as the electron distribution function in the presence of relaxation processes (see [5, 9, 10, 12]) is true only in one-polynomial approximation and for small u_n and $T - T_0$. This explains why our temperature relaxation coefficient λ_T in one-polynomial approximation coincides with the Landau one [5].

On the base of the obtained here results spatially nonuniform states of plasma in the presence of relaxation processes will be investigated in a subsequent paper.

Note finally, that developed here theory can be applied for investigation of relaxation phenomena in theory of polarons in the Fröhlich model (see, for example, [12]).

ORCID IDs
Alexander I. Sokolovsky, https://orcid.org/0000-0001-7988-6753; **Sergey A. Sokolovsky**, https://orcid.org/0000-0001-6772-647X
Oleh A. Hrinishyn, https://orcid.org/0000-0002-5620-3523

REFERENCES
[1] D. Jou, J. Casas-Vazques, and G. Lebon, *Extended Irreversible Thermodynamics,* (Springer, 2010).
[2] S.V. Peletminskii, Yu.V. Slyusarenko, and A.I. Sokolovsky, Physica A. **326**(3-4), 412-429 (2003), https://doi.org/10.1016/S0378-4371(03)00255-3.
[3] V.N. Gorev, A.I. Sokolovsky, in: *Actual Problems of Mathematical Physics and its Applications. Proceedings of Institute of Mathematics NASU*, **11**(1), **(**IM, Kyiv, 2014), pp. 67-92.
[4] H.A. Lorentz, Proc. Acad. Sci. Amsterdam, **7**, 438, 585 **(**1905).
[5] L.D. Landau, ZhETF, **7,** 203-209 (1936). (in Russian).
[6] A.I. Akhiezer, S.V. Peletminsky, *Methods of Statistical Physics*, (Pergamon Press, Oxford, 1981).
[7] S.A. Sokolovsky, A.I. Sokolovsky, I.S. Kravchuk, and O.A. Grinishin, Journal of Physics and Electronics, **26**(2), 17-28 (2018), https://doi.org/10.15421/331818.
[8] B.M. Smirnov, UFN, **172**(12), 1411-1445 (2002). (in Russian).
[9] A.F. Aleksandrov, L.S. Bogdankevich, and A.A. Rukhadze, *Principles of Plasma Electrodynamics*, (URSS, Moscow, 2013), pp. 504.
[10] E.M. Lifshitz, and L.P. Pitaevskii, *Physical kinetics*, (Pergamon Press, Oxford, 1981).
[11] I.S. Braginsky, ZhETF, **33**, 459 (1957).
[12] N.N. Bogolyubov, and N.N. Bogolyubov (Jr.), *Аспекты теории полярона [Aspects of polaron theory]*, (Fizmatlit, Moscow, 2004), pp. 175. (in Russian).
[13] V.N. Gorev, and A.I. Sokolovsky, Ukr. J. Phys. **60**(3), 232-246 (2015), https://doi.org/10.15407/ujpe60.03.0232.
[14] V. N. Gorev, S.A. Sokolovsky, and A.I. Sokolovsky, Vìsnik Dnìpropetrovs'kogo unìversitetu. Serìâ Fìzika, radìoelektronika, **24**(23/2), 83-93 (2016).
[15] S.A. Sokolovsky, A.I. Sokolovsky, I.S. Kravchuk, O.A. Grinishin, Journal of Physics and Electronics, **26**(2)**,** 17-28 (2018), https://doi.org/10.15421/331818.
[16] S.A. Sokolovsky, A.I. Sokolovsky, I.S. Kravchuk, O.A. Grinishin, in: *Proceedings of IEEE 40th International Conference on Electronics and Nanotechnology (ELNANO-2020)*, ISBN: 978-1-7281-9712-8, (Kyiv, Ukraine, 2020), pp. 284-287.
[17] S.A. Sokolovsky, and A.I. Sokolovsky, in: *Proceedings of IEEE 2nd Ukraine Conference on Electrical and Computer Engineering, (UKRCON-2019)*, ISBN: 978-1-7281-3882-4, (Lviv, Ukraine, 2019), pp. 783-787.
[18] S.A. Sokolovsky, A.I. Sokolovsky, I.S. Kravchuk, and O.A. Grinishin, Journal of Physics and Electronics, **27**(2), 29-36 (2019), https://doi.org/10.15421/3919/9.
[19] S.A. Sokolovsky, Theoretical and Mathematical Physics, **168**(2), 1150-1164 (2011), https://doi.org/10.1007/s11232-011-0093-z.

ДО РЕЛАКСАЦІЙНИХ ПРОЦЕСІВ У ПОВНО ІОНІЗОВАНІЙ ПЛАЗМІ
О.Й. Соколовськийᵃ**, С.О. Соколовський**ᵇ**, О.А. Грінішин**ᵃ

ᵃДніпровський національний університет імені Олеся Гончара, кафедра теоретичної фізики проспект Гагаріна, 72, Дніпро
ᵇПридніпровська державна академія будівництва та архітектури, кафедра фізики
вул. Чернишевського, 24А, Дніпро

Релаксація густин енергії та імпульсу електронів досліджується в просторово-однорідних станах повністю іонізованої плазми за наявності малого постійного і просторово-однорідного зовнішнього електричного поля. Плазма розглядається в

узагальненій моделі Лоренца, яка на відміну від стандартної моделі передбачає, що іони утворюють рівноважну систему. Дотримуючись Лоренца, нехтуємо електрон-електронними та іон-іонними взаємодіями. Дослідження засноване на лінійному кінетичному рівнянні, отриманому нами раніше з кінетичного рівняння Ландау. Тому в ньому далекодійна електрон-іонна кулонівська взаємодія описується послідовно. Дослідження моделі ґрунтується на спектральної теорії оператора інтеграла зіткнень. Цей оператор симетричний і позитивно визначено. Його власні вектори обираємо у вигляді симетричних незвідних тензорів, які описують кінетичні моди системи. Відповідні власні значення є коефіцієнти релаксації і визначають часи релаксації системи. Встановлюється, що скалярні і векторні власні функції описують еволюцію густин енергії та імпульсу електронів (векторну і скалярну моди системи). На цій основі нами виводиться точна система рівнянь для вказаних густин, які справедливі для всіх часів. Далі передбачається, що їх часи релаксації набагато більші часів релаксації всіх інших мод. У цьому випадку існує такий характерний час, що при відповідних великих часах еволюція системи скорочено описується асимптотичними значеннями густин енергії та імпульсу. При скороченому описі функція розподілу електронів залежить від часу тільки через асимптотичні густини і вони задовольняють замкнутій системі рівнянь. У нашій попередній роботі цей результат був доведений за відсутності зовнішнього електричного поля і була знайдена точна нерівноважна функція розподілу. Нами доводиться, що цей скорочений опис має місце і для малого однорідного зовнішнього електричного поля. Це можна розглядати як обґрунтування ідеї функціональної гіпотези Боголюбова для релаксаційних процесів в плазмі. Доказ проводиться в першому наближенні теорії збурень за полем. Однак його ідея правильна у всіх порядках за полем. Рухливість електронів в плазмі, її провідність і явище відмінності в рівновазі електронної та іонної температур досліджуються нами в точної теорії і наближено аналізуються. З цією метою, слідуючи нашій попередній роботі, обговорюється наближене рішення спектральної задачі методом усіченого розкладання власних функцій в ряди поліномів Соніна. У наближенні одного полінома показується, що нерівноважна функція розподілу електронів в околиці завершення релаксаційних процесів може бути апроксимована функцією розподілу Максвелла. Цей результат є обґрунтуванням припущення Лоренца–Ландау в їх теорії нерівноважних процесів в плазмі. Коефіцієнти релаксації температури і швидкості розраховувалися нами раніше в наближеннях одного і двох поліномів.

КЛЮЧОВІ СЛОВА: плазма, узагальнена модель Лоренца, коефіцієнти релаксації, оператор інтеграла зіткнень, спектральна теорія, наближення одного, полінома, функціональна гіпотеза

К РЕЛАКСАЦИОННЫМ ПРОЦЕССАМ В ПОЛНОСТЬЮ ИОНИЗИРОВАННОЙ ПЛАЗМЕ
А.Й. Соколовский[a], С.А. Соколовский,[b] О.А. Гринишин[a]
[a]Днепровский национальный университет имени Олеся Гончара, кафедра теоретической физики
проспект Гагарина, 72, Днипро
[b]Приднепровская государственная академия строительства и архитектуры, кафедра физики
вул. Чернишевського, 24А, Днипро

Релаксация плотностей энергии и импульса электронов исследуется в пространственно- однородных состояниях полностью ионизованной плазмы при наличии малого постоянного и пространственно-однородного внешнего электрического поля. Плазма рассматривается в обобщенной модели Лоренца, которая в отличие от стандартной модели предполагает, что ионы образуют равновесную систему. Следуя Лоренцу, пренебрегаем электрон-электронными и ион-ионными взаимодействиями. Исследование основано на линейном кинетическом уравнении, полученном нами ранее из кинетического уравнения Ландау. Поэтому в нем дальнодействующее электрон-ионное кулоновское взаимодействие описывается последовательно. Исследование модели основывается на спектральной теории оператора интеграла столкновений. Этот оператор симметричен и положительно определен. Его собственные векторы выбираем в виде симметричных неприводимых тензоров, которые описывают кинетические моды системы. Соответствующие собственные значения являются коэффициентами релаксации и определяют времена релаксации системы. Установлено, что скалярные и векторные собственные функции описывают эволюцию плотностей энергии и импульса электронов (векторную и скалярную моды системы). На этой основе нами выводится точная система уравнений для указанных плотностей, справедливая для всех времен. Далее предполагается, что их времена релаксации намного больше, чем времена релаксации всех остальных мод. В этом случае существует такое характерное время, что при соответствующих больших временах эволюция системы сокращенно описывается асимптотическими значениями плотностей. При сокращенном описании функция распределения электронов зависит от времени только через асимптотические плотности, и они удовлетворяют замкнутой системе уравнений. В нашей предыдущей работе этот результат был доказан в отсутствие внешнего электрического поля и была найдена точная неравновесная функция распределения. Здесь доказывается, что это сокращенное описание имеет место и для малого однородного внешнего электрического поля. Это можно рассматривать как обоснование идеи функциональной гипотезы Боголюбова для релаксационных процессов в плазме. Доказательство проводится в первом приближении теории возмущений по полю. Однако его идея верна во всех порядках по полю. Подвижность электронов в плазме, ее проводимость и явление различия в равновесии электронной и ионной температур исследуются нами в точной теории и приближенно анализируются. С этой целью, следуя нашей предыдущей работе, обсуждается приближенное решение спектральной задачи методом усеченного разложения собственных функций в ряды полиномов Сонина. В приближении одного полинома показывается, что неравновесная функция распределения электронов в окрестности завершения релаксационных процессов может быть аппроксимирована функцией распределения Максвелла. Этот результат является обоснованием предположения Лоренца–Ландау в их теории неравновесных процессов в плазме. Коэффициенты релаксации температуры и скорости рассчитывались нами ранее в приближениях одного и двух полиномов.

КЛЮЧЕВЫЕ СЛОВА: плазма, обобщенная модель Лоренца, коэффициенты релаксации, оператор интеграла столкновений, спектральная теория, приближение одного полинома, функциональная гипотеза

CHARMONIUM PROPERTIES

Tarek A. Nahool[a,*], A.M. Yasser[b,], Muhammad Anwar[a], Gamal A. Yahya[a]**

[a]Physics Department, Faculty of ScienceAswan University, Egypt
[b]Physics Department, Faculty of Science at Qena, South Valley University, Egypt
*Corresponding Authors: *tarek.abdelwahab@sci.svu.edu.eg, **Yasser.mostafa@sci.svu.edu.eg*
Receive February 29, 2020; revised June 19, 2020; accepted June 25, 2020

We calculated the mass spectra of charmonium meson by using matrix method to make the predictions of ground and radially excited states of charmonium mesons via non-relativistic potential model. We compared our results with other theoretical approaches and recently published experimental data. The predictions are found to be in a good accordance with the latest experimental results of Particle data group and with the results of other theoretical approaches. Besides, we calculated the momentum width coefficients β of charmonium meson. Since, there are no experimental data for the momentum width coefficients β of charmonium meson yet. Consequently, our calculated coefficients β are compared with other theoretical studies and it is found to be in a good agreement with our results. The obtained results of coefficients β have implications for decay constants, decay widths and differential cross sections for charmonium system and generally for heavy mesons system. Our study is considered as theoretical calculation of some properties of charmonium meson.

KEYWORDS: heavy mesons, matrix method, charmonium, momentum width

Charmonium is a group of fundamental particles that are held to consist of a charmed quark-antiquark pair. The lowest bound state of a charm and anti-charm quark is called the J/ψ, whose mass is about 3.5 times greater than the proton mass. The $c\bar{c}$ meson presents itself as an ideal system to test assumptions of QCD. By making precise measurement of the masses, widths, and branching ratios of charmonium states important information about the dynamics of quark anti-quark interaction can be extracted [1]. The charmonium systems may provide unique signs to the non-perturbative behavior of QCD in the low-energy regime and have attracted a great deal of care from the quarkonium physics community [2]. In 2007, the Belle Collaboration [3] reported the Y (4660) resonance, as the heaviest state among the charmonium-like states at present for the first time. Its mass was determined to be M = (4664 ± 16) MeV. In the past decade, the properties of the charmonium states were widely explored with various theoretical methods. Reliable perturbative approaches, like lattice QCD [4], heavy quark effective field theory [5] and potential models are trying to explain the phenomena of quark confinement and dynamics of QCD. Charmonium is produced in various reactions, and subsequently decays into other particles. Studying its production mechanism will give a prolific testing for the QCD. There are many potential models commonly used to study heavy quarkonium spectra [6-9]. One of the most successful potential for such systems is the non-relativistic potential model [10-13]. We adopt the Cornell plus hyperfine correction plus spin-dependent terms model [14] to accurately obtain the $c\bar{c}$ spectrum of quark interactions for S and P states. Then, we compare our present work to other theoretical approaches [15, 16] and experimental results [17] to stress the success of our model. On the other hand, the main motivation is to calculate the numerical values of coefficient β that is related to the root-mean-square radius of quarkonium for different states of $c\bar{c}$ meson. Momentum width parameter β can be used to calculate the decay widths [18], and differential cross sections [19] for quarkonium states. The produced calculations of the momentum width parameter β are compared with published theoretical calculations from [20, 21]. The main aim of this research is to study the spectrum of charmonium meson using the matrix method [22]. Moreover, we compute the numerical values of coefficient β for conventional charmonium mesons and compare the obtained results with recently published calculations. The chief advantage of our perspective method is that all the computational process, requires a remarkably little time. Our method is overwhelmingly easy and fast, and it gives very accurate results.

This article is organized as follows. In Section 1 we present some characteristics properties of charmonium mesons which in turn depend on the potential model, details of the used methods in our present work are given in Section 2. Results and discussion are given in Section 3. Finally, in the last section, we summarize our main results and conclusions.

1. Characteristics of charmonium mesons
1.1 The constituent potential model
One of the most successful ways of describing the mesonic system is to solve the non-relativistic Schrödinger equation for these quark-anti quark states with an appropriate potential model. In a non-relativistic constituent quark model, the non-relativistic description with the Schrödinger equation gives acceptable results. We used the standard color Coulomb plus linear scalar form, and also include contact hyperfine interaction then We treated the remaining spin-dependent terms as mass shifts using leading-order perturbation theory. Thus, the potential model used here can be written as [1]:

$$V(r) = \frac{-4\alpha_s}{3r} + br + \frac{32\pi\alpha_s}{9m_c^2}\delta(\vec{r})(\vec{S_c}.\vec{S_{\bar{c}}}) + \frac{1}{m_c^2}\left[\left(\frac{2\alpha_s}{r^3} - \frac{b}{2r}\right)\vec{L}.\vec{S} + \frac{4\alpha_s}{r^3}T\right], \tag{1}$$

where

$$\delta(\vec{r}) = \left(\frac{\sigma}{\sqrt{\pi}}\right)^3 e^{-\sigma^2 r^2}, \tag{2}$$

and μ is the reduced mass of the quark and anti-quark

$$\mu = \frac{m_c m_{\bar{c}}}{m_{c} + m_{\bar{c}}}. \tag{3}$$

Here α_s is the quark-gluon coupling, $\left(\frac{-4}{3}\right)$ is the appropriate color factor and (b) is the parameter of the string tension, and (r) is the distance between the quarks; m_c is the mass of the charm quark, and the last term is for the spin-orbit potential with where s is the total spin quantum number of the meson [24] and

$$\vec{S_c}.\vec{S_{\bar{c}}} = \frac{S(S+1)}{2} - \frac{3}{4}. \tag{4}$$

The last term is for the spin-orbit potential with

$$\langle \vec{L}.\vec{S} \rangle = \frac{[J(J+1)-(L(L+1)-S(S+1))]}{2}. \tag{5}$$

The spin-orbit operator is diagonal in a $|J, L, S >$ basis with the matrix elements. The tensor operator T [25] has non vanishing diagonal matrix elements only between $L > 0$ spin-triplet states, which are

$$T = \begin{cases} -\frac{L}{6(2L+3)}, J = L + 1 \\ +\frac{1}{6}, J = L \\ -\frac{(L+1)}{6(2L-1)}, J = L - 1 \end{cases}. \tag{6}$$

For the charmonium mesons, the parameters α_s, b, σ, and m_c are taken from [26] to be 0.4942, 0.1446 GeV^2, 1.1412 GeV and 1.4619 GeV, respectively.

1.2 The Radial Wave Functions of Charmonium Mesons

Charmonium mesons can be described by the wave function of the bound state of quark-antiquark. This wave function $\psi(r) = r R(r)$ can be found by solving the time independent Schrödinger equation for a particle of reduced mass μ moving in a spherically symmetric potential with a position vector $\vec{r}$ and it is can be expressed as:

$$\left[-\frac{\hbar^2}{2\mu}\Delta + V(r)\right]\psi(\vec{r}, \theta, \varphi) = E\psi(\vec{r}, \theta, \varphi). \tag{7}$$

In spherical coordinates the Schrodinger equation takes the form

$$\left[\left(-\frac{\hbar^2}{2\mu}\frac{1}{r}\frac{d^2}{dr^2}r + \frac{1}{2\mu}\frac{1}{r^2}\hat{\vec{L^2}}\right) + V(r)\right]\psi(\vec{r}, \theta, \varphi) = E\psi(\vec{r}, \theta, \varphi), \tag{8}$$

where $\hat{\vec{L}}$ is orbital angular momentum and (r) is the distance between the quarks.

Dividing the last equation into two parts, the first part is the radial kinetic energy and the second term is the potential energy.
The radial part can be written as

$$\left[-\frac{\hbar^2}{2\mu}\left(\frac{1}{r}\frac{d^2}{dr^2}r - \frac{l(l+1)}{r^2}\right) + V(r)\right]R(r) = ER(r), \tag{9}$$

Then

$$\psi(r) = rR(r) \tag{10}$$

The matrix method [27] is used to solve Schrödinger to get the spectrum of charmonium, the details of this method could be found in the following section.

1.3 The momentum width coefficient β

The meson wave function is characterized by a momentum width parameter β that is depending upon the angular momentum quantum numbers and related to the root mean square radius quark-anti quark separation r_{ms} of the meson by [28].

$$\beta = \sqrt{2(n-1) + (L) + \frac{3}{2}} \ \frac{1}{r_{ms}} \ . \tag{11}$$

Since, the root mean square radius r_{ms} depends on the wave functions $\psi(r)$, which results from solving Schrödinger equation by using our method, it is expected that, the β values will be very accurate.

2. Matrix method for solving Schrödinger equation

Matrix method is a numerical approach for solving the Schrodinger Equation where the eigenvalues of a matrix gives the total energies of the particle (spectra) and the Eigen functions are the corresponding wave functions. Let us re write the Schrodinger equation in Eq. (9) using natural units.
Then it will be expressed as:

$$-\frac{1}{2\mu}\frac{d^2\psi}{dr^2} + \left[V(r) + \frac{l(l+1)}{2\mu r^2}\right]\psi(r) = E\,\psi(r) \tag{12}$$

Next, the second derivate of $\psi(r)$ function takes the form

$$\frac{d^2\psi(r)}{dr^2} = \frac{\psi(r+h) - 2\psi(r) + \psi(r-h)}{h^2} + O(h^2), \tag{13}$$

here,

$$h = \frac{R_{max} - R_{min}}{N}, \tag{14}$$

where h is our step between two points, R_{min} and R_{max}, are minimum and maximum values for the variable (r) respectively with a given number of steps (N) all over the range.
We can rewrite the Schrödinger equation in Eq. (12) for r_i as follow:

$$-\frac{\psi(r_i+h) - 2\psi(r_i) + \psi(r_i-h)}{2\mu h^2} + \left[V(r_i) + \frac{l(l+1)}{2\mu r_i^2}\right]\psi(r_i) = E\psi(r_i), \tag{15}$$

where, $r_i = R_{min} + ih, i = 1, 2, \ldots\ldots, N-1$
Let us use a compact way of writing the previous equation as:

$$-\frac{\psi_{i+1} - 2\psi_i + \psi_{i-1}}{2\mu h^2} + \left[V(r_i) + \frac{l(l+1)}{2\mu r^2}\right]\psi_i = E\psi_i \tag{16}$$

where, $\psi_i = \psi(r_i), \psi_{i+1} = \psi(r_i + h), \psi_{i-1} = \psi(r_i - h)$

The last equation could be written as:

$$c_i\psi_{i+1} + d_i\psi_i + c_i\psi_{i-1} = E\psi_i \tag{17}$$

Where

$$d_i = \left[\frac{1}{\mu h^2} + V(r_i) + \frac{l(l+1)}{2\mu r^2}\right], \quad c_i = -\frac{1}{2\mu h^2} \tag{18}$$

Where d_i and c_i represent the diagonal and non-diagonal elements, respectively.
Eq. (17) could be transformed into a matrix form. Thus, we can rewrite it as a group of linear equations as follows:

$$\begin{array}{ccccccc}
c_1\psi_2 & + & d_1\psi_1 & + & c_1\psi_0 & = & E\psi_1 \\
c_2\psi_3 & + & d_2\psi_2 & + & c_2\psi_1 & = & E\psi_2 \\
c_3\psi_4 & + & d_3\psi_3 & + & c_3\psi_2 & = & E\psi_3 \\
\vdots & & \vdots & & \vdots & & \vdots \\
\vdots & & \vdots & & \vdots & & \vdots \\
c_N\psi_{N+1} & + & d_N\psi_N & + & c_N\psi_{N-1} & = & E\psi_N
\end{array} \tag{19}$$

Then the matrix takes the diagonal form as:

$$
\begin{pmatrix}
d_1 & c_2 & 0 & 0 & \dots & \dots & 0 & \dots \\
c_1 & d_2 & c_3 & 0 & \dots & \dots & 0 & \dots \\
0 & c_2 & d_3 & c_4 & \dots & \dots & \dots & \dots \\
\dots & \dots & \dots & \dots & \dots & \dots & \dots & \dots \\
\dots & \dots & \dots & \dots & \dots & d_{N-1} & c_{N-1} & \dots \\
\dots & \dots & \dots & \dots & \dots & c_{N-1} & d_{N-1} & c_N
\end{pmatrix}
\begin{pmatrix}
\psi_1 \\ \psi_2 \\ \psi_3 \\ \dots \\ \psi_{N-2} \\ \psi_{N-1}
\end{pmatrix}
= E
\begin{pmatrix}
\psi_1 \\ \psi_2 \\ \psi_3 \\ \dots \\ \psi_{N-2} \\ \psi_{N-1}
\end{pmatrix}
\tag{20}
$$

This is a tridiagonal matrix of dimension $(N-1)x(N-1)$, then this matrix can be solved as an eigenvalue problem and yields $(N-1)$ eigenvalues. We implemented our method to solve eigenvalue problems.

3. Results and discussion

In this article we have calculated the spectra of S and P wave states of charmonium meson by solving the Schrödinger equation numerically using matrix method. Coulomb plus linear plus hyperfine plus spin-dependent terms potential model are considered. By taking N = 200, R_{max} = 20 *fm* , $\alpha_s(c) = 0.4942$, $b = 0.1497$ GeV^2, $\sigma = 1.1412$ GeV and the charm quark mass = 1.4619 GeV for S-states and for P-states, the spectra were summarized in Tables (1, 2). We predict the masses of the twenty states of $c\bar{c}$ meson where we compared our theoretical predictions with those from [15, 16, 17]. By comparing present work with the recently published experimental data, we found that the maximum errors are 0.03 GeV for S-states and the maximum errors for P-states are 0.044 GeV. Similarly, we found that the maximum errors between our work and [15] are 0.03 GeV for S-states and P-states. In the same way, we calculate the maximum errors between our work and [16] and it was 0.02 GeV for S-states and 0.03 GeV for P-states. Hence, it can be seen that our calculated spectra are in close accordance with the PDG results and with the results of other theoretical studies, thus it can be concluded that this method gives satisfying results for predicting charmonium spectra. The normalized radial wave functions for charmonium mesons are graphically represented in Figures (1) and (2) respectively.
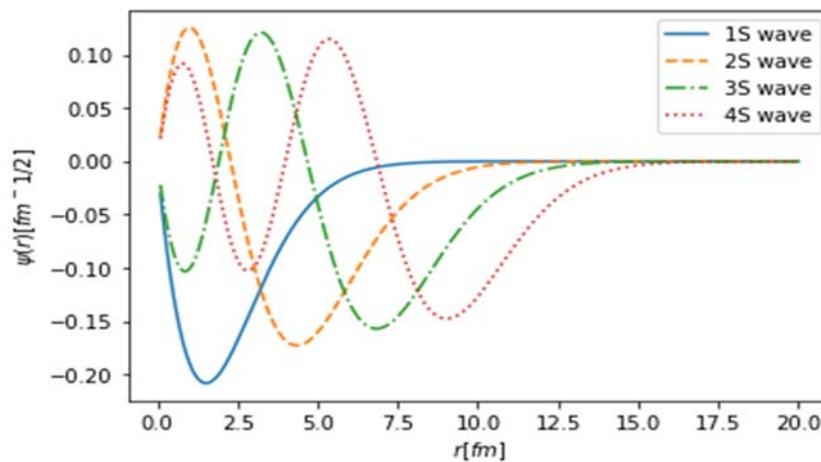
Figure 1. Charmonium S-states reduced radial wave functions.
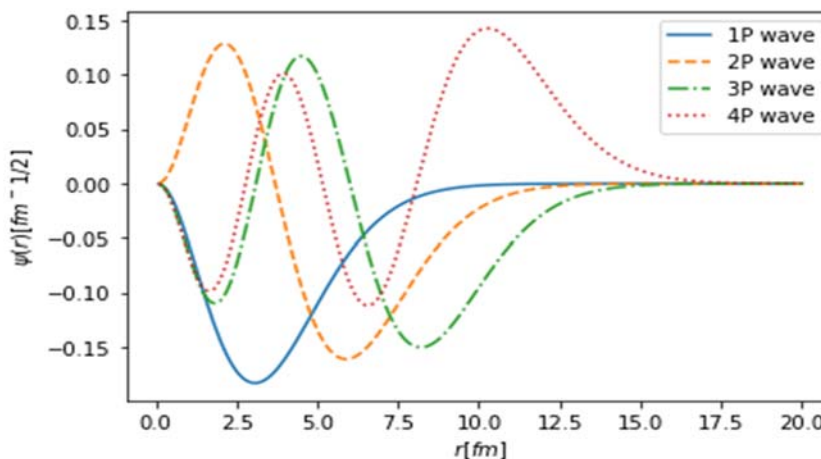
Figure 2. Charmonium P-states reduced radial wave functions.

In Figure (3), the present potential has been plotted for S and P states of charmonium. The predictions about the values of momentum width (Coefficient β) for charmonium S and P States in comparison between our results and those obtained in previous calculations [20, 21] are reported in Tables (3, 4) respectively.

a

b
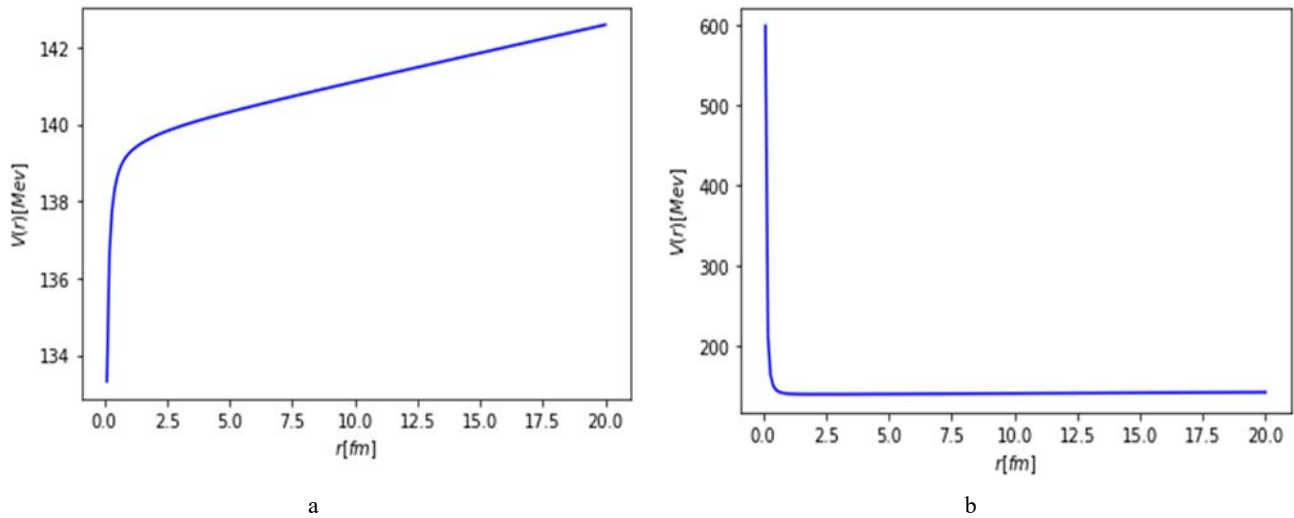
Figure 3. The present potential of charmonium meson for S and P States.

(a) - The present potential of charmonium meson for S States, (b) – The present potential of charmonium meson for P States

Table 1.

Mass spectrum for $c\bar{c}$ meson of S- states (in GeV) using matrix method.

State						Matrix method	[15]	[16]	PDG [17]
n	L	S	J	J^{PC}	Meson				
1^1S_0	0	0	0	0^{-+}	$\eta_c(1s)$	3.017	2.9816	3.004	2.9810 ± 0.0011
1^3S_1	0	1	1	1^{--}	J/ψ	3.113	3.0900	3.086	3.096916 ± 0.000011
2^1S_0	0	0	0	0^{-+}	$\eta_c(2s)$	3.637	3.6303	3.645	3.6389 ± 0.0013
2^3S_1	0	1	1	1^{--}	$\psi(2S)$	3.678	3.6718	3.708	3.6861 ± 0.000012
3^1S_0	0	0	0	0^{-+}	$\eta_c(3s)$	4.047	4.0432	4.124	
3^3S_1	0	1	1	1^{--}	$\psi(4040)$	4.076	4.0716	4.147	4.040 ± 10
4^1S_0	0	0	0	0^{-+}	$\eta_c(4s)$	4.388	4.3837	4.534	
4^3S_1	0	1	1	1^{--}	$\psi(4415)$	4.411	4.4061	4.579	4.415 ± 6

Table 2.

Mass spectrum of radially excited states (P-States) of $c\bar{c}$ meson (in GeV) using matrix method.

State						Matrix method	[15]	[16]	PDG [17]
n	L	S	J	J^{PC}	Meson				
1^1P_1	1	0	1	$\mathbf{1^{+-}}$	$h_c(1\mathcal{P})$	3.545	3.5156	3.496	3.52541 ± 0.00016
1^3P_1	1	1	1	$\mathbf{1^{++}}$	$\chi_{c1}(1\mathcal{P})$	3.524	3.5054	3.492	3.51066 ± 0.00007
1^3P_2	1	1	2	$\mathbf{2^{++}}$	$\chi_{c2}(1\mathcal{P})$	3.543	3.5490	3.511	3.556 ± 0.009
2^1P_1	1	0	1	$\mathbf{1^{+-}}$	$Z_c(3900)$	3.958	3.9336	3.991	
2^3P_1	1	1	1	$\mathbf{1^{++}}$	$\chi_{c1}(3872)$	3.94	3.9249	3.984	
2^3P_2	1	1	2	$\mathbf{2^{++}}$	$\chi_{c2}(3990)$	3.959	3.9648	4.007	3.927 ± 0.026
3^1P_1	1	0	1	$\mathbf{1^{+-}}$	$X(4020)$	4.303	4.2793	4.410	
3^3P_1	1	1	1	$\mathbf{1^{++}}$	$\chi_{c1}(4140)$	4.285	4.2707	4.401	
3^3P_2	1	1	2	$\mathbf{2^{++}}$	$\chi_{C2}(3\mathcal{P})$	4.306	4.3093	4.427	4.350 ± 0.007
4^1P_1	1	0	1	$\mathbf{1^{+-}}$	$Z_c(4430)$	4.61	4.5851	4.784	
4^3P_1	1	1	1	$\mathbf{1^{++}}$	$\chi_{c1}(4274)$	4.592	4.5762	4.771	
4^3P_2	1	1	2	$\mathbf{2^{++}}$	$\chi_{C2}(4\mathcal{P})$	4.613	4.6141	4.802	

Table 3.

Momentum width (Coefficient β) of ground states of charmonium mesons using matrix method.

State						Our work	[20]	[21]
n	L	S	J	J^{PC}	Meson			
1^1S_0	0	0	0	$\mathbf{0^{-+}}$	$\eta_c(1s)$	0.633	0.615	0.6642
1^3S_1	0	1	1	$\mathbf{1^{--}}$	J/ψ	0.562	0.596	0.5666
2^1S_0	0	0	0	$\mathbf{0^{-+}}$	$\eta_c(2s)$	0.436	0.435	0.4456
2^3S_1	0	1	1	$\mathbf{1^{--}}$	ψ(2S)	0.421	0.431	0.4249
3^1S_0	0	0	0	$\mathbf{0^{-+}}$	$\eta_c(3s)$	0.38	0.38	0.3858
3^3S_1	0	1	1	$\mathbf{1^{--}}$	ψ(4040)	0.373	0.378	0.3763
4^1S_0	0	0	0	$\mathbf{0^{-+}}$	$\eta_c(4s)$	0.351	0.351	0.3555
4^3S_1	0	1	1	$\mathbf{1^{--}}$	ψ(4415)	0.347	0.35	0.3499

Table 4.

Momentum width (Coefficient β) of radially excited states of charmonium mesons using matrix method.

State						Our work	[20]	[21]
n	L	S	J	J^{PC}	Meson			
1^1P_1	1	0	1	1^{+-}	$h_c(1\mathcal{P})$	0.437	0.458	0.3487
1^3P_1	1	1	1	1^{++}	$\chi_{c1}(1\mathcal{P})$	0.455	0.471	0.3487
1^3P_2	1	1	2	2^{++}	$\chi_{c2}(1\mathcal{P})$	0.432	0.439	0.3487
2^1P_1	1	0	1	1^{+-}	$Z_c(3900)$	0.379	0.389	
2^3P_1	1	1	1	1^{++}	$\chi_{c1}(3872)$	0.387	0.394	
2^3P_2	1	1	2	2^{++}	$\chi_{c2}(3990)$	0.376	0.38	
3^1P_1	1	0	1	1^{+-}	$X(4020)$	0.35	0.356	
3^3P_1	1	1	1	1^{++}	$\chi_{c1}(4140)$	0.356	0.359	
3^3P_2	1	1	2	2^{++}	$\chi_{C2}(3\mathcal{P})$	0.348	0.351	
4^1P_1	1	0	1	1^{+-}	$Z_c(4430)$	0.331		
4^3P_1	1	1	1	1^{++}	$\chi_{c1}(4274)$	0.336		
4^3P_2	1	1	2	2^{++}	$\chi_{C2}(4\mathcal{P})$	0.33		

4. Conclusion

The non-relativistic quark model is one of the most powerful frameworks to investigate the heavy meson spectra. The mass spectra of $c\bar{c}$ mesons were calculated in that framework based on the matrix method. Predictions from our method are found to be in good agreement with the PDG results and available theoretical results. Our results in comparison with the experimental data and other theoretical approaches results are reported in Tables (1, 2). It can be noticed that our calculated mass spectra are in close resemblance with the latest PDG results and also with the results of other theoretical studies, thus it can be concluded that this method gives satisfying results for S and P wave spectroscopy. On the other hand, we used the matrix method to obtain the radial wave functions of charmonium meson to calculate the coefficient β. Then, we compare our results with available published results which obtained from other studies and it was nearly commensurate. Our calculated coefficient β in comparison with other theoretical studies are reported in Tables (3, 4). As a remarkable result, we can point out that it is recommended to use the obtained values of coefficient β to calculate the decay widths and differential cross sections for charmonium system. Overall, the obtained results from the present study are reasonable when compared with the latest experimental results and available theoretical results which obtained from other approaches for the mass spectra of $c\bar{c}$ meson.

Finally, we may notice that the calculated values of coefficient β are the newer outputs where we did not find experimental data for comparison. So, we are looking forward to taking these data in consideration by other experimental and theoretical researchers.

ORCID IDs

Tarek A. Nahool https://orcid.org/0000-0002-3967-0103

REFERENCES
[1]   T. Barnes, S. Godfrey, and E.S. Swanson, Physical Review D, **72**(5), 054026 (2005), https://doi.org/10.1103/PhysRevD.72.054026.

[2]   H.X. Chen, W. Chen, X. Liu, and S.L. Zhu, Phys. Rep. **639**, 1-121 (2016), https://doi.org/10.1016/j.physrep.2016.05.004.
[3]   X.L. Wang et al. (Belle Collaboration), Phys. Rev. Lett. **99**, 142002 (2007), https://doi.org/10.1103/PhysRevLett.99.142002.
[4]   C. McNeile, C.T.H. Davies, E. Follana, K. Hornbostel, and G.P. Lepage (HPQCD Collaboration), Phys. Rev. D, **86**, 074503 (2012), https://arxiv.org/abs/1207.0994, https://doi.org/10.1103/PhysRevD.86.074503.
[5]   M. Neubert, Phys. Rep. **245**(5-6), 259-395 (1994), https://doi.org/10.1016/0370-1573(94)90091-4.
[6]   S. Godfrey, and N. Isgur, Phys. Rev. D, **32**, 189 (1985), https://doi.org/10.1103/PhysRevD.32.189.
[7]   C. Semay, and B. Silvestre-Brac, Nuclear Physics A, **618**, 455-482 (1997), https://doi.org/10.1016/S0375-9474(97)00060-2.
[8]   G. Bhanot, and S. Rudaz, Phys. Lett. B, **78**, 119-124 (1978), https://doi.org/10.1016/0370-2693(78)90362-3.
[9]   N. Brambilla, and A. Vario, Acta. Phys. Polon. B, **38**, 3429 (2007).
[10] S.S. Gershtein, V.V. Kiselev, A.K. Likhoded, and A.V. Tkabladze, Phys. Rev. D, **51**, 3613 (1995), https://doi.org/10.1103/PhysRevD.51.3613.
[11] Bhaghyesh, K.B.V. Kumar, and M. Yong-Liang, Int. J. Mod. Phys. A, **27**, 125001 (2009).
[12] A. B. Henriques, Z. Phys. C, Particles and Fields, **18**, 213 (1983), https://doi.org/10.1007/BF01571362.
[13] A.M. Yasser, G.S. Hassan, and T.A. Nahool, Journal of Modern Physics, **5**, 1938-1944 (2014). http://dx.doi.org/10.4236/jmp.2014.517188
[14] T.A. Nahool, A.M. Yasser and G.S. Hassan, EJTP, **12**(32), 113–120 (2015).
[15] M. Atif Sultan, Nosheen Akbar, Bilal Masud, and Faisal Akram, Phys. Rev. D, **90**, 054001 (2014), https://doi.org/10.1103/PhysRevD.90.054001.
[16] Raghav Chaturvedi and Ajay Kumar Rai, Eur. Phys. J. Plus, **133**(220) (2018), https://doi.org/10.1140/epjp/i2018-12044-8.
[17] C. Patrignani et al. (Particle Data Group), Chin. Phys. C, **40**, 100001 (2016).
[18] B. Patel, and P.C. Vinodkumar, Journal of Physics G, **36**, Article ID: 035003, (2009), http://dx.doi.org/10.1088/0954-3899/36/3/035003.
[19] C.H. Chaug, C.F Qiao and J.X. Wang, Physical Review D, **57**, Article ID: 4035, (1998). http://dx.doi.org/10.1103/PhysRevD.57.4035
[20] A.S. Ahmed, Studying of Some Charmonium Properties by Using Matrix Method, M.Sc. Thesis, South Valley University, Egypt, (2014).
[21] Jamil Ahmed, Rahila Manzoor and Alfredo Raya, Quant. Phys. Lett. **6**(2), 99-103 (2017). http://dx.doi.org/10.18576/qpl/060204
[22] B. Jonsson and S. T. Eng, IEEE journal of quantum electronics, **26**(11), 2025-2035 (1990).
[23] O. Lakhina, and E.S. Swanson, (2006) Physical Review D, **74**, Article ID: 014012. http://dx.doi.org/10.1103/PhysRevD.74.014012.
[24] N. Akbar, B. Masud, and S. Noor, The European Physical Journal A, **50**(7), 121 (2014), https://doi.org/10.1140/epja/i2014-14121-y.
[25] T. Barnes and G. I. Ghandour, Phys. Lett, B, **118**, 411-413 (1982), https://doi.org/10.1016/0370-2693(82)90214-3.
[26] A.A. Aly, *Heavy Meson Spectra Non-Relativistic Quark Model*, M. Sc. Thesis, (South Valley University, 2012).
[27] J. Förster, A. Saenz, and Ul. Wolff, Phys. Rev. E, **86**, 016701 (2012), https://doi.org/10.1103/PhysRevE.86.016701.
[28] Cheuk-Yin Wong, Phys. Rev. C, **69**, 055202, (2004), https://doi.org/10.1103/PhysRevC.69.055202.

ВЛАСТИВОСТІ ЧАРМОНІЮ
Тарек А. Нагул[a], А.М. Ясер[b], Мохаммад Анвар[a], Гамаль А. Яхья[a]
[a]Департамент фізики, Науковий факультет, Асуанський університет, Єгипет
[b]Департамент фізики, Науковий факультет Кени, Університет Південної долини, Єгипет

Ми розрахували мас-спектри мезона чармонію за допомогою матричного методу, щоб зробити передбачення основного і радіально збудженого станів мезонів чармонію за допомогою нерелятивістської потенційної моделі. Ми порівняли наші результати з іншими теоретичними підходами і недавно опублікованими експериментальними даними. Виявлено, що передбачення знаходяться в хорошому відповідно до останніх експериментальними результатами групи даних частинок і з результатами інших теоретичних підходів. Крім того, були розраховані коефіцієнти ширини імпульсу β мезона чармонію. Оскільки експериментальних даних для коефіцієнтів ширини імпульсу β мезона чармонію поки немає, тому наші розраховані коефіцієнти β порівнюються з іншими теоретичними дослідженнями, і показано, що вони добре узгоджуються з нашими результатами. Отримані результати за коефіцієнтами β мають значення для констант розпаду, ширин розпаду і диференціальних перерізів для системи чармонію і в цілому для системи важких мезонів. Наше дослідження розглядається як теоретичний розрахунок деяких властивостей мезона чармонію.
КЛЮЧОВІ СЛОВА: важкі мезони, матричний метод, Чармон, ширина імпульсу

СВОЙСТВА ЧАРМОНИЯ
Тарек А. Нагул[a], А.М. Ясер[b], Мухаммад Анвар[a], Гамаль А. Яхья[a]
[a]Департамент физики Научный факультет, Асуанский университет, Египет
[b]Департамент физики, Научный факультет Кени, Университет Южной долины, Египет

Мы рассчитали масс-спектры мезона чармония с помощью матричного метода, чтобы сделать предсказания основного и радиально возбужденного состояний мезонов чармония с помощью нерелятивистской потенциальной модели. Мы сравнили наши результаты с другими теоретическими подходами и недавно опубликованными экспериментальными данными. Обнаружено, что предсказания находятся в хорошем соответствии с последними экспериментальными результатами группы данных частиц и с результатами других теоретических подходов. Кроме того, были рассчитаны коэффициенты ширины импульса β мезона чармония. Поскольку экспериментальных данных для коэффициентов ширины импульса β мезона чармония пока нет, поэтому наши рассчитанные коэффициенты β сравниваются с другими теоретическими исследованиями, и показано, что они хорошо согласуются с нашими результатами. Полученные результаты по коэффициентам β имеют значение для констант распада, ширин распада и дифференциальных сечений для системы чармония и в целом для системы тяжелых мезонов. Наше исследование рассматривается как теоретический расчет некоторых свойств мезона чармония.
КЛЮЧЕВЫЕ СЛОВА: тяжелые мезоны, матричный метод, чармоний, ширина импульса

PRODUCTION OF HIGH-PURITY CADMIUM SINGLE CRYSTALS BY VERTICAL DIRECTED CRYSTALLIZATION METHOD

Alexey P. Shcherban[a,*], Gennadiy P. Kovtun[a,b], Dmitriy A. Solopikhin[a],
Yuri V. Gorbenko[a], Igor V. Kolodiy[a], Vladimir D. Virich[a]

[a]National Science Center "Kharkiv Institute of Physics and Technology"
1, Academichna str., 61108 Kharkiv, Ukraine
[b]V.N. Karazin Kharkiv National University, 4 Svobody Sq., 61022 Kharkiv, Ukraine
*Corresponding Author: shcherban@kipt.kharkov.ua

Received March 30, 2020; revised May 8; accepted May 12, 2020

The process of producing high-purity Cd crystals by the vertical directed crystallization (VDC) from a melt according to the Bridgman method is investigated. Single crystals with the preferred growth direction $[11.2]$ and $[10.3]$ were produced. The angles of deviation of the growth direction relative to the axis of the samples are $\alpha = 27.2°$ and $\alpha = 0.5°$. The crystal perfection, microstructure and microhardness of the grown crystals are determined. As shown by x-ray diffraction analysis, in this VDC variant of high-purity cadmium, a perfect single-crystal structure is not reached. In the start section there are separate grains with different orientations, the amount of which decreases in the end section of the single crystal. This results in the formation of a more perfect single-crystal structure with a preferred orientation, which occupies the entire cross section of the crystal. The microhardness of the upper and lower sections of single crystals was determined. The more contaminated end sections of the crystals have lower microhardness than the initial parts. The impurity composition of the start and end sections of single crystals produced from cadmium of various grades purity was studied. The efficiency of impurity elements redistribution along single crystals is the same for different grades of cadmium. The developed VDC process can be used for growing single crystals of low-melting metals, such as Zn, Pb, Te, In, Bi, Sn, etc.

KEY WORDS: cadmium, vertical directed crystallization, single crystals, growth direction, microstructure, microhardness, impurity composition

Recently, the need for single crystals of metals for practical and research purposes has been increasing. For this reason, a new industry has increased - single crystal growing. Single crystals of metals and semiconductors are produced by growing from a melt mainly in three ways: vertical directed crystallization (VDC) – the Bridgman method [1]; pulling from a melt onto a seed – the Czochralski method [2, 3] and crucibleless melting – the Pfann method [4].

The history of the development of technique for single crystals growing by the VDC method totals about 100 years. The first papers on the growth of VDC crystals were those of Tamman (1923) [5]. In 1924, L.V. Obreimov and L.V. Shubnikov implemented the VDC method in which single crystals were grown in a vertical fixed tubular container cooled by compressed air [6]. P. Bridgman in 1925 made constructive changes to the proposed VDC method. In this method the container became movable. D. Stockbarger in 1937 introduced additional design changes to the Bridgman VDC process. A two-section heater with a diaphragm in its middle was proposed here to provide a larger temperature gradient at the crystallization front. In 1925, Bridgman prepared single crystals of Sn, Cd, Zn, Sb, Bi, and Te by the VDC method. Since then, researchers have been working both on improving technological methods for growing single crystals, and on achieving a perfect structure and quality of the producing single crystals.

The advantage of the VDC method is that it allows one to grow large sizes single crystals of square, rectangular or round cross sections. The cross section of a single crystal is determined by the shape of the container. A significant drawback of this method is that the crystallization front is not visible during solidification process. This drawback can be partially overcome by installing thermocouples in a container for measuring temperatures and thus determining the position of the crystallization front and the temperature gradient at the crystallization front.

Goals of article is to study the process of producing high-purity bulk cadmium single crystals by the VDC method without use of seed.

MATERIALS AND METHODS

Two grades of metal were used as the initial material for producing high-purity cadmium single crystals by the VDC method: cadmium of initial purity > 99.99%, which corresponds to the technical grade Cd0A, and cadmium of high-purity > 99.999%, which corresponds to a cadmium grade of Cd00 high-purity. High-purity cadmium was produced by the complex method of distillation in vacuum [7, 8]. The directions of growth orientation were determined for the produced Cd single crystals, their structural perfection was studied, changes in the microhardness and impurity composition of the start and end parts of single crystals were determined.

Diffractometric studies of the samples were carried out on a DRON-2.0 X-ray diffractometer with cobalt Co-Kα radiation applying a Fe selectively absorbing filter. Diffracted radiation was detected by a scintillation detector.

Analysis of crystallographic orientation (CGO) and crystal perfection was carried out from the butt-end of the rods by the rotating crystal method. Samples for X-ray and microstructural studies were cut by electrospark cutting perpendicular to the axis of the rods (see Fig. 1). The surfaces of samples were prepared by grinding and polishing according to a standard technique followed by etching in a reagent of the following composition: chromic anhydride – 10 g; hydrochloric acid – 1 ml; water – 100 ml.

Microhardness was measured according to the Vickers method on a PMT-3 instrument with a load of 10 g. The microstructure was studied using an MMP-4 light microscope.

The impurity composition of single crystals was determined by laser mass spectrometry using the EMAL-2 type mass spectrometer.

EXPERIMENTAL SECTION

The process of growing single crystals by the Bridgman VDC method is carried out in special facilities in vacuum, inert atmosphere, hydrogen and in air. The Bridgman method is suitable for metals with a relatively low melting point and small chemical activity. These limitations arise due to the difficulty in selecting the material of the crucible-container. Typically, crucibles made of graphite, quartz, aluminum oxide are used.

The study of the process of producing cadmium single crystals was carried out in a facility, the heat unit and mounting of which were modernized for the process of single crystals growth by the vertical Bridgman method. A special device was manufactured, the scheme of which is given in paper [9]. A container with molten cadmium was pulled down from the heater to a cold region, where, as it was pulled, a single-crystal structure of arbitrary orientation was formed.

To carry out the processes of cadmium directed crystallization, a special container was made of high-purity dense graphite of MPG-7 grade. The impurity composition of such graphite is given in paper [10]. The container had a conical shape at the bottom with an apex angle of 40°. Before use, the container was annealed at ~ 1000 °C in a vacuum of 1 ... 3 Pa for half an hour. The crystals were grown with a crystallization rate of 0.37 to 0.24 mm/min under a pressure in the facility chamber within 1.7...1.9 atm of pure argon. The temperature gradient at the crystallization front ranged from 14.4 to 15.0 °C/cm.

RESULTS AND DISCUSSION

Figure 1 shows the external view of A and B cadmium single crystals produced by the described above method of vertical directed crystallization.

Figure 1. External view of single crystals of cadmium A and B with marked places of cutting samples for research

Figure 2 shows the diffraction patterns of the start a) and end b) sections of the single crystal A, recorded according to the «θ-2θ» scanning scheme. It can be seen that low-intensity diffraction lines are present on the diffraction patterns. The lines (11.2) are with the maximum intensity, that is, the crystallographic planes (11.2) are oriented parallel to the plane of the end face of the crystal. The presence of other lines in the diffractogram indicates the presence of grains in the sample with a different orientation.

An analysis of the crystallographic orientation (CGO) and the degree of perfection of the single crystal (Figure 3) showed that the deviation of the crystallographic direction from the normal to the butt-end part is $\alpha = 27°$. Also, from the start side a) the presence of a block with a misorientation angle $\Delta\alpha = 0.5°$ from the main maximum was revealed. In addition to the main maximum, additional maximums were also revealed at the angles of 3.3° and 0.6° with the start side a) (indicated by the arrow) and 3.0° with the end side, which also indicates the presence of grains with a different orientation.
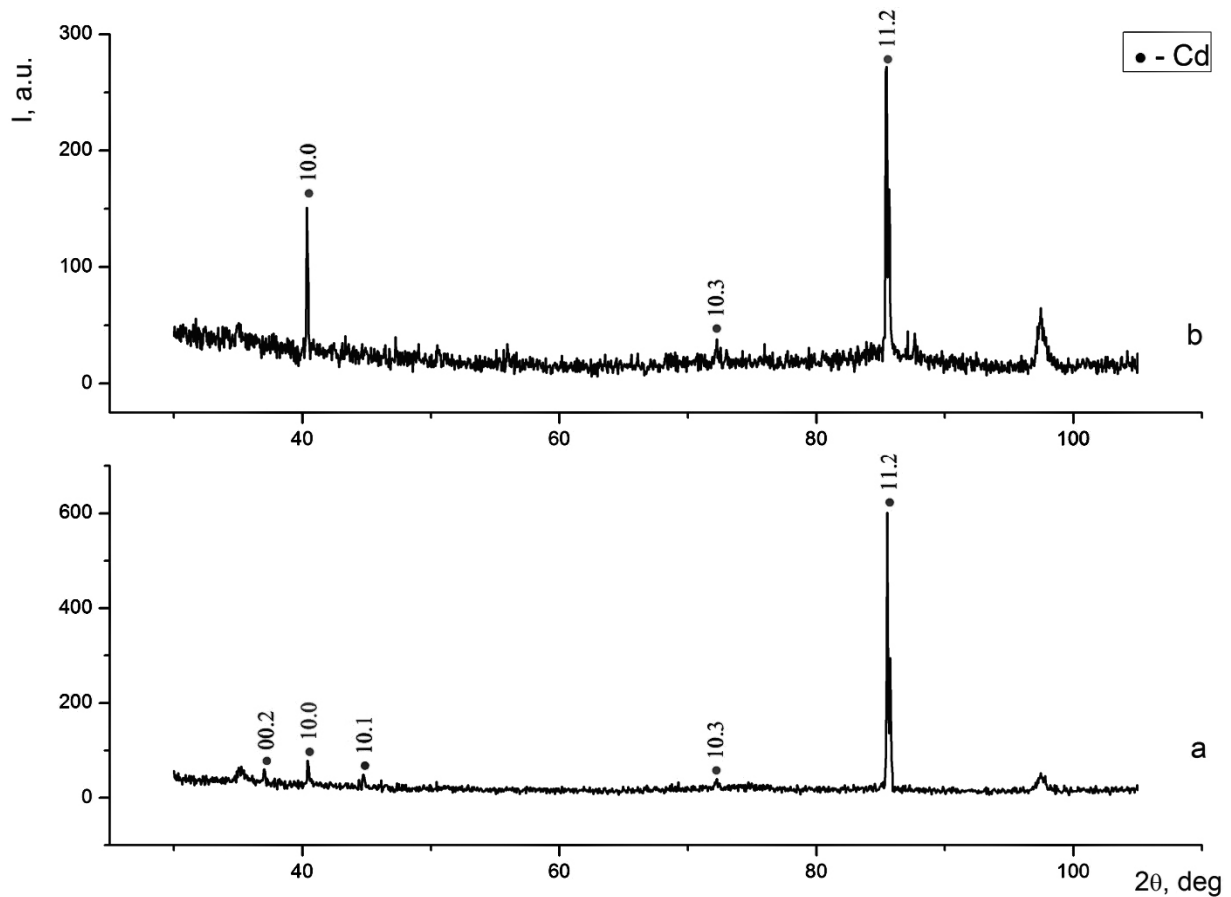
Figure 2. Diffraction patterns of the start a) and end b) sections of single crystal A
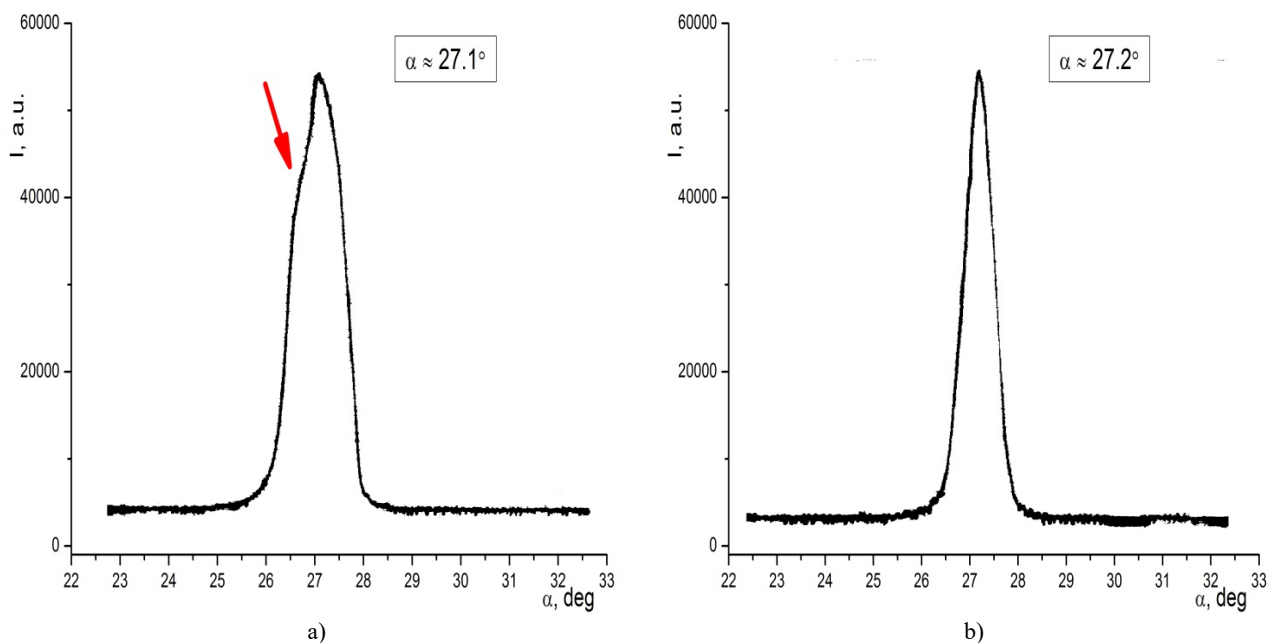
Figure 3. The plot of the diffraction pattern of sample A (determination of orientation)

Figure 2, 3 shows that the main direction of orientation of the lower and upper parts of the single crystal is retained, and hence it is hold over the entire length of the sample.

Similarly X-ray diffraction analysis was performed for single crystal B. The diffraction patterns of the starting a) and end b) part of the single crystal B are shown on Figure 4.

It can be seen that the lines (10.3) have the maximum intensity, i.e., the crystallographic planes (10.3) are oriented parallel to the plane of the crystal butt-end.
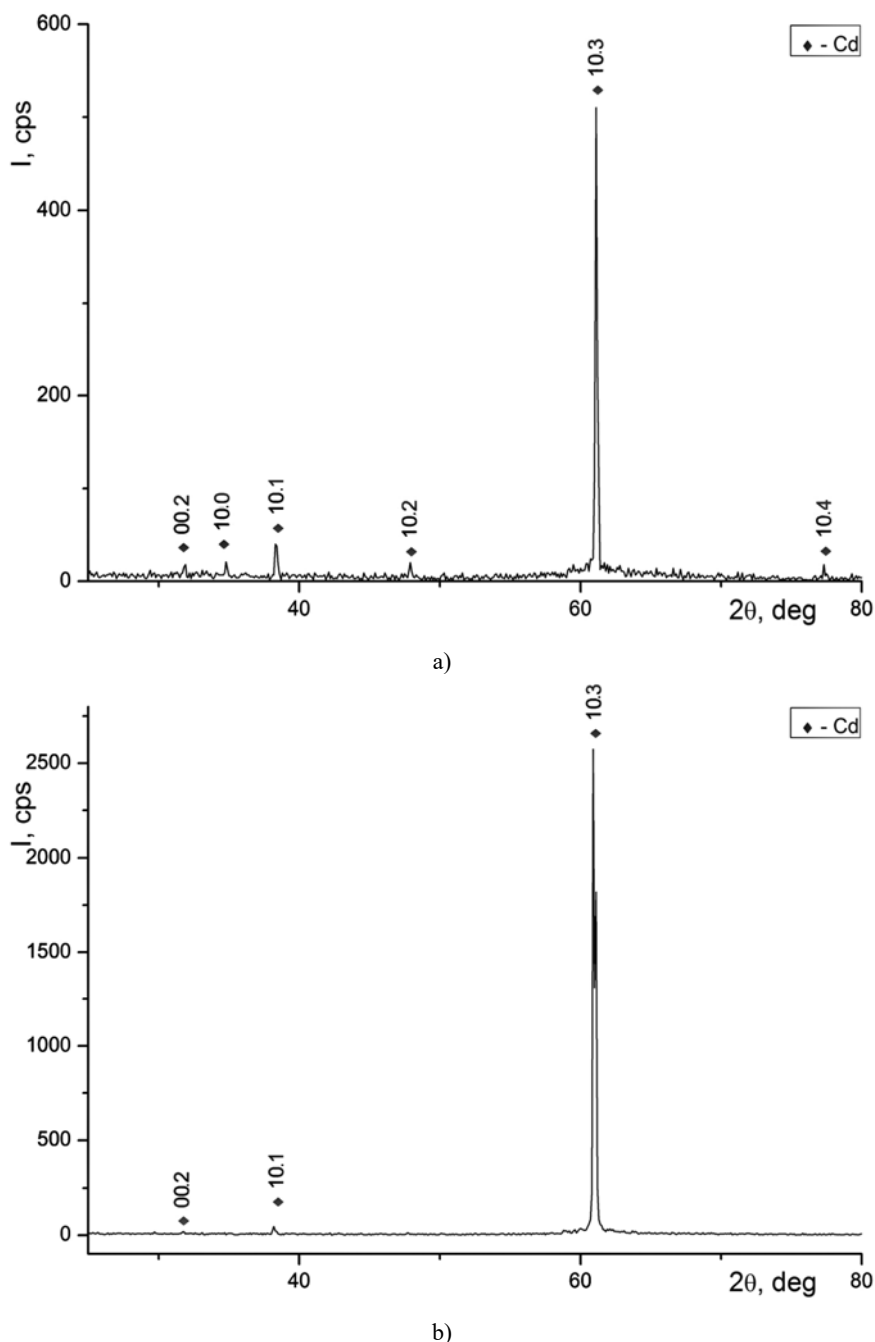
Figure 4. Diffraction patterns of the starting a) and end b) part of the single crystal B

The presence of other low-intensity lines in the diffractogram indicates the presence of grains with a different orientation. The determination of CGO and the analysis of the degree of perfection of single crystal B were performed by the upper part of the single crystal. Diffractometric studies showed that the deviation of the crystallographic direction from the normal to the end part is $\alpha = 0.5°$. The presence of a block with a misorientation angle of $0.8°$ relative to the main maximum was revealed. Thus, the studied crystals A and B are the single crystals with an imperfect structure. The development of grains with a different orientation in the initial stage of growth is a characteristic feature in seedless directed crystallization of low-melting metals [11].

During growth process, due to the preferential orientation of the crystal, the fine grains disappear, which leads to the formation of a more perfect single-crystal structure which occupies the entire cross section of the crystal. In the above variant of VDC of the high purity cadmium, as X-ray diffraction analysis shows, the complete disappearance of small grains does not occur nevertheless. The reason for this may be possibly a low gradient at the crystallization front. Metallography does not reveal the presence of grains in the upper section of the grown crystals (Figure 5).

Table 1 shows the microhardness of the starting and end section of cadmium single crystals A and B. The measurements were performed at the indenter load of 10 g. The Table 1 shows that the microhardness of cadmium crystals in the end section decreases compared with the starting section for both crystals, which does not correlate with

the overall purity of these parts. Reference data on microhardness values are $H_\mu = 29\pm1$ kg/mm^2 [12]. Microhardness measurements were performed on polycrystalline cadmium of the 99.8 % purity at a load of 10 g, as in our case.
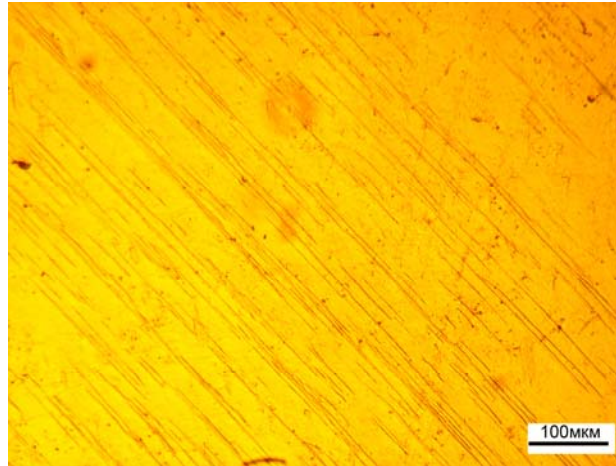
Figure 5. The microstructure of a high-purity cadmium single crystal B

Table 1

The microhardness of cadmium crystals H_μ, kg/mm^2 and their degree of purity, %

Crystal A		Crystal B	
start section	end section	start section	end section
24 ± 1	21 ± 2	21 ± 3	$18,5 \pm 2$
> 99.995	> 99.98	> 99.999	> 99.998

Table 2 shows the impurity composition of the start and end sections of cadmium single crystals A and B produced from a metal of various initial purities.

Table 2

The impurity composition of cadmium single crystals, $\times 10^{-4}$ wt. %

Element	Crystal A		Crystal B	
	start section	end section	start section	end section
Na	0.08	0.1	0.05	0.2
Mg	0.2	0.05	0. 1	0.04
Al	< 0.01	0.05	0.02	0.05
Si	< 0.1	< 0.1	< 0.1	< 0.1
S	0.1	0.5	0.2	0.4
Cl	0.03	0.4	0.08	0.2
K	0.05	0.04	0.1	0.1
Ca	0.4	0.5	0.2	0.4
Fe	< 0.1	< 0.1	< 0.1	< 0.1
Cu	30	80	3	7
Zn	1	3	0.7	2
Ag	7	6	< 0.2	< 0.2
Te	4	4	< 0.3	< 0.3
Pb	5	80	< 0.6	7.5
Cd, %	> 99.995	> 99.98	> 99.999	> 99.998

The content of the remaining 58 impurities from Li to U is below the detection limit of laser mass spectrometry - $< (0.7...0.07)\cdot10^{-4}$ wt. %.

The Table 2 shows that there is a slight redistribution of impurities along the crystals in accordance with the equilibrium distribution coefficients of impurities in cadmium. Most of the analyzed impurity elements in cadmium have equilibrium distribution coefficients $k_0 < 1$ and they displace to the end of the ingot. The exception is Mg and Ag impurities for which $\kappa_0 > 1$: $\kappa_{0Mg} = 1.9$ и $\kappa_{0Ag} = 2.73$ [13]. Therefore, redistribution of impurities to the start and end part of single crystals should occur, depending on the sign of k_0, which is confirmed by the data in Table 2. The cleanest part of the crystals will be the middle those. The degree of distribution of impurity elements along the length of the crystals, with the exception of Pb, is insignificant.

In continuation of this work, it is proposed to develop and manufacture a device for growing more perfect and oriented single crystals of cadmium and other low-melting metals.

CONCLUSIONS

1. The process of production of high-purity Cd single crystals by the VDC method from a melt without using monocrystalline seeds was investigated. As the crystal grows, an increase the perfection of the single-crystal structure is observed.

2. By the X-ray diffraction method the orientations of the studied Cd single crystals were determined, the growth direction of which is [11.2] and [10.3] The angles of deviation of the growth direction relative to the axis of the samples are $\alpha = 27.2°$ and $\alpha = 0.5°$.

3. The microstructure and microhardness of the start and end parts of the grown crystals were determined. The microhardness of the end part is lower compared to the microhardness of the start cleaner part of the crystal.

4. The content of impurities in the start and end parts of the grown cadmium single crystals of various degrees of purity was determined. It was revealed that the redistribution of impurity elements at VDC is insignificant along the length of the grown cadmium single crystals.

ORCID IDs

Alexey P. Shcherban, https://orcid.org/0000-0002-6004-0579; **Gennadiy P. Kovtun**, https://orcid.org/0000-0003-4242-7697; **Dmitriy A. Solopikhin**, https://orcid.org/0000-0003-1426-8713; **Yuri V. Gorbenko**, https://orcid.org/0000-0002-0652-8629; **Igor V. Kolodiy**, https://orcid.org/0000-0001-8598-9732

REFERENCES

[1] R.A. Laudise, and R.L. Parker, *Рост монокристаллов* [*The Growth of Single Crystals*], (Mir, Moscow, 1974), pp. 540. (in Russian)

[2] D.T.J. Hurle, Journal of Crystal Growth, **85**(1-2), 1-8 (1987); https://doi.org/10.1016/0022-0248(87)90197-7.

[3] G. Muller, Crystal Research and Technology, **42** (12), 1150-1161 (2007); https://doi.org/10.1002/crat.200711001.

[4] W.G. Pfann, *Зонная плавка* [*Zone Melting*], (Mir, Moscow, 1970), pp. 366. (in Russian)

[5] G. Carpenter, *Металлический кристалл [Metal Crystal]*, Physics-Uspekhi, **10** (5-6), 689-718 (1930); https://doi.org/10.3367/UFNr.0010.193005d.0689. (in Russian)

[6] O.G. Kozlova, *Рост кристаллов [Crystal Growth]*, Edited by N.V. Belov. (Moscow State University Publishing House, Moscow, 1967), pp. 238. (In Russian)

[7] G.P. Kovtun, D.A. Solopikhin, and A.P. Shcherban, *Глубокое рафинирование легкоплавких металлов дистилляцией в вакууме* [*Deep Refining of Fusible Metals by the Vacuum Distillation*], (Scientific World, Moscow, 2018), pp. 494-513. (In Russian)

[8] A.P. Shcherban, *Получение высокочистых металлов для производства низкофоновых сцинтилляционных детекторов редких событий* [*Obtaining High Purity Metals for Low Background Scintillating Detectors of Rare Events*], Problems of Atomic Science and Technology, Series" Vacuum, Pure Materials, Superconductors", **6**(76), 3-10 (2011). (in Russian)

[9] A.P. Shcherban, G.P. Kovtun, D.A. Solopikhin, Yu.V. Gorbenko, T.Yu. Rudycheva, D.G. Malykhin, I.V. Kolodiy, and V.D. Virych, Problems of Atomic Science and Technology, Series "Vacuum, Pure Materials, Superconductors", **1**(125), 17-20 (2020).

[10] V.K. Komar, and V.M. Pusikov, $A^{II}B^{VI}$*монокристаллы. Рост, свойства, применение* [$A^{II}B^{VI}$ *Single Crystals. Growth, Properties, Application*], (Institute of Single Crystals, Kharkiv, 2002), pp. 244 p. (in Russian)

[11] W.C. Winegard, *An Introduction to the Solidification of Metals,* (London, 1964), pp. 150.

[12] A.A. Ivanko, *Твердость. Справочник [Hardness. Reference Book]*, (Naukova Dumka", Kiev, 1968), pp. 127. (in Russian)

[13] G.P. Kovtun, A.P. Shcherban, and O.A Datsenko, *Классификация поведения примесей в цинке, кадмии и теллуре при кристаллизационной очистке* [*The Classification Behaviour of Impurities in Zinc, Cadmium and Tellurium under Purification by Crystallization*], Problems of Atomic Science and Technology, Series "Vacuum, Pure Materials, Superconductors", **6**, 16-20 (2004). (in Russian)

ОТРИМАННЯ ВИСОКОЧИСТИХ МОНОКРИСТАЛІВ КАДМІЮ МЕТОДОМ ВЕРТИКАЛЬНОЇ СПРЯМОВАНОЇ КРИСТАЛІЗАЦІЇ

О.П. Щербань[а], Г.П. Ковтун[а,b], Д.О. Солопіхін[а], Ю.В. Горбенко[а], І.В. Колодій[а], В.Д. Вірич[а]

[а]Національний науковий центр Харківський фізико-технічний інститут
вул. Академічна, 1, 61108, Харків, Україна
[b]Харківській національний університет ім. В.Н. Каразіна
майдан Свободи, 4, 61022, Харків, Україна

Досліджений процес отримання високочистих спрямованих кристалів Cd вертикальною спрямованою кристалізацією (ВСК) по методу Бриджмена з розплаву. Отримано монокристали з переважним напрямком росту [11.2] і [10.3] . Кути відхилення напрямку росту відносно осі зразків складають $\alpha = 27,2°$ і $\alpha = 0,5°$. Визначено кристалічну досконалість, мікроструктуру і мікротвердість вирощених монокристалів. Як показує рентгеноструктурний аналіз, в даному варіанті ВСК високочистого кадмію, досконала монокристалічна структура не досягається. У початковій частині присутні окремі зерна з різною орієнтацією, кількість яких зменшується в кінцевій частині монокристала. Це призводить до формування більш досконалої монокристалічної структури з переважною орієнтацією, яка займає весь переріз кристала. Визначена мікротвердість верхньої і нижньої частин монокристалів. Більш забруднені кінцеві частини кристалів мають більш низьку мікротвердість, ніж початкові частини. Досліджено домішковий склад початкової і кінцевої частин монокристалів, отриманих з кадмію

різної чистоти. Ефективність перерозподілу домішкових елементів вздовж монокристалів однакова для різних марок кадмію. Розроблений процес ВСК може бути використаний для вирощування монокристалів легкоплавких металів, таких як Zn, Pb, Te, In, Bi, Sn та ін.

КЛЮЧОВІ СЛОВА: кадмій, вертикальна спрямована кристалізація, монокристали, напрямок росту, мікроструктура, мікротвердість, домішковий склад

ПОЛУЧЕНИЕ ВЫСОКОЧИСТЫХ МОНОКРИСТАЛЛОВ КАДМИЯ МЕТОДОМ ВЕРТИКАЛЬНОЙ НАПРАВЛЕННОЙ КРИСТАЛЛИЗАЦИИ
А.П. Щербань[a], Г.П. Ковтун[a, b], Д.А. Солопихин[a], Ю.В. Горбенко[a], И.В. Колодий[a], В.Д. Вирич[a]
[a]Национальный научный центр Харьковский физико-технический институт
ул. Академическая, 1, 61108, Харьков, Украина
[b]Харьковский национальный университет им. В.Н. Каразина
пл. Свободы, 4, Харьков, Украина

Исследован процесс получения высокочистых монокристаллов Cd вертикальной направленной кристаллизацией (ВНК) по методу Бриджмена из расплава. Получены монокристаллы с преимущественным направлением роста [11.2] и [10.3]. Углы отклонения направления роста относительно оси образцов составляют $\alpha = 27,2°$ и $\alpha = 0,5°$. Определены кристаллическое совершенство, микроструктура и микротвердость выращенных монокристаллов. Как показывает рентгеноструктурный анализ, в данном варианте ВНК высокочистого кадмия, совершенная монокристаллическая структура не достигается. В начальной части присутствуют отдельные зерна с различной ориентацией, количество которых уменьшается в конечной части монокристалла. Это приводит к формированию более совершенной монокристаллической структуры с преимущественной ориентацией, которая занимает все сечение кристалла. Определена микротвердость верхней и нижней частей монокристаллов. Более загрязненные конечные части кристаллов имеют более низкую микротвердость, чем начальные части. Исследован примесный состав начальной и конечной частей монокристаллов, полученных из кадмия различной чистоты. Эффективность перераспределения примесных элементов вдоль кристаллов одинакова для различных марок кадмия. Разработанный процесс ВНК может быть использован для выращивания монокристаллов легкоплавких металлов, таких как Zn, Pb, Te, In, Bi, Sn и др.

КЛЮЧЕВЫЕ СЛОВА: кадмий, вертикальная направленная кристаллизация, монокристаллы, направление роста, микроструктура, микротвердость, примесный состав

SYSTEM FOR MEASURING EMITTANCE CHARACTERISTICS OF ION SOURCES

Vitalii I. Voznyi*, Mykola O. Sayko, Aleksandr G. Ponomarev, Serhii O. Sadovyi, Oleg V. Alexenko, Ruslan O. Shulipa

Institute of Applied Physics NAS of Ukraine
58, Petropavlivska Str., 40000 Sumy, Ukraine
*Corresponding Author: vozny56@gmail.com

The article presents the results of the development of a system for measuring emittance characteristics of ion sources studied at the IAP NAS of Ukraine with the aim of obtaining the ion beams with a high brightness. The emittance measurement system is based on the scheme of an electrostatic scanner and consists of two main parts: the scanner, which moves in the direction perpendicular to the beam axis using a stepper motor, and the electronic system of control, processing and data acquisition. The electronic system contains a Raspberry pi 3B microcomputer, precision DAC/ADCs, the high-voltage amplifier of a scanning voltage up to ±500 V on deflection plates of the scanner and a wide range current integrator. The determination of the emittance consists in measuring the ion beam intensity distribution when the scanner moves along the x-coordinate and the electrostatic scanning along the x' angle. The obtained two-dimensional data array allows determining the main characteristics of ion beam: geometric 90% emittance, the root mean square (rms) emittance, the Twiss parameters and phase ellipse of rms emittance, the beam current profile and the angle current density distribution. To test the performance and functionality of the system, the emittance characteristics of the penning type ion source were measured. The working gas was helium, and the beam energy varied within 7–15 keV. At 13 keV of beam energy the following emittances of the He$^+$ ions beam was obtained: 90% emittance is 30 π·mm·mrad, rms emittance is 8.4 mm·mrad, and the normalized rms emittance is equal to 0.022 mm·mrad. The developed system for measuring the emittance of the ion beams is characterized by a short measurement time of 10-15 minutes.

KEYWORDS: ion beam, electrostatic scanner, Gaussian distribution function, RMS emittance, normalized emittance, Twiss parameters, Penning ion source.

One of the main tools for conducting elemental analysis of various materials is accelerator machines that use focused ion beams (FIB). Accelerator FIB-machines are widely used in semiconductor industry, materials science and lithography. For many years the IAP NAS of Ukraine has successfully operated a FIB ion microprobe installation which is part of the Analytical Accelerator Complex based on an electrostatic accelerator with a maximum voltage at a high-voltage terminal of 2 MV [1]. The spatial resolution of the microprobe is about 2 μm. To increase the spatial resolution and make a transition to the submicron field of investigation, it is necessary to use ion beams with high brightness and, therefore, with the possibly small transverse emittance at a fixed beam current.

In the aim of obtaining high brightness ion beams the research of various ion sources is being conducted at the IAP NAS of Ukraine. A number of high frequency ion sources have been studied: an inductive, a helicon and a multicusp ion source [2], as well as a gas field ion source [3]. One of the important parameters of the ion source is the emittance of an ion beam because it describes the ability of a beam to focus, transport and accelerate. The concept of the phase space of the ion beam and its emittance is widely used in accelerator physics to describe the dynamics of the ion beam.

To measure the emittance of ion sources being studied at the IAP NAS of Ukraine, a new system for measuring the emittance characteristics of ion sources has been designed and manufactured. The system operation is based on the principle of electrostatic sweep scanner [4]. In comparison with other methods of the emittance measurement [5, 6] such a scheme allows to develop a more compact measuring system, to perform measurements in a shorter time, and as well to provide better conditions for automation of the process of measuring the beam emittance characteristics. To test the performance of the system and check the functionality of its units, emittance measurements of a penning ion source were carried out.

This paper presents description of the developed emittance measurement system, provides the procedure for calculating the ion beam emittance, and presents the results of emittance measurement of the penning ion source.

ION BEAM EMITTANCE DEFINITION

The parameters of the ion beam can be well described in terms of the phase space [7-9]. To describe the beam geometry, an orthogonal system of x, y, z coordinates is used in which transverse axes x and y are perpendicular to the beam propagation direction (longitudinal axis z). Each particle in a beam has six degrees of freedom: three spatial coordinates of the particle's position (x, y, z) and three momentum coordinates (p_x, p_y, p_z). With a large number of particles N, the state of the beam at a certain point in time can be represented by many points with phase density $f(x, y, z, p_x, p_y, p_z, t)$, which is often approximated by Gauss function. The N particles of a beam in 6-dimensional phase space occupy a certain phase volume which, according to Liouville's theorem, remains constant when the beam

particles move under the action of conservative forces. If longitudinal motion of the particles is not coupled to transverse motion, the 6-dimensional phase volume can be separated into 2-dimensional longitudinal volume and 4-dimensional transverse phase volume. In the case when the longitudinal momentum p_z is constant and much larger than the transverse momentum, the ratio p_x/p_z (or p_y/p_z) is equal to the angular divergence $x'=dx/dz$ (or $y'=dy/dz$). And since p_z is a constant value, p_x, p_y can be replaced by x' and x' respectively, i.e. by the quantities that can be directly observed. If there is no coupling between transverse movements in xz and yz planes, the beam can be described by the distribution of points in two independent planes of the trace space (x, x') and (y, y'). In this case the 4-dimensional phase volume can be separated into its components which form two 2-dimensional phase volumes Ω_x and Ω_y in trace space (x, x') and (y, y'), respectively.

The emittance in the x-direction is the projection area $A_{x,90}$ of the phase volume $\Omega_{x,90}$, containing 90% of all representative beam particles, divided by π:

$$\varepsilon_{x,90} = \frac{A_{x,90}}{\pi} = \frac{1}{\pi} \iint\limits_{\Omega_{x,90}} dx dx'. \tag{1}$$

An analogous definition holds for the emittance in the y-direction. For axisymmetric beams: $\varepsilon_x = \varepsilon_y = \varepsilon$ [10].

The emittance is a constant of the beam motion if the longitudinal velocity of the beam does not change along the optical axis. As the beam accelerates its emittance decreases because the transverse momentum of the particles remains unchanged while the longitudinal momentum increases, resulting in a reduction of x'. The quantity which remains constant at beam acceleration is the normalized emittance formed by multiplying the emittance by dimensionless relativistic relations β and γ, where $\beta = v/c$, $\gamma = (1-\beta^2)^{-1/2}$. Here v is a particle velocity and c is a light velocity. In the case of non-relativistic beams we get the expression for calculating of the normalized emittance:

$$\varepsilon_N = \beta\gamma\varepsilon = \varepsilon \cdot 4{,}6 \cdot 10^{-5} \sqrt{E/A}, \tag{2}$$

where E is the kinetic energy of the beam, eV, A- mass number of an ion.

Along with the geometric interpretation of the emittance as the contour area containing 90% of all beam particles, there is a statistical approach in which the beam is considered as a statistical array of points in 2-dimensional trace space with the distribution function $f(x, x')$ [9, 11, 12]. The particles inside the trace space (x, x') can be considered as a statistical distribution with average values $\langle x \rangle$ and $\langle x' \rangle$. In this case the root mean square (rms) emittance ε_{rms} is determined as standard deviations from these average values. The equation of the phase ellipse of rms emittance has the form: $\gamma x^2 + 2\alpha x x' + \beta x'^2 = \varepsilon_{rms}$, where α, β and γ are the Twiss parameters (the Twiss parameters β and γ are not to be confused with the relativistic relations). At that projections of the equivalent ellipse on the x and x' axis are equal to the standard deviations σ_x and $\sigma_{x'}$: $\sigma_x = \sqrt{\beta\varepsilon_{rms}}$, $\sigma_{x'} = \sqrt{\gamma\varepsilon_{rms}}$, $\sigma_{xx'} = -\alpha\varepsilon_{rms}$, where $\sigma_x^2 = \langle x^2 \rangle$, $\sigma_{x'}^2 = \langle x'^2 \rangle$ and $\sigma_{xx'} = \langle xx' \rangle$ are the second-order moments of the phase distribution function. The Twiss parameters are connected by the relation: $\gamma\beta - \alpha^2 = 1$. By substituting the Twiss parameters into this equation, we obtain the expression for determining the rms emittance:

$$\varepsilon_{rms} = \sqrt{\langle x^2 \rangle \langle x'^2 \rangle - \langle xx' \rangle^2} = \sqrt{\sigma_x^2 \sigma_{x'}^2 - \sigma_{xx'}^2}. \tag{3}$$

EMITTANCE MEASUREMENT SYSTEM

The work of the emittance measurement system is based on the principle of operation of an electrostatic scanner [4], which is a variation of emittance measurement by two slits method [5]. The system of emittance measurement consists of two main parts: the scanner, which moves in the direction perpendicular to the axis of the beam, and the electronic system of control, processing and data acquisition. The movement of only one entrance slit determines the compactness of the measuring system and the speed of measurements.

The scanner (Fig. 1a) contains the entrance (1) and exit (3) slits extended along the horizontal y-axis, two deflecting plates (2), which are supplied with a saw-tooth electric voltage V, a Faraday cup (8) for measuring the ion current passed through both the slits. In front of the Faraday cup there is a ring suppressor (4) to inhibit secondary electrons. The scanner is surrounded by a grounded electrostatic shield and moves in the vertical x-direction using a stepper motor.

Fig. 1b shows a photo of the scanner without an electrostatic shield. The entrance slit (1) and deflecting plates (2) are shown in the figure. The total length of the scanner is 145 mm. The Faraday cup is 10 mm in inner diameter and 12 mm in length.

a   b
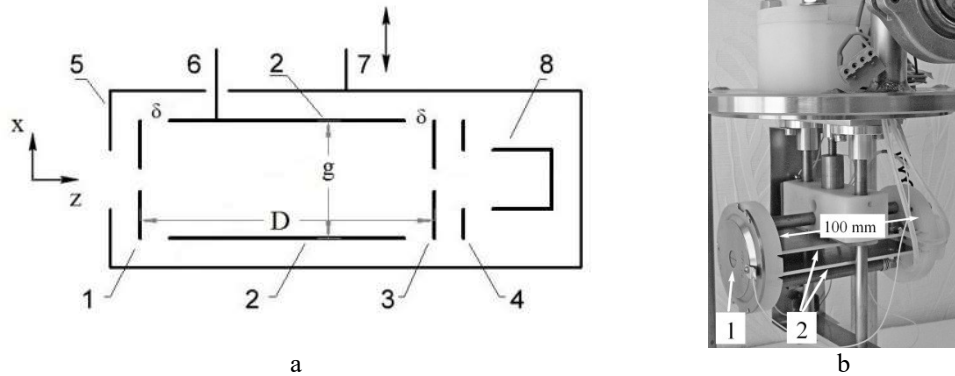
Figure 1. a – schematic of the electrostatic scanner: 1 – entrance slit, 2 – deflecting plates, 3 – exit slit, 4 – suppressor, 5 –electrostatic shield, 6 – saw-tooth voltage, 7 – stepper motor, 8 – Faraday cup; b – picture of the scanner (without electrostatic shield), the entrance slit (1) and the deflecting plates (2) are shown.

The determination of the emittance is concluded in measuring the distribution of ion current intensity $Z(x, x')$ over the x-coordinate and x' angle. At each x-coordinate the ion current passing through both slits is measured with simultaneous linear change in voltage V between the deflecting plates. Thus the distribution of the current intensity over the angle x' is determined. Repeating the measurements with a different value of x-coordinate, we obtain the complete distribution of the current intensity $Z(x, x')$.

The relationship between the angle x' and the deflecting voltage V is determined by the condition under which an ion with charge q and energy qU passing through the entrance slit at the x' angle is deflected and enters the exit slit. In this case angle x' is determined by the ratio [2]:

$$x' = V(D - 2\delta)/4Ug, \tag{4}$$

where V is the potential difference between the deflecting plates, U is the potential difference that the beam passed during acceleration, D is the distance between the slits, δ is the distance between the deflecting plates and the slits, g is the distance between the deflecting plates. In this design D=120 mm, δ=10 mm, g=10 mm, the width of the entrance and exit slits is s=200 µm. The length of the slits in y-direction is 12 mm.

The electrostatic scanner which contains both the slits and deflecting plates moves in a vertical plane along the precision guide axes with the help of a stepper motor and ball screw pair passing through the vacuum seal.

In Fig. 2 is shown the control and data acquisition system. The system consists of a microcomputer Raspberry pi 3B (1) by Raspberry Pi Foundation, precision DAC/ADCs, expansion board for Raspberry pi by Waveshare (2), stepper motor driver (3), wide range current integrator (5), high voltage amplifier for generating sweep voltage on deflecting plates (6), stepper motor (8), scanner position switches (9), computer with installed user interface software.
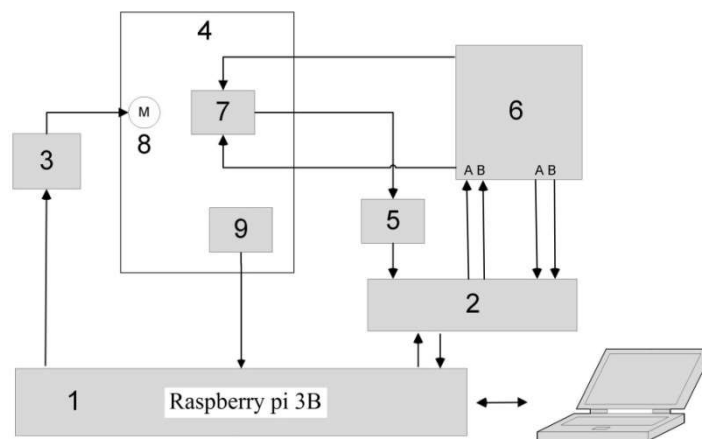
Figure 2. Block diagram of the control and data acquisition system. 1 – microcomputer Raspberry pi 3B, 2 – precision DAC/ADCs, 3 – opto-coupled stepper motor driver, 4 – vacuum chamber, 5 – current integrator, 6 – high voltage amplifier, 7 - electrostatic scanner, 8 – stepper motor, 9 – scanner position switches.

The microcomputer Raspberry pi 3B has free software installed: Linux based Jessie operating system; Hostapd; wi-fi access point DNSMASQ; server DHCP+DNS; Samba; free implementation of the network protocol SMB/CIFS; Empi program of own development in the high-level language C^{++}.

To form a sweep sawtooth voltage on the deflecting plates a specially developed two-channel high-voltage amplifier (6) is used. Parameters of the voltage amplifier: the gain is 100, the frequency is 0-1 kHz. Each of the amplifier channels converts the input signal in the range of 0-2.5 V, which is supplied from the DAC, into the output voltage from zero to ± 250 V. At that voltage on the plates at each moment of time is supported symmetrically opposite to zero. Thus, the potential difference between the plates is adjustable in the range of ±500 V.

The electrostatic scanner moves along the guides using a stepper motor (8). For positioning the scanner, two limit switches of upper and lower positions and a precision zero-position photosensor (9) are used.

The resolution of the scanner along x-coordinate is determined by a minimum movement step, which is 4.8 μm. Typically the movement step is set to 48 or 96 μm. The range of movement is 0–20 mm.

The angular resolution of the scanner is 1.7 mrad. The ratio between the angle x' and the scanning voltage V is determined from equation (4) and has the form: $x' = 2.5V/U$. At the maximum value of deflecting voltage $V=\pm500$ V and the beam energy $U=10$ kV we obtain the maximum value of the angle $x'=\pm125$ mrad.

EMITTANCE MEASUREMENT PROCEDURE

The measured two-dimensional array of ion beam intensity values $Z(x, x')$ is the distribution of the ion beam current density in the x-x' phase plane. The number of cells of the matrix $Z(x, x')$ can vary, and is usually equal to 153×201 with cell size $\Delta x=0.098$ mm in x-coordinate and $\Delta x'=0.385$ mrad in x' angle. The unit of measurement of the array elements $Z(x, x')$ is nA/(mm·mrad).

The measured array of intensity $Z(x, x')$ enables to determine the main characteristics of the ion beam: the geometric emittance ε_{90}, the rms emittance ε_{rms}, the Twiss parameters and the phase ellipse of rms emittance, the distribution of current density over the x-coordinate (a beam current profile) and the current density distribution over the angle. The total beam current I is proportional to the sum of array values $Z(x, x')$ over all the coordinates x and angles x': $I \propto \sum_{x}\sum_{x'} Z(x, x')$.

Geometric emittance ε_{90}. The projection of a distribution $Z(x, x')$ on the plane x- x' at a certain threshold value Z_{th} gives emittance diagram, the area of which divided by π is the emittance of a beam. The threshold value Z_{th} is determined as follows: a certain value of Z_{th} is set and the elements of matrix $Z(x, x')$ whose values are less than Z_{th} are zeroed. As a result matrix $M(x, x')$ is obtained. In the process the condition is checked to ensure that: $\sum_{x}\sum_{x'} M(x, x') = 0,9 \cdot \sum_{x}\sum_{x'} Z(x, x')$. In the result the projection of the matrix $M(x, x')$ onto the x-x' plane forms a contour containing 90% of all beam particles. The area of this contour divided by π is the emittance ε_{90}. The unit of measurement of the emittance is m·rad or usually mm·mrad. The symbol π is included in the emittance unit of measurement to indicate that the emittance was defined as the area divided by π.

RMS emittance ε_{rms}. The rms emittance is determined from the expression (3). The first order moments $\langle x \rangle$, $\langle x' \rangle$ and the second order moments σ_x^2, $\sigma_{x'}^2$ and $\sigma_{xx'}$ are calculated from the relations:

$$\langle x \rangle = \frac{\sum_{x}\sum_{x'} x \cdot Z(x,x')}{\sum_{x}\sum_{x'} Z(x,x')}, \quad \langle x' \rangle = \frac{\sum_{x}\sum_{x'} x' \cdot Z(x,x')}{\sum_{x}\sum_{x'} Z(x,x')}, \quad \sigma_x^2 = \langle x^2 \rangle = \frac{\sum_{x}\sum_{x'} (x - \langle x \rangle)^2 Z(x,x')}{\sum_{x}\sum_{x'} Z(x,x')},$$

$$\sigma_{x'}^2 = \langle x'^2 \rangle = \frac{\sum_{x}\sum_{x'} (x' - \langle x' \rangle)^2 Z(x,x')}{\sum_{x}\sum_{x'} Z(x,x')}, \qquad \sigma_{xx'} = \langle xx' \rangle = \frac{\sum_{x}\sum_{x'} (x - \langle x \rangle)(x' - \langle x' \rangle) Z(x,x')}{\sum_{x}\sum_{x'} Z(x,x')}. \qquad (5)$$

The Twiss parameters and phase ellipse. The Twiss parameters are determined from the expressions:

$$\beta = \frac{\sigma_x^2}{\varepsilon_{rms}}, \quad \gamma = \frac{\sigma_{x'}^2}{\varepsilon_{rms}}, \quad \alpha = -\frac{\sigma_{xx'}}{\varepsilon_{rms}}. \qquad (6)$$

They define the phase ellipse equation, which taking into account the average values $\langle x \rangle$ and $\langle x' \rangle$ has the form:

$$\gamma(x - \langle x \rangle)^2 + 2\alpha(x - \langle x \rangle)(x' - \langle x' \rangle) + \beta(x' - \langle x' \rangle)^2 = \varepsilon_{rms}. \qquad (7)$$

Beam current profile. The distribution of current density over x-coordinate is obtained by summing the elements

of the array $Z(x, x')$ over all the values of the x' angle for each x coordinate:

$$Z(x) = \sum_{x'} Z(x, x'), \text{ nA/mm.} \tag{8}$$

The distribution of current density over the angle. A similar way can be done in determining the current density distribution of the ion beam over the angle. Summing up the elements of the array $Z(x, x')$ over all the values of the x-coordinate for each value of x' angle we obtain:

$$Z(x') = \sum_{x} Z(x, x'), \text{ nA/mrad.} \tag{9}$$

RESULTS OF MEASUREMENTS

To test the performance and functionality of the emittance measurement system, the emittance characteristics of the penning ion source were measured. The ion source is a penning type ion source with a cold cathode [13]. It is an economical ion source and it does not create electromagnetic interference disturbing the operation of electronic equipment. The power consumption of the source is about 5 W, the full ion current is 5-20 µA. The source consists of a cylindrical anode, a cathode with an aperture for beam extraction and an anticathode. The inner diameter of the anode is 25 mm, the distance between a cathode and anticathode is 43 mm and the diameter of the extraction aperture is 0.8 mm. A magnetic system consisting of 4 ring ferrite magnets is located coaxial to the anode. The longitudinal component of magnetic induction on the discharge axis is equal to 0.085-0.09 T, the voltage between an anode and cathode is 5 kV, the discharge current is I_d=0.22 mA.

The emittance of the penning ion source was measured at a stand for studying the ion sources parameters. The scheme of the experimental setup is shown in Fig. 3.
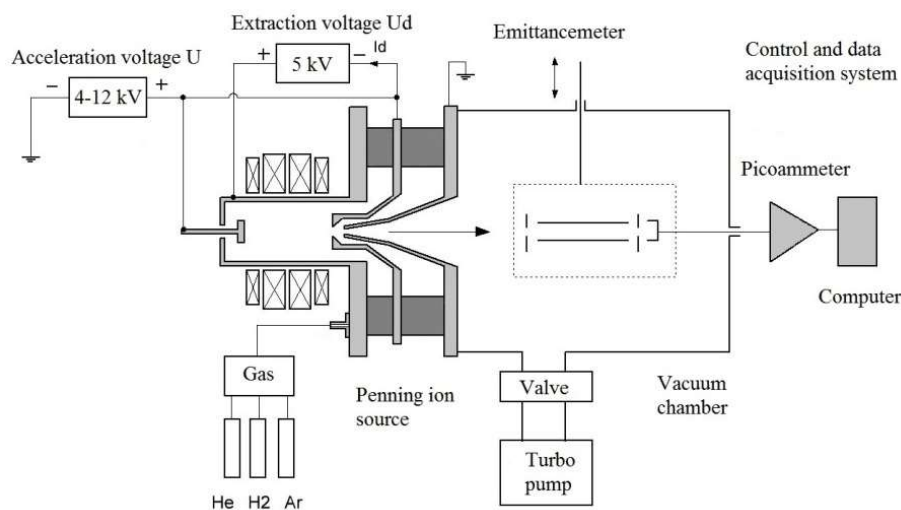
Figure 3. Experimental setup for emittance measurement of a penning ion source.

The ion beam energy varied within E=7–15 keV, the working gas was helium. While measuring the emittancemeter was located at a distance of 40 mm from the base of the accelerating electrode of the source.

In Fig. 4a is shown a 3-dimensional surface of the current intensity distribution $Z(x, x')$ at the energy E=13 keV. By its form the current intensity distribution $Z(x, x')$ is close to Gaussian distribution function. In Fig. 4b the 2-dimensional emittance diagram is presented which is a projection of the $Z(x, x')$ array on x-x' plane. The emittance diagram depicts the contour of the geometric emittance which contains 90% of all the beam particles. At the beam energy of E=13 keV the geometrical emittance equals ε_{90}=30 π·mm·mrad.

The rms emittance is determined from equation (3). With increasing beam energy in the range E=9–15 keV rms emittance decreases from 10 mm·mrad to 8.3 mm·mrad. At the energy of E=13 keV rms emittance is equal to ε_{rms}=8.4 mm·mrad.

Normalized rms emittance is determined from equation (2) and equals $\varepsilon_{N, rms}$ =0.022 mm·mrad. This value of emittance is conserved when the beam energy changes.

The moments of the first and second orders as well as the Twiss parameters for ion beam with energy E=13 keV have the following values: $\langle x \rangle$=8.4 mm, $\langle x' \rangle$=14.5 mrad, σ_x=1.9 mm, $\sigma_{x'}$=15.4 mrad, $\sigma_{xx'}$=28.2 mm·mrad, γ=28.4 mrad/mm, α = -3.35, β =0.43 mm/mrad. These parameters define equation (7) of the phase ellipse of rms

emittance which has the form: $28.4(x-8.4)^2 - 6.7(x-8.4)(x'-14.5) + 0.43(x'-14.5)^2 = 8.4$. The graph of the phase ellipse is shown in Fig. 5a.
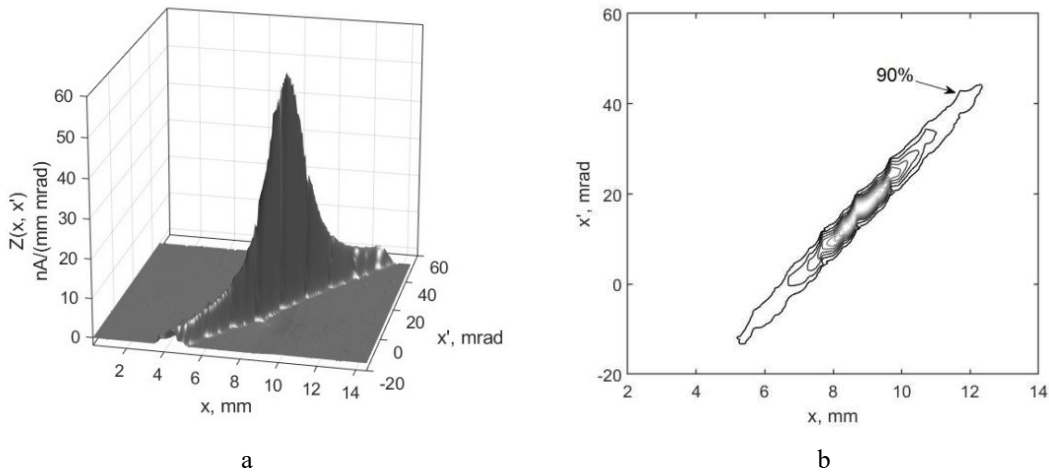
Figure 4. a – 3D surface of the current intensity distribution $Z(x, x')$ of He$^+$ ion beam with energy E=13 keV, b – diagram of the geometric 90% emittance of helium ion beam in the x-x' plane.

The inclination angle θ of the phase ellipse to axis x is given by the expression [7]: $tg\,2\theta = \dfrac{2\sigma_{xx'}}{\sigma_x^2 - \sigma_{x'}^2}$. Considering the scale of Fig. 5a this ratio looks like: $tg\,2\theta = 2\sigma_{xx'}/mn\left(\sigma_x^2/m - \sigma_{x'}^2/n\right)$, where m=12 mm, n=80 mrad. If θ <0 then angle 90° must be added to its value. As a result the inclination angle is equal to θ=51°.

The position and shape of the ellipse of rms emittance ε_{rms} in Fig. 5a coincides well with the graph of the geometric emittance ε_{90} (Fig. 4b). This indicates that calculations of the emittance by geometric and statistical methods are in good agreement.

In Fig. 5b shows the ion beam current profile calculated from expression (8).
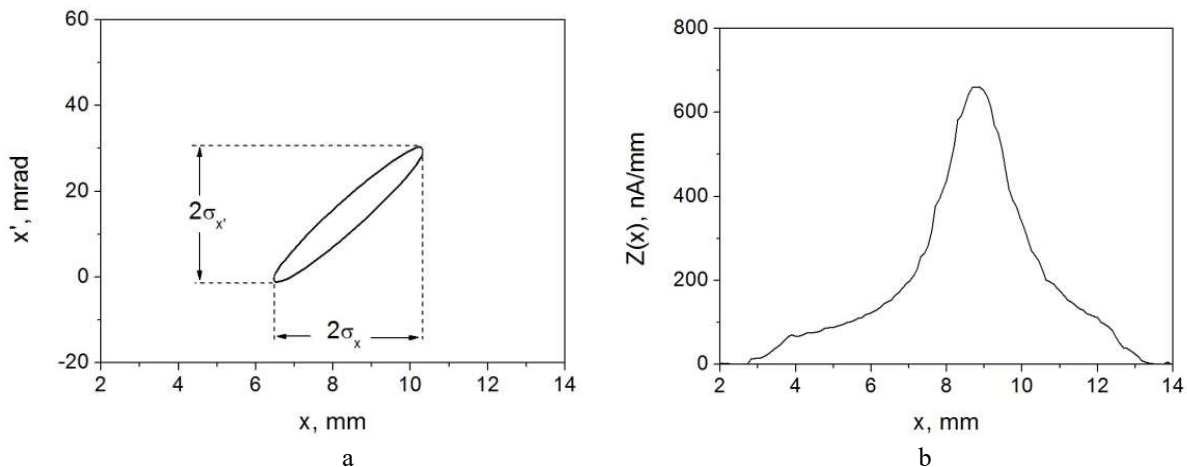
Figure 5. a – phase ellipse of rms emittance, b – ion beam current profile.

Since the Twiss parameter α< 0, the beam is diverging. The divergence angle is equal to $2\sigma_{x'}$ =30.8 mrad, and the beam envelope width (beam diameter) is $2\sigma_x$ =3.8 mm.

CONCLUSION

The study of ion sources is being conducted at the IAP NAS of Ukraine in order to obtain the high brightness ion beams. High brightness beams of charged particles are necessary for use in various FIB-accelerator machines, in nanotechnology, and ion nanolithography. To measure the emittance of ion beams, a system for measuring emittance characteristics of ion sources has been designed and manufactured.

The measuring system consists of the electrostatic scanner moving in the direction perpendicular to the beam axis, and the electronic system of control and data acquisition, which contains a Raspberry microcomputer, precision DAC/ADCs, a high-voltage amplifier for a scanning saw-tooth voltage up to ±500 V, and a wide-band current integrator.

The performance of measurement system was checked when measuring the emittance of a penning ion source. The working gas was helium, the energy of the ion beam varied within 7–15 keV. The beam emittance was determined both geometrically, measuring the emittance ε_{90} of the phase contour containing 90% of beam particles, and statistically, determining the rms emittance ε_{rms}. At the beam energy E=13 keV the following values of the emittance are obtained: ε_{90}=30 π·mm·mrad, ε_{rms}=8.4 mm·mrad, the normalized rms emittance is equal to $\varepsilon_{N,rms}$=0.022 mm·mrad. The Twiss parameters that describe the phase ellipse of rms emittance are determined, and the ion beam profile, the divergence angle and the beam envelope width are measured. The first moments $\langle x \rangle$ and $\langle x' \rangle$ determine the position and direction of the ion beam propagation. These data can be used to correct the position of the beam during its transportation.

The obtained emittance of 30 π·mm·mrad (or 3.4 π·mm·mrad·(MeV)$^{1/2}$ in terms of the ion beam energy) has a value typical for penning's ion sources with cold cathode. In particular the penning ion source with cold cathode from High Voltage Engineering Europa B.V. (HSEE) has the emittance of 3 π·mm·mrad·(MeV)$^{1/2}$ [14].

This emittance measurement system is characterized by relatively small dimensions and short measurement time of 10-15 min., which are due to the movement of only one entrance slit and the control of one stepper motor. It distinguishes the developed system favorably from emittancemeters that use the movement of two slits.

The system for measuring emittance characteristics is designed for the stand researches of ion sources with the beam energy of tens keV. At the same time, the measuring system can be used in the studies on optimization of beam transport systems at the output of the small- sized electrostatic accelerators used for elemental analysis of materials with ion beams.

ORCID IDs
Vitalii I. Voznyi, https://orcid.org/0000-0002-9979-639X; **Mykola O. Sayko**, https://orcid.org/0000-0002-3393-4753;
Aleksandr G. Ponomarev, https://orcid.org/0000-0002-4517-5635; **Serhii O. Sadovyi**, https://orcid.org/0000-0002-9427-1033;
Oleg V. Alexenko, https://orcid.org/0000-0002-4310-0920; **Ruslan O. Shulipa**, https://orcid.org/0000-0002-9571-3059.

REFERENCES
[1] D.V. Magilin, A.G. Ponomarev, V.A. Rebrov, N.A. Sayko, K.I. Melnik, V.I. Miroshnichenko, and V.Y. Storizhko, Nucl. Instr. and Meth. B. **267**, 2046-2049 (2009). https://doi.org/10.1016/j.nimb.2009.03.015.
[2] V. Voznyi, V. Miroshnichenko, S. Mordyk, D. Shulha, V. Storizhko, and V. Tokman, J. Nano Electron. Phys. **5**(4), 04060 (2013), https://jnep.sumdu.edu.ua/download/numbers/2013/4/articles/en/jnep_2013_V5_04060.pdf.
[3] V.I. Vozny, V.Yu. Storizhko, V.I. Miroshnichenko, V.V. Tokman, Ye.A. Mironets, and Ye.O. Batura. Nauka innov. **6**(5), 72-76 (2010). https://doi.org/10.15407/scin6.05.072, (in Russian)
[4] P.W. Allison, J.D. Sherman, and D.B. Holtkamp, IEEE Trans. Nucl. Sci. **30**(4), 2204-2206 (1983), https://doi.org/10.1109/TNS.1983.4332762.
[5] C. Lejeune, and J. Aubert, in: *Applied Charged Particle Optics*, Part A, edited by A.Septier, (Academic Press, New York, 1980), pp.159-259.
[6] V.V. Kuz'menko, V.G. Bogdalin, and V.M. Pistrjak. Problems of Atomic Science and Technology. Series: General and Nuclear Physics, **2**(12), 74-77 (1980). (in Russian)
[7] J. Buon, in: *CAS-CERN Accelerator School: 5th General Accelerator Physics Course*, (1992), pp. 89-116. http://dx.doi.org/10.5170/CERN-1994-001.
[8] M. Reiser, *Theory and Design of Charged Particle Beams*, 2nd ed. (Wiley-VCH, Weinheim, 2008), pp. 51-61, pp. 128-134, pp. 320-326. http://dx.doi.org/10.1002/9783527622047.
[9] J.D. Lawson, *The Physics of Charged Particle Beams*, 2nd ed. (Clarendon Press, Oxford, 1988), pp. 200.
[10] H. Zhang, *Ion Sources*, (Science Press, Springer, New York, 1999), pp. 59.
[11] P.M. Lapostolle, IEEE Trans. Nucl. Sci. **18**(3), 1101 (1971), https://doi.org/10.1109/TNS.1971.4326292.
[12] M. Ferrario, in: *CERN Accelerator School: Plasma Wake Acceleration,* (CERN, Geneva, 2014), pp. 159-179. http://dx.doi.org/10.5170/CERN-2016-001.159.
[13] V.I. Voznyi, D.P. Shulha, O.O. Drozdenko, M.I. Zakharets, E.A. Mironets, and O.S. Brichenko, Nuclear Physics and Atomic Energy, **18**(2), 194-200 (2017). https://doi.org/10.15407/jnpae2017.02.194, (in Russian)
[14] Cold Cathode Penning Ion Source, Model SO-60, http://www.highvolteng.com/media/Leaflets/model_so-60__cold_cathode_penning_ion_source.pdf

СИСТЕМА ВИМІРЮВАННЯ ЕМІТТАНСНИХ ХАРАКТЕРИСТИК ІОННИХ ДЖЕРЕЛ
В.І. Возний, М.О. Сайко, О.Г. Пономарьов, С.О. Садовий, О.В. Алексенко, Р.О. Шуліпа
Інститут прикладної фізики НАН України
58, вул. Петропавлівська, 40000 Суми, Україна
У статті представлені результати розробки системи вимірювання еміттансних характеристик іонних джерел, досліджуваних в ІПФ НАН України з метою отримання іонних пучків з високою яскравістю. Система вимірювання еміттанса виконана за схемою електростатичного сканера і складається з двох основних частин: сканера, який переміщається в напрямку, перпендикулярному осі пучка за допомогою крокового двигуна, і електронної системи управління, збору і обробки даних. Система управління та обробки даних містить мікрокомп'ютер Raspberry pi 3B, прецизійні ЦАП/АЦП, високовольтний

підсилювач для генерування напруги ±500 В на відхиляючих пластинах сканера, широкодіапазонний інтегратор струму. Визначення еміттанса полягає у вимірюванні розподілу інтенсивності іонного пучка при переміщенні сканера по координаті x і електростатичному скануванні по куту x'. Отриманий двовимірний масив даних дозволяє визначити основні еміттансні характеристики іонного пучка: геометричний 90% еміттанс, середньоквадратичний еміттанс, параметри Твісса і рівняння фазового еліпса середньоквадратичного еміттанса, профіль струму пучка і розподіл щільності струму по куту. Для перевірки працездатності і функціональності вузлів системи були проведені вимірювання еміттансних характеристик іонного джерела пеннінговского типу. Робочим газом був гелій, енергія пучка змінювалася в межах 7-15 кеВ. При енергії пучка 13 кеВ отримані наступні величини еміттанса пучка іонів He^+: 90% еміттанс дорівнює 30 π·мм·мрад, середньоквадратичний еміттанс дорівнює 8,4 мм·мрад, величина нормалізованого середньоквадратичного еміттанса становить 0,022 мм·мрад. Дана система вимірювання еміттанса іонних пучків характеризується малим часом проведення вимірювання, що становить 10-15 хв.

КЛЮЧОВІ СЛОВА: іонний пучок, електростатичний сканер, функція розподілу Гаусса, середньоквадратичний еміттанс, нормалізований еміттанс, параметри Твісса, пеннінговскє джерело іонів.

СИСТЕМА ИЗМЕРЕНИЯ ЭМИТТАНСНЫХ ХАРАКТЕРИСТИК ИОННЫХ ИСТОЧНИКОВ

В.И. Возный, Н.А. Сайко, А.Г. Пономарев, С.А. Садовой, О.В. Алексенко, Р.А. Шулипа.

Институт прикладной физики НАН Украины
58, ул. Петропавловская, 40000 Сумы, Украина

В статье представлены результаты разработки системы измерения эмиттансных характеристик ионных источников, исследуемых в ИПФ НАН Украины с целью получения ионных пучков с высокой яркостью. Система измерения эмиттанса выполнена по схеме электростатического сканера и состоит из двух основных частей: сканера, который перемещается в направлении, перпендикулярном оси пучка с помощью шагового двигателя, и электронной системы управления, сбора и обработки данных. Система управления и обработки данных содержит микрокомпьютер Raspberry pi 3B, прецизионные ЦАП/АЦП, высоковольтный усилитель сканирующего напряжения до ±500 В на отклоняющих пластинах сканера, широкодиапазонный интегратор тока. Определение эмиттанса состоит в измерении распределения интенсивности ионного пучка при перемещении сканера по координате x и электростатическом сканировании по углу x'. Полученный двумерный массив данных позволяет определить основные эмиттансные характеристики ионного пучка: геометрический 90% эмиттанс, среднеквадратичный эмиттанс, параметры Твисса и уравнение фазового эллипса среднеквадратичного эмиттанса, профиль тока пучка и распределение плотности тока по углу. Для проверки работоспособности и функциональности узлов системы проведены измерения эмиттансных характеристик ионного источника пеннинговского типа. Рабочим газом являлся гелий, энергия пучка изменялась в пределах 7-15 кэВ. При энергии пучка 13 кэВ получены следующие величины эмиттанса пучка ионов He^+: 90% эмиттанс равен 30 π·мм·мрад, среднеквадратичный эмиттанс равен 8,4 мм·мрад, нормализованный среднеквадратичный эмиттанс составляет 0,022 мм·мрад. Данная система измерения эмиттанса ионных пучков характеризуется малым временем проведения измерения, составляющим 10-15 мин.

КЛЮЧЕВЫЕ СЛОВА: ионный пучок, электростатический сканер, функция распределения Гаусса, среднеквадратичный эмиттанс, нормализованный эмиттанс, параметры Твисса, пеннинговский источник ионов.

COUNTING EFFICIENCY AND NEUTRON/GAMMA RATIO FOR KDP: TL+ AND UPS-923A SCINTILLATORS IN A SINGLE PHOTON DETECTION MODE

Gennadiy Onyshchenko[a,b], Ivan Yakymenko[b,*], Borys Grynyov[a],
Volodymyr Ryzhikov[a], Olexiy Voronov[a], Sergei Naydenov[a]

aInstitute for Scintillation Materials, STC "Institute for Single Crystals", National Academy of Sciences of Ukraine
60 Nauky Ave., 61001 Kharkiv, Ukraine
bKarazin Kharkiv National University, 4 Svobody Sq., Kharkov, 61022, Ukraine
*Corresponding Author: ivan.yakymenko@gmail.com
Received June 5, 2020; revised June 21, 2020; accepted June 30, 2020

This research related to registration of the fast neutrons with a detector based on the inorganic KDP: TL+ mono crystal (KH_2PO_4 potassium dihydrogen phosphate) and plastic UPS-923A. The crystal of the KDP: TL+ detector grown from a water solution by the method of lowering the temperature. The high concentration of hydrogen nuclei in the KDP: TL+ crystal grid makes it possible to detect neutron radiation with an efficiency comparable to polystyrene scintillators. KDP: TL+ crystals have a high radiation resistance (up to 10^{10} neutrons/cm^2), which significantly expands the spectrum of their application in high-energy physics applications, intense neutron fields. In this work, we used a technique for recording the detector response in the photon counting mode and pulse filtering mode. Since the detector operates on the principle of detecting gamma quanta from the reactions (n, n 'γ), (n, n' γ)$_{res}$, (n, γ)$_{cap}$ and others, this makes it possible (in a filtering mode) to isolate the mechanisms of cascade generation processes in the volume of the detector caused by secondary gamma quanta from excited states of compound nuclei. The gamma quanta of the elastic scattering reaction (n, n' γ) for the KDP: TL+ scintillator nuclei are the start of the cascade process of the discharge of excited isomeric states of the input, intermediate, and final nuclei. Measurements of the detection efficiency of fast neutrons were carried out with a KDP: TL+ crystal of size 18x18x42 mm in spherical geometry. The obtained detector reviews in units of impulse / particle for sources and ^{239}Pu-Be and ^{137}Cs were 3.57 and 1.44. In this case, a broadband path with a speed of 7 ns was used. In addition, the counting efficiency of the narrow-band tract measured simultaneously with a processing time of 1 μs and 6.4 μs. The received response from the KDP: TL+ detector (in units of impulse/particle) for both sources ^{239}Pu-Be and ^{137}Cs was 0.09 and 0.00029. The n/γ ratio coefficient was 310. The given measurements of a polystyrene-based scintillator size of 40×40×40 mm. The received response in a single photon-counting mode from the plastic detector (in units of impulse/particle) for both sources ^{239}Pu-Be and ^{137}Cs was 19.4 and 3.9. The n/γ ratio coefficients for detectors are also given: KDP: TL+ - 2.47 and UPS-923A - 4.97 in the 7 ns mode. The statistical error in measurements of the neutron detection efficiency was about ~ 5%.
KEY WORDS: neutron, detector, fast neutron, KDP: TL+ crystals, detection efficiency, registration threshold, PX-5, counting rate, radiation monitor

In the previous works [1, 2] are shown that mechanism of inelastic scattering could be useful for the fast neutron registration. In these detectors, fast neutrons could be detected by counting impulses from the secondary gamma-quanta, inside the detector volume. Since a spectrometric path with an integration time of ~ 1 μs and 6 μs was used in our studies for registration purposes, this ensured almost complete suppression of the registration of cascade processes in the detector. If a neutron detector uses only the one mechanism of inelastic scattering, in which one the secondary gamma-quanta are generated due to the discharge of single-particle excitations of nuclei, this allows the use of a narrow-band detection path (1 μs). In this case, the counted efficiency coincides with the energy of the registration efficiency, which cannot exceed one. The mechanism of inelastic scattering of fast neutrons is a starting process that can be as a trigger for the process of resonant scattering, radiation capture and secondary nuclear reactions. In this case, excited states in the nuclei of the crystals under study generate cascades of gamma rays with energies ranging from E ~ 2-3 MeV to units of keV. Note that the energy of the secondary neutron n' from the reaction (n, n'γ)$_{res}$ can exceed the energy of the incident neutron from the reaction (n, n′γ) due to the binding energy, so the channel (n, n′γ)$_{res}$ is also an effective source of secondary gamma rays. Secondary neutrons can subsequently be captured by nuclei in the radiation capture reaction (n, γ)$_{cap}$. For applications, secondary gamma rays are of interest, the emission times of which are in the range of ~ 1 ns - 100 μs. Also in this interval are the collision times of secondary neutrons from these reactions with scintillator nuclei. Therefore, secondary neutrons can participate in reactions (n, n′γ)$_{res}$ and thereby increase the number of cascade gamma rays. Note that the nuclear composition of oxide scintillators significantly affects the intensity of the gamma-ray cascades of the discharge of excited nuclear states, and hence the detector counting efficiency [2]. Earlier [1-2], for the purpose of recording efficiency, a counting path operating in the spectrometric mode (t = 1 μs and 6 μs) was used. As long as the lifetimes of highly excited states of compound nuclei, which could be also excited in the fast neutron reactions, are stay in the range from a few nanoseconds to hundreds of microseconds. To increase the contribution of various mechanisms that are possible when the neutron is slowed down in the detector the single-photon detection mode [1] was used in this work and have a significantly lower registration threshold. In view of the increased radiation resistance (~ 10^{10} neutron/cm^2) of the obtained new crystals, an urgent task is to study the interaction of neutron radiation with the substance of KDP: TL+. As shown in

our previous works [1–10], neutron radiation can be detected using scintillation crystals of potassium dihydrogen phosphate KH_2PO_4 (KDP), which are doped with thallium ions Tl^+ [5]. This paper presents the experimental results of a study of the efficiency of fast neutron detection in water-soluble crystals in the photon-counting mode and pulse time-filtering mode. The purpose of the work is to study the scintillation properties, efficiencies of detecting fast neutron and gamma fluxes and n/γ coefficients by the new KDP crystal and UPS-923A scintillator.

RESEARCH AND METHODS

Inorganic crystals of KDP: TL^+ are grown by the method of the temperature lowering. The crystals have a wide optical transparency band, low dislocation density $<10^2$ cm^{-2}, and high radiation resistance when exposed to fast neutron fluxes of $\sim 10^{10}$ neutrons/cm^2. The presence of hydrogen bonds in the KDP lattice provides the possibility of doping with additives [5]. In Figure 1 shows KDP: TL^+ crystals grown on a seed of orientation (101), in the form of 18×18×42 mm plate. The concentration of thallium additives is 0.1%.

Figure 1. The KDP: TL⁺ crystal sample was grown from water solution.

The physical parameters of measured crystals are shown in the Table 1.

Table 1.

Parameters comparison table of hydrogen based organic UPS-923A and inorganic KDP scintillators.

Scintillator	Z_{eff}	Density, g/cm^3	Hydrogen nuclei density, cm^{-3}	Neutron run-length l_n, cm
Plastic UPS-923A, 4×4×4 cm^3	5.7	1.04	4.82×10^{22}	3.30
KDP: Tl⁺ (0.1 wt.% Tl), 1.8×1.8×4.2 cm^3	14.3	2.34	2.07×10^{22}	3.93

The neutron energy from radioactive sources during slowing in the detector to a complete stop changes more than 10^8 times - from 10 MeV to 0.025 eV. This energy region can be conditionally divided into three specific regions, which differ in the interaction mechanisms and cross sectional values: the inelastic scattering region (n, n 'γ) from 10 to 0.1 MeV, the resonant scattering region (n, n' γ)$_{res}$ from 0.1 to 0.001 MeV and the radiation capture region (n, γ)$_{cap}$ from 1 keV to 0.025 eV. Currently, the most common fast neutron detectors using one specific energy conversion mechanism - either a reaction with the formation of recoil protons, or a deceleration method using a radiation capture reaction. Both of these methods have disadvantages - either the low efficiency of neutron flux conversion during deceleration, or the complex electronic for the neutron/gamma separation systems.

In the present work, it is proposed to register cascade signals as from the reaction of inelastic scattering, resonance scattering, and radiation capture. For this purpose, a technique was developed that is a further improvement of the technique used in our works [2, 3]. The detection efficiency of fast neutrons and gamma rays by KDP: TL^+ crystals and UPS-923A polystyrene was measured by the following method. The block diagram of the experiment is shown in Fig. 2. The KDP: TL^+ crystal with dimensions 18x18x42 mm^3 was wrapped with a PTFE tape reflector. The UPS-923A 40×40×40 mm^3 with polished edges was wrapped with a PTFE tape reflector also. A ^{239}Pu-Be source was used as a neutron source (neutron energies from 0.1 to 10 MeV, average neutron energy $E_n = 4.2$ MeV, 4×10^5 neutrons per second). The source is placed in a lead spherical shield to attenuate the accompanying gamma radiation (photons with $E_γ \sim 59$ keV from ^{241}Am impurity arising from ^{239}Pu decay products, as well as high-energy gamma rays with $E_γ \sim 0.1$- 4.43 MeV from the accompanying reactions in the source). The distance between the center of the neutron source and the detector window was in range of 20 - 50 cm.

As the photodetector, the PMT Hamamatsu R1307 was used [12]. The voltage of the PMT was 1250 V. The lower threshold of the pulse counter in the fast channel was obtained using an Amptek DPP PX-5 [13] digital analyzer and monitored with GDS-3504 GW Instek oscilloscope (500MHz bandwidth). The lifetimes of isomeric states excited in reactions with fast neutrons are in the range [3] from a few nanoseconds to hundreds of microseconds. Therefore, the measuring path includes a fast preamplifier [4] with a gain of 70 dB and an intrinsic rise time of ~ 1.5 ns. The preamplifier

is used to register signals in the photon-counting mode. The application of this mode is due to the need to register signals of small amplitudes and durations resulting from the discharge of excited states in the compound nuclei, the need for separate registration of signals caused by slowed neutron collisions in a crystal. The amplitude of the single-photon response signal was ~ 1.5 V.
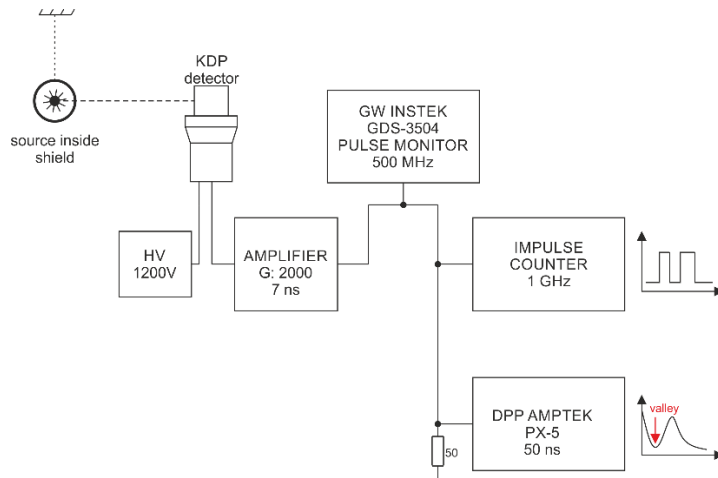
Figure 2. The experimental setup diagram

Figure 3 represents the signal from the preamplifier output during neutron registration with the KDP: TL$^+$ scintillator. The pulse width at the half maximum is about 20 ns, the pulse amplitude is ~ 1.5 V, and the background pulse load is ~ 200 s^{-1}.
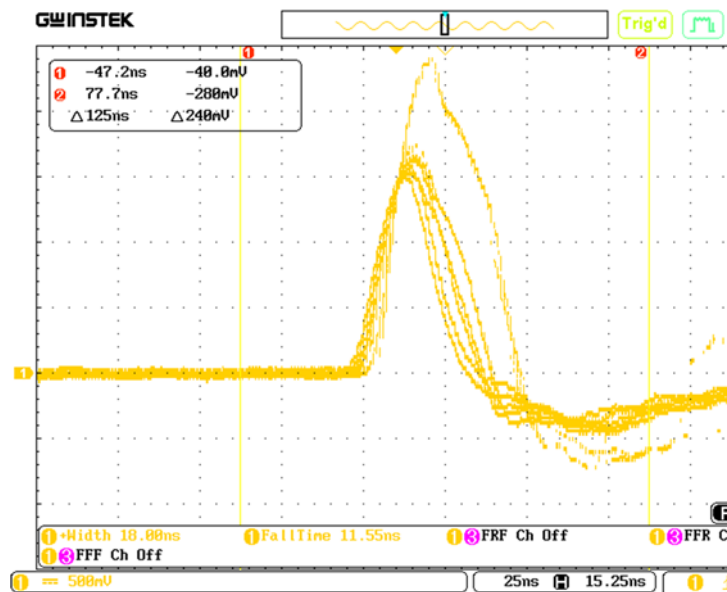
Figure 3. The shape of pulses reached from KDP: TL$^+$ under fast neutron radiation of ^{239}Pu-Be source
Y – 1 V, X - 25 ns.

Figure 4 shows the hardware spectrum of the investigated scintillator sample upon irradiation with a neutron source; the maximum height of a single-photon peak is in the 1600 channel. The rise time of the signal from the PMT output is ~ 8 ns. The time for collecting statistics in one exposure was 20 minutes, the time for collecting background radiation was 20 minutes, and the number of exposures was 5.

As discussed earlier [2, 3], the response of the detectors is formed by registering cascades of gamma-quanta. The primary gamma-quantum arises from the inelastic scattering reaction. Since the crystal dimensions are comparable with the mean run length of neutrons before moderation, therefore, other than inelastic scattering, other mechanisms leading to the formation of compound nuclei with subsequent removal of excitation by emission of cascades of gamma quanta, such as resonance capture (n, n' γ)$_{res}$, radiation capture of the neutrons (n, γ)$_{cap}$. Secondary "daughter" gamma-quanta can also arise as a result of a slowdown in the elastic scattering reaction and neutron capture on hydrogen (E = 2223.2 keV).

Thus, the effective registration of signals generated by the scintillator nuclear subsystem is explained when considering the parameters of the nuclei that make up the scintillators. The most significant parameters of scintillator nuclei are cross sections in the region of inelastic scattering, resonance capture, the density of nuclear levels in the resonance region, and the magnitude of the upper boundary of the energies of the resonance region. The cross section of

the resonance region has an effect only if it has a region width of ~ 100 keV or more [2]. Figure 5 shows neutron cross sections in the energy range 0.01 MeV - 10 MeV for the nuclei of a natural mixture of potassium, phosphorus, carbon and hydrogen that are part of KDP and polystyrene.
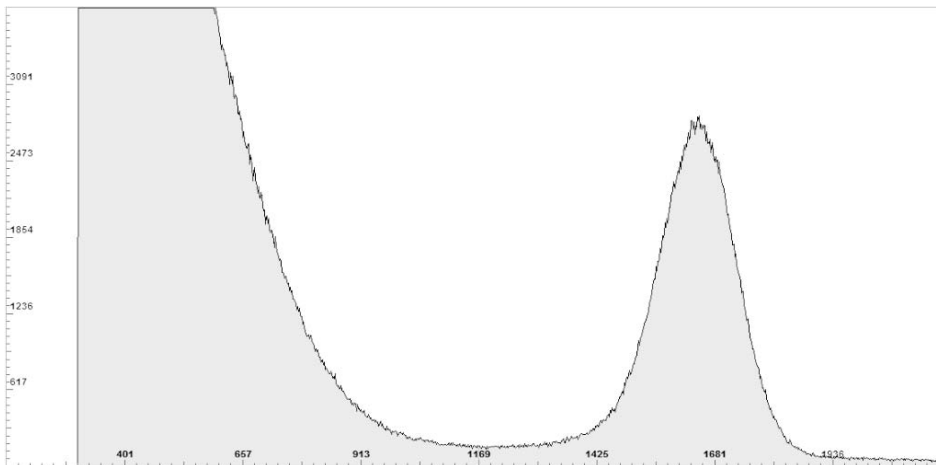
Figure 4. The amplitude spectrum in a photon counting mode from the KDP: TL⁺ initiated by the ^{239}Pu-Be source, accumulated by Amptek DPP PX-5 with:
Peak Time = 50 ns.
PMT voltage = 1250 V.
Y– counts, X – channels.
Single photon peak position – 1600 ch., with amplitude of 1.5 V.

a)

b)

c)

d)
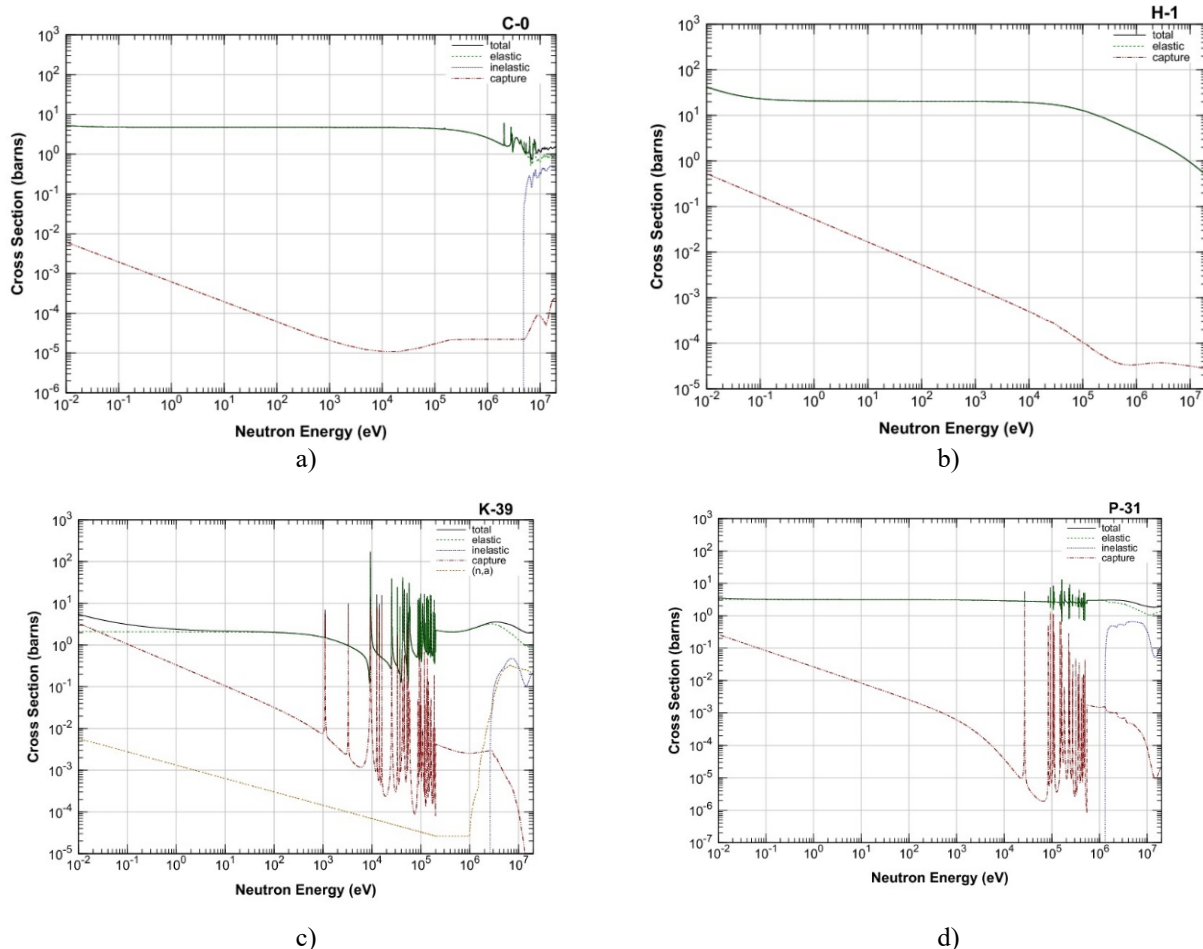
Figure 5. The neutron cross sections for: ^{1}H (a), ^{12}C (b), ^{39}K (c), ^{31}P (d) in a region of inelastic scattering region, resonant region and radiation capture area [14, 16].

Table 2 [15, 16] shows the parameters of the cross sections for the interaction of neutrons with nuclei for a natural mixture of isotopes of KDP: TL⁺ scintillator nuclei and polystyrene.

In the range of neutron energies E_n ~ 0.1-10 MeV on hydrogen, reaction (n, p) is observed with the formation of recoil protons (σ ~ 2 b), which can contribute to the detector response if the proton moderation volume is a scintillator. When a neutron is slowed down, a reaction of elastic neutron scattering on hydrogen (σ$_{el}$ ~ 30 b) (n, n) is significant, which one leads to a slowdown of neutrons to an energy of 0.025 eV and radiation capture by protons, with the formation of a deuteron and an emission of gamma rays with an energy of E_γ = 2.223 MeV (energy deuteron coupling).

Table 2.
The parameters of neutron cross sections σ, barn, quantity of N_γ output and energy E_γ of gamma-quanta from reactions with neutrons from ^{239}Pu-Be ($E_n \sim 0.1$- 10 MeV)

for the natural abundance of KDP: TL$^+$ isotopes mixture and UPS-923A.	σ (n, γ)$_{cap}$ E = 0.0253 eV	σ$_{el}$ E$_n \sim$ 0.0253 eV	σ (n, n' γ)$_{res}$, E$_n \sim$ 0.5 eV – 10 MeV	σ (n, n' γ)$_{inel}$, E$_n \sim$ 0.1 – 10 MeV	σ$_{el}$ E$_n \sim$ 4.5 MeV	N$_\gamma$, Emitted gamma from capture	N$_\gamma$, Emitted gamma from inelastic
H-1	0.3320 ^{2}H, E$_\gamma$ = 2.2232 MeV	30.27	0.1492	-	~ 2	1	p recoil
12-C-6	0.00386 13-C, E$_\gamma$ = 0.595, 1.2618, 1.8567, 3.0891, 3.6839, 4.9453 MeV 6 gamma quants		0.001885 13-C, E$_\gamma$ = 0.595, 1.2618, 1.8567, 3.0891, 3.6839, 4.9453 MeV 6 gamma quants	0.34 E$_n \sim$ 10 MeV 12C, E$_\gamma$ = 4.438 MeV	~ 2.4	6 + 6	1
13-C-6	~0.0045 14-C, E$_\gamma$ = 0.4957, 1.5869, 6.0925 MeV	4.922	0.00162 14-C, E$_\gamma$ = 0.4957, 1.5869, 6.0925 MeV	-	0.803 E$_n \sim$ 14 MeV	7 + 7	1
31-P-15	0.1662 32-P, E$_\gamma$ = 0.0781, 0.5126, 0.6367, 1.0713, 2.1145 MeV 158 gamma quants	3.186	0.08079 32-P, E$_\gamma$ = 0.0781, 0.5126, 0.6367, 1.0713, 2.1145 MeV 158 gamma quants	0.0539 E$_n \sim$ 14 MeV 31-P, E$_\gamma$ = 1.266, 2.028, 2.148 MeV 14 gamma quants	~2 E$_n \sim$ 4.5 MeV	158+158	14
39-K-19	2,098 39-K, E$_\gamma$ = 0.0298, 0.7703, 1.1589, 1.2472, 1.3035 MeV 308 gamma quants	2.089	1,081 39-K, E$_\gamma$ = 0.0298, 0.7703, 1.1589, 1.2472, 1.3035 MeV 308 gamma quants	0,25 E$_n \sim$ 4.5 MeV 39-K, E$_\gamma$ = 0.3469, 0.7837, 0.9233, MeV 15 gamma quants	~2 E$_n \sim$ 4.5 MeV	308+308	15

In the resonance energy region $E_n \sim 0.5$ eV - 10 MeV), due to the absence of excited states at the deuteron itself, gamma-ray emission is not observed. Thus, on the nuclei of hydrogen from one incident neutron there is 1 gamma quantum response, in addition, signals from recoil protons will be observed. On carbon nuclei with neutron energies above $E_n = 4.812$ MeV, an inelastic scattering reaction is observed with excitation of the first ^{12}C level and emission of gamma rays with an energy of $E_n = 4.438$ MeV. In the resonance region ($E_n \sim 0.5$ eV - 10 MeV), up to 6 response gamma rays can occur. If the secondary neutron after deceleration is again captured in the scintillator by a carbon nucleus in the radiation capture reaction, then another 6 gamma rays can be excited. Thus, up to 13 responses of gamma-quanta arise from one incident neutron on carbon nuclei. Similarly, on potassium nuclei (see Table 2), a noticeable amount of gamma quanta is emitted from resonance and radiation capture reactions, which is confirmed by noticeable reaction cross sections

reaching 2.098 bar (radiation capture reaction) and 1.8 bar (resonance capture) for ^{19}K. It should be noted that the energy of the upper boundary of the resonance region for ^{19}K is ~ 200 keV. In combination with a sufficiently high density of levels of the ^{19}K nucleus, this explains a significant amount (more than 300) of emitted gamma rays during neutron moderation in KDP: TL$^+$. For the ^{19}P nuclei the cross section of inelastic and resonance scattering is significantly low, so the obtained impulse response formed mainly by ^{19}K nuclei.

RESULTS

The measurement results of the counting efficiency of the KDP: TL$^+$ scintillator in mode of counting single photons (mode 7 ns, i.e., registration of single-photon signals in the interval of rise times about 7 ns) are shown in Table 3.

Table 3.

Registration efficiency of the fast neutrons and γ-quanta
by KDP: TL$^+$ and UPS-923A scintillators in a different filtration time

#	Scintillator	Size, mm	Mode	ε_n, imp/n	ε_γ, imp/γ	$\varepsilon_n/\varepsilon_\gamma$
1	Plastic UPS-923A	40×40×40	6.4 μs	0.24	0.071	3.42
	Plastic UPS-923A	40×40×40	1.0 μs	0.95	0.26	3.65
	KDP: Tl$^+$ (0.1 wt.% Tl)	18×18×42	6.4 μs	0.037	0.00024	154
	KDP: Tl$^+$ (0.1 wt.% Tl)	18×18×42	1.0 μs	0.09	0.00029	310
2	Plastic UPS-923A	40×40×40	7 ns	19.4	3.9	4.97
	KDP: Tl$^+$ (0.1 wt.% Tl)	18×18×42	7 ns	3.57	1.44	2.47
3	Plastic UPS-923A	Ø16×9	6 μs	0.30	0.071	4.2
	KDP: Tl$^+$ (0.1 wt.% Tl)	10×10×10	6 μs	0.124	0.004	31
	KDP: Ce^{3+} (0.01 wt.% Ce)	10×10×10	6 μs	0.162	0.006	27

For comparison purposes, the results of measuring the counting efficiency of the scintillator are given based on UPS-923A. In addition, all measurement results were obtained in the spectrometric signal counting mode with an integration time of 1 - 6.4 μs. It can be seen that the calculated efficiency for KDP upon transition from 6 μs to 7 ns (single-photon mode) increases by 3.57 / 0.09 = 40 times, i.e. In the photon counting mode, not only inelastic scattering is realized, but also resonance and radiation captures. A similar effect of an increase in the counted efficiency is also observed for UPS-923A - the counting efficiency increases from 1 μs to 7 ns (single-photon mode) by 19.4/0.95 = 20.4 times.

The measurement results of the KDP: TL$^+$ scintillator of small sizes (10x10x10 mm) [5] in the τ = 6 μs mode are consistent with the results of the KDP: TL$^+$ scintillator with dimensions of 18x18x42 mm in the τ = 6.4 μs mode adjusted for the size effect.

In this work, for the KDP: TL$^+$ and UPS-923A scintillators, the n/γ ratio was also determined (Table 3). It can be seen that the n/γ ratio for the KDP: Tl$^+$ of 10x10x10 mm size crystal measured in [5] is ~ 30, which is explained by the small crystal size. The registration in the photon counting mode with filtering time 7 ns provide 2.47 value for n/γ ratio of KDP: Tl$^+$. The registration in the filtration mode with filtering time 1 μs provide 310 value for n/γ ratio of KDP: Tl$^+$. In the present work, the path threshold selected at 1 μs that was about 25 keV energy region, which provide n/γ ratio of ~ 3.57. The efficiency of the UPS-923A scintillator measured in this work in the photon counting mode, was 19.4 pulses/neutron, and the n/γ ratio ~ 5.

Figure 6 shown bar diagram of counting efficiencies for KDP: TL$^+$ (a) and Plastic UPS-923A (b), obtained for ^{239}Pu-Be and ^{137}Cs sources for filtration times 7 ns and 1 μs.
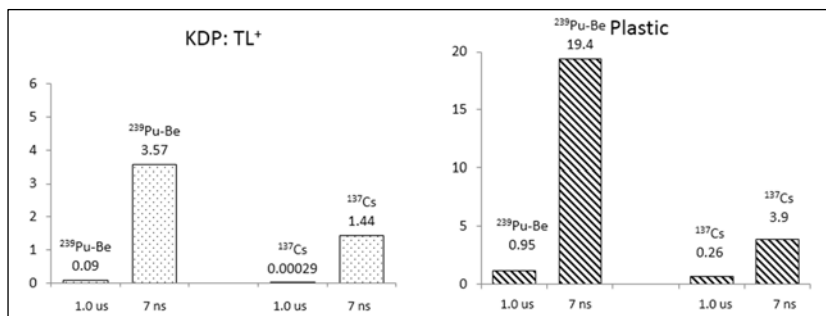
Figure 6. The counting efficiency for KDP: TL$^+$ and Plastic UPS-923A scintillators, obtained for ^{239}Pu-Be and ^{137}Cs sources for filtration modes 7 ns and 1 μs.

Figure 7 shows the n/γ ratio in bars representation for KDP: TL$^+$ and UPS-923A. Results are obtained for ^{239}Pu-Be and ^{137}Cs sources for 7 ns and 1.0 us filtration modes.

Figure 7. n/γ ratio for scintillators KDP: TL$^+$ and Plastic UPS-923A, obtained for ^{239}Pu-Be and ^{137}Cs sources for filtration modes 7 ns and 1.0 us

CONCLUSIONS

In this work, we calculated the counting efficiencies and n/γ ratios of KDP: TL$^+$ crystals and UPS-923A polystyrene when irradiated with fast neutrons and gamma rays from ^{239}Pu-Be and ^{137}Cs sources using a single-photon detection mode. The obtained efficiency values could be explained by the mechanism of inelastic scattering of fast neutrons (as the primary starting process), which, under certain conditions, can trigger for the process of resonance scattering and radiation capturing. In this case, excited states in the crystal nuclei generate cascades of gamma quanta with an energy in the range from high-energy values etc. $E \sim 2\text{-}3$ MeV and higher, to low-energy values, with an energy of few keV. Accordingly, three types of neutron interaction mechanisms contribute to the efficiency: inelastic scattering (n, n 'γ), resonant scattering (n, n' γ)$_{res}$, and radiation capture (n, γ)$_{cap}$. The counted detection efficiency of fast neutrons for KDP scintillation crystals with a thickness of 40 mm was about 3.57 pulse/particle in a photon counting mode. The ratio for neutrons and gamma reaches ~ 2.47. The counting efficiency of fast neutron registration for Plastic UPS-923A with a thickness of 40 mm was about 19.4 pulse/neutron. The ratio of the efficiencies for neutrons and gamma reaches ~ 4.97. The calculated statistical error with [17] approach for measurements of the neutron detection efficiency was about $\sim 5\%$.

The obtained result of n/γ for KDP: TL$^+$ in a filtration mode with 1 us time filtration was about 310. That is mean that filtration registration mode can be used for the efficient detection of fast neutrons by the small size KDP: TL$^+$ scintillators with high n/γ ratio.

ACKNOWLEDGEMENTS

ORCID IDs
Ivan Yakymenko, https://orcid.org/0000-0002-0194-8376; **Gennadiy Onyshchenko**, https://orcid.org/0000-0001-6945-8413
Borys Grynyov, https://orcid.org/0000-0003-1700-0173; **Volodymyr Ryzhikov**, https://orcid.org/0000-0002-2833-2774
Olexiy Voronov, https://orcid.org/0000-0001-6945-8413; **Sergei Naydenov**, https://orcid.org/0000-0002-5585-763X

REFERENCES
[1] M.B. Das, S. Bose, and R. Bhattacharya, Nuclear Instruments and Methods in Physics Research Section A: Accelerators, Spectrometers, Detectors and Associated Equipment, **242**(1), 156–159 (1985), https://doi:10.1016/0168-9002(85)90902-7.
[2] V. Ryzhikov, G. Onyshchenko, I. Yakymenko, S. Naydenov, A. Opolonin, and S. Makhota, East European Journal of Physics, **2**, 11-18 (2019), https://doi.org/10.26565/2312-4334-2019-2-02.
[3] G. Onyshchenko, V. Ryzhikov, I. Yakymenko, V. Khodusov, S. Naydenov, A. Opolonin, and S. Makhota, East European Journal of Physics, **3**, 54-62 (2019), https://doi.org/10.26565/2312-4334-2019-3-07.
[4] G. Onyshchenko, V. Ryzhikov, I. Yakymenko, and O. Shchus', East European Journal of Physics, **4**, 91-94 (2019), https://doi.org/10.26565/2312-4334-2019-4-10.
[5] A. Voronov, S. Naydenov, I. Pritula, G. Onyshchenko, A. Shchus', and I. Yakymenko, East European Journal of Physics, **5**(3), 45-52 (2018), https://doi.org/10.26565/2312-4334-2018-3-05.
[6] B. Grinyov, V. Ryzhikov, G. Onyshchenko, I. Yakymenko, S. Naydenov, O. Opolonin and S. Makhota, in: *Sixth International Conference "Engineering of scintillation materials and radiation technologies ISMART"*, (Minsk, 2018), pp. 46.
[7] V.D. Ryzhikov, G.M. Onishenko, I.I. Yakymenko, S.V. Najdenov, A.D. Opolonin and S.V. Mahota, in: *XVII конференция по физике высоких энергий и ядерной физике* [*XVII Conference on High Energy Physics and Nuclear Physics*], (NSC "KIPT", Kharkiv, 2019), pp. 96, https://www.kipt.kharkov.ua/conferences/ihepnp/2019/collection_of_theses_%D0%A5VII_hepnp.pdf.
[8] V.D. Ryzhikov, G.M. Onishenko, I.I. Yakymenko, S.V. Najdenov, A.D. Opolonin and S.V. Mahota, in: *XV International Scientific and Technical Conference Young Scientists and Specialists «Problems of Modern Nuclear Power»*, (Kharkiv, 2019), pp. 25, https://ukrns.org/images/activity/2019/2019__isbn.pdf, (in Ukrainian)
[9] B. Grynyov, V. Ryzhikov, L. Nagornaya, G. Onishcenko, and L. Piven'. US Patent No 8.058.624 B2 (15 November 2011).
[10] V.D. Ryzhikov, B.V. Grinyov, G.M. Onyshchenko, L.A. Piven, O.K. Lysetska, O.D. Opolonin, S.A. Kostioukevitch and C.F. Smith, in: *XVI SPIE Optical Engineering Proceedings, "Hard X-Ray, Gamma-Ray, and Neutron Detector Physics"*, edited by Arnold Burger, Larry Franks, Ralph B. James, and Michael Fiederle (IEEE, San Diego, 2014), https://doi.org/10.1117/12.2058185.

[11] V.D. Ryzhikov, S.V. Naydenov, G.M. Onyshchenko, L.A. Piven, T. Pochet, and C.F. Smith, Nucl. Inst. Meth. Phys. Res. A, **903**, 287–296 (2018), https://doi.org/10.1016/j.nima.2018.06.074.

[12] Hamamatsu Photonics K.K., https://www.hamamatsu.com/resources/pdf/etd/R1307_TPMH1214E.pdf.

[13] Amptek, Inc., https://www.amptek.com/-/media/ametekamptek/documents/products/px5.pdf.

[14] Japan Atomic Energy Agency, Nuclear Data Center, Japan, https://wwwndc.jaea.go.jp/jendl/j40/j40nat.html.

[15] G.L. Molnár, editor, *Handbook of Prompt Gamma Activation Analysis*, (Springer, Boston, MA, 2004), https://doi.org/10.1007/978-0-387-23359-8.

[16] R.B. Firestone, H.D. Choi, R.M. Lindstrom, G.L. Molnar, S.F. Mughabghab, R. Paviotti-Corcuera, Zs. Revay, A. Trkov, C.M. Zhou, and V. Zerkin, https://escholarship.org/content/qt1wj43711/qt1wj43711.pdf?t=lnpgga.

[17] I. Yakimenko, N. Styervoyedov, A. Shchus, and G. Onyshchenko, East European Journal of Physics, **3**(2), 65-69 (2016), https://doi.org/10.26565/2312-4334-2016-2-09.

ЛІЧИЛЬНА ЕФЕКТИВНІСТЬ ТА ГАММА/НЕЙТРОННЕ ВІДНОШЕННЯ ДЛЯ KDP: TL$^+$ ТА UPS-923A СЦИНТИЛЯТОРІВ В ОДНОФОТОННОМУ РЕЖИМІ ДЕТЕКТУВАННЯ

Генадій Онищенко^{a,b}, Іван Якименко^b, Борис Гриньов^a, Володимир Рижиков^a, Олексій Воронов^a, Сергій Найденов^a

^{a}*Інститут сцинтиляційних матеріалів, НТЦ «Інститут монокристалів» НАН України*
Пр. Науки 60, 61001 Харків, Україна
^{b}*Харьковский национальный университет имени В.Н. Каразина,*
пл. Свободи, 4, Харків, 61022, Україна

Метою даної роботи є реєстрація швидких нейтронів детектором на основі неорганічного монокристала KDP: TL$^+$ (KH$_2$PO$_4$ дигідрофосфат калію) та пластику UPS-923A. Кристал детектора KDP: TL$^+$ вирощено з водного розчину методом зниження температури. Висока концентрація ядер водню в гратці KDP: TL$^+$ дає змогу реєструвати нейтронне випромінення з ефективністю, порівняною з полістирольними сцинтиляторами. Кристали KDP: TL$^+$ мають високу радіаційну стійкість (10^{10} нейтрон/см^2), що суттєво розширює спектр їх застосування в фізиці високих енергій, інтенсивних нейтронних полях. В роботі використана методика реєстрації відгуку детектора в режимі лічення фотонів та імпульсному режимі часової фільтрації. Оскільки детектор працює за принципом реєстрації гамма квантів з реакцій (n, n' γ), (n, n' γ)$_{res}$, (n, γ) та інших, це дає змогу, при певному виборі порогу реєстрації в режимі фільтрації, виділити складові частини каскадних процесів генерації в об'ємі детектора вторинних гамма квантів із збуджених станів компаунд-ядер. Гамма-кванти реакції непружного розсіяння (n, n′γ) для ядер сцинтилятора KDP: TL$^+$ є стартом каскадного процесу розрядки збуджених ізомерних станів вхідних, проміжних і кінцевих ядер. Виміри ефективності реєстрації швидких нейтронів здійснювалися кристалом KDP розмірами 18х18х42 мм в сферичній геометрії. Отримані відгуки детектора в однофотонному режимі, в одиницях імпульс/частинка для джерел та ^{239}Pu-Be та ^{137}Cs склали 3.57 та 1.44. При цьому був використаний широкополосний тракт з швидкодією 7 нс. Також одночасно проводилися виміри лічильної ефективності вузькополосним трактом з часом обробки 1 мкс та 6.4 мкс. Отримані відгуки KDP: TL$^+$ детектора в режимі 1 мкс (в одиницях імпульс/частинка) для джерел та ^{239}Pu-Be та ^{137}Cs склали 0.09 та 0.00029. При цьому відношення n/γ склало 310. Для порівняння наведені результати вимірів сцинтилятора на основі полістиролу розміром 40×40×40 мм. Отримані відгуки полістирольного детектора (в одиницях імпульс/частинка) в однофотонному режимі для джерел та ^{239}Pu-Be та ^{137}Cs склали 19.4 та 3.9. Також наведені коефіцієнти n/γ відношення для KDP: TL$^+$ – 2.47 і UPS-923A – 4.97. Статистична похибка вимірів ефективності реєстрації нейтронів склала ~ 5 %.

КЛЮЧОВІ СЛОВА: нейтрон, детектор, швидкі нейтрони, KDP: TL$^+$ кристал, ефективність реєстрації, поріг реєстрації, PX-5, швидкість лічення, радіаційний монітор

СЧЕТНАЯ ЕФФЕКТИВНОСТЬ И ГАММА/НЕЙТРОННОЕ ОТНОШЕНИЕ ДЛЯ KDP: TL$^+$ AND UPS-923A СЦИНТИЛЛЯТОРОВ В ОДНОФОТОННОМ РЕЖИМЕ РЕГИСТРАЦИИ

Геннадий Онищенко^{a,b}, Иван Якименко^b, Борис Гриньов^a, Владимир Рижиков^a, Алексей Воронов^a, Сергей Найденов^a

^{a}*Институт сцинтилляционных материалов, НТЦ «Институт монокристаллов», НАН Украины*
пр-т Науки 60, 61001 Харьков, Украина
^{b}*Харьковский национальный университет имени В.Н. Каразина*
майдан Свободы, 4, 61022, Харьков, Украина

Целью данной работы является регистрация быстрых нейтронов детектором на основе неорганического монокристалла KDP: TL$^+$ (KH$_2$PO$_4$ дигидрофосфат калия) и пластика UPS-923A. Кристалл детектора выращено из водного раствора методом снижения температуры. Высокая концентрация ядер водорода в решетке KDP позволяет регистрировать нейтронное излучения с эффективностью, сопоставимой с полистирольными сцинтилляторами. Кристаллы KDP: TL+ имеют высокую радиационную стойкость (10^{10} нейтрон/см^2), что существенно расширяет спектр их применения в физике высоких энергий, интенсивных нейтронных полях. В работе использована методика регистрации отклика детектора в режиме счета фотонов. Поскольку детектор работает по принципу регистрации гамма квантов из реакций (n, n' γ), (n, n' γ)$_{res}$, (n, γ)$_{cap}$ и других, это позволяет выделить составные части каскадных процессов генерации в объеме детектора вторичных гамма квантов с возбужденных состояний компаунд-ядер. Гамма-кванты реакции упругого рассеяния (n, n' γ) для ядер сцинтиллятора KDP: TL$^+$ являются стартом каскадного процесса разрядки возбужденных изомерных состояний входных, промежуточных и конечных ядер. Измерения эффективности регистрации быстрых нейтронов осуществлялись кристаллом KDP: TL$^+$ размером 18×18×42 мм в сферической геометрии. Полученные отзывы детектора в единицах импульс / частица для источников и ^{239}Pu-Be и ^{137}Cs составили 3.6 и 1.44. При этом был использован широкополосный тракт с быстродействием 7 нс. Также одновременно проводились измерения счетной эффективности узкополосных трактом со временем обработки 1 мкс и 6.4 мкс. Получены отклики KDP: TL$^+$ детектора в режиме 1 мкс (в единицах импульс/частица) для источников ^{239}Pu-Be и ^{137}Cs составил 0.09 и 0.00029. При этом отношение n/γ составило 310. Для сравнения приведены результаты измерений сцинтиллятора на основе полистирола размером 40x40x40 мм. Полученный отклик полистирольного детектора (в единицах импульс/частица) в однофотонном режиме для источников ^{239}Pu-Be и ^{137}Cs составил 19.4 и 3.9. Также приведены коэффициенты n/γ отношения для KDP: TL$^+$ – 2.47 i UPS-923A – 4.97. Статистическая погрешность измерений эффективности регистрации нейтронов составила ~ 5%.

КЛЮЧЕВЫЕ СЛОВА: нейтрон, детектор, быстрые нейтроны, KDP: TL$^+$ кристалл, эффективность регистрации, порог регистрации, PX-5, скорость счета, радиационный монитор

NUCLEAR BURNING WAVE CONCEPT
AND THEORETICAL APPROACHES FOR ITS DESCRIPTION

Maksym S. Malovytsia[a],*, Alex S. Fomin[b], Sergii P. Fomin[a,b],†

[a]V.N. Karazin Kharkiv National University
4, Svobody sq., 61022, Kharkiv, Ukraine
[b]National Science Center "Kharkov Institute of Physics and Technology"
1, Akademichna str., Kharkiv, Ukraine, 61108
†E-mail: sfomin@kipt.kharkov.ua
*Corresponding Author: jcm2027@gmail.com

After two major nuclear power plant accidents in Chernobyl (1986) and Fukushima (2011), one of the main requirements for the nuclear power engineering is the safety of the nuclear reactors in operation, as well as new nuclear power plants of the fourth generation, which are being developed now. One of such requirements is presence of the so-called "inherent safety" mechanism, which renders the uncontrolled reactor runaway impossible under any conditions, moreover, the implementation of such a mechanism should be ensured on the level of physical principles embedded in the reactor design. Another important problem of the nuclear power engineering is the need of the transition to the large-scale use of the fast-neutron breeder reactors, with which it would be possible to set up expanded reproduction of the nuclear fuel and by that means solve the problem of supplying humanity with relatively cheap energy for thousands of years. Moreover, at present an unresolved problem is the disposal of spent nuclear fuel containing radioactive nuclides with long half-lives, which presents a long-term danger to the ecology. One of the promising conceptions of the fast-neutron breeder reactor, which can, in the case of successful implementation, partially or even entirely solve the problems of the nuclear power engineering mentioned above, is the reactor that operates in the nuclear burning wave mode, which is also known as "Traveling wave reactor", CANDLE and by some other names. This paper presents a short review of the main theoretical approaches used for description of such a physical phenomenon as slow nuclear burning (deflagration) wave in the neutron multiplication medium initially composed of the fertile material ^{238}U or ^{232}Th. A comparative analysis of the possibilities of different mathematical models for describing this phenomenon is performed, both for those based on the deterministic approach (i.e. solving neutron transport equations) and for models that use Monte Carlo methods. The main merits of the fast breeder reactor, working in the nuclear burning wave mode, and problems related to the practical realization of the considered concept are discussed.
KEY WORDS: nuclear power, fast reactor, breed and burn, nuclear burning wave, traveling wave reactor

The fast growth of the planet population along with the general striving for more comfortable life leads to the rapid increase of the world energy consumption. As a matter of fact, with the doubling of the human population over the past 50 years, the total global energy consumption has increased three times. In the face of the limited Earth resources of conventional energy sources, such as coal, oil, gas, there arises more urgently a problem of searching for new alternative energy sources. Moreover, the widespread use of the combustible carbon-based fuel in the industry, transport and in everyday life leads to the catastrophic environment pollution with carbon dioxide (CO_2 problem) and other toxic emissions. Apart from the direct influence on the people's health and environment, this leads to the greenhouse effect, which is probably one of the causes of global climate change. All of this urges scientists to look for new reliable, clean, preferably renewable energy sources that can support sustainable development of humanity for a long time.

As far back as the middle of the previous century the mankind discovered an absolutely novel source of energy with the incomparable power, namely, the energy of atomic nucleus. By the colossal efforts of leading scientists of several countries, in a quite short period not only the problem of releasing this energy was solved but also the possibility was found to use it as a controlled process in nuclear power plants and other installations. However, despite the high efficiency, the nuclear energy has not become the primary energy source of humanity. At present, its share is less than 5% in the total energy production and slightly more than 10% in the production of electricity.

The main reason behind the rather meager usage of the nuclear energy in the world, as well as the complete rejection of its usage in some countries, is not technological problems, but rather problems of psychological nature, caused by radiophobia, which swept the world after two major accidents of nuclear power plants: Chernobyl (1986) and Fukushima (2011). Analysis of the causes of those accidents has shown that, with responsible approach to the designing and operation of the nuclear power plants and training of the staff, this type of accidents should not be possible. The result of this analysis was a considerable increase in the requirements for the safety of the nuclear reactors in operation, as well as new nuclear power plants of the fourth generation that are being developed now. One of such requirements is the presence of the so-called "inherent safety" mechanism, which renders the uncontrolled reactor runaway impossible under any conditions, moreover, the implementation of this mechanism should be performed on the level of physical principles, which should be laid down in the reactor construction.

From the physics point of view, the most concentrated energy source, which can be practically utilized, is the binding energy of nucleons in the atom and its nature is due to the strong interaction. For one act of the nucleus fission

the energy released equals to approximately two hundred millions of electron-volts. For comparison, the energy released in the process of carbon oxidation, $C + O_2 = CO_2$, is equal to several electron-volts. The carbon oxidation process or "chemical burning", which is the essence of the "combustion energy", has its origins in the electromagnetic interaction between electron shells of the atoms. As can be seen, the difference of the energy release per atom between nuclear and chemical reactions is almost eight orders in favour of the nuclear ones.

Recently, the so-called renewable energy sources, which include hydropower, wind power, solar power, and biofuel, have been growing in popularity. The highest share of the renewables in the total energy balance belongs to hydropower (approximately 7%). The hydropower is based on the mechanical energy of water falling in the gravitational field. It is well known that the gravitational constant is rather small, therefore a large amount of the "working medium" (water) is required to get considerable quantities of energy. The same goes for the wind power generators.

Let us compare the efficiency of different kinds of energy sources in terms of the concentrations of stored energy that can be utilized by human. From 1 cm^3 of the pure ^{235}U, theoretically, i.e. by the fission of all the nuclei present in this volume, the energy of $5 \cdot 10^5$ kW·h can be released, which is equivalent of the energy released by the combustion of 100 m^3 of anthracite coal or by dropping 100 millions of m^3 of water from the height of 25 m.

Thus, theoretically, the nuclear power should undoubtedly be leading in terms of efficiency among other types of Earth resources. However, the high density of the energy release of the nuclear chain reaction requires a high technological culture of controlling such processes. The principal possibilities and main technical solutions of the problems, related to the nuclear reactor control, were discovered as far back as middle of the past century. However, the accumulated world experience in the operation of nuclear power plants, both positive and negative, indicates the need to revise priorities in this area from maximum economy to the safety.

The history of nuclear power goes back a little over 70 years. In many countries, this is an important component in energy production, and in several of them, such as France, Ukraine, Belgium, Hungary, Slovakia, it plays the decisive role. Some of the rapidly developing countries, such as China, India, Russia, South Korea, have plans of accelerated construction of new nuclear power plants. At the same time, some developed countries, such as Belgium, Germany, Spain, Italy, Switzerland, Sweden, have decided to gradually remove the use of nuclear power. The last-mentioned fact is caused by the wave of radiophobia which swept the world after three major nuclear power plants accidents: Three Mile Island (1979), Chernobyl (1986), and Fukushima (2011), especially due to the last two. An important lesson learned from those accidents was the radical revision of the safety requirements for the nuclear systems. In particular, IAEA has formulated general requirements for the nuclear power plants of new generation, where one of the most important requirements is to ensure the so-called "inherent safety" property, which would exclude the possibility of uncontrolled reactor runaway owing to any of the internal or external influences, including operator's mistake.

Another important problem in the nuclear energy is the limited natural resources of ^{235}U, which is the main component of nuclear fuel of the thermal nuclear reactors, which are a majority among the 449 working power plants and those 54 that are being built. The solution of this problem lies in the need of a large-scale transition to the fast neutron breeder reactors, in which, in addition to the energy production, artificial fissile products, such as ^{239}Pu and ^{233}U, can also be produced from the natural ^{238}U and ^{232}Th, respectively. In this way, by means of the production of fuel for new reactors in the fast-neutron breeder reactors, the nuclear power could be considered as a renewable energy source in the future.

Another not yet resolved problem in nuclear energy is the recycling of the spent nuclear fuel. Certainly, the volumes of the nuclear waste are by orders smaller than waste volumes of usual "combustion" energy. However, some of the radioactive components of a spent nuclear fuel, mainly the transuranium elements (minor actinides, MAs), have quite large half-times (thousands of years) and present a certain danger to the future generations if stored in large quantities. In this connection, an important direction of studies in the nuclear energy field is the problem of disposal of the long-lived radioactive isotopes.

The focus of this paper is on one of the promising concepts of a fast-neutron breeder reactor (FR) that works in the nuclear burning wave (NBW) mode, which, if successfully implemented, will solve partly or even entirely the problems of the nuclear energy discussed above. The purpose of this paper is to concisely describe the physical basis of the considered concept and to perform a comparative analysis of different mathematical models used for describing this NBW phenomenon, both those based on the deterministic approach (i.e. solving the neutron transport equations) and the models using Monte Carlo methods. Different theoretical approaches are presented in this paper in the chronological order. The main merits of the NBW reactor and problems related to its implementation are discussed.

NUCLEAR BURNING WAVE CONCEPT

The idea of a fast breeder reactor in which the process of production and burnup of fissile nuclides takes place with the continuous supply of fertile ^{238}U fuel and withdrawal of fission products was mentioned for the first time by the Soviet academician S.M. Feinberg during discussing the reports on the fast reactors at the II International UN conference dedicated to the peaceful usage of the atomic energy (September 1958, Geneva, Switzerland) [1]. The criticality of such reactor is maintained by means of plutonium accumulation in the reactor. However, as was noted by S.M. Feinberg, lack of knowledge about the precise dependence of the cross-section values on the energy for the fast

neutrons did not allow accurate calculations of such a reactor. Furthermore, the fuel elements, being able to withstand a sufficiently large fuel burnup, which could reach up to 30% by the theoretical estimations of E.P. Kunegin [1], were not available at that time.

In search of the concept of safe nuclear reactor after the Chernobyl accident, another soviet academician L.P. Feoktistov [2, 3] considered the possibility of a self-sustaining and self-controlled mode of propagation of a nuclear chain reaction in a medium filled with fertile material (for example, ^{238}U) in the form of a traveling wave. He called this phenomenon as the neutron-fission wave. The phenomenon consists in the gradual movement of the reactor core area, in which the chain reaction takes place, into the breeding zone, in which, under the neutron irradiation, the production and accumulation of fissile nuclides (plutonium in such a case) occurs. When the concentration of plutonium in the breeding region reaches a critical value, the conditions for the development of nuclear chain reaction are realized in it, and the nuclear burning process also captures this region. At the same time, at the site of the previous active zone, the chain reaction gradually extinguishes as a result of depletion of fertile material and the accumulation of a large number of fission products that intensively absorb neutrons and thereby suppress the chain reaction in this region. The physical picture of the nuclear burning wave (NBW) propagation through the medium filled with initially pure ^{238}U is represented in Figure.
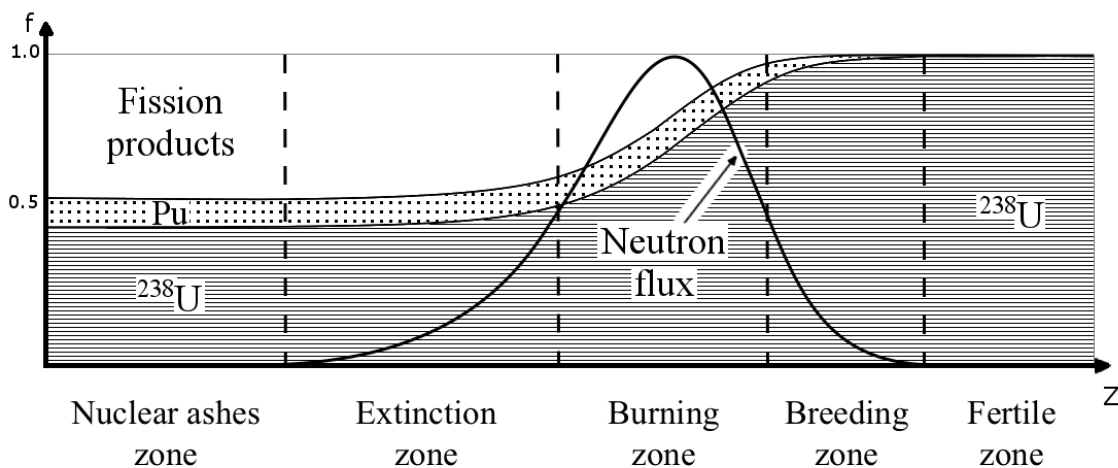
Figure. The nuclear burning wave propagation from left to right in the pure ^{238}U medium. f denotes the volume fractions of fuel components: pure ^{238}U (area filled with lines), plutonium (area filled with dots) and the fission products (white area). The bold solid curve is the neutron flux distribution. All curves are the result of calculations.

THEORETICAL APPROACHES FOR NBW DESCRIPTION
Feoktistov's analytical approach and criterion of the NBW existence

The problem that Feoktistov set himself was to find out whether such a self-sustaining regime is possible and, if so, to determine the conditions for its existence. In an attempt to solve this problem analytically, Feoktistov was forced to simplify his mathematical model as much as possible, highlighting the main factors and omitting the secondary ones.

He first considered the processes in a semi-infinite fuel region, consisting of pure ^{238}U and irradiated from the open border with neutrons. As a result of the (n,γ) reaction, the nuclide ^{239}U is produced, and after two beta decays it turns into ^{239}Pu via an intermediate nuclide ^{239}Np:

$$^{238}\mathrm{U} + n \rightarrow {}^{239}\mathrm{U} \xrightarrow{\beta} {}^{239}\mathrm{Np} \xrightarrow{\beta} {}^{239}\mathrm{Pu} \ . \tag{1}$$
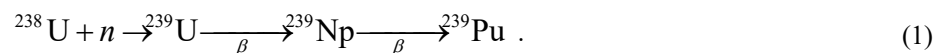
In this case, the concentration of ^{239}Pu in the medium N_{Pu} is determined by two opposite processes: production and burnup, and can be described by the following equation:

$$\frac{dN_{Pu}}{dt} = n\, v_n \left(\sigma_{a8} N_8 - \left(\sigma_a + \sigma_f \right)_{Pu} N_{Pu} \right), \tag{2}$$

where n and v_n are the concentration and velocity of neutrons, σ_{a8} is the neutron absorption cross-section for ^{238}U, N_8 is the concentration of ^{238}U nuclei, $\sigma_{a,f}$ are the absorption and fission cross-sections for ^{239}Pu nuclei and N_{Pu} is the ^{239}Pu concentration. Basing on this equation, Feoktistov introduced a parameter of the equilibrium plutonium concentration $\tilde{N}_{Pu}$, assuming the change of the ^{239}Pu concentration in (2) to be zero:

$$\tilde{N}_{Pu} = \frac{\sigma_{a8}}{\left(\sigma_a + \sigma_f\right)_{Pu}} N_8 \; .$$

(3)

The physical meaning of this parameter is quite simple: it is such a concentration of plutonium to which the system approaches when it is left to itself under a persistent neutron irradiation.

Another important parameter of the problem is the critical concentration of ^{239}Pu in this medium N_c, which provides a constant value of the neutron concentration in the system or, in other words, this means that the so-called neutron multiplication coefficient k_{eff} is equal to unity. This parameter can be obtained from the neutron balance equation:

$$\frac{dn}{dt} = n\, v_n \left((v-1)\sigma_{fPu} N_{Pu} - \sum_i \sigma_{ai} N_i \right),$$

(4)

by equating the derivative dn/dt to zero. Here, v is the number of fission neutrons. Thus, the expression for the critical concentration of plutonium N_c is

$$N_c = \frac{\sum_i \sigma_{ai} N_i}{(v-1)\sigma_{fPu}}$$

(5)

If $N_{Pu} = N_c$, it means that the system stays in the exact critical state with constant neutron concentration and energy production as well. If $N_{Pu} > N_c$, then the system will be above-critical ($k_{\text{eff}} > 1$) and the chain reaction will occur, while the neutron concentration will increase exponentially. Otherwise, at $N_{Pu} < N_c$, the system will be subcritical and the neutron flux will decrease quickly without an external neutron source.

Since expressions (3) and (5) for the parameters $\tilde{N}_{Pu}$ and N_c show different dependences on the cross sections and nuclide concentrations, in principle, various realizations of the relation between these two parameters are possible.

If $\tilde{N}_{Pu} < N_c$ is fulfilled, that takes place, in particular, for the nuclear system with the thermal neutron spectrum [2, 3], then the critical state cannot be achieved without an external neutron source, and a self-sustained nuclear burning process is impossible.

In case of the fast neutrons, we have $\tilde{N}_{Pu} > N_c$, which creates conditions for the chain reaction being sustained. In a literal sense, it means that the plutonium concentration tends to its equilibrium value exceeding the critical one. This fact looks dangerous as it means that the reactor might go into an explosive chain reaction. But at the same time a neutron lifetime in the core ($\tau = l/v_n \sim 10^{-8}\,s$) is much smaller than the time of plutonium creation (2.4 days), thus an entire excess plutonium will be burned out before the reactor goes into an "explosive" state. It is just this property which is usually referred to as an intrinsic safety.

Further in his articles, Feoktistov considers equations of the neutron diffusion and fuel burn-up describing the simplest variant of reactor which consists of ^{239}Pu, ^{238}U, and only one intermediate nuclide ^{239}U, which effectively represents the two intermediate nuclides in (1). This set of equations is considered in the one-dimensional geometry and in the one neutron-energy group approximation under the assumption that the absorption cross-section values are equal for all involved nuclides, including the fission products, which made it possible to reduce all needed neutron reaction cross-sections to only two material constants, namely, to $\tilde{N}_{Pu}$ and N_c. Then, assuming that the NBW mode exists, and making the corresponding Galilean transformation ($x' = x + Vt$), i.e., passing into the co-moving frame of reference moving with the wave velocity V, these equations were solved for the case of the steady-state nuclear burning wave moving along the considered infinite ^{238}U medium with a constant velocity. This allowed Feoktistov to find the solution in a self-similar form depending only on the space variable x' in the co-moving frame. From this consideration, Feoktistov described the main features of the steady-state NBW regime, and one of the largest achievements of this work was the formulation of a simple criterion $\tilde{N}_{Pu} > N_c$, which provides the feasibility of functioning of a NBW reactor.

Further it was pointed out that it could be also possible to implement such a reactor for the ^{232}Th $-$ ^{233}U fuel cycle. The problems of the huge thermal energy release that were mentioned by Feoktistov are still actual.

In the context of discussing the Feoktistov approach, it is worth to mention the work [4] by V. Pilipenko et al., in which the NBW mode was studied in the framework of the Feoktistov model on the basis of both the analytical analysis in the steady-state-solution approach, which was described in detail, and of the simulation of the initiation and evolution of the NBW by numerically solving the non-stationary problem for the set of Feoktistov's equations. In particular, a

consideration was given to the NBW realization with the use of an external neutron source, accompanying and irradiating the moving nuclear burning area, under the conditions when the NBW mode would be impossible without this source.

Goldin's and Anistratov's approach for numerical calculations

Goldin and Anistratov [5, 6] further developed Feoktistov's approach trying to solve numerically an evolutionary problem. In their work, they used 16 fissile isotopes and three groups of fission products. They also take into account the presence of coolant and structural materials in the fast reactor core. To describe the neutron processes in the reactor they used the neutron transport, neutron kinetics and fuel-burnup equations. In their approach, the non-stationary equation of neutron transport was considered in the one-group diffusion approximation. The one-group constants were calculated using an averaging spectrum function derived from solving the multi-group homogenous model for initial stationary reactor assembly.

To describe the reactor criticality, it is convenient to use the reactivity $\rho = (k_{eff} - 1)/k_{eff}$ or the reactor time parameter λ. The parameter λ is introduced into the equations by assuming the exponential dependence of the fluxes on time:

$$\phi(\vec{r}, t) = \phi(\vec{r}) e^{\lambda t} \tag{6}$$

By using this expression in the non-stationary multi-group and effective one-group set of diffusion equations, while taking into account the delayed neutrons, it is possible to get equations for the determination of λ, group scalar and vector fluxes. It is also possible to get the reactor time constant from solving the non-stationary transport and kinetics equations:

$$\lambda = \frac{d}{dt}\left(\ln\left(\int_G \psi \, d\vec{r} \right) \right), \tag{7}$$

here G is the solution region of the problem.

Goldin and Anistratov solved the above-mentioned equations using numerical calculations. The results show, that such a type of reactor is stable against considerable perturbations. According to the claim of the authors, the wave will be propagating during one year, after which the wave will start to decay. It should be mentioned, that these results were obtained without recalculating the averaged one-group cross-sections with the change of the space-energy distribution of the neutron flux.

Teller's Monte Carlo simulations calculations

Edward Teller [7, 8] with his team used Monte-Carlo-method based calculations to simulate the neutron-induced reactions and neutron transport in the fast reactor operating in the mode they called as a nuclear deflagration wave in their work. In their work, they used TART95 program package for modeling processes occurring in this reactor. In the initial assembly, the fuel in the main region of the reactor core was composed of ^{232}Th, while in the ignition region, where the nuclear burning was initiated, it was 10% enriched by ^{235}U. For the simulation, the TART95 mode with 175 neutron-energy groups was used. In the calculations, the presence of several other nuclides was also taken into account, representing actinides, construction materials, coolant, fission products and neutronic poisons.

The authors of the paper claimed some results based on their simulation. It was found that the ^{232}Th fuel burned well with possible generation of power around 1 GW in the case of the fuel cylinder of diameter less than 1 meter. The fuel burnup can be achieved in the range from 10% to 50% (which confirms Feoktistov's predictions). There is possibility to make NBW-reactor thermostatic by internal physics. They proposed also a scheme of automatic thermostatic and reactor power control by using ^{6}Li as a neutron absorber in the core. Their simulation predicts a relatively small total mass (< 0.1 ton) of the fissile material in the ignition zone.

In general, their work showed quite promising results for the considered NBW-reactor.

Sekimoto's CANDLE burnup strategy

The work performed in the Tokyo Institute of Technology by Hiroshi Sekimoto and his team [9, 10] is directed toward study of the NBW reactor. In their works it is called CANDLE as the acronym standing for "Constant Axial shape of Neutron flux, nuclide densities and power shape During Life of Energy production". Like Feoktistov, the Sekimoto group used the Galilean transformation $z' = z + Vt$ to the accompanying co-moving frame to consider steady-state solutions in the form of the NBW for the stationary neutron balance (diffusion) equation and the set of nuclide balance equations, describing the system under consideration. For solving these equations, an iteration procedure was proposed. To find the optimal velocity V of movement of the nuclear burning region, in the course of these iterations Sekimoto used the following iteration formula:

$$V^{(i+1)} = V^{(i)}V^{(i-1)} \frac{\Delta z_C^{(i)} - \Delta z_C^{(i-1)}}{\Delta z_C^{(i)}V^{(i)} - \Delta z_C^{(i-1)}V^{(i-1)}} \tag{8}$$

Here, $\Delta z_C^{(i)} = z_C^{(i)} - z_C^{(i-1)}$ is the shift of the neutron flux distribution center during successive iterations. This scheme required a good initial guess of the $V^{(1)}$ and $V^{(2)}$ values. The iterations were performed until the distributions of the calculated neutron flux and nuclide densities stopped to move along z-axis.

The numerical calculations for solving the obtained equations were performed using 21-group approximation. The needed cross-sections were taken from the JENDL-3.2 library. The nuclide transformation chains comprised 20 fissile nuclides and 66 fission products nuclides. The fertile fuel in this reactor was [238]U and the reactor had the cylindrical geometry with 8 meters in length and with the radius of 2 meters. The found neutron flux was normalized to have 3 GW power output.

As a result of the simulations, a steady-state self-similar neutron distribution was shown to be moving at the velocity of 4 cm/yr. The burnup depth in the spent fuel behind the NBW was around 40%, which is much higher than in traditional reactors. This work is important since it showed the possibility of the NBW implementation in the [238]U fuel basing on the fairly realistic theoretical model. It is also important to note that the Tokyo group used two-dimensional models and wide range of nuclides.

In a large number of subsequent works based on the approach described above, Sekimoto with co-authors considered the possibility of various options for implementing the CANDLE burnup strategy by varying the use of different coolants (Na, Pb, Pb-Bi eutectic, gas), sizes and compositions of the core, reactor power, and other parameters. However, since the calculation scheme which they use in these works is based on the self-similar solution to the problem, it is impossible to study transient processes in such a reactor and to study the stability of the NBW mode within the framework of this mathematical approach.

Hugo van Dam analytical considerations and its modifying by Chen and Maschek

An original model of the NBW reactor was developed by Hugo van Dam in papers [11, 12], where he called this mode as the criticality wave. In his work, the set of several fuel burnup equations was replaced by the effective burnup function $k_\infty(\psi)$ and the feedback coefficient γ as an arbitrary parameter. These substitutions are then included in the neutron balance equation. To get analytical solutions, Hugo van Dam also considered a quasistatic approximation, which is possible due to the fact that the neutron diffusion occurs much faster than the process of propagation of the criticality wave. Using the Galilean transformation of coordinates $\xi = x + Vt$, he obtains the following equation for the scalar neutron flux $\phi(\xi)$:

$$L_0^2 \frac{d^2\phi}{d\xi^2} + \left[k_\infty(\psi) - 1 + \gamma\phi \right]\phi = 0 \tag{9}$$

where ψ is the neutron fluence and L_0 is the diffusion length.

By selecting the burnup function in a simple (parabolic) form, which is close to the real one, and certain feedback coefficient values, it is possible to obtain analytical solutions of the neutron balance equation. Despite the seeming simplicity of this model, it was able to predict some characteristics of the behavior of the NBW reactor.

Results of the analytical model solution show that the burning wave can exist only in the case of a negative feedback coefficient and when the following ignition condition is fulfilled:

$$2k_{max} + k_0 > 3 \tag{10}$$

Here k_{max} and k_0 are the maximum and initial values of the chosen burnup function. The velocity of such a wave is proportional to the maximum neutron flux density which is determined through the feedback coefficient and burnup function.

Hugo van Dam also performed numerical calculations for the developed model. This part of the work was done to determine the burning wave ignition characteristics and to consider possibility of a power control in such a reactor. It was shown that an external neutron source should have certain optimal strength and duration to initiate a self-sustained wave propagation. The power control is possible by changing the feedback coefficient value. Choosing different burnup function gives different results for the total fuel burnout and wave velocity.

In the work of X.-N. Chen and W. Maschek [13] this approach was modified by means of using an original perturbation method and the radial buckling approximation, that gave them an opportunity to reduce the initially three-dimensional problem to a one-dimensional one taking into account a transverse neutron leakage. Later in [14] they used

this calculation scheme for description of the pebble-bed type reactor, in which, de facto, the fuel moves with the NBW velocity through a stationary reactor (see also Sekimoto's book [10]). Such a concept of "standing burning wave" is a full analogue of the "running" NBW from the physical point of view, but may have some constructive advantages for its practical realization.

Khotyayintsev et al. NBW velocity study

In works [15, 16] by Khotyayintsev et. al., behaviour of the NBW velocity, as an important characteristic of the NBW mode, was studied depending on a number of parameters of the reactor model in the framework of a planar one-dimensional model, basing on the neutron diffusion equation together with the equations of burn-up of the U-Pu fuel components including 9 nuclides as well as the fission products in the one-group approximation. A possibility of burning out of a part of the fission products was also admitted. The authors also studied the influence of a temperature feedback of not specified origin in the simplest model form by including a corresponding term with an arbitrary thermal feedback coefficient in the diffusion equation. Analogously to the Feoktistov approach, the solution of this set of equations was sought in the form of a steady-state wave moving with a constant velocity along a reactor of infinite length.

According to the aforesaid, the authors presented the neutron diffusion equation in the following general dimensionless form:

$$\frac{d^2\phi}{dz^2} + g \cdot \phi = 0, \quad g = \sum_i c_i N_i - p + \gamma w \phi \left(\sum_i c_{ai} N_i + p \right) \tag{11}$$

Here N_i are the dimensionless nuclear densities that obey the fuel burn-up equations, c_i and c_{ai} are the dimensionless coefficients that depend on the corresponding microscopic absorption and fission cross sections, w is the dimensionless NBW velocity, p is the effective absorber density which includes the absorption by non-fuel nuclides and, if allowed for, the effect of transverse neutron leakage, γ is the phenomenological thermal feedback parameter. By integrating the Eq. (11), the authors studied the conditions for existence of a stationary NBW solution. Numerical calculations with certain values of the problem parameters, allowed authors to solve the diffusion equation along with the burn-up equations and get distributions of the flux and nuclide concentrations in the wave. The authors also proposed and used an analytical approach for obtaining the solutions of the steady-state NBW type basing on the method of successive approximations in which the wave velocity w was considered as a small parameter. This approach allowed them to derive analytical expressions for the dependence of the NBW velocity on the problem parameters, including the arbitrary parameters p and γ.

From the obtained calculation results, the authors performed a comparison between feedback parameters caused by the thermal and fuel burn-up effects. An interesting result was derived at low NBW velocity values, where authors' calculations showed a bifurcation of the velocity dependence at the same control parameter, which authors attributed to the effect of [241]Pu instability. However, only the upper branch of the velocity dependence turned out to have a physical meaning, which indicated existence of a small but finite minimum value of the velocity.

Fomin et al. non-stationary solution of the NBW problem

The work performed by the Kharkiv group [17-25] was aimed at the study of non-stationary processes occurring in the fast reactor of cylindrical form with two initial homogeneous axial zones (the ignition and breeding ones) at the stages of the NBW initiation and its propagation along the reactor axis in the framework of an original deterministic approach, developed by the authors. This approach is based on numerically solving the non-stationary equations of neutron diffusion in the reactor medium together with the burnup equations for fuel components, which include 10 nuclides, and with the nuclear kinetics equations for the delayed neutron precursors with using realistic nuclear constants and cross sections. The authors have developed original packages of computer programs to perform numerical calculations for solving this non-stationary evolution problem. The needed realistic nuclear data were obtained from the BNAB Nuclear Data Library [26, 27] in the 26 neutron-energy group approximation. The fuel in the breeding zone is composed of the fertile [238]U (the variants with [232]Th fuel and the mixed of U–Th fuel were also considered), the fuel in the ignition zone consists of [238]U enriched by 10% of [239]Pu.

First the authors used a simplified model [17–20], where the transverse neutron leakage was either neglected [17, 18] or it was described by employing the radial buckling approximation [19, 20]. These calculations were performed in the so-called effective multigroup diffusion approximation, where the problem was reduced to a non-stationary one-group problem with making use of effective neutron-nucleus cross-sections averaged by the local neutron spectra found from the corresponding stationary multigroup criticality problem for the current time moment, which allows one to effectively take into account the changes in the cross sections according to variations of the energy-space distribution of the neutron flux. According to this approach, it is possible to write down the one-group non-stationary diffusion equation using the radial buckling concept taking into account delayed neutrons in the following form:

$$\frac{1}{v_n}\frac{\partial \Phi}{\partial t} - \frac{\partial}{\partial z}D\frac{\partial \Phi}{\partial z} + DB_r^2\Phi + \Sigma_a\Phi - \left(1-\overline{\beta}\right)\left(\nu_f\Sigma_f\right)\Phi = \sum_i\sum_l\lambda_l^i C_l^i \qquad (12)$$

where v_n is the neutron velocity, Φ is the scalar neutron flux, Σ_f and Σ_a are effective macroscopic absorption and fission cross-sections, $D = 1/3\Sigma_{tr}$ is the diffusion coefficient, ν_f is the mean number of neutrons produced per nucleus fission, $\overline{\beta}$ is the effective fraction of delayed neutrons, C_l^i and λ_l^i are the concentration and decay constant of precursor nuclei of the i-th group for the l-th fissile nuclide.

The important results of these studies are that they proved the feasibility of initiating and using the NBW mode in the nuclear reactor with the fuel of the U–Pu cycle, as well as revealed a number of essential details of the NBW evolution course, in particular the dependence of the NBW velocity on the radius of the reactor core was studied and a critical radius at which the wave cannot propagate was found. However, the results obtained for the reactor based on the [232]Th fuel showed serious difficulties in implementing the NBW mode, which had suggested appropriateness of further consideration of variants of the NBW reactor with mixed fuel composed of both with [238]U and [232]Th at roughly equal concentrations.

The shortcomings of using the radial buckling is that it gives an approximate allowance for the radial neutron leakage and ignores the effects of radial non-uniformity of the burnup of fuel components. Moreover, it does not allow one to describe reactor systems with any radial inhomogeneity, for example, in the presence of the radial neutron reflector, and in these cases it is necessary to consider the exact two-dimensional (2D) cylindrical problem of neutron transport in the reactor under discussion. Such a 2D problem with using the exact 26 neutron-energy groups approach has been further considered by the authors [21] for a simple cylindrical reactor model with a single radial zone without the radial reflector. The comparison between the results of calculations in these two approaches [16, 17] and [18] has shown that the simplified calculations with the radial buckling and effective multigroup approximation give a reasonable qualitative description of the NBW evolution but with some quantitative discrepancies with the exact 2D multigroup approach [21]. However, the calculations in the exact approach [21] are rather time-consuming and require much more computational resources. For this reason, in the works [22–25] the authors used the simplified approach, similar to that of papers [19, 20], for further studying different issues concerning the NBW initiation and propagation in the cylindrical reactor variants with the metal fuel of both U-Pu and mixed Th-U-Pu fuel cycle. In these works, they analyzed different transient processes in the NBW reactor and investigated the NBW mode stability (see [24]). The used non-stationary approach allowed Fomin's group to study the startup behaviour of the NBW reactor and the conditions for realizing a "smooth" startup with parameters acceptable from the practical point of view [23, 25], which is an important problem. Besides, the authors studied the features of processes of the forced temporary shutdown of the NBW reactor and further restarting the NBW mode [25].

Study of standing NBW by Yu. Leleko, V. Gann, and A. Gann

In the papers of Yu. Leleko, V. Gann, A. Gann [28, 29] the concept of the nuclear burning standing wave (NBSW) in the neutron multiplication medium is considered. From the point of view of the physics of neutron-nucleus processes, this concept is analogous to Feoktistov's nuclear burning wave, in which instead of the self-sustained process of the NBW propagation in the stationary neutron-multiplication medium (fertile [238]U), the fertile material is considered to be moving with the NBW propagation velocity, so that the active burning area were not moving relative to the reactor vessel. From the mathematical point of view, the only difference is in the transition from the rest frame to the frame which moves with the NBW velocity. In the judgment of the authors of those papers, such a change can essentially simplify the design of reactor as compared to the case of the moving active area in the classical NBW approach. Additionally, it is assumed that slightly changing the velocity of the "fresh" fuel movement, it could be possible to regulate the fuel burnup depth.

A significant difference between the NBSW concept considered in the papers [28, 29] and the self-sustained NBW propagation process, where the need of external control of the reactor reactivity is absent, is the fundamental need for such control in the case of NBSW.

In the papers [28, 29] the implementation of the NBSW concept is considered in both cylindrical and spherical reactors. In the first case, the NBW should "move" in the radial direction from the cylinder axis, and the fuel ([238]U) moves in the opposite direction, i.e. to the cylinder center, where the spent fuel is continuously being removed from reactor [28]. In the case of spherical geometry, the NBW is to be moving from the center of the sphere to the outside, and the fuel moves from periphery to the center of the spherical reactor, where it is being continuously removed [29]. If the speed of the fuel movement to the center is precisely equal to the velocity of the NBW propagation, we have the NBSW.

In its cylindrical variant, this concept is close to the "standing wave" concept with periodical "shuffling" of fuel assemblies, which was proposed by "Terra Power" [30]. The main difference between them is that in the variant of the reactor from [28] the supply of the fuel is considered to be continuous, while in [30] to shuffle the fuel assemblies the reactor must be stopped.

The mathematical calculation model that was used in the works [28, 29] is based on the solving of the one-dimensional diffusion equation together with a maximally simplified set of the burnup equations for the fuel components (only four ones: ^{238}U, ^{239}Np, ^{239}Pu, and fission products). The transition from the variables of coordinate (radius) and time to the integral variable of fluence, allowed the authors of those papers to obtain an analytical expressions for the stationary approximation of the NBW, which can be used to analyze the dependence of the radial neutron distribution on the problem parameters. The performed analysis showed the possibility of the existence of the radial and cylindrical standing waves of nuclear burning for some parameters of considered systems.

In those papers, a comparison between results calculated with the analytical expressions and by numerical calculations of such a reactor with the MCNPX code was performed, which showed their quite good agreement. Such a powerful computation instrument as the MCNPX code, which is based on the Monte-Carlo method for the simulation of neutron-nucleus processes simulation in the three-dimensional geometry, has wide possibilities for taking into account the complex nuclide composition of the reactor core, including not only the extended nuclear transformation chain of fuel components, but also the presence of the coolant and construction materials in the core of the reactor. Unfortunately, in those papers there is no data about calculations for more realistic component compositions, which may sufficiently influence not only the numerical results, but also some of the conclusions of those papers.

In addition, we should mention one more feature of using the MCNPX code, which has been developed for modeling processes in reactors of the conventional type with the external reactivity control that is realized by using control rods. The matter is that when simulating with MCNPX, the reactor power is a parameter that is set externally and is kept constant automatically. At the same time, the power of the reactor operating in the steady-state NBW mode is an internal self-consistent parameter of the system, which is determined only by the initial composition of the system and its size.

CONCLUSIONS

This article provides an overview of a number of the most significant works on the problem of a nuclear burning wave reactor. Using various approaches and calculation models, in general, the authors of these studies have proven the fundamental possibility of implementing the NBW mode. The considered papers also investigate the most important characteristics of a nuclear burning wave, such as the propagation velocity, energy density, the power dependence on various parameters of the reactor, the problems of start-up, forced shutdown and restart of the reactor.

The reactor operating in the NBW mode has very attractive features, such as:

- the absence of the need for operational control of reactivity, which significantly reduces the role of the "human factor" in the reactor control;

- the property of "intrinsic safety", provided by the presence of a specific mechanism of negative reactivity feedback;

- the possibility of using natural or depleted uranium and thorium as the main fuel, capable of solving the problem of providing the Mankind with relatively cheap energy resources for thousands of years;

- the possibility of using the spent fuel of other reactors, which can help to solve the environmental problem of nuclear waste disposal;

- the absence of the need to reload the fuel throughout the entire reactor campaign reduces the risks of a theft of fissile materials during their transportation, helping to solve the problems of non-proliferation and prevention of nuclear terrorism;

- high fuel burnup depth, and, therefore, high efficiency of its use, will allow abandoning the organization of a closed fuel cycle and, thereby, significantly reduce the cost of nuclear energy of the future.

Therefore, if the NBW reactor is implemented, it will be a good candidate for a new generation of nuclear reactors.

However, there are also a number of unsolved problems that impede the speedy implementation of this concept. The main one among them is a high level of radiation damage in the fuel (swelling problem) and cladding materials. According to estimates, they significantly exceed the values that the present-day materials can withstand.

Nevertheless, the continuous progress in the development of new types of nuclear fuel and structural materials, which has been observed in recent years, as well as the search for unconventional constructive solutions (see, for example [30]) inspire confidence that the NBW reactor can become one of the main solutions to the growing world energy needs.

ORCID IDs
Maksym S. Malovytsia, https://orcid.org/0000-0002-8652-5806; **Alex S. Fomin**, https://orcid.org/0000-0002-3631-0604
Sergii P. Fomin, https://orcid.org/0000-0002-1495-0512

REFERENCES
[1]. S.M. Feinberg, in Record of Proceedings: *Session B-10, Int. Conf. on the Peaceful Uses for Atomic Energy*. (Geneva, Switzerland: United Nations, 1958), **9(**2), 447.
[2]. L.P. Feoktistov, Preprint IAE-4605/4. IAE, Moscow, (1988).
[3]. L.P. Feoktistov, Dokl. Akad. Nauk SSSR, **309**, 864 (1989).
[4]. V. Pilipenko, D. Belozorov, L. Davydov, N. Shul'ga, in CD: Proceedings of ICAPP 03, (Cordoba, Spain, May 4-7, 2003), Paper 3169.
[5]. E. Teller, M. Ishikawa, L. Wood, et al. In: *Int. Conf. on Emerging Nuclear Energy Systems*, 1 (1996).

[6]. E. Teller, Preprint UCRL-JC-129547, LLNL, Livermore, CA, USA (1997).

[7]. H. Sekimoto, K. Ryu, Y. Yoshimura, Nuclear Science and Engineering. **139**, 306–317 (2001), https://doi.org/10.13182/NSE01-01.

[8]. H. Sekimoto, *Light a CANDLE: New Burnup Strategy*, (Tokyo Institute of Technology, Tokyo, 2005).

[9]. V.Ya. Goldin and D. Yu. Anistratov, Mathematical Modelling, **7**, 12 (1995).

[10]. V.Ya. Goldin, N.V. Sosnin, Yu.V. Troshchiev, Dokl. Ros. Acad. Nauk., **358**, 747-748 (1998). (in Russian).

[11]. Hugo van Dam, Annals of Nuclear Energy, **27**, 1505 (2000), https://doi.org/10.1016/S0306-4549(00)00035-9.

[12]. Hugo van Dam, Annals of Nuclear Energy, **30**, 1495–1504 (2003), https://doi.org/10.1016/S0306-4549(03)00098-7.

[13]. X.-N. Chen, and W. Maschek, Annals of Nuclear Energy, **32**, 1377-1390 (2005). https://doi.org/10.1016/j.anucene.2005.01.012.

[14]. X.-N. Chen, E. Kiefhaber, and W. Maschek, Progress in Nuclear Energy. **50**, 219-224 (2008). https://doi.org/10.1016/j.pnucene.2007.11.064.

[15]. V.M. Khotyayintsev, V.M. Pavlovych, and O.M. Khotyayintseva, In: *Proceeding of Int. Conf. "Advances in Reactor Physics to Power the Nuclear Renaissance" (PHYSOR 2010)*, (Pittsburgh, PA, USA, 9–14 May 2010).

[16]. V.M. Khotyayintsev, A.V. Aksonov, O.M. Khotyayintseva, V.M. Pavlovych. V. Gulik, and A.H. Tkaczyk, Annals of Nuclear Energy. **85C**, 337 – 345 (2015). https://doi.org/10.1016/j.anucene.2015.04.044.

[17]. S. Fomin, Yu. Mel'nik, V. Pilipenko, and N. Shul'ga, Annals of Nuclear Energy. **32**, 1435 (2005). https://doi.org/10.1016/j.anucene.2005.04.001.

[18]. S. Fomin, Yu. Mel'nik, V. Pilipenko and N. Shul'ga, In: *Nuclear Science and Safety in Europe*, p. 239, Springer, the Netherlands (2006), https://doi.org/10.1007/978-1-4020-4965-1_20.

[19]. S. Fomin, Yu. Mel'nik, V. Pilipenko and N. Shul'ga, Problems of Atomic Science and Technology. Series: Nuclear Physics Investigations. **3**, 156 (2007), https://vant.kipt.kharkov.ua/TABFRAME_poisk_c.html

[20]. S. Fomin, Yu. Mel'nik, V. Pilipenko and N. Shul'ga, Progress in Nuclear Energy. **50**, 163 (2008), https://doi.org/10.1016/j.pnucene.2007.10.020.

[21]. S.P. Fomin, A.S. Fomin, Yu.P. Mel'nik, V.V. Pilipenko, N.F. Shul'ga, In CD: *Proc. of 1st Int. Conf. "Global 2009"* (Paris, France, 2009), Paper 9456.

[22]. S.P. Fomin, O.S Fomin., Yu.P. Mel'nik, V.V. Pilipenko, N.F. Shul'ga, Progress in Nuclear Energy. **53,** 800–805 (2011). https://doi.org/10.1016/j.pnucene.2011.05.004.

[23]. O.S. Fomin, S.P. Fomin, Yu.P. Mel'nik, V.V. Pilipenko, and N.F. Shul'ga, Journal of Kharkiv National University, physical series «Nuclei, Particles, Fields», **58**(2), 49–56 (2013), https://periodicals.karazin.ua/eejp/article/view/13512.

[24]. S.P. Fomin, A.S. Fomin, Yu.P. Mel'nik, V.V. Pilipenko, N.F. Shul'ga, in: Topical Issues in Fast Reactors and Related Fuel Cycles, (Proc. Conf. FR-13, Paris, 2013), IAEA, Vienna, 2014, Contributed Paper IAEA-CN-199-457, 10 p., http://www-pub.iaea.org/MTCD/Publications/PDF/SupplementaryMaterials/P1665CD/Track3_Safety.pdf.

[25]. O.S. Fomin, S.P. Fomin, Yu.P. Mel'nik, V.V. Pilipenko, N.F. Shul'ga, in: *Proc. of Int. Conf. "Global 2015"* (Paris, France, 2015), Paper 5254.

[26]. L.P. Abagyan, N.O. Bazazjanc, I.I. Bondarenko, and M.N. Nikolaev, *Group Constants for Calculations of Reactor and Shielding,* (Energoizdat, Moscow, 1981) pp. 231. (in Russian).

[27]. I.I. Bondarenko, et al. *Group Constants for Nuclear Reactor Calculations*. (Consultants Bureau Inc., New York, 1964).

[28]. Yu.Y. Leleko, V.V. Gann, A.V. Gann, Problems of Atomic Science and Technology. **2 (108)**, 138-143 (2017).

[29]. Yu.Y. Leleko, V.V. Gann, A.V. Gann, Problems of Atomic Science and Technology. **5 (123)**, 18-24 (2019).

[30]. J. Gilleland, R. Petroski, and K. Weaver, Engineering, **2**, 88–96 (2016), https://doi.org/10.1016/J.ENG.2016.01.024.

КОНЦЕПЦІЯ РЕАКТОРУ З ХВИЛЕЮ ЯДЕРНОГО ГОРІННЯ ТА ТЕОРЕТИЧНІ ПІДХОДИ, ЯКІ ЇЇ ОПИСУЮТЬ
Максим С. Маловиця[a], О.С. Фомін[b], Сергій П. Фомін[a,b]
[a]Харківський національний університет імені В.Н. Каразіна
м-н Свободи 4, Харків, Україна, 61022
[b]Національний науковий центр «Харківський фізико-технічний інститут»
вул. Академічна 1, Харків, Україна, 61108

Після двох великих аварій на атомних електростанціях у Чорнобилі (1986) та Фукусімі (2011) однією з головних вимог до ядерної енергетики стало забезпечення безпеки як діючих, так і нових реакторів четвертого покоління, що розробляються зараз. Однією з таких вимог є наявність механізму «внутрішньої безпеки», який робить неконтрольований розгін реактора неможливим ні при яких обставинах, причому, втілення такого механізму повинно бути забезпечене на рівні фізичних принципів, які закладені в конструкцію реактора. Наступною важливою проблемою ядерної енергетики є необхідність переходу на широкомасштабне використання реакторів-бридерів на швидких нейтронах, за допомогою яких можливо налаштувати розширене виробництво ядерного палива і, таким чином, вирішити проблему забезпечення людства відносно дешевою енергією на тисячі років. Крім того, не вирішеною на сьогодні проблемою є утилізація відпрацьованого ядерного палива, в складі якого є радіонукліди з великим періодом напіврозпаду, що становить довгострокову екологічну загрозу. Однією з перспективних концепцій реактора-бридера на швидких нейтронах, який здатен, у випадку реалізації, частково або навіть повністю вирішити проблеми ядерної енергетики, які були наведені вище, є реактор, що працює в режимі хвилі ядерного горіння, також відомий під назвами «Реактор на рухомій хвилі», CANDLE і деякими іншими. У цій роботі представлений короткий огляд основних теоретичних підходів, які використовуються для опису такого фізичного явища, як хвиля повільного ядерного горіння (дефлаграція) у середовищі, що мультиплікує нейтрони, яке початково складається з фертильного матеріалу урану-238 або торію-232. Проведений порівняльний аналіз можливостей різноманітних математичних моделей для опису цього явища, які побудовані як на детерміністичному підході (тобто розв'язанні рівняння транспорту нейтронів), так і моделей з використанням метода Монте-Карло. Обговорюються основні переваги швидкого реактора-бридера, що працює в режимі хвилі ядерного горіння, а також проблеми, які пов'язані з практичним втіленням концепції, яка розглядається.
КЛЮЧОВІ СЛОВА: ядерна енергетика, швидкий реактор, напрацювання та спалювання, хвиля ядерного горіння, реактор рухомої хвилі

КОНЦЕПЦИЯ РЕАКТОРА С ВОЛНОЙ ЯДЕРНОГО ГОРЕНИЯ
И ТЕОРЕТИЧЕСКИЕ ПОДХОДЫ, КОТОРЫЕ ЕЁ ОПИСЫВАЮТ

Максим С. Маловица[a], А.С. Фомин[b], Сергей П. Фомин[a,b]
[a]Харьковский национальный университет имени В.Н. Каразина
пл. Свободы 4, Харьков, Украина, 61022
[b]Национальный научный центр «Харьковский физико-технический институт»
ул. Академичная 1, Харьков, Украина, 61108

После двух крупных аварий на атомных электростанциях в Чернобыле (1986) и Фукусиме (2011) одним из главных требований к ядерной энергетике является обеспечение безопасности как действующих, так и разрабатываемых в настоящее время новых реакторов четвертого поколения. Одним из таких требований является наличие механизма так называемой «внутренней безопасности», который делает неконтролируемый разгон реактора невозможным ни при каких обстоятельствах, причем, осуществление такого механизма должно обеспечиваться на уровне физических принципов, заложенных в конструкцию реактора. Следующей важной проблемой ядерной энергетики является необходимость перехода на широкомасштабное использование реакторов-бридеров на быстрых нейтронах, с помощью которых можно наладить расширенное воспроизводство ядерного топлива и, тем самым, решить проблему обеспечения человечества относительно дешевой энергией на тысячи лет. Кроме того, нерешенной на сегодня проблемой является утилизация отработавшего ядерного топлива, в составе которого есть радионуклиды с большим периодом полураспада, представляющие собой долговременную экологическую угрозу. Одной из многообещающих концепций реактора-бридера на быстрых нейтронах, способного в случае реализации частично или даже полностью решить перечисленные выше проблемы ядерной энергетики, является реактор, работающий в режиме волны ядерного горения, известный также под названиями «Реактор бегущей волны», CANDLE и некоторыми другими. В настоящей работе представлен краткий обзор основных теоретических подходов, используемых для описания такого физического явления, как волна медленного ядерного горения (дефлаграция) в нейтроно-мультиплицирующей среде, изначально состоящей из фертильного материала урана-238 или тория-232. Проведен сравнительный анализ возможностей различных математических моделей для описания этого явления, основанных как на детерминистском подходе (т.е. решении уравнения транспорта нейтронов), так и моделей с использованием метода Монте Карло. Обсуждаются основные достоинства быстрого реактора-бридера, работающего в режиме волны ядерного горения, а также проблемы, связанные с практической реализацией рассматриваемой концепции.
КЛЮЧЕВЫЕ СЛОВА: ядерная энергетика, быстрый реактор, наработка и выгорание, волна ядерного горения, реактор бегущей волны

SIMULATION STUDY OF ENERGY RESOLUTION OF THE ELECTROMAGNETIC SHASHLYK CALORIMETER FOR DIFFERENT OF LAYERS AND ABSORBER COMBINATIONS

Oleg P. Gavrishchuk[a], Vladimir E. Kovtun[b,*], Tetiana V. Malykhina[b]

aJoint Institute for Nuclear Research (JINR),
6 Joliot-Curie St, Dubna, Moscow Region, 141980, Russia
bKharkiv V.N. Karazin National University
4, Svobody sq., 61022, Kharkiv, Ukraine
*Corresponding Author: kovtun@univer.kharkov.ua

The response simulation of an ideal KOPIO-type electromagnetic sampling calorimeter was carried out in the energy range of 50 MeV – 16 GeV using Geant4-10.6.0 toolkit. In this work, we obtained energy resolution parameters for prototypes of Shashlyk calorimeter modules (ECAL SPD) of the NICA collider SPD setup for different thicknesses of a lead absorber with different numbers of layers. The NICA scientific experiment provides a unique opportunity to study parton distributions and correlations in hadron structure when working with high-intensity polarized relativistic ion beams. The ECAL electromagnetic calorimeter is one of the key detectors of the SPD device. There are some preliminary requirements for an electromagnetic calorimeter, in particular, for energy resolution in the energy range from 50 MeV to 16 GeV. It has been shown in detail that a more accurate obtaining of stochastic as well as permanent coefficients acting as parameters of the energy resolution parameterization formula is possible when longitudinal energy leakages from the calorimeter tower are taken into account. Such leakages are always present even in small amounts. Thus, the energy resolution parameterization of an ideal sampling calorimeter with a good χ^2/ndf value is fitted with function of the type: $\frac{\sigma_E}{E} = \frac{a}{\sqrt{E}} \oplus b \oplus \left(p_1 \cdot \ln^1 E + p_2 \cdot \ln^2 E + p_2 \cdot \ln^3 E \right)$, where the logarithm $\ln E$ means $\ln \frac{E}{E_c}$, where E_c is the effective critical energy. Based on the results of detailed modeling, the dependence of these parameters on the number of calorimeter plates and absorber thicknesses was found. The approach is based on careful selection and analysis of the energy spectra obtained by modeling according to the χ-square criterion and an adequate choice of the approximation functions of the energy resolution. The methods proposed in this paper can be easily extended to other combinations of absorber-scintillator thicknesses.

KEY WORDS: sampling calorimeter, Shashlyk detector, electromagnetic calorimeter, Geant4 simulation

The NICA SPD experiment [1] provides a unique opportunity to study parton distributions and correlations in the structure of hadrons when working in beams of high-intensity polarized relativistic ions.

One of the key detectors of the SPD project is the $4 \cdot \pi$ electromagnetic calorimeter (ECAL), which consists of the central barrel part and two end-cap. The total weight of the electromagnetic calorimeter is about 120 tons. is that The energy resolution in the 50 MeV-16 GeV energy range should be at the level $5\%/\sqrt{E(GeV)}$. It is the main preliminary requirement for the ECAL SPD. As known [2], the electromagnetic calorimeter energy resolution depends on several factors [2], which can be varied and evaluated by the Monte Carlo method with the aim of further optimization:

- sampling fluctuation;
- longitudinal and lateral energy leakage due to limited module size;
- the effect of heterogeneity of the calorimeter module medium due the design features: holes for fibers, steel studs for coupler module, fibers etc;
- fiber attenuation length;
- inhomogeneous light collection in scintillator layer;
- inaccuracies in the dimensions of calorimeter parts due the manufacturing technological features in mass production;
- photo statistics;
- electronic noise.

The total energy resolution of the ideal electromagnetic calorimeter is usually parameterized by the (in quadrature) sum of the stochastic term a, due to fluctuations of the Poisson type, and constant term b, associated with systematic effects:

$$\frac{\sigma_E}{E} = \frac{a}{\sqrt{E}} \oplus b \qquad (1)$$

The parameter $a = \sqrt{a_1^2 + a_2^2}$ has statistical nature and represents a combination fluctuation sampling effects (a_1) and photo statistics fluctuations (a_2). In this paper we considered for the ideal calorimeter when fluctuations $a_2 = 0$.

The parameter b is associated with heterogeneous effects in medium of ECAL module which begins to dominate at high energies. Therefore, at high energies, the energy resolution is determined only by the magnitude of the constant term. The term b must be zero if we take into account only sampling of fluctuations. This is clearly insufficient and uninformative to study the features of even an ideal electromagnetic calorimeter.

The purpose of this work is the correct determination the parameter b for all energy range for Shashlyk ideal calorimeter. The good agreement on the χ^2 criterion will be after added (in quadrature) the energy leakage terms. In this case, the correct definition of the constant term is obtained for the prototypes of ECAL SPD modules. The dependence of the a, b terms from various combinations of absorber thicknesses Pb and number of plates L was obtained from the Monte-Carlo calorimeter simulation.

ECAL KOPIO MODULE CHARACTERISTICS

Proposed for as a prototype ECAL SPD [1] Shashlyk calorimeter based on the experience of various developments of the installation KOPIO [3] calorimeter module. This calorimeter is a lead-scintillator-type sandwich structure with a wavelength shifter (WLS) fiber. At first module KOPIO was designed and manufactured in Institute for Nuclear Research (Moscow) in 1991 for KOPIO (E865, BNL) [3, 4] experiment.

The module had experimental energy resolution $8\%/\sqrt{E(GeV)}$. The calorimeter worked for a long time in the experiment and showed good stability of the parameters. Good physical characteristics with low cost and understandable design made it attractive for many other experiments. In the future, similar calorimeters were used in PHENIX (RHIC, BNL) [5], HERA-B (DESY) [6] and other installations.

Subsequently for the purposes of the KOPIO experiment resolution improvement was required to $3\%/\sqrt{E(GeV)}$. This requirement led to the creation and development of new prototypes, testing in particle beams, the detailed Monte Carlo simulation. The new module prototype [7] in the 3×3 assembly tested on positrons and pions beam AGS BNL accelerator in the range $0.5 \div 2\ GeV/c$.

Monte Carlo simulations the optimal energy resolutions of the prototype KOPIO module and results of testing in particle beams are shown in Figure 1 [7, 8].
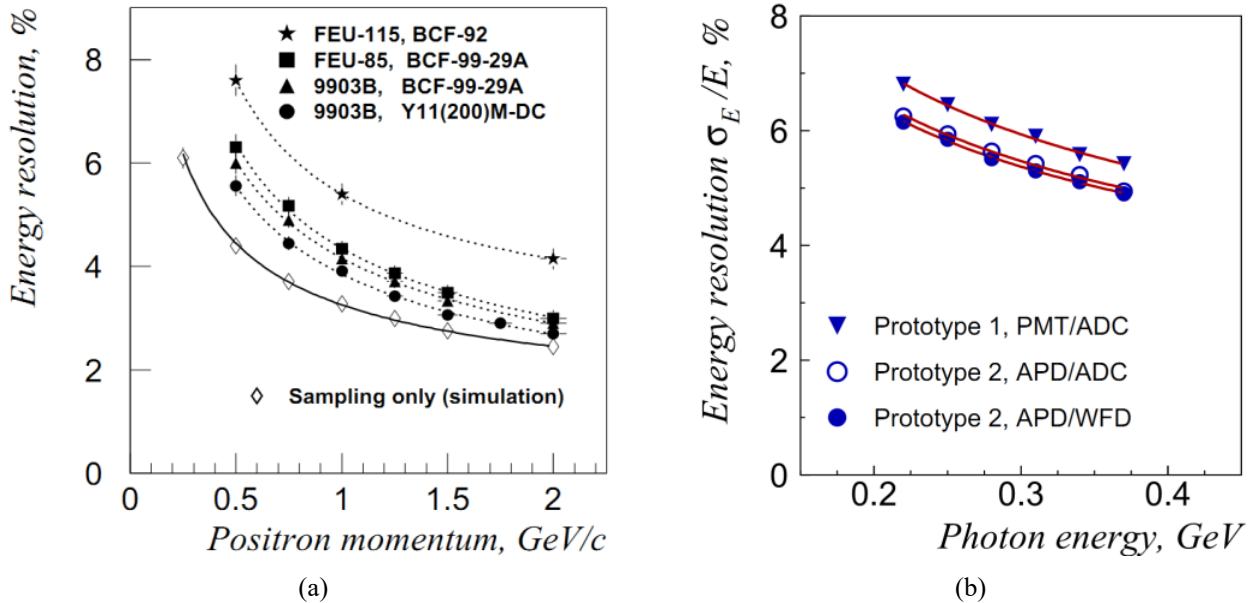
Figure 1. Test results KOPIO module prototypes: in particle beams (a) and computer simulation (b) by Geant3

An improved module prototype was developed and studied in detail in [8]. The final calorimeter energy resolution was obtained in the new design with best optical fibers and scintillator on the photon beam in the range of 50 - 1000 MeV.

$$\frac{\sigma_E}{E} = \frac{(2.74 \pm 0.05)\%}{\sqrt{E}} \oplus (1.96 \pm 0.1)\% \qquad (2)$$

Relatively large constant term (~2%) authors explained of the small radiation length equal to $15.9 X_0$, when X_0 – effective radiation length. Further it was supposed to improve the energy resolution by increasing the length of the module.

In works on improving the electromagnetic calorimeter parameters, the authors [7, 8], drew attention to the dependence of the constant term on energy. Using Geant3 computer simulation of the module parameters with 6000

layers showed the "ideal" resolution of the calorimeter (see Fig. 1.), which depended only the calorimeter sampling structure. The final module design had next parameters: D_{Pb}=0.275 mm, D_S=1.5 mm, L=300. Thus, it was not possible to improve the resolution due to the improvement of the calorimeter structure and the choice of fibers and scintillator with better parameters. In reality, the energy resolution was obtained $\sim 5\%/\sqrt{E(GeV)}$ on the beam.

In our opinion, formula (1), which was used by the developers of the KOPIO calorimeter, is not quite accurate, because the constant term, as we will show below, depends on energy. Formula (1) gives a good approximation of the energy resolution for small energy leakage from the module. Therefore, in real designs of calorimeters, the analysis of experimental data was not very accurate, and the desired resolution was not achieved. We illustrate (Fig. 2) the incorrectness of formula (1) in the following example. Take a very large number of layers $L = 3000$. Then, in this case, formula (1) gives good agreement with the simulation results ($\chi^2 / ndf = 1.2$). In the practical case of a small number of layers with $L = 140$ we have: $\chi^2 / ndf = 42.7$ and the application of formula (1) is incorrect. For comparison, the approximation of the same data is given by our refined formula (4).

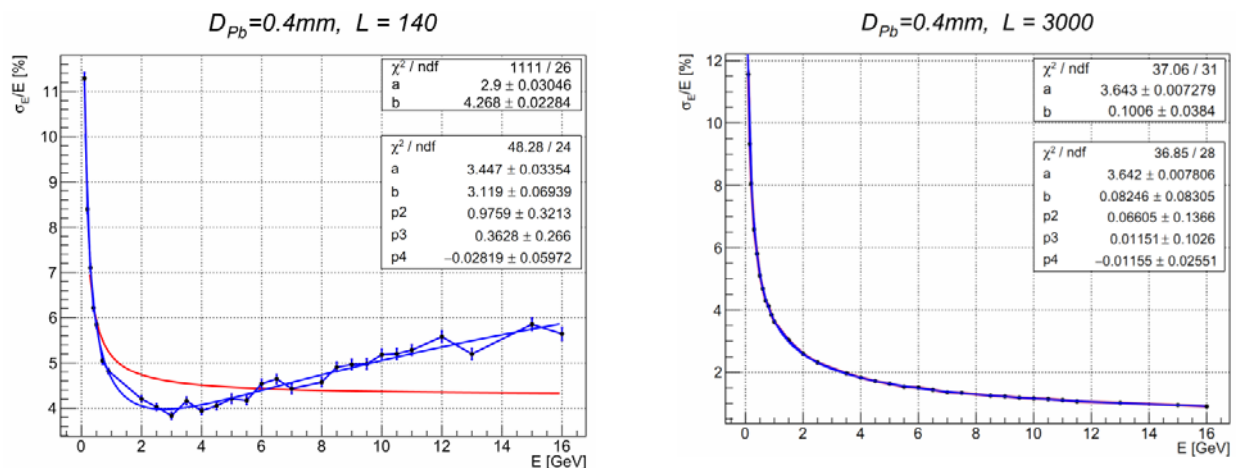
Figure 2. The approximations of the energy resolution curve for modules with L=140 (large leakage) and L=3000 (minor leakage)

For the purposes of solving physical problems at the SPD, it is desirable that ECAL have a high resolution in a wider energy range of 0.05 - 10 GeV than at the KOPIO. The addition of terms to formula (1) that describe explicitly longitudinal energy leakages allows making correct parameter estimates also in a wide energy range. The energy dependence associated with energy leakage is transferred to these additional terms and the constant term is really independent of energy. The chi-square test also performs well over a wide range of energies.

SIMULATION OF THE ELECTROMAGNETIC SAMPLING CALORIMETER

Computer simulation of the deposit energy in the Shashlyk calorimeter modules was performed using the Monte Carlo method using C++ and the Geant4 class library [9] version 10.6 (December 6, 2019) in the Linux Ubuntu operating system 18.04. The ROOT6 framework [10] was used to process large amounts of modeling data.

For computer simulation of absorbed energy in sandwich-calorimeter modules, the most suitable model of physical processes is QGSP_BERT [11, 12] for primary electrons with energies in the range from 50 MeV to 20 GeV.

The Monte Carlo counting speed and the accuracy of the results are significantly affected by simulation parameters that require a certain setting. One of them in the PhysicsList from Geant4 class library is cutting energy E_{cut}. If the particle energy value is lower than the threshold energy value, then the particle is considered stopped and is not monitored programmatically for most processes. In the PhysicsList Geant4 class, the threshold value is specified in units of length, and is converted into values in energy units for each particle and for each material included in the simulated instrument and described in the DetectorConstruction class.

The dependence of the simulated energy resolution of the Shashlyk calorimeter from E_{cut} parameter (length units) is shown in Fig. 3. The following module design was used: $D_{Pb} = 0.3\ mm$, $D_S = 1.5\ mm$, $L = 220$.

Thus, when the parameter E_{cut} changing from 10 μm to 1000 μm calorimeter response varies within 1%. We used the value $E_{cut} = 100\ \mu m$ in the simulation.

In this work, the so-called ideal calorimeter is studied in detail. That is, only sampling and longitudinal leaks are taken into account. Transverse leakage were excluded by the appropriate choice of module dimensions ($YZ = 300\ mm$).The response of the calorimeter during the passage of an electron along the X axis is proportional the total energy loss in all L layers of the scintillator.
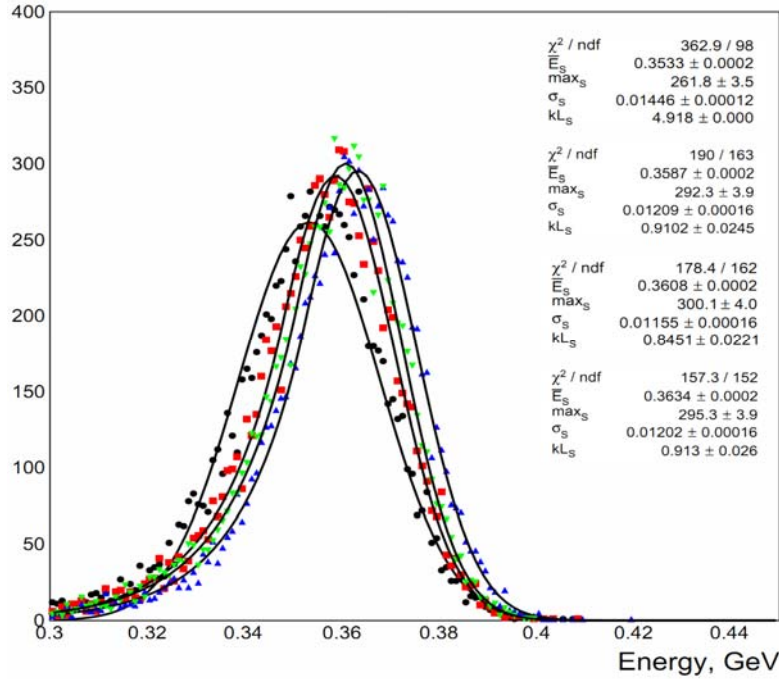
Figure 3. The calorimeter response depending on the Geant4 *cut* parameter. The beam energy E_0=1000 MeV.
■-10000 μm, ▲-1000 μm, ● -100 μm, ▼-10 μm.

For each energy point (beam energy E_0), the same number of events $N = 10^4$ was simulated.

OBTAINING PARAMETERS $\overline{E}_S, \sigma_S$ FROM ENERGY SPECTRUM

In the first step calorimeter response was simulated for a fixed incoming beam energy $E_0(i)[i = 1-60]$. for The beam energy points i unevenly distributed throughout the energy range from 50 MeV to 16 GeV. From the energy spectrum of the response calorimeter module by the ROOT the average energy $\overline{E}_S(i)$ and standard deviation $\sigma_S(i)$ values was obtained (index S means that the values refer to the scintillator). This procedure was equally performed for a different number of layers pairs: *L=30, 100, 120, 140, 160, 180, 200, 220, 240, 300, 500, 600,* and *3000.* A similar calculation of the calorimeter was made and a new set of pairs of points was obtained $\overline{E}_S(i, L)$ and $\sigma_S(i, L)$. These values used to obtain a detailed dependence on the calorimeter energy resolution σ_E / E from the beam energy $E_0(i)$.

Usually the calorimeter response in high-energy physics is approximated using the CBF function, first used Crystal Ball Collaboration [13, 14]. It has the following disadvantages: poor convergence and dependence on the obtained parameters from statistics. Therefore, the approximation was carried out by the same type function (3) proposed in [15], but with better convergence in the entire energy range and the independence of the obtained values from statistics and a smaller number of parameters.

$$f(E; \overline{E}_S, \sigma_S, kL_S, kH_S) = \begin{cases} e^{\frac{kL_S^2}{2} + kL_S \cdot \left(\frac{E - \overline{E}_S}{\sigma_S}\right)}, & for \quad \frac{E - \overline{E}_S}{\sigma_S} \leq -kL_S \\ e^{-\frac{1}{2}\left(\frac{E - \overline{E}_S}{\sigma_S}\right)^2}, & for \quad -kL_S < \frac{E - \overline{E}_S}{\sigma_S} \leq kH_S \\ e^{\frac{kH_S^2}{2} - kH_S \cdot \left(\frac{E - \overline{E}_S}{\sigma_S}\right)}, & for \quad kH_S < \frac{E - \overline{E}_S}{\sigma_S} \end{cases} \quad (3)$$

The parameter values in function (3) have a clear meaning. Parameters kL_S and kH_S show the boundary values at which the "cross linking" of the Gaussian peak with exponential "tails" occurs. Data sampling $\overline{E}_S$ and σ_S produced

in the range χ^2/NDF [0.8÷1.5]. Those energy points for which the value χ^2/ndf went beyond the specified range, did not participate in further consideration.
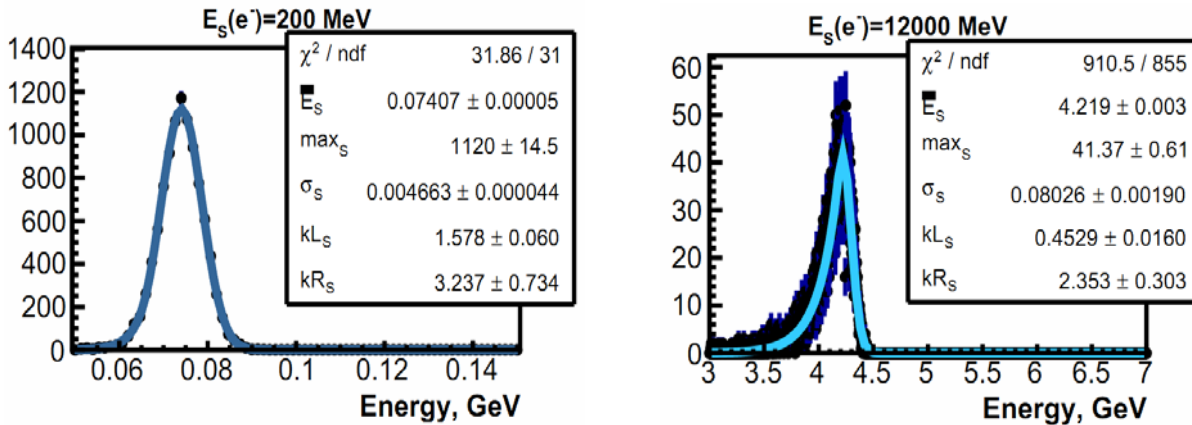

Figure 4. Examples of approximating the energy response of a calorimeter by function (3)

The approximation is performed on channels with filled bins in the all channel range from 0.0 to 16.0 GeV. Examples of good approximation results are shown in Fig. 4. In the entire range of energies of primary particles function (3) gives good convergence for χ^2. Sometimes the peak parameters are not determined (nan) during automated processing of a large number of spectra by ROOT. Such energy points do not take part in further analysis, but there are no more 10 %.

After simulation calorimeter responses the values $\overline{E}_S$ and σ_S are founded and energy resolution curves of an ideal calorimeter are built.

DETERMINATION ENERGY RESOLUTION COEFFICIENTS
FOR THE APPROXIMATION FUNCTION

For small number of plates the approximation function of the energy resolution of an ideal calorimeter has poor convergence according to the criterion χ^2, especially for modules with few plates. Also the poor convergence may occur in the following cases: a small number significant energy points $E_0(i)$, a narrow energy range. Accordingly, the constant term will also have different values depending on the energy range and the number of energy points $E_0(i)$.

We take into account longitudinal leakage in the energy resolution by adding additional terms to the quadratic sum of formula (1). The form these terms is proposed for leakage in [16].

The final formula that we will use to approximate the energy resolution of the calorimeter will take the form:

$$\frac{\sigma_E}{E} = \frac{a}{\sqrt{E}} \oplus b \oplus \left(p_1 \cdot \ln^1 E + p_2 \cdot \ln^2 E + p_2 \cdot \ln^3 E \right) \tag{4}$$

The designation $\ln E$ implies that the quantity $\ln \frac{E}{E_c}$ - dimensionless, when E_c – effective critical energy.

Table 1 shows the values χ^2/ndf for approximated functions of energy resolution according to formula (4) with longitudinal energy leakage from module. Families of energy resolution dependency curves $\frac{\sigma_E}{E}$ from beam energy E_0 shown in Fig. 5 – 7 for different absorber thicknesses D_{Pb}. Only the selected energy points according to the criterion χ^2 were used.

Data analysis (Table) shows that formula (4) works well in a wide range of layers numbers. In those rare cases, when χ^2/ndf is relatively large, the situation can be improved by increasing the number of simulated energy points $\overline{E}_S(i)$ and narrowing the energy range. Very big $\chi^2/ndf = 17.5$ for $L = 100$ means that necessary next logarithmic terms of a higher order to add in the formula (4). This indicates a very large energy leakage from the calorimeter module. From a physical point of view, we can assume that the calorimeter at such small radiation lengths ceases to work as a calorimeter. Most of the energy of an electromagnetic shower goes away in the form of leaks.

From a consideration on Fig. 5 families of curves, it can be seen that approximation (4) also well describes the energy resolution data for different D_{Pb} and L. It is important to note that in this approach, the constant term b will really not depend from energy of an ideal calorimeter.

Table.

Values χ^2 / ndf for approximated energy resolution functions

L	$D_{Pb} = 0.3$ mm	$D_{Pb} = 0.4$ mm	$D_{Pb} = 0.5$ mm
100	17.5	1.37	2.20
120	4.00	2.30	1.61
140	3.18	2.01	1.14
160	2.33	1.54	0.89
180	1.29	0.53	2.07
200	1.71	1.23	1.61
220	1.66	0.85	2.65
240	1.18	1.64	3.37
300	1.69	1.27	1.23
500	2.09	1.94	2.55
600	2.04	2.18	0.98
3000	1.96	1.05	1.32

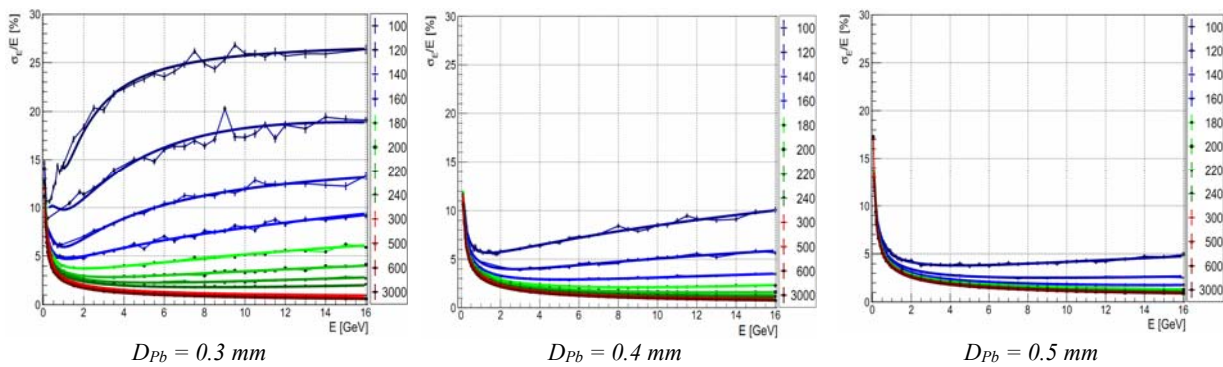$D_{Pb} = 0.3$ mm $D_{Pb} = 0.4$ mm $D_{Pb} = 0.5$ mm

Figure 5. Energy resolution of Shashlyk calorimeter depending of the layers number at different absorber thicknesses D_{Pb}

GETTING DEPENDENCE OF ECAL PARAMETERS FROM THE NUMBER
OF PLATES AND THEIR THICKNESS

From the families of energy resolution curves, we can obtain (Fig. 6) the dependences of the stochastic and constant terms from the number of plates and different absorber thicknesses. The family of curves of the stochastic term a was approximated by a linear function. The family of curves of the constant term b was approximated by a power function.
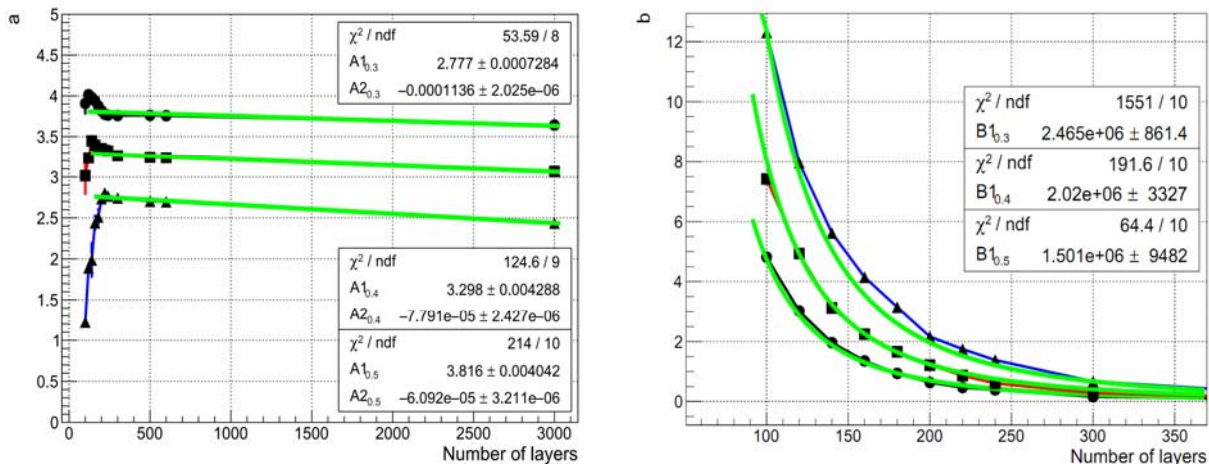
Figure 6. The dependences of the stochastic coefficient a (on left) and constant coefficient b (on right)
ideal calorimeter on the number of plates at different absorber thicknesses.
The curves designations: ▲ - $D_{Pb} = 0.3$ mm; ■ - $D_{Pb} = 0.4$ mm; ● - $D_{Pb} = 0.5$ mm.

With a small number of plates, their deviation from the linear function can be explained by the small number of energy points in the region 50 MeV – ~1 GeV after selecting pairs of points $\overline{E}_S(i,L)$ and $\sigma_S(i,L)$ according to selection criteria χ^2 / ndf and the inapplicability of the formula with such a small amount of substance.

Based on the results presented in Fig. 6, let's consider an improved prototype ECAL KOPIO [8] with module parameters: $D_{Pb} = 0.275\,mm$, $D_S = 1.5\,mm$, $L = 300$. We got the limiting estimates: $a = 2.5 \cdot \sqrt{GeV}\,\%$, $b = 0.75\%$ from the figures for an ideal KOPIO calorimeter. Thus, a resolution of 3% at 1 GeV cannot be reached. Our approach shows that longitudinal leakage with such a large number of plates do not lead to a decrease the constant term, and the magnitude $b = \sim 2\%$ refers to other reasons indicated above (in particular, the dependence on energy).

Similar estimates can be made for the module ECAL SPD [1]: $D_{Pb} = 0.3\,mm$, $D_{Sc} = 1.5\,mm$, $L = 220$. We have: $a = 2.5 \cdot \sqrt{GeV}\,\%$, $b = 1.75\%$ and the limit resolution at 1 GeV is value about 4.25%.

CONCLUSIONS

This paper shows that it is possible to obtain an ideal sampling calorimeter with a constant term which independent of energy by a computer simulation. The physical basis for this fact is the explicit accounting of calorimeter leakage. It was also shown that poor convergence χ^2 can be associated with an insufficient number of energy points and/or a narrow region of approximation of the energy resolution.

The basis of the used approach is a rigorous selection of electromagnetic showers obtained by the Monte Carlo method in a narrow range of χ^2/ndf values. The approximation function (3) was used for these purposes, which describes the asymmetric shape of the spectrum peak with account for leakage much better than the CBF function. The curve of energy resolution depends on energy is built on the basis of a set of selected pairs of points $\overline{E}_S$ and σ_S. The correct values of the stochastic and constant terms are obtained from approximation this curve by the new formula (4) with a good convergence. Families of curves are obtained for stochastic and constant terms for lead absorber thicknesses $D_{Pb} = 0.3, 0.4, 0.5\,mm$. It is possible to make estimates of a, b parameters for almost any sampling and the number of calorimeter module layers based on the analysis of these curves. ECAL SPD calorimeter parameters are obtained in comparison with its prototype KOPIO of the Shashlyk type calorimeter.

ORCID IDs

Vladimir E. Kovtun, https://orcid.org/0000-0001-8966-7685
Tetiana V. Malykhina, https://orcid.org/0000-0003-0035-2367

REFERENCES

[1] Conceptual design of the Spin Physics Detector, JINR, Dubna, 2018, http://spd.jinr.ru.
[2] A. Roy, et al., FERMILAB-PUB-17-186-E, 1-32 (2017).
[3] I-H. Chiang, et al., *AGS Experiment Proposal 926*, (1996).
[4] R. Appel, et al., Nucl. Instrum. Meth. A, **479**(2-3), 249-406 (2002), https://doi.org/10.1016/S0168-9002(01)00906-8.
[5] L. Aphecetche, et al., Nucl. Instrum. Meth. A, **499**(2-3), 521-536 (2003), https://doi.org/10.1016/S0168-9002(02)01954-X.
[6] G. Avoni, et al., Nucl. Instrum. Meth. A, **461**(1-3), 332-336 (2001), https://doi.org/10.1016/S0168-9002(00)01237-7.
[7] G.S. Atoian, et al., Nucl. Instrum. Meth. A, **531**(3), 467-480 (2004), https://doi.org/10.1016/j.nima.2004.05.094.
[8] G.S. Atoian, et al., Nucl. Instrum. Meth. A, **584**(2), 291-303 (2008), https://doi.org/10.1016/j.nima.2007.10.022.
[9] J. Allison et al., Nucl. Instrum. Meth. A, **835**(1), 186-225 (2016), https://doi.org/10.1016/j.nima.2016.06.125.
[10] ROOT6, https://root.cern.ch.
[11] Physics List Guide, 1-63, (2017), http://cern.ch/geant4-userdoc/UsersGuides/PhysicsListGuide/fo/PhysicsListGuide.pdf.
[12] Physics Reference Manual, 1-454, (2019), http://cern.ch/geant4-userdoc/UsersGuides/PhysicsReferenceManual/fo/PhysicsReferenceManual.pdf.
[13] M. Oreglia, *A study of the Reactions $\psi' \to \gamma\gamma\psi$*, *PhD thesis,* (SLAC, 1980).
[14] T. Skwarnicki, *A study of the radiative CASCADE transitions between the Upsilon-Prime and Upsilon resonances. PhD thesis*, (INP, Cracow, 1986).
[15] S. Das, https://arxiv.org/abs/1603.08591.
[16] G. Grindhammer, and S. Peters, https://arxiv.org/abs/hep-ex/0001020.

МОДЕЛЮВАННЯ ЕНЕРГЕТИЧНОЇ РОЗДІЛЬНОЇ ЗДАТНОСТІ SHASHLYK-КАЛОРИМЕТРУ ПРИ РІЗНИХ КОМБІНАЦІЯХ КІЛЬКОСТІ ПЛАСТИН ТА ТОВЩИН ПОГЛИНАЧА
О.П. Гаврищук[a], В.Є. Ковтун[b], Т.В. Малихіна[b]
[a]Об'єднаний інститут ядерних досліджень
вул. Жолио-Кюри, 6, 141980, м. Дубна, Московська обл., Росія
[b]Харківський національний університет імені В.Н. Каразіна
майдан Свободи, 4, 61022, Харків, Україна

Моделювання відгуку ідеального електромагнітного семплінг-калориметру типу KOPIO проведено у діапазоні енергій 50 МеВ – 16 ГеВ із використанням бібліотеки класів Geant4 версії 10.6.0. В роботі отримані параметри енергетичної роздільної здатності для прототипів модулів Shashlyk-калориметр (ECAL SPD) установки SPD коллайдера NICA для різної товщини свинцевого абсорбера при різних кількостях пластин. Науковий експеримент NICA надає унікальну можливість для вивчення партонних розподілів і кореляцій в структурі адронів при роботі з пучками високоінтенсивних поляризованих релятивістських іонів. Одним з ключових детекторів установки SPD є електромагнітний калориметр ECAL. Існують певні попередні вимоги до електромагнітного калориметру, зокрема, до енергетичної роздільної здатності у діапазоні енергій від

50 МеВ до 16 ГеВ. У роботі детально доведено, що більш точне отримання стохастичного, а особливо, константного коефіцієнтів у якості параметрів формули параметризації енергетичної роздільної здатності можливо при врахуванні поздовжніх витоків енергії з калориметру, які завжди присутні навіть у малої кількості. Таким чином, формула для апроксимації енергетичної роздільної здатності ідеального семплінг-калориметру з прийнятним значенням χ^2/ndf

набирає вигляду: $\frac{\sigma_E}{E} = \frac{a}{\sqrt{E}} \oplus b \oplus \left(p_1 \cdot \ln^1 E + p_2 \cdot \ln^2 E + p_2 \cdot \ln^3 E \right)$, де під знаком логарифма $\ln E$ мається на увазі величина

$\ln \frac{E}{E_c}$, де E_c - ефективна критична енергія За результатами детального моделювання знайдена залежність цих параметрів від числа пластин калориметру і товщини абсорбера. Підхід заснований на ретельному відборі і аналізі отриманих при моделюванні спектрів енергії згідно з критерієм χ-квадрат та адекватному виборі функцій апроксимації енергетичної роздільної здатності. Метод легко може бути розширений на інші комбінації товщини абсорбер-сцинтилятор.

КЛЮЧОВІ СЛОВА: семплінг-калориметр, Shashlyk-детектор, електромагнітний калориметр, Geant4 моделювання

МОДЕЛИРОВАНИЕ ЭНЕРГЕТИЧЕСКОГО РАЗРЕШЕНИЯ ЭЛЕКТРОМАГНИТНОГО SHASHLYK-КАЛОРИМЕТРА ПРИ РАЗЛИЧНЫХ КОМБИНАЦИЯХ КОЛИЧЕСТВА ПЛАСТИН И ТОЛЩИН ПОГЛОТИТЕЛЯ

О.П. Гаврищук[a], В.Е. Ковтун[b], Т.В. Малыхина[b]

[a]Объединенный институт ядерных исследований
ул. Жолио-Кюри, 6, 141980, г. Дубна, Московская обл., Россия
[b]Харьковский национальный университет имени В.Н. Каразина
майдан Свободы, 4, 61022, Харьков, Украина

Моделирование отклика идеального электромагнитного сэмплинг-калориметра типа KOPIO проведено в диапазоне энергий 50 МэВ –16 ГэВ с использованием библиотеки классов Geant4 версии 10.6.0. В работе получены параметры энергетического разрешения для прототипов модулей Shashlyk-калориметра (ECAL SPD) установки SPD коллайдера NICA [1] для разных толщин свинцового абсорбера при разных количествах пластин. Научный эксперимент NICA предоставляет уникальную возможность для изучения партонных распределений и корреляций в структуре адронов при работе с пучками высокоинтенсивных поляризованных релятивистских ионов. Одним из ключевых детекторов установки SPD является электромагнитный калориметр ECAL. Существуют определенные предварительные требования к электромагнитному калориметру, в частности, к энергетическому разрешению в диапазоне энергий от 50 МэВ до 16 ГэВ. В работе показано, что более точное получение стохастического, а особенно, константного коэффициентов в качестве параметров формулы параметризации энергетического разрешения возможно при учёте продольных утечек энергии из калориметра, которые всегда присутствуют даже в малых количествах. Таким образом, формула для аппроксимации энергетического разрешения идеального сэмплинг-калориметра с приемлемым значением χ^2/ndf принимает вид:

$\frac{\sigma_E}{E} = \frac{a}{\sqrt{E}} \oplus b \oplus \left(p_1 \cdot \ln^1 E + p_2 \cdot \ln^2 E + p_2 \cdot \ln^3 E \right)$, где под знаком логарифма $\ln E$ подразумевается величина $\ln \frac{E}{E_c}$, где E_c – эффективная критическая энергия. По результатам детального моделирования найдена зависимость этих параметров от числа пластин калориметра и толщин абсорбера. Подход основан на тщательном отборе и анализе получаемых при моделировании спектров энергии согласно критерию χ-квадрат и адекватном выборе функций аппроксимации энергетического разрешения. Метод легко может быть расширен на другие комбинации толщин абсорбер-сцинтиллятор.

КЛЮЧЕВЫЕ СЛОВА: сэмплинг калориметр, Shashlyk-детектор, электромагнитный калориметр, Geant4 моделирование

INFLUENCE OF LIQUIID QUENCHING ON PHASE COMPOSITION AND PROPERTIES OF Be-Si EUTECTIC ALLOY

Valerij F. Bashev*, **Sergey I. Ryabtsev,** **Oleksandr I. Kushnerov,**
Nataliya A. Kutseva, **Sergey N. Antropov**

Department of Experimental Physics, Oles Honchar Dnipro National University
72 Gagarin ave., Dnipro, 49010 Ukraine
*Corresponding Author: bashev_vf@ukr.net
Received May 10, 2020; accepted May 24, 2020

By the method of quenching from the liquid state (splat-quenching), it is first revealed the formation of mixture of metastable supersaturated substitutional solid solutions in the eutectic alloy Be-33at.% Si. Cast samples are obtained by pouring melt into a copper mold. High cooling rates during liquid quenching are achieved throw the well-known splat-cooling technique by spreading a drop of melt on the inner surface of a rapidly rotating, heat-conducting copper cylinder. The maximum cooling rates are estimated by the foil thickness. The melt cooling rates (up to 10^8K/s), used in the work, are sufficient to form amorphous phases in some eutectic alloys with similar phase diagrams, but it is found those rates are insufficient to obtain them in the Be-Si eutectic alloy. The X-ray diffraction analysis is carried out on a diffractometer in filtered Cobalt K_α radiation. Microhardness is measured on a micro-durometer at a load of 50 g. The electrical properties, namely the temperature dependences of relative electrical resistance, are studied by the traditional 4-probe method of heating in vacuum. The accuracy of determining the crystal lattice period of the alloy, taking into account extrapolation of the reflection angle by 90^0, is $\pm\, 3\cdot10^{-4}$ nm. It is found that even at extremely high rate of quenching from the melt, instead of the amorphous phase formation, the occurrence of two supersaturated substitutional solid solutions, based on Beryllium and Silicon, is revealed. This fact is established by the obtained dependences of their lattice periods values on the alloying element content. So, during the formation of metastable eutectic structure, a supersaturated with Beryllium solid solution of Silicon has period $a = 0.5416$ nm, and a supersaturated with Silicon solid solution of low-temperature hexagonal Beryllium has periods $a = 0.2298$ nm, $c = 0.3631$ nm. The positive role of the liquid quenching method in increasing the level of mechanical characteristics (microhardness and microstresses) in rapidly cooled Be-Si films is shown. It has been demonstrated that the difference in the atomic radii of the elements significantly affects the distortion of crystal lattices of the formed supersaturated solid solutions, and a significant value of microstresses (second-order stresses) in the Silicon lattice supersaturated with Beryllium is estimated, which, of course, leads to a significant increase in the microhardness, namely: there is an increase in microhardness in the Be-Si alloy under the conditions of applied method of quenching from the liquid state by more than 1.7 times compared to cast eutectic alloy and more than 6 times higher in comparison with the eutectoid cast Iron-Carbon alloy. The obtained polytherm of electrical resistance of the alloy under conditions of continuous heating in vacuum confirms the metastable nature of obtained new phases during quenching from the liquid state.

KEYWORDS: Splat-quenching, eutectic, highly supersaturated solid solution, microhardness, microstresses, temperature coefficient of resistance

Currently, the following approaches are used to obtain new metallic materials with improved characteristics: 1) applying of modern methods of fast crystallization with cooling rates from 10^6 K/s (liquid quenching) to 10^{12} K/s (vapor quenching) [1-4]; 2) evaluation of properties of the crystal lattices at the atomic level [5,6]; 3) the development of multicomponent high-entropy alloys [7,8]; 4) the use of practical experience in quenching methods improving [9].

The application of liquid quenching (LQ) method with cooling rates of up to 10^8 K/s allows one to obtain new metastable states in alloys, including highly supersaturated solid solutions (HSSS) and intermediate metastable phases, in particular, a solid amorphous state, with improved physical characteristics. When considering the effects that occur during the LQ, it is necessary to take into account the type of state diagrams of alloys. Alloys of the Be-Si system have so far been studied in the entire concentration range under standard crystallization conditions. The phase diagram of the Be-Si system is characterized by the presence of simple eutectic at 33 at.% Silicon, with eutectic temperature 1090^0C, and practically zero mutual solubility of elements in the solid state [10-12] at room temperature. A feature of cast Be-Si alloys is their significant brittleness, even with a small Silicon content in the alloy [10]. It should be noted that Beryllium alloys are currently receiving special attention since Beryllium has a promising combination of many physical characteristics: high specific strength, corrosion resistance, and low density. Therefore, Be-Si alloys in the form of thin films can be used in some modern branches of technology: for example, in X-ray technology as strong foils due to the presence of phases based on Beryllium and Silicon with distorted crystal lattices in the eutectic structure of the alloy due to supersaturation of solid solutions. Beryllium-based alloys are widely used as Beryllium windows in X-ray tubes, allowing to pass the X-rays coming out of the tube with a small loss in intensity and at the same time, due to its strength characteristics, maintain the necessary high vacuum in the X-ray tube. Therefore, the improved strength characteristics of the Be-Si LQ-alloy can contribute to a decrease in the thickness of protective foil with a simultaneous increase in the intensity of the rays emerging from the X-ray tube, and, consequently, to an increase in its working power.

In this work, we investigate the influence of the phase diagram type and the method of rapid quenching from melt on the features of the formation of metastable states and on the improvement of some physical properties, in particular, the microhardness of eutectic Be-Si alloy.

The Be–Si phase diagram is identical in appearance to a simple eutectic Au–Si phase diagram, in which the mutual solubility of elements at room temperature is also practically absent, however, the eutectic temperature is 720 K lower than the eutectic temperature in the Be–Si alloy.It should be noted that in the Au–Si eutectic alloy, along with the Pd–Si system, amorphous phases were first obtained by quenching from the liquid state [13]. Therefore, it is of scientific and practical interest to study also the influence of features of the eutectic-type state diagram on the propensity of alloys to form metastable states in them under the conditions of LQ.

MATERIALS AND METHODS

High cooling rates during LQ were achieved by the well-known splat-cooling technique by spreading a drop of melt on the inner surface of a rapidly rotating, heat-conducting copper cylinder. The maximum cooling rates estimated by the foil thickness were $\sim 10^8$ K/s [13,14]. The as-cast samples were obtained by pouring the melt into a copper mold. X-ray diffraction analysis (XRD) was carried out on a URS-2.0 diffractometer in filtered cobalt K_α radiation. Microhardness was measured on a PMT-3 microhardness meter at a load of 50 g. The electrical properties, namely the temperature coefficient of electrical resistance and the temperature dependence of electrical resistance were studied by the traditional 4-probe method of heating in vacuum. The accuracy of determining the period of the crystal lattice of the alloy, taking into account extrapolation of the reflection angle by 90^0, was $\pm 3 \cdot 10^{-4}$ nm.

RESULTS AND DISCUSSION

As a result of studying the effect of the LQ method on the tendency to form metastable states in a Be-Si eutectic alloy, it was found that even at extremely high (up to 10^8K/s) rate of quenching from the melt, in contrast to the Au-Si system, instead of the amorphous phase formation, the occurrence of two supersaturated substitutional solid solutions based on Beryllium and Silicon was recorded. This fact was established by the obtained dependences of the values of their lattice periods on the content of the alloying element. So, during the formation of a metastable eutectic structure, a supersaturated with Beryllium solid solution of Silicon has a period $a = 0.5416$ nm (the tabular value of the Silicon lattice period is $a = 0.5431$ nm), and a supersaturated with Silicon solid solution of low-temperature hexagonal Beryllium has periods $a = 0.2298$ nm, $c = 0.3631$ nm (tabular values of the periods of the Beryllium lattice [15] are respectively: $a = 0.2287$ nm and $c = 0.3583$ nm). Due to the absence in the literature of the established dependences on the influence of alloying elements on the periods of the crystal lattices of solid solutions of the substitution type in the Be-Si system, it is difficult to evaluate the composition of supersaturated solid solutions obtained during liquid crystal cooling.

Previously, numerous experiments have established criteria that contribute to the formation at LQ of amorphous phases in eutectic alloys, which, in particular, include the temperature criterion: the criterion of "deep eutectic". An analysis of this criterion showed that if for an Au–Si eutectic alloy, a drop in the liquidus temperature by 1 at.% of the alloying element for the left (on the Gold side) and right (on the Silicon side) branches of the phase diagram is 23K/at.% and 15 K/at.% respectively, then for the studied Be–Si eutectic alloy, this drop is respectively 6 K/at.% (from the Beryllium side) and 5 K /at.% (from the Silicon side). The lower slope of the liquidus lines for the Be-Si alloy and the higher temperature of eutectic reaction naturally lead to the realization of lower value of supercooling of this melt achieved at LQ, which, in turn, does not allow, due to the relatively high viscosity under the indicated temperature conditions of supercooled melt, transfer the Be-Si melt to a solid amorphous state at LQ. At the same time, the level of supercooling achieved was sufficient for the formation of a Be-Si eutectic alloy in the structure due to a change in the corresponding distribution coefficients at the crystallization front of two supersaturated substitutional solid solutions based on Silicon and Beryllium (the atomic radii of Silicon and Beryllium are respectively: $a = 0.117$ nm and $a = 0.113$ nm). The indicated difference in the atomic radii of elements, as it's turned out, significantly affects the distortion of crystal lattices of the formed supersaturated solids, for example, the magnitude of microstresses $\Delta a/a$ (second-order stresses) in the Silicon lattice supersaturated with Beryllium, estimated according to the proposed expression in the approximation method [16] ($\Delta a/a = \beta / 4 \cdot tg\Theta$, where β – is the integral half-width of diffraction line; Θ – is the angle of reflection from the line (531)), has a significant value which is equal to $\Delta a/a = 3.45 \cdot 10^{-3}$.This fact, of course, naturally leads to a significant increase in the microhardness (H_μ), so if for a cast eutectic alloy the value $H_\mu = 4100$ MPa, then for the Be-Si LQ-alloy this value already averages 6900 MPa, i.e. an increase in microhardness in this alloy is observed under the conditions of the applied LQ method by more than 1.7 (Fig.1). This makes it possible to classify the Be-Si LQ-alloy within the reduced microhardness H_μ/ρ (ρ – is the alloy density) to very hard metal alloys: for example, in a eutectoid cast Iron-Carbon alloy, such microhardness is more than 6 times lower.

The metastable nature of supersaturated solid solutions obtained is also confirmed by the results of the heat treatment when heated to 973 K, namely: the crystal lattice period of a supersaturated Silicon-based solid solution increases to 0.5422 nm due to its decay and, therefore, less supersaturation of Silicon lattice with Beryllium, and with a corresponding reduction in the degree of tension of Silicon lattice up to $\Delta a/a = 2.79 \cdot 10^{-3}$. Unfortunately, it is very difficult to obtain experimentally such dependencies of microstresses at large reflection angles for the lattice of a supersaturated solid solution based on Beryllium due to the low reflectivity of X-rays from Beryllium and "shading" of adjacent reflection lines from the Silicon lattice on the X-ray diffraction pattern.
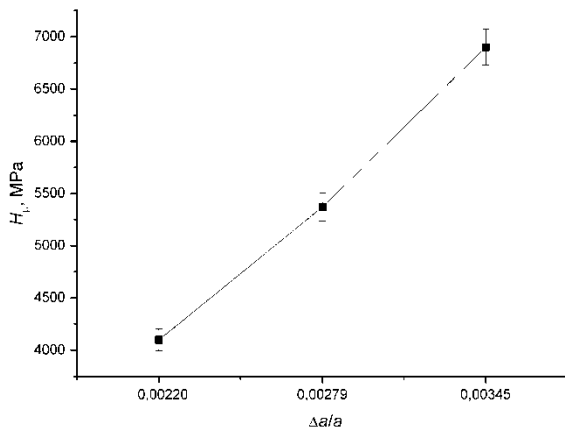
Figure 1. The dependence of microhardness value H_μ on magnitude of microstresses $\Delta a/a$
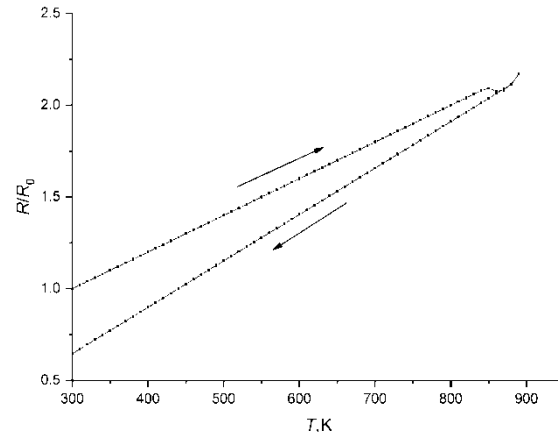

Figure 2. Temperature dependence of relative electrical resistance of the eutectic Be-Si LQ alloy

Additional confirmation of the metastable nature of phases obtained at LQ is the received temperature dependence of electrical resistance of the alloy under conditions of continuous heating in a vacuum (Fig.2). It can be seen that only at a temperature of 860 K, an inflection is observed, associated with the decomposition of a supersaturated Silicon-based solid solution, indicating a high temperature stability of the metastable state of the Be-Si alloy that appeared during the LQ. It should be noted that the temperature coefficient of resistance (TCR) of eutectic Be-Si LQ-alloy is characterized by a significant decrease: for example, if for cast Beryllium and Silicon samples it is $6.6 \cdot 10^{-3}$ K^{-1} and $(-1,8) \cdot 10^{-3}$ K^{-1} respectively, then for the Be-Si LQ-alloy after annealing, the TCR is in the range of $\sim 2 \cdot 10^{-3}$ K^{-1}. It should be noted that, in comparison with the cast state, the metastable structure of eutectic Be-Si LQ-alloy is characterized by a slight increase in its ductility, which is expressed in the possibility of plastic deformation of LQ-foils.

CONCLUSIONS

It is established that, as a result of quenching from a liquid state of eutectic Be-Si alloy, the spectrum of obtained metastable states expands in comparison with the traditional method for producing cast alloys.

The values of crystal lattice periods of supersaturated substitutional solid solutions based on Beryllium and Silicon are determined. The essential role of the temperature criterion of "deep eutectics" on the tendency of simple eutectic alloys to form a solid amorphous or nanocrystalline state in them is confirmed. The positive role of the stressed state of crystal lattices of solid solutions due to the difference in the atomic radii of Beryllium and Silicon by a significant increase in the level of microstresses and microhardness in the Be-Si LQ- alloy, as well as some improvement in its plastic characteristics, is noted.

Declaration of interest none.

ORCID IDs

Valerij F. Bashev, https://orcid.org/0000-0002-3177-0935; **Sergey I. Ryabtsev,** https://orcid.org/0000-0002-2889-5278
Oleksandr I. Kushnerov, https://orcid.org/0000-0002-9683-2041; **Nataliya A. Kutseva,** https://orcid.org/0000-0002-6580-120X
Sergey N. Antropov, https://orcid.org/0000-0002-3248-6389

REFERENCES

[1] V.F. Bashev, O.I. Kushnerov, E.V. Il'chenko, S.I. Ryabtsev, N.A. Kutseva, and A.A. Kostina, Metallofizika i Noveishie Tekhnologii, **40**(9), 1231-1245 (2018), https://doi.org/10.15407/mfint.40.09.1231.
[2] S. Ryabtsev, P. Gusevik, V. Bashev, and F. Dotsenko, J. Mater. Sci. Eng. **A2**(9), 648-653 (2012).
[3] F.F. Dotsenko, V.F. Bashev, S.I. Ryabtsev, and A.S. Korchak, Phys. Met. Metallogr. **110**(3), 223-228 (2010). (in Russian), https://doi.org/10.1134/S0031918X1009005X.
[4] S.I. Ryabtsev, V.F. Bashev, A.I. Belkin, and A.S. Ryabtsev, The Physics of Metals and Metallography, **102**(3), 305-308 (2006).
[5] Z.A. Matysina, D.V.Schur, S.N.Antropov, and S.Yu. Zaginaichenko, Metallofizika i Noveishie Tekhnologii, **29**(7), 909-936 (2007).
[6] F.E. Wang, *Bonding Theory for Metals and Alloys*, 2nd Ed. (Elsevier, 2018), p. 230.
[7] V.F. Bashev, and O.I. Kushnerev, The Physics of Metals and Metallography, **115**(7), 692-696 (2014), https://doi.org/10.1134/S0031918X14040024.
[8] V.F. Bashev, and O.I. Kushnerev, The Physics of Metals and Metallography, **118**(1), 39-47 (2017), https://doi.org/10.1134/S0031918X16100033.
[9] E.S. Skorbyaschensky, V.F. Bashev, A.N. Polishko, and S.N. Antropov, Journal of Physics and Electronics, **27**(2), 51-54 (2019)
[10] A.E. Vol, *Строение и свойства двойных металлических систем. Т.1: Физико-химические свойства элементов системы азота, актиния, алюминия, америция, бария, бериллия, бора Т.1 [Structure and properties of binary metal systems. Vol.1: Physico-chemical properties of elements of the system of nitrogen, actinium, aluminum, americium, barium, beryllium, boron Vol.1* (Fiz.-Mat. Lit., Moscow, 1959), Vol. 1, p.755. (in Russian).

[11] T.B. Massalskii, *Binary Alloy Phase Diagrams*, (ASM International, Materials Park, Ohio, USA, 1990).

[12] M. Khansen, K. Anderko, *Структуры двойных сплавов [Structures of double alloys]*, (Publishinghouse NTL, Moscow, 1962). (in Russian).

[13] I.S.Miroshnichenko,*Закалка изжидкого состояния[QuenchingFromTheLiquidState],*(Metallurgy,Moscow,1982).(in Russian)

[14] V.K. Nosenko, A.Yu. Rudenko, T.N. Moiseeva, V.V. Maksimov, M.S. Nizameev, A.I. Limanovskiy, A.M. Semirga, and V.I. Tkatch, Metallofizika i Noveishie Tekhnologii, **37**(12), 1681 (2015).

[15] G.V. Samsonov, *Свойства элементов.Ч.1 [Properties of the elements. Ch.1]*, (Metallurgy, Moscow, 1976), Ch.1. p. 599.

[16] S.S. Gorelik, Yu.A. Skakov, and L.N. Rastorguev, *Рентгенографический и электронно-оптический анализ [X-ray and electron-optical analysis]*, (Moskva:MISIS:2002). (in Russian).

ВПЛИВ ЗАГАРТУВАННЯ З РІДКОГО СТАНУ НА ФАЗОВИЙ СКЛАД І ВЛАСТИВОСТІ ЕВТЕКТИЧНОГО СПЛАВУ Be-Si

В.Ф. Башев, С.І. Рябцев, О.І. Кушнерьов, Н.А. Куцева, С.М. Антропов

Кафедра експериментальної фізики, Дніпровський національний університет імені Олеся Гончара

72 пр. Гагаріна, Дніпро, 49010 Україна

Методом гарту з рідкого стану (splat-загартування) вперше виявлено утворення суміші метастабільних пересичених твердих розчинів заміщення в евтектичному сплаві Be-33at.% Si. Литі зразки отримують шляхом заливки розплаву в мідну форму. Високі швидкості охолодження під час рідинного загартування досягаються завдяки відомій техніці splat-охолодження, коли крапля розплаву розподіляється на внутрішній поверхні швидко обертового теплопровідного мідного циліндра. Максимальні швидкості охолодження оцінюються по товщині фольги. Використовувані в роботі швидкості охолодження розплаву (до 10^8 K/s) достатні для утворення аморфних фаз в деяких евтектичних сплавах з аналогічними фазовими діаграмами, але встановлено, що ці швидкості недостатні для отримання таких фаз в евтектичному сплаві Be-Si. Рентгеноструктурний аналіз проводиться на дифрактометрі у відфільтрованому випромінюванні кобальту K_α. Мікротвердість вимірюється на мікротвердомірі при навантаженні 50 Г. Електричні властивості, а саме, температурні залежності відносного електричного опору, вивчаються традиційним 4-зондовим методом нагріву в вакуумі. Точність періоду кристалічної решітки сплаву з урахуванням екстраполяції кута відображення на 90^0 становить $\pm 3\cdot10^{-4}$ нм. Виявлено, що навіть при надзвичайно високій швидкості гарту з розплаву замість утворення аморфної фази виявляється наявність двох пересичених твердих розчинів заміщення на основі Берилію і Кремнію. Продемонстровано, що різниця в атомних радіусах елементів істотно впливає на спотворення кристалічних решіток пересичених твердих розчинів, що формуються, і оцінена значна величина мікронапруг (напруг другого роду) в решітці Кремнію, яка пересичена Берилієм, що, природно, і обумовлює суттєве зростання величини мікротвердості, а саме: спостерігається збільшення мікротвердості у Be-Si сплаві в умовах застосованого методу загартування з рідкого стану більш, ніж в 1,7 рази в порівнянні з литим евтектичним сплавом і більш ніж в 6 разів вище в порівнянні з евтектоїдним литим сплавом Залізо-Вуглець. Отримана політерма електроопору сплаву в умовах безперервного нагріву його в вакуумі підтверджує метастабільний характер сформованих нових фаз при загартуванні з рідкого стану.

КЛЮЧОВІ СЛОВА: гарт з розплаву, евтектика, мікротвердість, пересичений твердий розчин, мікронапруги, температурний коефіцієнт опору

ВЛИЯНИЕ ЗАКАЛКИ ИЗ ЖИДКОГО СОСТОЯНИЯ НА ФАЗОВЫЙ СОСТАВ И СВОЙСТВА ЭВТЕКТИЧЕСКОГО СПЛАВА Be-Si

В.Ф. Башев, С.И. Рябцев, А.И. Кушнерев, Н.А. Куцева, С.Н. Антропов

Кафедра экспериментальной физики, Днепровский национальный университет имени Олеся Гончара

72 пр. Гагарина, Днепр, 49010 Украина

Методом закалки из жидкого состояния (splat-закалка) впервые выявлено образование смеси метастабильных пересыщенных твердых растворов замещения в эвтектическом сплаве Be-33at.%Si. Литые образцы получают путем заливки расплава в медную форму. Высокие скорости охлаждения во время жидкостного закаливания достигаются благодаря известной технике splat-охлаждения, путем размазывания капли расплава на внутренней поверхности быстро вращающегося теплопроводящего медного цилиндра. Максимальные скорости охлаждения оцениваются по толщине фольги. Используемые в работе скорости охлаждения расплава (до 10^8 K/s) достаточны для образования аморфных фаз в некоторых эвтектических сплавах с аналогичными фазовыми диаграммами, но установлено, что эти скорости недостаточны для их получения в эвтектическом сплаве Be-Si. Рентгеноструктурный анализ проводится на дифрактометре в отфильтрованном излучении кобальта K_α. Микротвердость измеряется на микротвердомере при нагрузке 50 Г. Электрические свойства, а именно, температурные зависимости относительного электрического сопротивления, изучаются традиционным 4-зондовым методом нагрева в вакууме. Точность определения периода кристаллической решетки сплава с учетом экстраполяции угла отражения на 90^0 составляет $\pm 3\cdot10^{-4}$ нм. Обнаружено, что даже при чрезвычайно высокой скорости закалки из расплава вместо образования аморфной фазы обнаруживается наличие двух пересыщенных твердых растворов замещения на основе Бериллия и Кремния. Продемонстрировано, что разница в атомных радиусах элементов существенным образом влияет на искаженность кристаллических решеток формирующихся пересыщенных твердых растворов, и оценена значительная величина микронапряжений (напряжений второго рода) в решетке Кремния, пересыщенной Бериллием, что, естественно, и обусловливает существенный рост величины микротвердости, а именно: наблюдается увеличение микротвердости в Be-Si сплаве в условиях примененного метода закалки из жидкого состояния более, чем в 1,7 раза по сравнению с литым эвтектическим сплавом и более чем в 6 раз выше в сравнении с эвтектоидным литым сплавом Железо-Углерод. Полученная политерма электросопротивления сплава в условиях непрерывного нагрева его в вакууме подтверждает метастабильный характер сформированных новых фаз при закалке из жидкого состояния.

КЛЮЧЕВЫЕ СЛОВА: закалка из расплава, эвтектика, пересыщенный твердый раствор, микротвердость, микронапряжения, температурный коэффициент сопротивления

DEGRADATION UNDER INFLUENCE OF RADIATION DEFECTS OF DETECTOR PROPERTIES OF Cd$_{0.9}$Zn$_{0.1}$Te IRRADIATED BY NEUTRONS

Alexandr I. Kondrik[a,*], Gennadij P. Kovtun[a,b]

[a]*National Science Center "Kharkiv Institute of Physics and Technology"*
1, Academichna str., 61108 Kharkiv, Ukraine
[b]*V.N. Karazin Kharkiv National University, 4 Svobody Sq., 61022 Kharkiv, Ukraine*
Corresponding Author: kondrik@kipt.kharkov.ua
Received April 18, 2020; revised June 18, 2020; accepted June 30, 2020

This work is devoted to the study by computer simulation of the mechanisms of the influence of radiation defects, arising under the influence of neutron irradiation, on the changes in electrical properties: resistivity ρ, electron mobility μ_n, lifetime of nonequilibrium electrons τ_n and holes τ_p in Cd$_{0.9}$Zn$_{0.1}$Te and charge collection efficiency η of uncooled ionizing radiation detectors based on this material. Radiation defects, which are corresponded by deep energy levels in the band gap, act as trapping centers of nonequilibrium charge carriers, noticeably affect the degree of compensation by changing ρ of the detector material, the recombination processes, decreasing τ_n and τ_p, and also the scattering of conduction electrons, decreasing μ_n, that ultimately can cause degradation of the charges collection efficiency η. The specific reasons for the deterioration of the electrophysical and detector properties of this semiconductor under the influence of neutron irradiation were identified, and the main factors affecting the increase in the resistivity of Cd$_{0.9}$Zn$_{0.1}$Te during its bombardment by low-energy and high-energy neutrons, leading to complete degradation of the recording ability of detectors based on this materials, were found. The recombination of nonequilibrium charge carriers is noticeably stronger than the decrease in μ_n affects the degradation of detector properties, therefore, the effect of recombination processes at deep levels of radiation defects on the degradation of τ_n, τ_p, and η of detectors based on Cd$_{0.9}$Zn$_{0.1}$Te was studied. A comparative analysis of the properties of Cd$_{0.9}$Zn$_{0.1}$Te with the previously studied CdTe:Cl was made. An attempt was made to explain the higher radiation resistance of Cd$_{0.9}$Zn$_{0.1}$Te compared to CdTe:Cl under neutron irradiation by the influence of the radiation self-compensation mechanism with participation of deep donor energy levels: interstitial tellurium and tellurium at the site of cadmium. In addition, the rate of recombination at defect levels in Cd$_{0.9}$Zn$_{0.1}$Te is, ceteris paribus, lower than in CdTe:Cl due to the smaller difference between the Fermi level and the levels of radiation defects in cadmium telluride. The relationship between the band gaps of Cd$_{0.9}$Zn$_{0.1}$Te and CdTe:Cl, the concentration of radiation defects, the Fermi level drift during irradiation, and the radiation resistance of the detectors were also noted. The important role of purity and dopant shallow donor concentration in initial state of the detector material is indicated.
KEY WORDS: detector properties, simulation, CdTe, CdZnTe, neutron irradiation, radiation defects

The Cd$_{0.9}$Zn$_{0.1}$Te compound is considered to be a promising semiconductor material for room temperature detectors, which are intended for recording x-ray and gamma radiation and can be used in astronomy, dosimetric environmental monitoring and nuclear medicine imaging. Cd$_{0.9}$Zn$_{0.1}$Te is the material of good electrophysical properties [1–4]: high resistivity $\rho = 10^9$–10^{11} $\Omega\cdot$cm, high electronic mobility $\mu_n = 1100$–1200 cm^2/(V·sec), acceptable values of the lifetimes of nonequilibrium electrons $\tau_n \sim 10^{-6}$ sec and nonequilibrium holes $\tau_p \sim 10^{-6}$ sec. Along with Cd$_{0.9}$Zn$_{0.1}$Te, CdTe is often considered as a detector material. During operation, the detectors are exposed to ionizing radiation, the effect of which on the crystals is the subject of research, for example, irradiation with protons [5], electrons [6], gamma rays [7], and neutrons [8] which have increased penetrating power. As a result of neutron bombardment, the radiation defects arise in a semiconductor crystal, which correspond to energy levels in the band gap, acting as centers of capture and recombination of nonequilibrium charge carriers generated by the detected radiation. These defects noticeably affect upon the degree of compensation, changing ρ of the detector material, and upon the recombination processes, decreasing τ_n and τ_p, and also on the scattering of conduction electrons, decreasing μ_n. Ultimately, the radiation defects are capable to cause complete degradation of the charges collection efficiency η of detector, the specific reasons for which are not fully understood. To increase the radiation resistance and improve the detector quality of Cd$_{0.9}$Zn$_{0.1}$Te, it is necessary to study and try to understand the mechanisms of the influence of radiation defects, which arise in a crystal under the neutron irradiation, on the electrophysical and detector properties of this material. However, due to the high resistivity of Cd$_{0.9}$Zn$_{0.1}$Te, such a task is practically impossible to resolve only by experimental methods [8-10], therefore, it is very important to apply additionally the numerical simulation basing on known experimental results using as initial data.

The aim of the work was to study by modeling method the mechanisms of the influence of radiation defects arising in Cd$_{0.9}$Zn$_{0.1}$Te under the influence of neutron irradiation on the change in resistivity ρ, electron mobility μ_n, lifetimes of nonequilibrium electrons τ_n, nonequilibrium holes τ_p, and charge collection efficiency η in radiation detectors based on this material, as well as a comparative analysis of the properties of Cd$_{0.9}$Zn$_{0.1}$Te and cadmium telluride which was previously studied in [11].

PHYSICAL MODELS AND MATERIAL COMPOSITION

The applied models and their testing are described in detail in [12], and the spectral characteristics of the initial and irradiated CdTe:Cl and Cd$_{0.9}$Zn$_{0.1}$Te are taken from paper [10]. First the electroneutrality equation was compiled with including of all impurities and defects experimentally recorded in [10]. This equation was numerically solved with respect

to the Fermi level F, then the concentrations of free electrons **n** and holes **p** were determined in the approximation of parabolic zones. The electron mobility μ_n was calculated using an approximation of the pulse relaxation time (tau approximation) with taking into account scattering mechanisms at ionized and neutral centers, acoustic phonons, piezoelectric phonons, optical phonons, as well as scattering on clusters of point defects and doping inhomogeneities. The hole mobility μ_p was assumed to be unchanged and equal to 70 cm^2/(V·s). The specific conductivity was calculated by the formula: $e \cdot n \cdot \mu_n + e \cdot p \cdot \mu_p$. The resistivity was calculated as the reciprocal of the conductivity, consisting of electronic and hole components. The lifetime of nonequilibrium charge carriers was calculated according to the Shockley - Read - Hall recombination model, and the detector charges collection efficiency was determined by the Hecht equation [13, p. 489]. The distance between the detector electrodes was assumed to be equal 5 mm, and the electric field strength - 1000 V/cm.

The changes in F, ρ, μ_n, τ_n, τ_p, and η have been simulated depending on the content of radiation defects and doping shallow donor, for which the aluminum, indium, bismuth and lead can be used in $Cd_{0.9}Zn_{0.1}Te$. The simulation was carried out using the following characteristics of the i-ths impurities and defects levels as the initial data, experimentally measured and published in the technical literature: concentration N_i, position in the bandgap E_i, and capture cross section for nonequilibrium charge carriers σ_i.

The initial compositions of background impurities and defects were determined which ensured that the calculated value $\rho = 1 \cdot 10^{11}$ $\Omega \cdot$cm for $Cd_{0.9}Zn_{0.1}Te$ coincides with the value experimentally measured in [10] before neutron exposure. A typical initial composition of the $Cd_{0.9}Zn_{0.1}Te$ detector material is presented in Table. Similar composition was described, for example, in [7, 10, 14, 15]. The specific composition of the material is taken from [10]. The Table also show the capture cross sections for the levels σ_i, the order of magnitude of which was determined in [16], where the contributions of all levels to the currents of charge carriers emitted into the corresponding zones were taken into account. The charge state of defects is indicated by a plus sign for donors whose energy is measured relative to the conduction-band bottom E_C, and a minus sign - for acceptor levels with energy relative to the valence band top E_V.

The notation and probable nature of some levels are taken from [7, 10, 15]. Doping impurity of shallow donor, introduced into the matrix of the materials under study, are intended to compensate for shallow acceptors (A, A1, C, X) and to achieve a high-resistance state necessary for the operation of the detectors. The levels of A, A1, C, X, according to opinion of most researchers, are complexes of cadmium vacancies with various background impurities. The cadmium vacancy appears to correspond to DX or J.

Table

Composition of $Cd_{0.9}Zn_{0.1}Te$ before irradiation with a specific resistance of $1 \cdot 10^{11}$ $\Omega \cdot$cm [10].

Defect	A^-	$A1^-$	C^-	X^-	DX^{2-}	J^-	Z^+	Y^-	W^-	$Te_{Cd}{}^+$	$V_{Te}{}^+$
E_i, eV	0.14	0.16	0.25	0.29	0.41	0.45	0.52	0.67	0.70	0.74	1.1
σ_i, cm^2	10^{-19}	$2 \cdot 10^{-19}$	$3 \cdot 10^{-19}$	10^{-18}	10^{-16}	10^{-16}	10^{-17}	10^{-17}	10^{-17}	10^{-18}	10^{-16}
N_i,cm^{-3}	$5 \cdot 10^{15}$	$5 \cdot 10^{14}$	$5 \cdot 10^{14}$	$5 \cdot 10^{14}$	$3 \cdot 10^{15}$	$3 \cdot 10^{15}$	$1 \cdot 10^{15}$	$3 \cdot 10^{15}$	$3 \cdot 10^{15}$	$1.45 \cdot 10^{16}$	$1 \cdot 10^{16}$

The calculated electrophysical properties of unirradiated material corresponded to well-known values: $\mu_n = 1200$ cm^2/(V·sec), lifetimes τ_n, $\tau_p \sim 10^{-6}$ sec. The changes in ρ, μ_n, τ_n, τ_p, the position of the Fermi level **F** in the band gap of $Cd_{0.9}Zn_{0.1}Te$, and variation in the charges collection efficiency η of detector based on this material have been simulated depending on the content of radiation defects and the doping shallow donor at T = 20°C – operating temperature of the detector. It should be noted that since in paper [10] all the results, and conclusions are of a qualitative nature, the model dependences and modeling results obtained in this paper can also be only of qualitative those.

RESULTS AND DISCUSSION

In paper [10], the studied material $Cd_{0.9}Zn_{0.1}Te$ was irradiated by the fluxes of low-energy neutrons (~ 10 eV) with fluences from 10^{10} to 10^{14} N/cm^2 and high-energy neutrons ($\sim 0.5 - 1$ MeV) with fluences from 10^{11} to 10^{13} N/cm^2. The radiation donor level Z in cadmium telluride occurs already after the first stage of irradiation and it is present in the crystal at all subsequent stages, and at the moment of complete degradation of the detector recording properties, this defect reaches the maximum amplitude in spectrum. According to the authors of [10], tellurium interstitial Te(I) can be considered as a defect Z which causes complete degradation of the detector properties. In $Cd_{0.9}Zn_{0.1}Te$, the same Z level with an energy of $E_C - 0.52$ eV was also present, but it was often suppressed in the spectra by the peak of the acceptor level J, the content of which noticeably correlated with the degree of radiation damage of the irradiated sample. In addition, during irradiation of the studied materials, the amplitudes of the peaks and the concentration of defects Te_{Cd}, V_{Te}, and also the complex V_{Cd}–Im (cadmium vacancy–impurity) increase significantly. It was of interest to simulate the dynamic of change in the resistivity of $Cd_{0.9}Zn_{0.1}Te$ with an increase in the concentration of radiation defect Z which causes an abrupt decrease in the charge collection efficiency and complete degradation of detector properties, while the content of radiation defects J, Te_{Cd}, V_{Te} is increasing. The result of simulation is shown in Fig. 1. The concentration of the radiation defect J monotonically increases from $3 \cdot 10^{15}$ to $2.1 \cdot 10^{16}$ cm^{-3}, and the concentration of the Te_{Cd} defect does from $1.45 \cdot 10^{16}$ to $3.2 \cdot 10^{16}$ cm^{-3}. It can be seen from Figure 1, that as the concentration of defect Z increases during irradiation, the resistivity of material increases monotonically, which was observed experimentally in [10]. However, after higher doses of irradiation by high-energy neutrons with a fluence of 10^{13} N/cm^2 and radiation damage which can

be associated with a concentration of $N(Z) = 2 \cdot 10^{16}$ cm^{-3}, the resistance of $Cd_{0.9}Zn_{0.1}Te$ reaches almost the maximum value $\rho = 2.12 \cdot 10^{11}$ $\Omega \cdot$cm, which corresponds to the qualitative results of paper [10]. When comparing with similar model dependences for CdTe:Cl from [11] (Fig. 1), we can see that in $Cd_{0.9}Zn_{0.1}Te$ there is no sharp jump in the resistivity $\Delta\rho$ at $N(Z) = 2 \cdot 10^{16}$ cm^{-3}, as in CdTe.
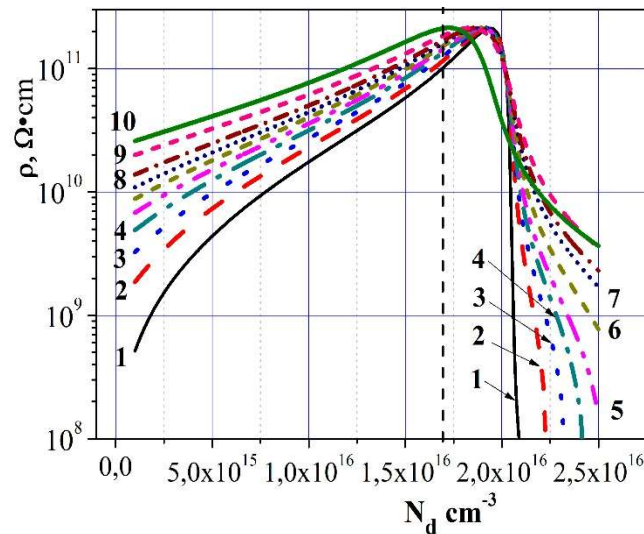

Figure 1. Specific resistance of $Cd_{0.9}Zn_{0.1}Te$ depending on the content of doping shallow donors at various concentrations of defect Z. Z content, cm^{-3}: $1 - 1 \cdot 10^{15}$, $2 - 2 \cdot 10^{15}$, $3 - 3 \cdot 10^{15}$, $4 - 4 \cdot 10^{15}$, $5 - 5 \cdot 10^{15}$, $6 - 7 \cdot 10^{15}$, $7 - 1 \cdot 10^{16}$, $8 - 1.4 \cdot 10^{16}$, $9 - 1.6 \cdot 10^{16}$, $10 - 2 \cdot 10^{16}$. The vertical dashed line corresponds to the studied sample.

On the contrary, a monotonic increase in the $Cd_{0.9}Zn_{0.1}Te$ resistivity is observed, which occurs due to the gradual drift of the Fermi level to the middle of the band gap towards the radiation level Z with increasing its concentration. This increasing of ρ is also confirmed experimentally. In this case, a displacement of the F level closer to the conduction band, observed in [11] for CdTe, does not occur due to the action of the radiative self-compensation mechanism, which appears in an increase of the concentration of radiation defects J (E_V + 0.45 eV) and Te$_{Cd}$ (E_C - 0.74 eV), that together with the defect Z (E_C - 0.52 eV) hold F near the middle of the band gap. In addition, a pivotal role also here is that $Cd_{0.9}Zn_{0.1}Te$ has a larger band gap in comparison with E_G of CdTe:Cl; therefore, in order for Fermi level to reach the middle of E_G in $Cd_{0.9}Zn_{0.1}Te$, a higher content of the radiation defect Z is required than in CdTe:Cl. Fig. 2 shows the behavior of Fermi level in $Cd_{0.9}Zn_{0.1}Te$.

Figure 2 demonstrates that in $Cd_{0.9}Zn_{0.1}Te$ there is an insignificant difference in the F position between the initial state with $N(Z) = 1 \cdot 10^{15}$ cm^{-3} and after irradiation with the concentration of defect Z $N(Z) = 2 \cdot 10^{16}$ cm^{-3}, while for CdTe:Cl in [11] this difference in position of Fermi level is significant. In other words, during irradiation, the electrophysical properties of $Cd_{0.9}Zn_{0.1}Te$ change noticeably less than the properties of cadmium telluride. This simulation result is confirmed by the well-known fact, experimentally confirmed also in [10], of the higher radiation resistance of $Cd_{0.9}Zn_{0.1}Te$ in comparison with CdTe:Cl.
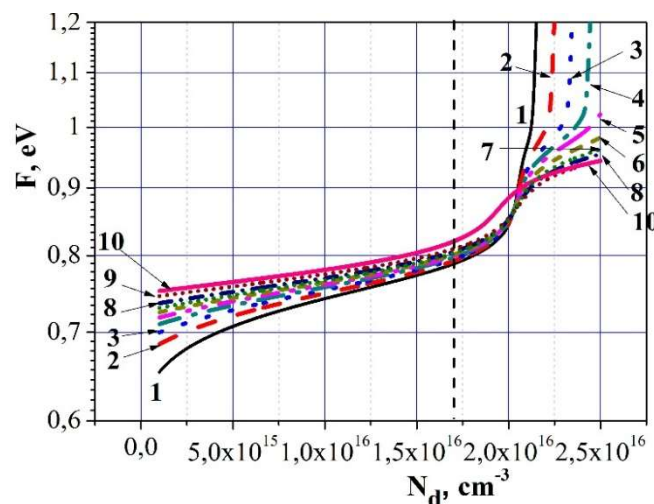

Figure 2. The positions of the Fermi level in $Cd_{0.9}Zn_{0.1}Te$, measured from the top of valence band, depending on the content of shallow donor at different concentrations of the radiation donor defect Z (cm^{-3}). Z concentrations in $Cd_{0.9}Zn_{0.1}Te$ are the same as for the numbered dependences in Fig. 1. The vertical dashed line corresponds to the studied sample.

Neutron irradiation of $Cd_{0.9}Zn_{0.1}Te$ also leads to the expansion of the region of the high-resistance state, which makes it possible to maintain the working capacity of the detector during irradiation. Figure 3 shows the behavior of the resistivity $Cd_{0.9}Zn_{0.1}Te$ at the concentration $N(Te_{Cd}) = 1.45 \cdot 10^{16}$ cm^{-3} (a) and after irradiation with high-energy neutrons at the concentration $N(Te_{Cd}) = 3.2 \cdot 10^{16}$ cm^{-3} (b) depending on concentrations of radiation defects: acceptor J (N_{DA}) and donor Z (N_{DD}). We see that the expansion of the high-resistance region occurs due to an increase in the concentration of the Te_{Cd} anti-structural defect during neutron irradiation.
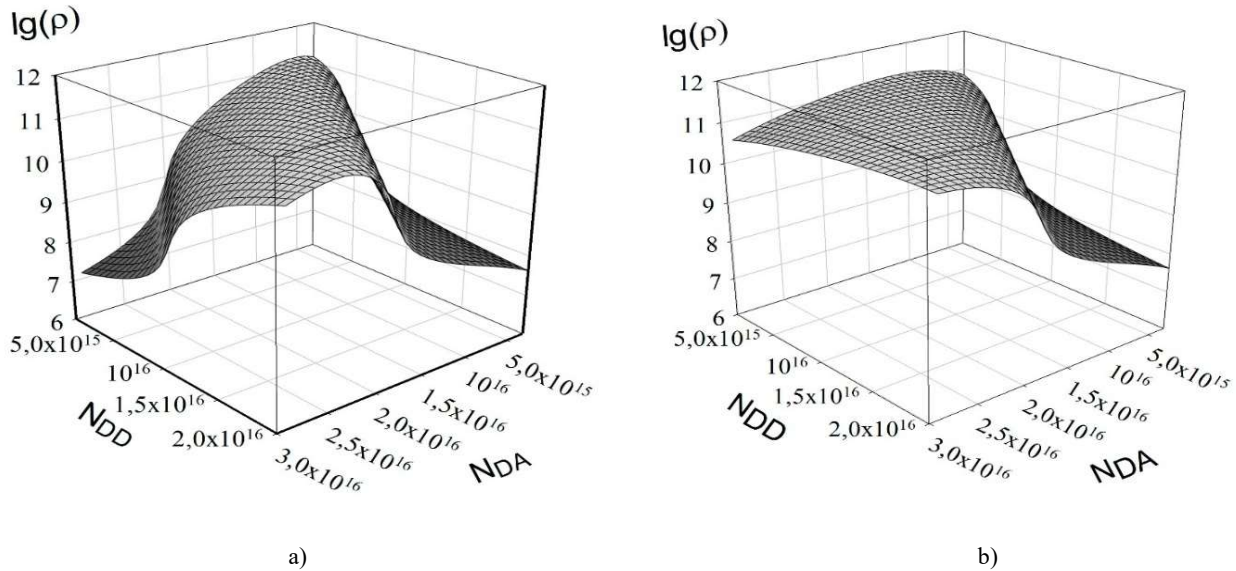

a)   b)

Figure 3. Dependences of the decimal logarithm of the $Cd_{0.9}Zn_{0.1}Te$ resistivity on the concentration N_{DA} of the acceptor defect J and the concentration N_{DD} of the donor defect Z: a) the content of Te_{Cd} is $1.45 \cdot 10^{16}$ cm^{-3}; b) the content of Te_{Cd} is $3.2 \cdot 10^{16}$ cm^{-3}.

The initially measured fluences of neutron irradiation of investigated sample were 10^{11} N/cm^2 for high-energy neutrons and 10^{10} N/cm^2 for low-energy neutrons. In the process of further irradiation, the material gradually lost its detector properties until complete degradation after bombardment by low-energy neutrons with the fluence of 10^{14} N/cm^2. The integrated flux of high-energy neutrons, after which the detector properties $Cd_{0.9}Zn_{0.1}Te$ were completely degraded, was 10^{13} N/cm^2. Since the specific resistance of material increases after neutron irradiation, degradation of the detector properties can occur due to a decrease in the electron mobility μ_n and to a decrease in the lifetimes of nonequilibrium charge carriers τ_n, τ_p. In earlier paper [12, Fig. 3] it was shown that a decrease of μ_n in $Cd_{0.9}Zn_{0.1}Te$ can be caused by the scattering of conduction electrons by clusters of point defects, but no more than two to three times, and it is not capable to lead to complete degradation of detector properties. Thus, a complete loss of recording properties should occur due to a significant decrease in the lifetime of nonequilibrium charge carriers. Approximate quantitative estimates based on the experimental results of paper [17] showed that the rate of band-to-band recombination of nonequilibrium charge carriers is about by ten orders of magnitude lower than the rate of recombination at deep levels of defects in wide-gap semiconductors such as CdTe and $Cd_{0.9}Zn_{0.1}Te$. Figure 4 shows the donor content dependence of the charges collection efficiency η in detectors based on $Cd_{0.9}Zn_{0.1}Te$, calculated according to the Hecht equation for which the lifetimes of nonequilibrium electrons and holes were calculated according to the Shockley-Read statistics describing recombination of charge carriers at the energy levels of impurities and structural defects. Basing on a comparison of the graphs of Fig. 4 and the results of paper [10], it follows that the concentration of the radiation defect Z in the studied materials N (Z) = $(1-2) \cdot 10^{16}$ cm^{-3} approximately corresponds to the content of this radiation defect after the high-energy neutrons fluence of 10^{13} N/cm^2.

The concentration of radiation defects Z, equaled to $N(Z)=(1-3) \cdot 10^{15}$ cm^{-3}, approximately corresponds to its content in $Cd_{0.9}Zn_{0.1}Te$ after irradiation by low-energy neutrons with fluences 10^{12}–10^{13} N/cm^2. Figure 4 also shows that when the content of the radiation defect Z: N (Z) = $(1-3) \cdot 10^{15}$ cm^{-3}, the registering properties of the detectors based on $Cd_{0.9}Zn_{0.1}Te$ are partially lost, which qualitatively corresponds to the experiment of paper [10].

Quantitative studies have shown that the degradation of $Cd_{0.9}Zn_{0.1}Te$ detector charge collection η occurs due to capture and recombination of nonequilibrium charge carriers at the radiation level of a deep donor with an energy $E = E_C - 0.52$ eV, presumably Te (I), as well as at the deep level of Te_{Cd} defect with energy $E_C - 0.74$ eV. It was established also that in $Cd_{0.9}Zn_{0.1}Te$ the radiation defect of the tellurium vacancy V_{Te}, which is dominant in the spectra in peak amplitude [10], does not participate in compensation and does not capture nonequilibrium charge carriers due to the large difference between the V_{Te} energy level and the Fermi level in the semi-insulating state at room temperature.

The simulation established also that the degradation of the detector properties of the material under study occurs mainly due to a noticeable decrease in the lifetime of nonequilibrium electrons by several tens of times. Capture and

recombination of nonequilibrium holes at radiation levels have little effect on the degradation of charge collection in $Cd_{0.9}Zn_{0.1}Te$ detectors during its irradiation. It can be seen from Fig. 5, where the behavior of the lifetime of nonequilibrium electrons τ_n (a) and holes τ_p (b) was shown.
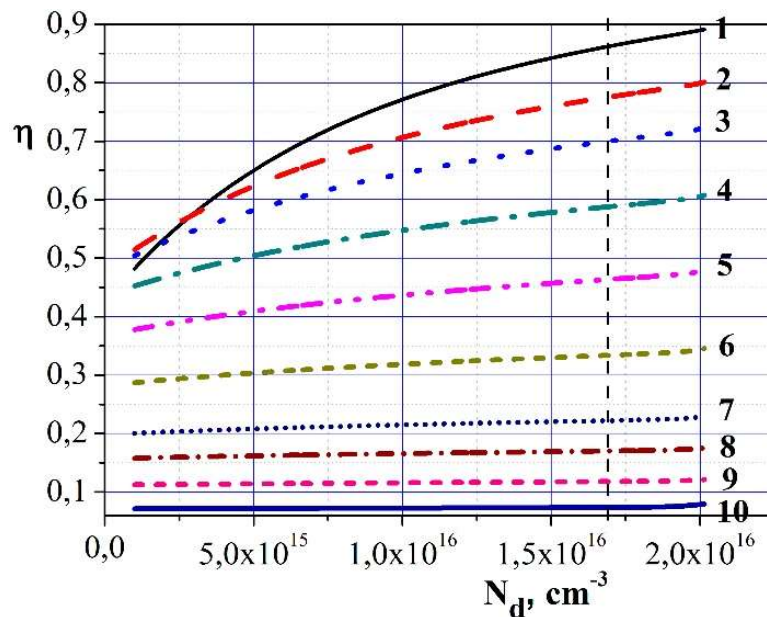

Figure 4. Charge collection efficiency of detectors based on $Cd_{0.9}Zn_{0.1}Te$ depending on the content of doping shallow donors for different concentrations of radiation defect Z, which are equaled to concentrations for numbered curves in Fig. 1,2. The vertical dashed line corresponds to the studied sample.
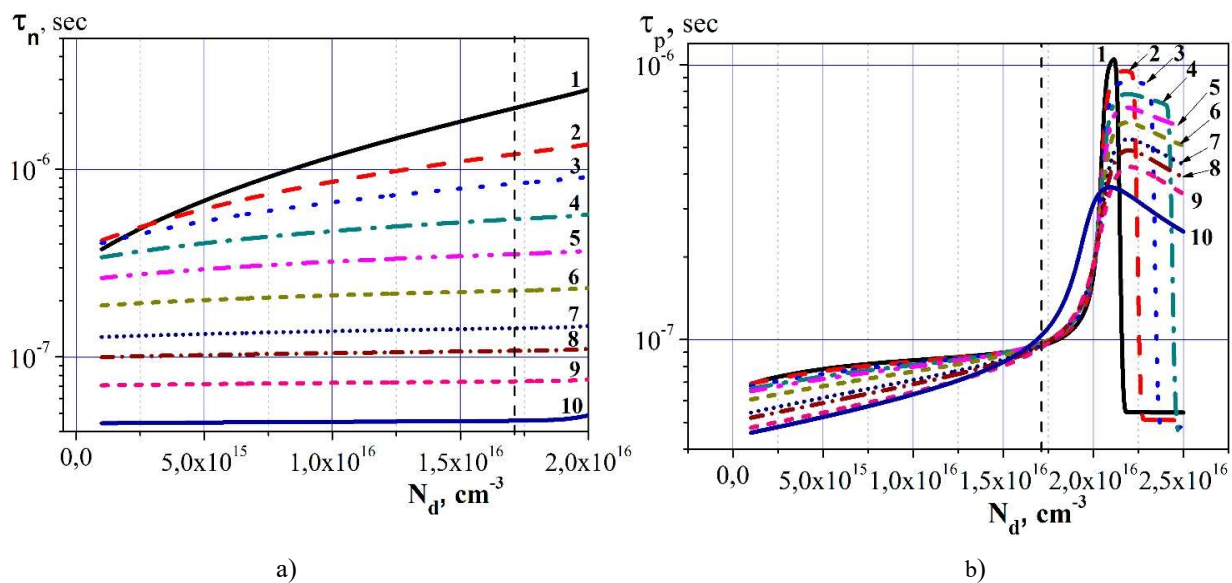

a)

b)

Figure 5. Dependences of the lifetimes of nonequilibrium electrons (a) and holes (b) in $Cd_{0.9}Zn_{0.1}Te$ on the concentration of doping shallow donors for different concentrations of the radiation defect Z, which are the same as in the numbered curves in Fig. 1, 2, 4. The vertical dashed lines correspond to the studied sample.

Figure 5 demonstrates that the lifetime of nonequilibrium electrons τ_n in the studied $Cd_{0.9}Zn_{0.1}Te$ decreases quite significantly compared to the lifetime of nonequilibrium holes τ_p as the concentration of radiation defects, arising under neutron irradiation, increases. The jump in τ_p by an order of magnitude (Fig. 5b) in the concentration range $N_d = 2 \cdot 10^{16}$-$2.5 \cdot 10^{16}$ cm^{-3} is explained by the fact that within this interval the Fermi level passes far from the energy levels of defects, capture and recombination centers (see Table and Fig. 2), therefore, the rate of recombination of nonequilibrium charge carriers decreases significantly.

The results obtained in this and earlier studies can be compared with the data of [18], where, using the SRIM program, the Monte Carlo method was used to simulate the effect of neutron radiation with an energy of 1–2 MeV on the formation of radiation damage in $Cd_{0.9}Zn_{0.1}Te$ crystals. The type and number of originating radiation defects was investigated. The calculated data were compared with the experimental results of the study of the operation of $Cd_{0.9}Zn_{0.1}Te$ detector, both

the initial one and the material irradiated with a [252]Cf source of fast neutrons. The defect concentration was measured using thermally stimulated current spectroscopy (TSC), and the detector spectra were recorded for [241]Am gamma radiation source (59.5 keV). It was shown that the concentration of vacancies, anti-structural defects of cadmium substitution at the site of tellurium, interstitial atoms, and related defects increases during neutron irradiation, which, according to the authors of [18], caused a deterioration in the detector characteristics of $Cd_{0.9}Zn_{0.1}Te$. Besides, the complete degradation of the detector occurred already after an irradiation dose of $5 \cdot 10^{10}$ N/cm², while in the experiment of paper [10], the detector degraded only after an irradiation dose of 10^{13} N/cm² by fast neutrons. The position of the Fermi level in the band gap, measured in [18], relative to the bottom of the conduction band E_C in the initial sample was equal to 0.707 eV, and in the sample irradiated with a dose of $5 \cdot 10^{10}$ N/cm² it became E_C–0.513 eV with a decrease in resistivity from $3.49 \cdot 10^9$ to $6.12 \cdot 10^8$ Ohm·cm.

We carried out a comparative analysis of the simulation results based on the experimental data of [10] with the experimental results of paper [18]. As a result, it was found that the very low radiation resistance of the detector in [18] can be explained by the fact that the as-grown $Cd_{0.9}Zn_{0.1}Te$ crystal there turned out to be a material of lower detector quality. Namely, in the initial state, they produced a semiconductor with a high content of interstitial Cd^{++} (Cd_I) and substitutional defect of cadmium in site of tellurium (Cd^+_{Te}), which are defects of the donor type. Under the influence of these electrically active deep donors, the Fermi level already in the as-grown material was above the middle of the band gap, which determined the electronic conductivity registered in [18] using Hall measurements. The bombardment of such a material by fast neutrons led to a further increase in the concentration of Cd_I and Cd_{Te} defects with a shift of the Fermi level even closer to the conduction band and, as a result, a noticeable drop in resistivity, a sharp increase in the leakage current and complete detector degradation, which required a relatively small irradiation dose - $5 \cdot 10^{10}$ N/cm². There can be two main reasons for such a low radiation resistance of the detector described in [18]. First, the as-grown material could be doped with an excessively large amount of indium, which immediately led to electronic conductivity, while hole conductivity is required for the detector to operate. Therefore, a relatively small dose of radiation was required in order to increase the concentration of deep donors and thus shift the Fermi level even closer to the conduction band, lowering the specific resistance ρ. Secondly, there was a weak effect of the radiative self-compensation process of the irradiated detector material due to a possible insufficient removal of background impurities from the as-grown crystal. Namely, cadmium vacancies formed under the influence of neutron irradiation interacted with background impurities and In dopant and formed A centers – neutral or with a charge increased by one with respect to initial state of double charged cadmium vacancy (V^{2-}_{Cd}), which, in turn, prevented the stabilization of the Fermi level and led to its drift to the conduction band decreasing resistivity ρ. Moreover, some of these complexes have such shallow energy levels that their registration could not be possible at a starting temperature of 80 K in the TSC technique. And neutral complexes are not electrically active; therefore, they are not recordable at all. The decrease in ρ led to an increase in noise which finally completely suppressed the main peak of the spectrum. The much more radiation-resistant detector in paper [10] demonstrated a much different behavior, namely it was the material which only increased the resistivity under the influence of high-energy neutron irradiation, since there the Fermi level in the initial state located below the middle of the band gap. And degradation of this detector material occurred for another reason: due to a decrease in the charge collection efficiency owing to capture and recombination of nonequilibrium carriers at deep levels of radiation defects.

CONCLUSIONS

The experimentally registered gradual increase in the $Cd_{0.9}Zn_{0.1}Te$ resistivity during bombardment by neutrons is caused by a gradual increase in the concentration of interstitial tellurium Te(I) with an energy level of 0.52 eV, measured relative to the bottom of the conduction band E_C. An increase in the content of Te(I) shifts the Fermi level to the middle of the band gap. The resistivity of $Cd_{0.9}Zn_{0.1}Te$ increases monotonically due also to an increase in the content of the anti-structural donor defect Te_{Cd}, which increases the size of the region of the high-resistance state in the ranges of concentration of radiation defects and also shifts Fermi level to the middle of band gap. The absence of degradation of resistivity occurred due to the action of the radiation self-compensation mechanism with the formation of a sufficient number of individual acceptor cadmium vacancies not creating the complexes with impurities.

The degradation of the charge collection efficiency of $Cd_{0.9}Zn_{0.1}Te$ under neutron irradiation occurs due to capture and recombination of nonequilibrium electrons at the radiation level of a deep donor with energy $E = E_C - 0.52$ eV, presumably Te (I), as well as at deep level of Te_{Cd} defect with energy $E_C - 0.74$ eV.

The well-known fact of higher radiation resistance of $Cd_{0.9}Zn_{0.1}Te$ compared to CdTe:Cl under neutron irradiation can be explained by the fact that in $Cd_{0.9}Zn_{0.1}Te$ there is a stronger mechanism of radiation self-compensation with the participation of deep donor levels (Te (I) and Te_{Cd}) than in CdTe:Cl. Perhaps this is why in the $Cd_{0.9}Zn_{0.1}Te$ material, unlike CdTe:Cl, there is no rearrangement of the crystal structure after neutron irradiation with ultimate fluence 10^{13} N/cm² of high-energy neutrons (E ~ 10^5 eV). In addition, due to the higher difference between the Fermi level and the deep levels of radiation defects in $Cd_{0.9}Zn_{0.1}Te$, the rate of recombination at the levels of radiation defects, ceteris paribus, is lower in it than in CdTe:Cl. It can also be noted that, due to the larger band gap of the E_G in $Cd_{0.9}Zn_{0.1}Te$, the Fermi level drifts in this material to a larger depth than in CdTe and therefore a higher concentration of the corresponding radiation defects is required to reach a middle of E_G and maximum of ρ, and therefore higher radiation doses are needed.

ORCID IDs

Alexandr I. Kondrik, https://orcid.org/0000-0001-9428-4830; Gennadij P. Kovtun, https://orcid.org/0000-0003-4242-7697

REFERENCES

[1] Penfei Wang, Ruihua Nan, and Zengyun Jian, Journal of Semiconductors, **38**, 062002 – 062002-6 (2017), https://dx.doi.org/10.1088/1674-4926/38/6/062002.

[2] Lingyan Xu, Wanqi Jie, Gangqiang Zha, Tao Feng, Ning Wang, Shouzhi Xi, Xu Fu, Wenlong Zhang, Yadong Xu, and Tao Wang, Applied Physics Letters, **104**, 232109–232109-5 (2014), https://dx.doi.org/10.1063/1.4883403.

[3] A. Castaldini, A. Cavallini, and B. Fraboni, Journal of Applied Physics, **83**, 2121–2126 (1997), https://doi.org/10.1063/1.366946.

[4] N. Krsmanovich, K.G. Lynn, M.H. Weber, R. Tjossem, Th. Gessmann, Cs. Szeles, E.E. Eissler, J.P. Flint, and H.L. Glass, Physical Review B, **62**, R16 279 – R16 282 (2000), https://dx.doi.org/10.1103/PhysRevB.62.R16279.

[5] D.A. Lamb, C.I. Underwood, V. Barriozet, R. Gwilliam, J. Hall, Mark A. Baker, and Stuart J.C. Irvine, Progress in Photovoltaics, **25**, 10059–1067 (2017), https://dx.doi.org/10.1002/pip.2923.

[6] Yu.Yu. Loginov, A.V. Mozzherin, and N.N. Paklin, 21st Int. Scientific Conference Reshetnev Readings-2017. IOP Conf. Series: Materials Science and Engineering, **467**, 012007–012007-5 (2019), https://dx.doi.org/10.1088/1757-899X/467/1/012007.

[7] Ruihua Nan, Wanqi Jie, Gangqiang Zha, and Bei Wang, Journal of Electronic Materials, **41**, 2044–2049 (2012), https://dx.doi.org/10.1007/s11664-012-2204-5.

[8] S.V. Plyatsko, L.V. Rashkovetskiy, Semiconductors/Physics of the Solid State, **52**(3), 322–326 (2018), https://dx.doi.org/10.21883/FTP.2018.03.45615.8373. (in Russian)

[9] Xianf Chen, Hetong Han, Gang Li, and Yi Lu, Nuclear Instruments and Methods in Physics Research B, **394**, 97-102 (2017), https://doi.org/10.1016/j.nimb.2017.01.001.

[10] A. Cavallini, and B. Fraboni, J. Appl. Phys. **94**(5), 3135–31422003 (2003), https://dx.doi.org/10.1063/1.1600529.

[11] A.I. Kondrik, G.P. Kovtun, Tekhnologiya i Konstruirovanie v Elektronnoi Apparature, no. 1-2, 22–29 (2020), https://dx.doi.org/10.15222/TKEA2020.1-2.22 . (in Russian)

[12] A.I. Kondrik, G.P. Kovtun, Tekhnologiya i Konstruirovanie v Elektronnoi Apparature, no. 5-6, 43–50 (2019), https://dx.doi.org/10.15222/TKEA2019.5-6.43. (in Russian)

[13] G.F. Knoll, *Radiation detection and measurement*, 4th ed. (John Wiley & Sons, Inc., 2010), p. 864.

[14] B. Fraboni, L. Pasquini, A. Castaldini, and A. Cavallini, Journal of Applied Physics, **106**, 093713 – 093713-6 (2009), https://dx.doi.org/10.1063/1.3253748 .

[15] Ruihua Nan, Tao Wang, Gang Xu, Man Zhu, and Wanqi Jie, Journal of Crystal Growth, **451**, 150–154 (2016). https://doi.org/10.1016/j.jcrysgro.2016.07.032 .

[16] Rui-hua NAN, Wan-qi JIE, Gang-qiang ZHA, Xu-xu BAI, Bei WANG, and Hui YU, Transactions of Nonferrous Metals Society of China, **22**, 148–152 (2012), https://doi.org/10.1016/S1003-6326(12)61700-2.

[17] G.F. Novikov, and N.A. Radychev, Russian Chemical Bulletin, **56**(5), 890–894 (2007), https://doi.org/10.1007/s11172-007-0134-9.

[18] Lei Bao, Gangqiang Zha, Lingyan Xu, Binbin Zhang, Jiangpeng Dong, Yingrui Li, and Wanqi Jie, Materials Science in Semiconductor Processing, **100**, 179–184 (2019), https://doi.org/10.1016/j.mssp.2019.05.002.

ДЕГРАДАЦІЯ ПІД ВПЛИВОМ РАДІАЦІЙНИХ ДЕФЕКТІВ ДЕТЕКТОРНИХ ВЛАСТИВОСТЕЙ $Cd_{0.9}Zn_{0.1}Te$, ОПРОМІНЕНОГО НЕЙТРОНАМИ

О.І. Кондрик[a], Г.П. Ковтун[a,b]

[a]Національний науковий центр «Харківський фізико-технічний інститут» НАНУ
61108, вул. Академічна 1, Харків, Україна.
[b]Харківський національний університет імені В.Н. Каразіна
майдан Свободи, 4, 61022, Харків, Україна

Представлена робота присвячена дослідженню методом комп'ютерного моделювання механізмів впливу радіаційних дефектів, що виникають під дією нейтронного опромінення, на зміну електрофізичних властивостей - питомого опору ρ, електронної рухливості μ_n, часу життя нерівноважних електронів τ_n та дірок τ_p, в $Cd_{0.9}Zn_{0.1}Te$ і ефективності збору зарядів неохолоджуваного детектору іонізуючих випромінювань η на основі цього матеріалу. Радіаційні дефекти, яким в забороненій зоні відповідають глибокі рівні енергії, діють як центри захоплення нерівноважних носіїв заряду, помітно впливають на ступінь компенсації, змінюючи ρ детекторного матеріалу, на процеси рекомбінації, знижуючи τ_n і τ_p, а також на розсіювання електронів провідності, зменшуючи μ_n, що зрештою здатне викликати деградацію ефективності збору зарядів η. Були з'ясовані конкретні причини погіршення електрофізичних та детекторних властивостей під дією нейтронного опромінення та встановлені основні фактори, які впливають на підвищення питомого опору $Cd_{0.9}Zn_{0.1}Te$ при бомбардуванні тепловими та високоенергетичними нейтронами, що призводять до повної деградації реєструвальної здатності детекторів на основі цього матеріалу. Рекомбінація нерівноважних носіїв заряду помітно сильніше ніж зниження μ_n впливає на деградацію детекторних властивостей, тому був досліджений вплив процесів рекомбінації через глибокі рівні радіаційних дефектів на деградацію τ_n, τ_p, η детектору на основі $Cd_{0.9}Zn_{0.1}Te$. Проведено порівняльний аналіз властивостей $Cd_{0.9}Zn_{0.1}Te$ і раніш дослідженого CdTe:Cl. Зроблена спроба пояснення більш високої радіаційної стійкості $Cd_{0.9}Zn_{0.1}Te$ у порівнянні з CdTe:Cl при нейтронному опроміненні впливом механізму радіаційної самокомпенсації за участю більш глибоких донорних рівнів енергії: міжвузлового телуру, телуру на місці кадмію. Крім того, внаслідок меншої різниці між рівнем Фермі і рівнями радіаційних дефектів в телуриді кадмію темп рекомбінації через рівні дефектів в $Cd_{0.9}Zn_{0.1}Te$ при інших рівних умовах нижчий, ніж в CdTe:Cl. Також був відзначений зв'язок між шириною забороненої зони $Cd_{0.9}Zn_{0.1}Te$ і CdZn:Cl, концентрацією радіаційних дефектів, дрейфом рівня Фермі в процесі опромінення та радіаційною стійкістю детекторів. Вказано на важливу роль чистоти і концентрації легуючого мілкого донора в початковому стані детекторного матеріалу.

КЛЮЧОВІ СЛОВА: детекторні властивості, моделювання, CdZnTe, CdTe, опромінення нейтронами, радіаційні дефекти

ДЕГРАДАЦИЯ ПОД ВЛИЯНИЕМ РАДИАЦИОННЫХ ДЕФЕКТОВ ДЕТЕКТОРНЫХ СВОЙСТВ $Cd_{0.9}Zn_{0.1}Te$, ОБЛУЧЁННОГО НЕЙТРОНАМИ

А.И. Кондрик[a], Г.П. Ковтун[a,b]

[a]Национальный научный центр «Харьковский физико-технический институт» НАНУ
61108, ул. Академическая 1, Харьков, Украина.
[b]Харьковский национальный университет имени В.Н. Каразина
пл. Свободы, 4, 61022, Харьков, Украина

Данная работа посвящена исследованию методом компьютерного моделирования механизмов влияния радиационных дефектов, возникающих под действием нейтронного облучения на изменение электрофизических свойств - удельного сопротивления ρ, электронной подвижности μ_n, времени жизни неравновесных электронов τ_n и дырок τ_p, в $Cd_{0.9}Zn_{0.1}Te$ и эффективности сбора зарядов неохлаждаемых детекторов ионизирующих излучений η на основе этого материала. Радиационные дефекты, которым в запрещённой зоне соответствуют глубокие уровни энергии, действуют как центры захвата неравновесных носителей заряда, заметно влияют на степень компенсации, изменяя ρ детекторного материала, на процессы рекомбинации, снижая τ_n и τ_p, а также на рассеяние электронов проводимости, уменьшая μ_n, что в конечном итоге приводит к деградации эффективности сбора зарядов η. Были выяснены конкретные причины ухудшения электрофизических и детекторных свойств под действием нейтронного облучения и установлены основные факторы, влияющие на повышение удельного сопротивления $Cd_{0.9}Zn_{0.1}Te$ при бомбардировке тепловыми и высокоэнергетическими нейтронами, приводящих к полной деградации регистрирующей способности детекторов на основе этого материала. Рекомбинация неравновесных носителей заряда заметно сильнее чем снижение μ_n влияет на деградацию детекторных свойств, поэтому было исследовано влияние процессов рекомбинации через глубокие уровни радиационных дефектов на деградацию τ_n, τ_p, η детектора на основе $Cd_{0.9}Zn_{0.1}Te$. Проведён сравнительный анализ свойств $Cd_{0.9}Zn_{0.1}Te$ и ранее исследованного CdTe:Cl. Сделана попытка объяснения более высокой радиационной стойкости $Cd_{0.9}Zn_{0.1}Te$ по сравнению с CdTe:Cl при нейтронном облучении влиянием механизмом радиационной самокомпенсации с участием более глубоких донорных уровней энергии: межузельного теллура, теллура на месте кадмия. Кроме того, вследствие меньшей разницы между уровнем Ферми и уровнями радиационных дефектов в теллуриде кадмия темп рекомбинации через уровни дефектов в $Cd_{0.9}Zn_{0.1}Te$ при прочих равных условиях ниже, чем в CdTe:Cl. Также был отмечена связь между шириной запрещённой зоны $Cd_{0.9}Zn_{0.1}Te$ и CdZn:Cl, концентрацией радиационных дефектов, дрейфом уровня Ферми в процессе облучения и радиационной стойкостью детекторов. Указано на важную роль чистоты и концентрации легирующего мелкого донора в исходном состоянии детекторного материала.

КЛЮЧЕВЫЕ СЛОВА: детекторные свойства, моделирование, CdZnTe, CdTe, облучение нейтронами, радиационные дефекты

STRUCTURAL FEATURES AND OPERATIONAL CHARACTERISTICS OF STEEL T91

Victor Voyevodin, Mikhail Tikhonovsky, Galyna Tolstolutska, Hanna Rostova,
Ruslan Vasilenko, Oleksandr Kalchenko, Natalya Andrievska, Oleksii Velikodnyi

National Science Center "Kharkov Institute of Physics and Technology"
1, Akademicheskaya Str., Kharkov 61108, Ukraine
*E-mail: rostova@kipt.kharkov.ua
Received May 20, 2020; accepted June 30, 2020

The microstructure and radiation resistance of T91 martensitic steel were studied after thermomechanical treatment. The physical and technological foundations of the process of creating of a nanostructured state in T91 reactor steel have been developed. This structure was received by severe plastic deformation of T91 steel by the multiple "upsetting-extrusion" method (developed at the NSC KIPT) in two temperature ranges of deformation: in the region of austenite existing and with a successive decrease in the deformation temperature and an increase in cycles of "upsetting-extrusion" in the field of ferrite existence. For the further heat treatment the particular temperature range and deformation modes were chosen to obtain optimal structure. Also, the optimum temperature of tempering to receive the uniform structure was established. It was found that the average grain size of T91 steel decreases from 20 μm in the initial state to ~ 140 nm after 5 cycles of "upsetting-extrusion" in the ferrite interval and to ~ 100 nm after 3 cycles of deformation in the austenitic region. It was determined that with an increase in the number of cycles and a decrease in the deformation temperature, a rise in the degree of uniformity of grain size distribution occurs. In this case, the microhardness increases from 2090 MPa to 2850 MPa after 5 cycles of "upsetting-extrusion" in the ferritic interval. In the austenitic region, the microhardness values increase from 3400 to 3876 MPa. The swelling of T91 steel in two structural states, martensitic and ferritic, was determined. Thus, steel swelling at a high dose of irradiation with argon ions with an energy of 1.4 MeV (120 displacements per atom, irradiation temperature 460 ° C) is $\Delta V / V = 0.26\%$ in the initial state (martensitic structure) and 0.65% for samples with a ferritic structure.
KEYWORDS: martensitic steel, thermomechanical treatment, microhardness, nanostructure, severe plastic deformation, radiation resistance.

The creation of GenIV fission and fusion reactors poses new problems in materials science in terms of higher operating temperatures, increased neutron doses, as well as ensuring the safe and efficient operation of reactors. The problem of conventional structural materials, in particular austenitic steels, lies in the fact that they will not be able to be operated under more severe irradiation conditions due to their low radiation resistance. Ferritic and / or martensitic steels are considered as potential structural materials for their good resistance to irradiation, less swelling, better ductility, etc. [1, 2]. In particular, T91 martensitic steel is considered as a promising material for future new generation nuclear reactors [3]. However, the steels of these classes have a significant drawback - heat resistance, which limits the maximum working temperature to ~ 500 °C. The main way of solving this problem is thermomechanical treatment, which allows not only to qualitatively improve the mechanical characteristics, but also to increase the radiation resistance of the material.

The standard technological scheme for the heat treatment of T91 martensitic steel consists in normalization at temperatures of 1040–1080 °C followed by air cooling [4]. In this case, the microstructure of quenched martensite is formed, which leads to high strength but low ductility of steel. To increase ductility, steel is tempered at temperatures of 730–780 °C. As a result, there is a formation of a coarse-grained microstructure with inhomogeneity in grain size. Although ductility increases considerably, the strength characteristics are reduced. A significant improvement in mechanical properties can be expected when an ultrafine-grained or nanostructured state is produced in steel, which usually contributes to an increase in the radiation tolerance of the material [5, 6]. The creation of such a microstructure is possible using thermomechanical treatment using severe plastic deformation (SPD), carried out by various methods [7 - 9].

A distinctive feature of T91 steel in comparison with other steels of the ferritic-martensitic class is the high sensitivity of its structure to the composition and type of heat treatment, and, as a result, a large data scattering of the swelling values for the same exposure conditions [10-12]. Optimization of the factors of the structural-phase state of T91 steel and study of its swelling in various structural states is needed.

The excellent swelling resistance of ferritic-martensitic alloys compared to austenitic stainless steels is well proven. The mechanisms of this phenomenon (higher self-diffusion rate, low preference factor for high dislocation density, low rate of helium generation, strong defect capture, microstructural lamellas and subgrains, boundary effects, etc.) are well described in the literature [13]. However, a comparison of the swelling of 9-12 wt. % Cr ferritic-martensitic steels shows a significant data scattering [14]. The reason for this scatter may be a difference in the structure and composition of the studied steels.

The aim of the study was to optimize the factors of the structural-phase state (grain size, parameters of secondary phase precipitation, degree of decomposition of the solid solution) to increase operational characteristics and to compare the level of swelling for two different structure states.

To achieve the goal of the study, the following tasks were set:
- to develop a technology for creating an ultrafine-grained structure, which can be used on an industrial scale;
- determine the optimal parameters of deformation and heat treatment to obtain a uniform and stable microstructure;
- to examine the effect of thermomechanical treatment and the type of obtained structures on the radiation tolerance of T91 steel.

MATERIAL AND METHODS

T91 steel manufactured by INDUSTELL, Belgium (melting: 504/3, heat: 82566-4) was supplied in the form of a 40 mm thick plate obtained by hot rolling followed by heat treatment. The heat treatment includes normalization at 1040 °C for 30 minutes, followed by air cooling and then tempering at 730 °C for 60 minutes with air cooling to room temperature (the so-called N&T state). The chemical composition of T91 steel is shown in Table 1.

Table 1.
The chemical composition of T91, (wt.%)

Fe	*Cr*	*Mo*	*Mn*	*Si*	*V*	*Ni*	*Nb*	*Cu*
bulk	8.76	0.862	0.597	0.317	0.186	0.099	0.073	0.054
Al	*C*	*N*	*P*	*S*	*Sn*	*B*	*Co*	*As*
0.021	0.088	0.003	0.019	0.0006	0.005	0.0001	0.019	0.007

In the present study the multi-cycle "upsetting-extrusion" method was chosen to carry out the SPD. The method was developed in NSC KIPT and it has proved itself both in laboratory research and in the industrial production of a number of materials with high characteristics [15, 16]. This method consists in multiple reiterations of operations of upsetting and extrusion on a hydraulic press ДБ 2432 with a force of 160 tf. The method is described in more detail in [17].

Deformation was carried out in two temperature regions: austenitic-ferritic at a temperature 870 °C and ferritic at temperatures 750 - 575 °C. Samples with a 20 mm diameter and a 60 mm height were subjected to upsetting to a diameter 30 mm and then again extruded to a diameter of 20 mm.

"Upsetting-extrusion" cycles in the ferritic region were carried out with a gradual decrease in the deformation temperature from 750 °C on the first cycle to 575 °C on the last, fifth cycle. In general, the temperature regime of the "upsetting-extrusion" cycles was as follows: 750-700-650-635-575 ° C.

To determine the stability of microstructures formed as a result of SPD, heat treatments were carried out in the temperature range 550–750 ° C for 1–50 hours.

Understanding the evolution of the microstructure during irradiation and its effect on the decline of mechanical properties is of a paramount importance. Neutron irradiation has several disadvantages, including high cost, residual activity, and prolonged irradiation of samples. Furthermore, many nuclear facilities, such as FFTF, RAPSODIE, DFR, PFR, Superfenix, EBR-II, BR-10, BN-350, etc. - are shut down.

The applying of heavy ion implantation to simulate neutron irradiation in a reactor is common practice by reason of the high rate of achievement of relatively high levels of damage and the absence of induced radioactivity.

Samples of steel T91 in the initial state (martensitic structure) and after severe plastic deformation (ferritic structure) were irradiated with argon ions with energy 1.4 MeV to a dose 120 dpa at a temperature 460 °C. This irradiation temperature was chosen due to the fact that the peak of temperature swelling for steel T91 falls on ~ 460 °C. All irradiations were carried out using the acceleration-measuring system "ESU-2" containing the Van de Graaff accelerator. The depth distribution of Ar atoms concentration and damage was calculated by SRIM 2008 [18] (Fig. 1). Damage calculations are based on the Kinchin-Pease model, with a displacement energy of 40 eV for Fe and Cr, as recommended in ASTM E521-96 (2009) [19].
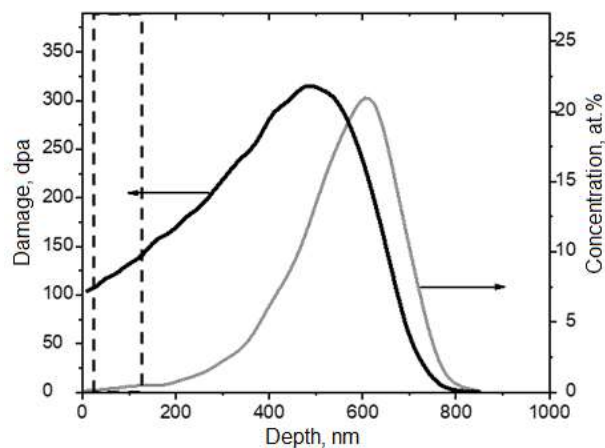

Figure 1. Calculated profiles of damages and concentrations of 1.4 MeV Ar ions implanted in T91 steel to a dose of $5×10^{17}$ cm^{-2}. The area of study is marked with a dash.

The steel structure was studied by metallography and electron microscopy using electron microscopes JEM-100CX and JEM-2100. Microhardness was measured on a semi-automatic microindenter LM 700AT at a load 200 g.

RESULTS AND DISSCUSSION

The microstructure of T91 steel in initial state is shown in Fig. 2. The structural state of tempered martensite is characterized by the presence of prior austenite grain boundaries. These boundaries are decorated with $M_{23}C_6$ carbide precipitates. The prior austenite grain size is about 20 μm, the size (thickness) of $M_{23}C_6$ precipitates varies from about 100 to 200 nm. Inside the prior austenite grains, martensitic lamellas with a transverse size of 0.25-0.5 μm are observed.

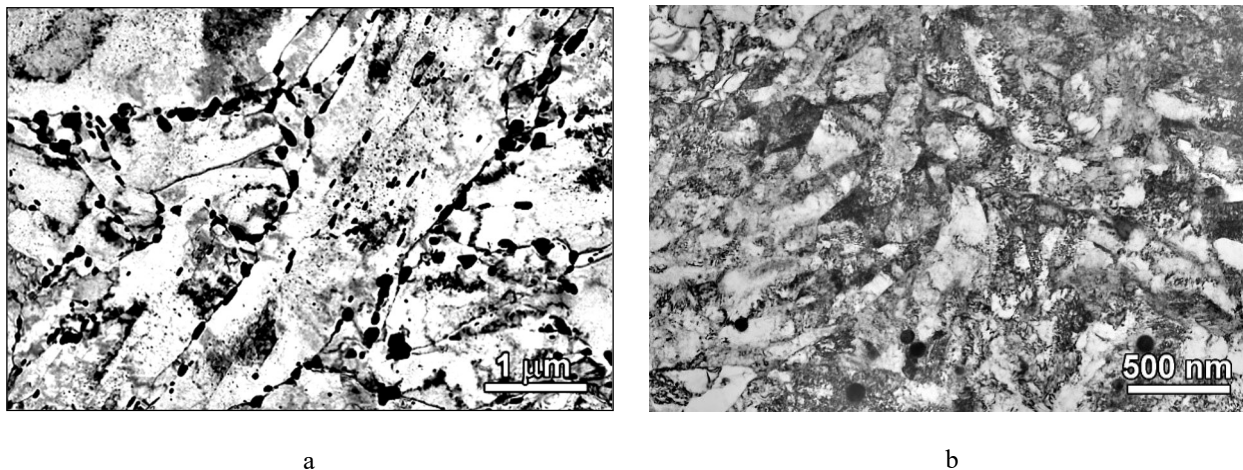a   b

Figure 2. The microstructure of steel T91: a – in initial state, b – after 3 cycles of "upsetting-extrusion" at 870 ºC

The finely dispersed microstructure of steel after 3 cycles of "upsetting-extrusion" at a temperature 870 °C belongs to the martensitic-ferritic type (Fig. 2b). From a comparison of Fig. 2a and b, it can be seen that the SPD led to a significant refinement of the martensitic structure.

The microstructure that formed after treatment in the ferritic range with a gradual decrease in temperature and the ferrite grains size distribution are shown in Fig. 3. The average grain size was 145 nm.
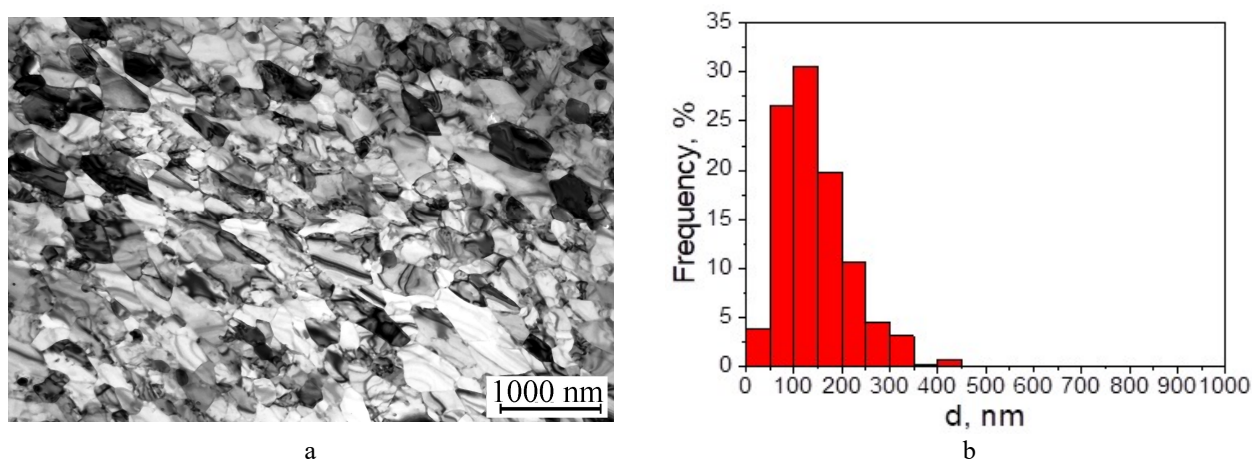

a   b

Figure 3. The microstructure of steel after 5 cycles of "upsetting-extrusion"in the ferritic range (a) and grain size distribution (b)

The results of the microhardness measuring of the samples after heat treatment in the temperature range of 550-750 °C for 1-50 hours showed that high mechanical characteristics are maintained during exposure at a temperature of 550 °C. It was found, that, the temperature of 550 °C is the optimal regime for tempering, which allow to stabilize the structure, since at higher temperatures there is recrystallization and, as a result, a decrease in hardness. Therefore, for further studies, a sample that underwent heat treatment for 25 hours at a temperature of 550 °C was selected. The average grain size for sample with a ferritic structure was 210 nm, and the microhardness was at the level of 2948 MPa. The microstructure of the sample is shown in Fig. 4.

To compare the degree of swelling, austenitic steel SS316 was chosen which is now used as a structural material of the current generation of reactors. Herewith, irradiation of SS316 steel was carried out under the following conditions: dose - 80 dpa, temperature - 615 °C. The microstructure of irradiated steels is shown in Fig. 5. For three types of samples, namely, T91 steel with martensitic and ferritic structures and steel SS316 with an austenitic structure, the formation of a void structure is observed.
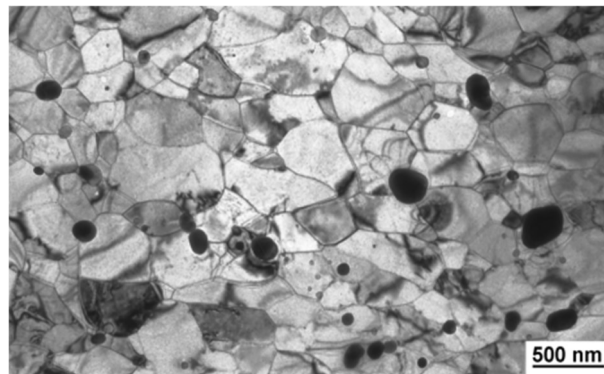
Figure 4. The microstructure of the sample of steel T91 after heat treatment at 550°C for 25 h after the SPD in a ferritic range
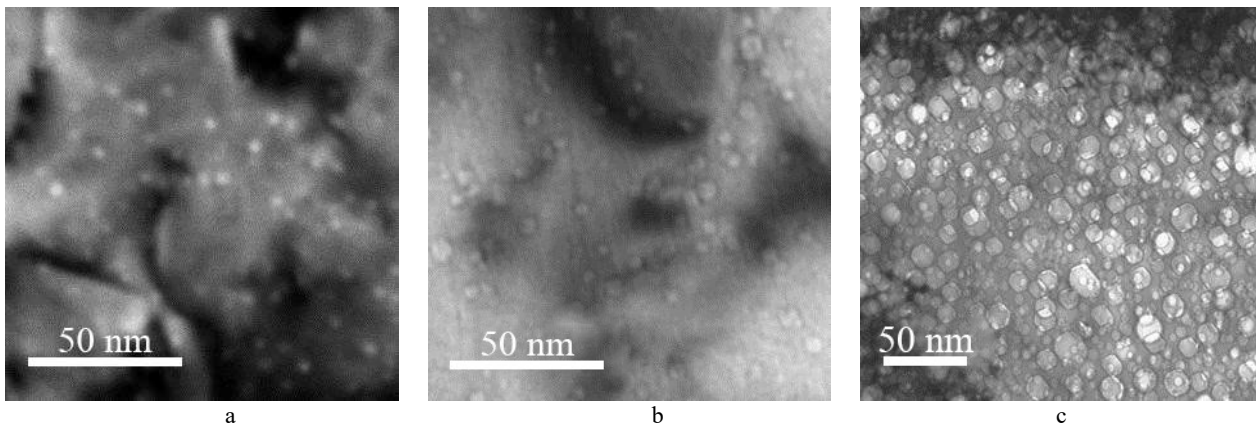

a b c

Figure 5. The microstructure of steel T91 for samples with martensitic (a) and ferritic (b) structures, irradiated to a dose 120 dpa
(E = 1,4 MeV Ar⁺) at 460°C and austenitic steel SS316, irradiated to a dose 80 dpa at 615°C (c)

Using experimentally determined parameters of a void structure, the swelling value S was calculated by the formula (1):

$$S = \frac{\frac{\pi}{6 \cdot A \cdot h} \sum_{i=1}^{N} d_i^3}{1 - \frac{\pi}{6 \cdot A \cdot h} \sum_{i=1}^{N} d_i^3} \cdot 100\%, \qquad (1)$$

where d_i-diameter of i-th void; N- the number of voids on the image; A- area of the image with which the calculations were carried out; h- sample foil thickness.

The parameters of void structure and the magnitude of the swelling are shown in Table 2.

Table 2.
Diameter d, number density ρ of voids and swelling values S

Sample	d, nm	ρ, 1/m³	S, %
T91 Martensitic	2,9	1×10^{23}	0,26
T91 Ferritic	6,6	$5,8 \times 10^{22}$	0,65
SS316 Austenite	18	$9,3 \times 10^{21}$	15,6

A comparison of the steel with a martensitic and ferritic structure (Fig. 5 a, b) showed that the level of swelling of the sample in the martensitic state is 2.5 times lower than in the ferritic state. It should be noted that the swelling of the ferritic structure (BCC) is 24 times less than the austenitic structure (FCC). Such a large difference in the levels of swelling is associated with the difference in the types of crystal lattices of these materials, and as a result, with different mechanisms of the development of radiation damage.

In [14], data on the swelling of ferritic-martensitic steels irradiated with neutrons up to a dose of 208 dpa in a temperature range from 400 to 443 °C were compared (Fig. 6). Let's note several key features. There is a general tendency to swelling at a rate of ~ 0.01% / dpa, although the data are very scattered. In general, there is a large difference in swelling between alloys (HT9 and T91), though T91 tends to swell more for a given level of damage. Finally, the swelling of HT9 steel of the same heat of 9607R2, but of different heat treatment, differs by an order of

magnitude (see Fig. 6). Our data - indicated by a triangle and a star in a dashed rectangle - show that the scatter may be due to the different microstructure states that form before irradiation (ferrite (★) or martensite (▲)).

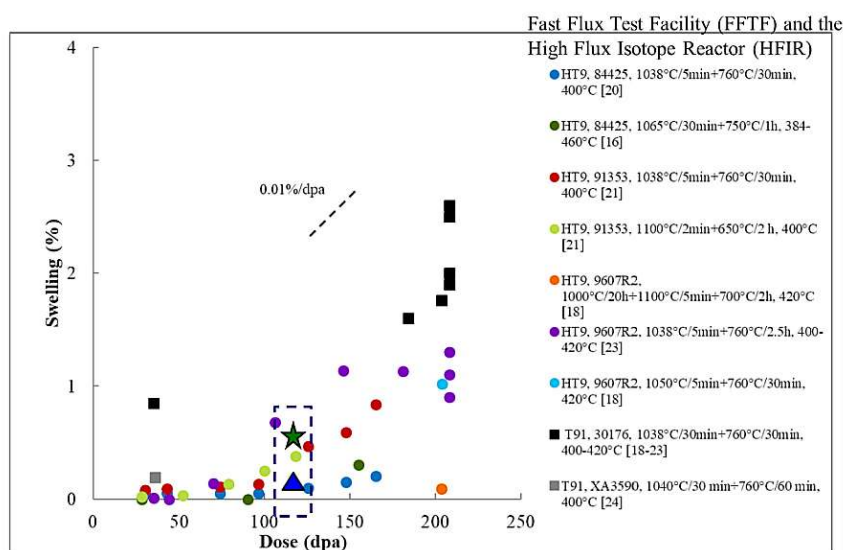Further studies are needed to study the level of swelling at even higher radiation doses.

Figure 6. Generalized data for steels HT9 and T91 irradiated in a reactor to a dose 208 dpa at temperatures from 400 to 443ºC [14]

CONCLUSIONS

The effect of thermomechanical treatment on the type of obtained structures of T91 steel is investigated. It was shown that the receiving of a nanostructure can be achieved by severe plastic deformation method. The factors of the structural-phase state of T91 martensitic steel have been optimized during thermomechanical treatment by the method of multiple "upsetting-extrusion". The optimal parameters of deformation and temperature regimes for obtaining a uniform ultrafine-grained structure are determined.

Severe plastic deformation combined with heat treatment allows to reduce the average grain size. After 5 cycles of multiple "upsetting-extrusion" in the ferritic range, the minimum average grain size of ~ 140 nm was achieved. The average grain size of the initial steel (martensitic structure) is 20 μm.

A study of the development of void structure after irradiation of steel T91 in various structural states was carried out. It was shown that after irradiation with Ar ions with an energy 1.4 MeV to a dose 120 dpa at T = 460 °C, the swelling in the ultrafine-grained ferritic structure is 0.65% compared with 0.26% for the initial martensitic structure, which confirms the influence of structural-phase state of steel T91 on its swelling.

The swelling of steel with an austenitic structure is ~ 15.6%, which is 24 times more than the level of swelling of steel with a ferritic structure.

ORCID IDs

Victor Voyevodin, https://orcid.org/0000-0003-2290-5313; **Mikhail Tikhonovsky** https://orcid.org/0000-0001-5889-0366,
Galyna Tolstolutska https://orcid.org/0000-0003-3091-4033; **Hanna Rostova** https://orcid.org/0000-0003-1329-9016,
Ruslan Vasilenko https://orcid.org/0000-0002-4029-9727; **Oleksandr Kalchenko** https://orcid.org/0000-0003-0856-1868,
Natalya Andrievska https://orcid.org/0000-0001-5326-4235; **Oleksii Velikodnyi** https://orcid.org/0000-0001-5088-6143

REFERENCES

[1] R. Klueh and D. Harries, *High-Chromium Ferritic and Martensitic Steels for Nuclear Applications,* ed. (ASTM International, West Conshohocken, 2001), pp. 221, https://doi.org/10.1520/MONO3-EB.
[2] R. Klueh, Philosophical Magazine. **98**(2012), 2618-2636 (2008), https://doi.org/10.1080/14786435.2018.1497307.
[3] S. Baindur, Bulletin of the Canadian Nuclear Society, **29**(1), 32-38 (2008).
[4] https://www.astm.org/Standards/A213.htm.
[5] M. Song, C. Sun, Z.Fan, Y. Chen, R.Zhu, K.Y. Yu, K.T. Hartwig, H.Wang, and X.Zhang, Acta Materialia, **112**, 361-377 (2016), https://doi.org/10.1016/j.actamat.2016.04.031.
[6] R.A. Andrievskii, The Physics of Metals and Metallography. **110**(3), 229–240 (2010), https://doi.org/10.1134/S0031918X10090061.
[7] M.V. Karavaeva, M.A. Nikitina, A.V. Ganeev, R.K. Islamgaliev, IOP Conf. Series: Materials Science and Engineering. **179**, 012037 (2017), https://doi.org/10.1088/1757-899X/179/1/012037.

[8] D.C. Foley, K.T. Hartwig, S.A. Maloy, P. Hosemann, X. Zhang, Journal of Nuclear Materials. **389**, 221-224 (2009), http://doi.org/10.1016/j.jnucmat.2009.02.005.

[9] Z.Q. Fan, T. Hao, S.X. Zhao, G.N. Luo, C.S. Liu, Q.F. Fang, Journal of Nuclear Materials. **434**, 417–421 (2013), https://doi.org/10.1016/j.jnucmat.2012.12.009.

[10] D.S. Gelles, Journal of Nuclear Materials. **233-237**, 293-298 (1996), https://doi.org/10.1016/S0022-3115(96)00222-X.

[11] J.J. Kai, R.L. Klueh, Journal of Nuclear Materials. **230**, 116-123 (1996), https://dx.doi.org/10.1016/0022-3115(96)00165-1.

[12] J. Van Den Bosch, O. Anderoglu, R. Dickerson, M. Hartl, et al., Journal of Nuclear Materials. **440**, 91-97 (2013), https://dx.doi.org/10.1016/j.jnucmat.2013.04.025.

[13] M.B. Toloczko, F.A. Garner, C.R. Eiholzer, Journal of Nuclear Materials. **215**, 604-607 (1994), https://doi.org/10.1016/0022-3115(94)90131-7.

[14] E. Getto, K. Sun, A.M. Monterrosa, et al., Journal of Nuclear Materials. **480**, 159-176 (2016), https://doi.org/10.1016/j.jnucmat.2016.08.015.

[15] O.V. Chorniy, Ya.D. Starodybov, O.I. Volchok, G.E. Storozhilov, Patent Ukraine No. 42487 A (15 January 2001). (in Ukrainean)

[16] I.I. Papirov, G.F. Tikhinskiy, The Physics of Metals and Metallography. **29**(5), 1057-1060 (1970). (in Russian)

[17] V.M. Azhazha, O.V. Chorniy, G.E. Storozhilov, N.F. Andrievskaya, T.U. Rydicheva, Problems of Atomic Science and Technology, Series: "Vacuum, Pure Materials, Superconductors", **6**(14), 136 -139 (2004). (in Russian)

[18] J.F. Ziegler, Version – SRIM-2008.04, www.srim.org.

[19] ASTM E521-96, *Standard Practice for Neutron Radiation Damage Simulation by Charged-Particle Irradiation*, https://www.astm.org/DATABASE.CART/HISTORICAL/E521-96.htm.

СТРУКТУРНІ ОСОБЛИВОСТІ ТА ЕКСПЛУАТАЦІЙНІ ХАРАКТЕРИСТИКИ СТАЛІ Т91
В.М. Воєводін, М.А. Тихоновський, Г.Д. Толстолуцька, Г.Ю. Ростова, Р.Л. Василенко,
О.С. Кальченко, Н.Ф. Андрієвська, О.М. Великодний
Національний науковий центр «Харківський фізико-технічний інститут»
вул. Академічна 1, Харків 61108, Україна

Досліджено мікроструктуру і радіаційну стійкість мартенситної сталі Т91 після термомеханічної обробки. Розроблено фізико-технологічні основи процесу створення наноструктурного стану в реакторній сталі Т91. Ця структура була отримана в результаті інтенсивної пластичної деформації сталі Т91 методом багаторазового «осадження-вичавлювання», розробленим в ННЦ ХФТІ, в двох температурних діапазонах: в області існування аустеніту і з послідовним зниженням температури деформації і збільшенням циклів «осадження-вичавлювання» в області існування фериту. Для подальшої термообробки були обрані особливі температурний діапазон і режими деформації для отримання оптимальної структури. Також була знайдена оптимальна температура відгартовування для отримання однорідної структури. Було виявлено, що середній розмір зерна сталі Т91 зменшується з 20 мкм в вихідному стані до ~ 140 нм після 5 циклів «осадження-вичавлювання» в феритному інтервалі і до ~ 100 нм після 3 циклів деформації в аустенітній області. Було встановлено, що зі збільшенням кількості циклів і зниженням температури деформації відбувається підвищення ступеню однорідності розподілу зерен за розмірами. В цьому випадку мікротвердість збільшується з 2090 МПа до 2850 МПа після 5 циклів «осадження-вичавлювання» в феритному інтервалі. В аустенітній області значення мікротвердості збільшуються з 3400 до 3876 МПа. Визначено розпухання сталі Т91 в двох структурних станах - мартенситному та феритному. Так, розпухання сталі при високій дозі опромінення іонами аргону з енергією 1,4 МеВ (120 зсувів на атом, температура опромінення 460ºС) становить $\Delta V / V$ = 0.26% в вихідному стані (мартенситна структура) і 0,65% для зразків з феритною структурою.

КЛЮЧОВІ СЛОВА: мартенситна сталь, термомеханічна обробка, мікротвердість, наноструктура, інтенсивна пластична деформація, радіаційна стійкість.

СТРУКТУРНЫЕ ОСОБЕННОСТИ И ЭКСПЛУАТАЦИОННЫЕ ХАРАКТЕРИСТИКИ СТАЛИ Т91
В.Н. Воеводин, М.А. Тихоновский, Г.Д. Толстолуцкая, А.Ю. Ростова, И.Е. Копанец,
Р.Л. Василенко, А.С. Кальченко, Н.Ф. Андриевская, А.Н. Великодный
Национальный научный центр «Харьковский физико-технический институт»
ул. Академическая 1, Харьков 61108, Украина

Исследована микроструктура и радиационная стойкость мартенситной стали Т91 после термомеханической обработки. Разработаны физико-технологические основы процесса создания наноструктурного состояния в реакторной стали Т91. Эта структура была получена в результате интенсивной пластической деформации стали Т91 методом многократной «осадки-выдавливания», разработанным в ННЦ ХФТИ, в двух температурных диапазонах: в области существования аустенита и с последовательным снижением температуры деформации и увеличением циклов «осадки-выдавливания» в области существования феррита. Для дальнейшей термообработки были выбраны особые температурный диапазон и режимы деформации для получения оптимальной структуры. Также была найдена оптимальная температура отпуска для получения однородной структуры. Было обнаружено, что средний размер зерна стали Т91 уменьшается с 20 мкм в исходном состоянии до ~ 140 нм после 5 циклов «осадки-выдавливания» в ферритном интервале и до ~ 100 нм после 3 циклов деформации в аустенитной области. Было установлено, что с увеличением числа циклов и уменьшением температуры деформации происходит повышение степени однородности распределения зерен по размерам. В этом случае микротвердость увеличивается с 2090 МПа до 2850 МПа после 5 циклов «осадки-выдавливания» в ферритном интервале. В аустенитной области значения микротвердости увеличиваются с 3400 до 3876 МПа. Определено распухание стали Т91 в двух структурных состояниях - мартенситном и ферритном. Так, распухание стали при высокой дозе облучения ионами аргона с энергией 1,4 МэВ (120 смещений на атом, температура облучения 460ºС) составляет $\Delta V/V$ = 0.26% в исходном состоянии (мартенситная структура) и 0,65% для образцов с ферритной структурой.

КЛЮЧЕВЫЕ СЛОВА: мартенситная сталь, термомеханическая обработка, микротвердость, наноструктура, интенсивная пластическая деформация, радиационная стойкость.

DUCTILE AND METALLIC NATURE OF Co₂VZ (Z= Pb, Si, Sn) HEUSLER COMPOUNDS: A FIRST PRINCIPLES STUDY

Sukhender[a], Pravesh Pravesh[b], Lalit Mohan[a], Ajay Singh Verma*,[a]

ᵃDepartment of Physics, Banasthali Vidyapith, Banasthali 304022, India
ᵇDepartment of Electronics and Communication Engineering, KIET Group of Institutions
Ghaziabad, Uttar Pradesh (India) 201206
*Corresponding Author: ajay_phy@rediffmail.com
Received April 21, 2020; accepted May 25, 2020

Herein, optoelectronic, elastic and magnetic properties of L2₁ structured Co₂VZ (Z= Pb, Si, Sn) full Heusler compounds have been investigated by two methods. One is full potential linearized augmented plane wave (FP-LAPW) method as implemented in WIEN2k and second is pseudo potential method as implemented in Atomistic Tool Kit-Virtual NanoLab (ATK-VNL). All these compounds shows zero band gap in majority spin channel in the both simulation codes and a finite band gap are 0.33 and 0.54 eV in Co₂VZ (Z= Pb, Sn) alloys (semiconducting) respectively. This is due to minority-spin channel near the Fermi level as implemented in WIEN2k code and showing 100% spin polarization except Co₂VSi (metallic) with zero band gap. These compounds found to be perfectly half-metallic ferromagnetic (HMF). However, above mentioned compounds shows finite band gaps in ATK-VNL code. The calculated magnetic moment of these compounds Co₂VZ (Z= Pb, Si, Sn) are 3.00 and 3.00, 3.02 and 2.96, 3.00 and 3.00μ_B in WIEN2k and ATK-VNL codes respectively. Thus, we have observed that the calculated vales by these simulation codes and Slater-Pauling rule have nice tuning. Optical properties of these compounds like as reflectivity, refractive index, excitation coefficient, absorption coefficient, optical conductivity and electron energy loss have been analyzed. Absorption coefficient and electron energy - loss function values are increases as we increase the value of energy. The vales of Pugh's ratio B/G is greater than 1.75 for all compounds and showing ductile nature with positive value of Cauchy pressure (C_P = C₁₂ − C₄₄) and shows metallic behavior of Co₂VZ (Z= Pb, Si, Sn) compounds.
KEYWORDS: Half-metallic ferromagnetic, band gap, Spintronics, magnetic moment, elastic constants

Half metallic ferromagnetic behavior of Heusler alloys fascinates the new researchers towards it, because exclusive approach in Spintronics [1-3]. If either one spin channel shows band gap and other shows zero band gap at Fermi level then the Heusler compounds exhibit 100% spin polarization [4-7]. Half metallic ferromagnetic was first discovered by de Groot in the year of 1983 in a half Heusler compound NiMnSb [8-9]. Due to high Curie temperature and spin magnetic moment, researchers show intensive interest in Heusler [10-11]. We are here going to investigate the properties of Co-based full Heusler compounds Co₂VZ (Z= Pb, Si, Sn). Half metallic ferromagnetism in Co- based full Heusler compounds Co₂MnSn, Co₂TiAl and Co₂TiSn was firstly scouted by Ishida et al. [12] using LDA method. But they are failure to observe half metallic ferromagnetism in these compounds. Kubler et al. [13] have resolved this complexity by analysis of formation and coupling of magnetic moment in the compounds Co₂MnSn and similarly Co-based alloys in the same year. They also represent the linear relationship between numbers of valence electrons and spin magnetic moment. Further, this relationship is main backbone of Slater-Pauling rule. According to this rule, if count of valence electron is equal to 24, then that compound shows zero magnetic moment and if, count of valence electron is different to 24, and then difference between the total number of valence electron and 24 represent the net amount of spin magnetic moment [14]. Kubler et al. [15] have observed in Co-based compound that there exists a straightforward relationship between Curie temperature and spin magnetic moment i.e. Curie temperature is directly proportional to the spin magnetic moment. Spintronics have vast area of application in the fields of magnetic memory device, magnetic sensor, tunnel junction, increased data processing speed, increased integration intensities and it also reduce the consumption of electricity [16-19]. Galanakis et al. [20] and Block et al. [21] have investigated the electronic and magnetic properties of a number of Heusler compounds and observed that most of them are half metallic and go along with Slater-Pauling rule. we are going to calculate the structural, electronic, optical, elastic and magnetic properties of Co₂VZ (Z= Pb, Si, Sn) compounds, by using WIEN2k code and Atomistic Tool Kit-Virtual NanoLab (ATK-VNL) code within Generalized-gradient approximation (GGA) for exchange correlation functions.

COMPUTATION DETAILS

The physical fundamental properties of full Heusler alloys have been performed by full-potential linearized augmented plane wave (FP-LAPW) [22] method incorporated in Wien2k code [23]. We have chosen suitable approximation of Perdew, Burke and Ernzerhof (PBE) [24-26] for regulate the exchange and correlation potential energy to the optimization of parameters like RKmax, K-Point and lattice constant and optimized energy. Spin orbit coupling effect was considered to perform all the calculations. Electronic structure calculations are accurately calculated by WIEN2k code for solids. Core states are considered relativistic and valence states are considered as semi-

relativistic way and energy between these two states (cut off parameter) was set -6.0Ry. In first Brillouin zone 1000 k-points have been used for this code. But we need to set the number of k-points for the calculation of optical properties and this new value of k-points used are 10000. The size of the basis sets are controlled by convergence or cutoff parameter, whose value is $R_{mt} K_{max}$ set to 7.0. Here plane wave smallest radius of muffin-tin sphere is denoted by R_{mt} and maximum modulus for reciprocal lattice vector used in elaboration of flat wave function is denoted by K_{max}. The energy convergence criterion was taken as 0.0001Ry. To expand the spherical harmonics in the atomic sphere the value of angular momentum maximum (l_{max}) is taken as 10. In the central region the charge density and potential were elaborated as a cheerier series with wave vector up to $G_{max}=10$. For the each atom muffin tin sphere radii (R_{MT}) are tabulated in Table 1.

Table 1.

Muffin tin radius (R_{MT}) for Co_2VZ (Z= Pb, Si, Sn).

R_{MT} (a.u.)	Compounds		
	Co_2VPb	Co_2VSi	Co_2VSn
Co	2.36	2.30	2.21
V	2.36	2.19	2.15
Z	2.48	1.91	2.21

Atomistic Tool Kit-Virtual NanoLab (ATK-VNL) package [27] is a Pseudo-potential method carried out in the framework of density functional theory (DFT) [28, 29]. It is a commercially licensed tool kit. Above mentioned properties have also investigated with the help of this tool kit. These calculations have been applied to investigate electronic and magnetic properties of Co_2VZ (Z= Pb, Si, Sn) using Pulay Mixer algorithm [30]. For investigations, we have used double-zeta (ζ) polarized basis set for electron wave function expanding and GGA for exchange-correlation functional. The structures are permitted to optimize until each atom achieve force convergence criteria 0.05 eV/Å and maximum stress is 0.05 eV/Å³. Maximum numbers of step performed are 200 for the optimization and during this process maximum step size 0.2 Å is also fixed. Convergence is achieved by deciding mesh cutoff energy on the ground of convergence principle and for this computation 150 Ryd has been projected all over calculation as the most favorable after several convergence tests. For spin polarization, up and down initial state have been selected for the atoms. We used 10 x 10 x 10 Monkhorst-Pack k-mesh [31] for brillouin zone sampling to maintain balance between computational time and results accuracy. Further, all constrain in x, y and z directions are removed for optimization of structures.

RESULTS AND DISCUSSIONS
Structural parameters
Space group of full Heusler compound is 225 Fm-3m. The chemical formula for full Heusler is Co_2VZ (Z = Pb, Si, Sn) having $L2_1$ structure showing their composition 2:1:1. Its structure is formed by three penetrating FCC-lattices with atomic positions at X_1 (1/4, 1/4, 1/4), X_2 (3/4, 3/4, 3/4), Y (1/2, 1/2, 1/2) and Z (0, 0, 0). Where X and Y atoms are transition metal and Z is main group metal or semimetal [32, 33]. The equation of state given by Murnaghan [34] gives the value of total energy and pressure as a function of volume is stated as:

$$E(V) = E_O + \left[\frac{BV}{B_P} \left(\frac{1}{(B_P - 1)} \left(\frac{V_O}{V} \right)^{B_P} + 1 \right) - \frac{BV_O}{(B_P - 1)} \right]$$

$$P(V) = \frac{B}{B_P} \left\{ \left(\frac{V_O}{V} \right)^{B_P} - 1 \right\},$$

where, Pressure $(P) = -\frac{dE}{dV}$, $B_P = -V\frac{dP}{dV} = V\frac{d^2E}{dV^2}$

In the above equations E_0 is the minimum energy at T = 0K, B is the bulk modulus, B_P is the pressure derivative of the bulk modulus and V_o is the equilibrium volume. We perform the operation volume optimization for stable structure and their results are shown in Figure 1. Optimized lattice constant of WIEN2k and ATK-VNL are slightly differing from each other. Lattice constant in WIEN2k for the compounds Co_2VZ (Z= Pb, Si, Sn) are slightly greater than the lattice constant optimized in ATK-VNL. Compared values of bulk modulus by these two codes revels the results that value of bulk modulus of compounds Co_2VPb and Co_2VSn are less and Value of the compound Co_2VSi is more in WIEN2k code than ATK-VNL code. The compound Co_2VSi has showing largest value of bulk modulus in comparison to the others. Calculated values of the optimized lattice parameter, equilibrium energy and pressure derivative have been presented in Table 2.

Table 2.
Lattice parameter, Bulk modulus, Equilibrium energy and Pressure derivative for Co₂VZ (Z= Pb, Si, Sn).

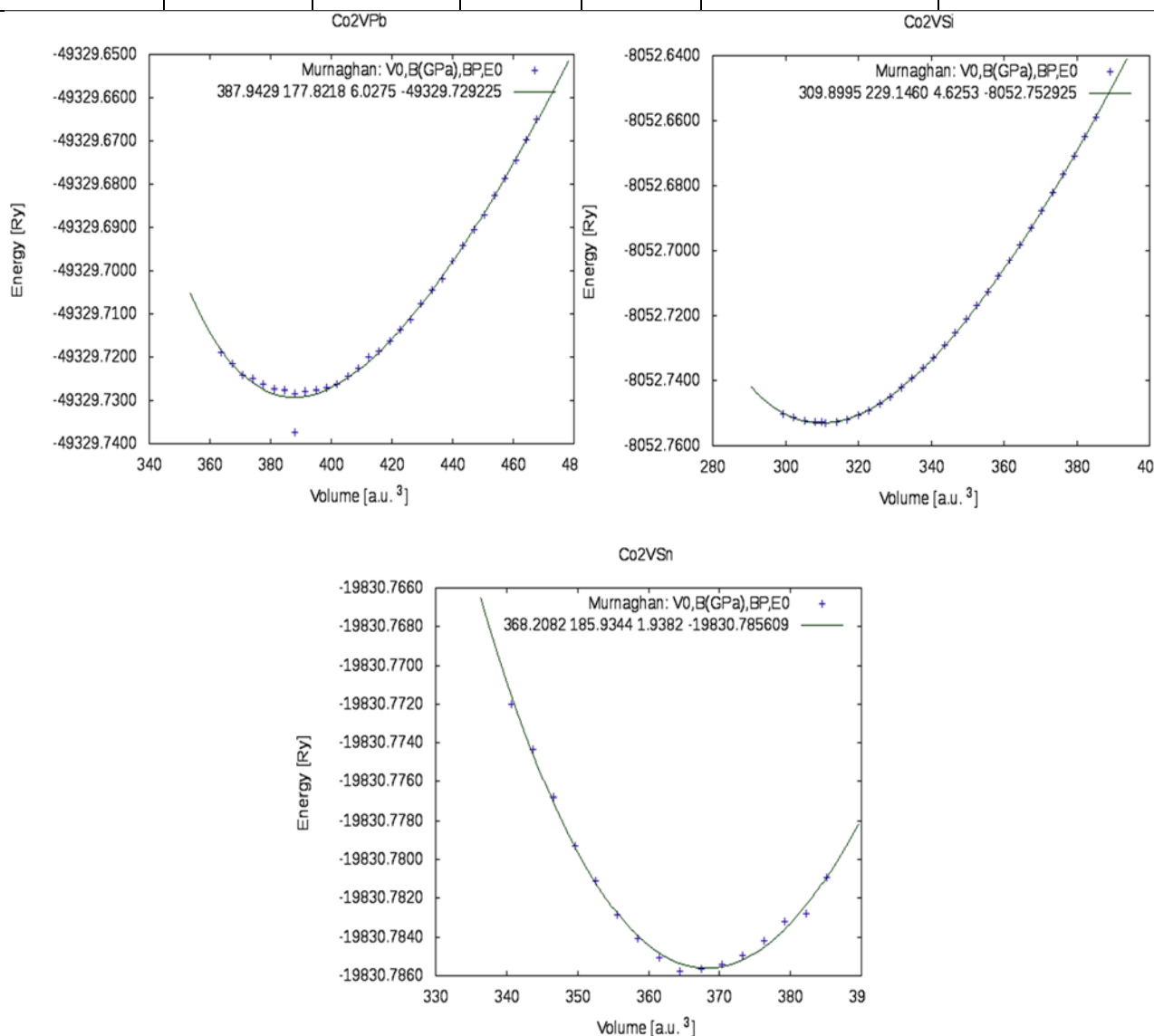| Compounds	Lattice Constants a_0 (Å)		Bulk modulus (GPa)		Equilibrium Energy (Ry)	Pressure derivative
	Calculated		Calculated			
	WIEN2k	ATK	WIEN2k	ATK		
Co₂VPb	6.125	6.073	179.50	195.74	-49329.729	6.872
Co₂VSi	5.685	5.638	234.36	233.94	-8052.753	5.406
Co₂VSn	6.021	5.957	186.08	206.20	-19830.786	1.851

Figure 1. Volume optimization for the lattice parameters

Electronic and magnetic properties

Due to spin of electron magnetic moment of a material can change. This change in magnetic moment is studied from the band structure and density of state of Heusler compounds. If that compound shows metallic behavior in one spin channel and semiconducting or insulating behavior in other spin channel at Fermi level then that compound is known as half metallic ferromagnetic representing 100% spin polarization. This phenomenon is known as Spin polarization. In the present era Spintronics is very interesting area of research. The advantages of Spintronics devices are nonvolatile magnetic memory, magnetic sensor, tunnel junction, increased data processing speed, increased integration intensities and processing speed of data is very high. These devices reduce electric power consummation and there is decrease in heat dissipation. Spin polarized calculations of Co₂VZ (Z= Pb, Si, Sn) compounds within Generalized-gradient approximation (GGA) full Heusler have been carried out at the optimized lattice parameters. Intrinsic spin of electron is responsible for magnetic moment. Theoretical value of spin polarization can be calculated using the formula as given below.

$$P_n = \frac{n\uparrow - n\downarrow}{n\uparrow + n\downarrow}$$

If either $n_\uparrow = 0$ or $n_\downarrow = 0$, then $P_n = 1$ or -1. It means, if either up or down spin exists then the spin polarization is 100%. These types of materials are known as half metals ferromagnetic [35]. If the value of P_n is vanishes then the materials are paramagnetic or anti-ferromagnetic even below the magnetic transition temperature. The difference between the highest energy occupied point in valence band region and the lowest unoccupied energy point in conduction band is known as energy gap. Study of energy gap from DOS and band structure of the compounds Co_2VZ (Z= Pb, Si, Sn) shows the result that out of three compounds only Co_2VSi does not show a band gap in minority spin channel through WIEN2k code and showing 100% spin polarization. Other two listed compound (Co_2VPb and Co_2VSn) shows band gaps 0.33 eV and 0.54 eV, when code executed in WIEN2k and showing semiconducting behavior. Outcome of ATK-VNL code revels that all three compound shows band gap in down spin and there is no any band gap observed in up spin channel. Obtained energy gap and spin polarization for the above full Heusler compound is summarized as under in Table 3. The detailed results of band structures and density of states are shown in Figures 2-5.

Table 3.

Energy gap and spin polarization for Co_2VZ (Z= Pb, Si, Sn)

Compounds	Energy gap E_g (eV)				Spin polarization	
	WIEN2k		ATK		WIEN2k	ATK
	Up spin	Down spin	Up spin	Down spin		
Co_2VPb	0.0	0.33	0.0	-0.51	100%	100%
Co_2VSi	0.0	0.0	0.0	-0.82	P_n vanishing	100%
Co_2VSn	0.0	0.54	0.0	-0.97	100%	100%
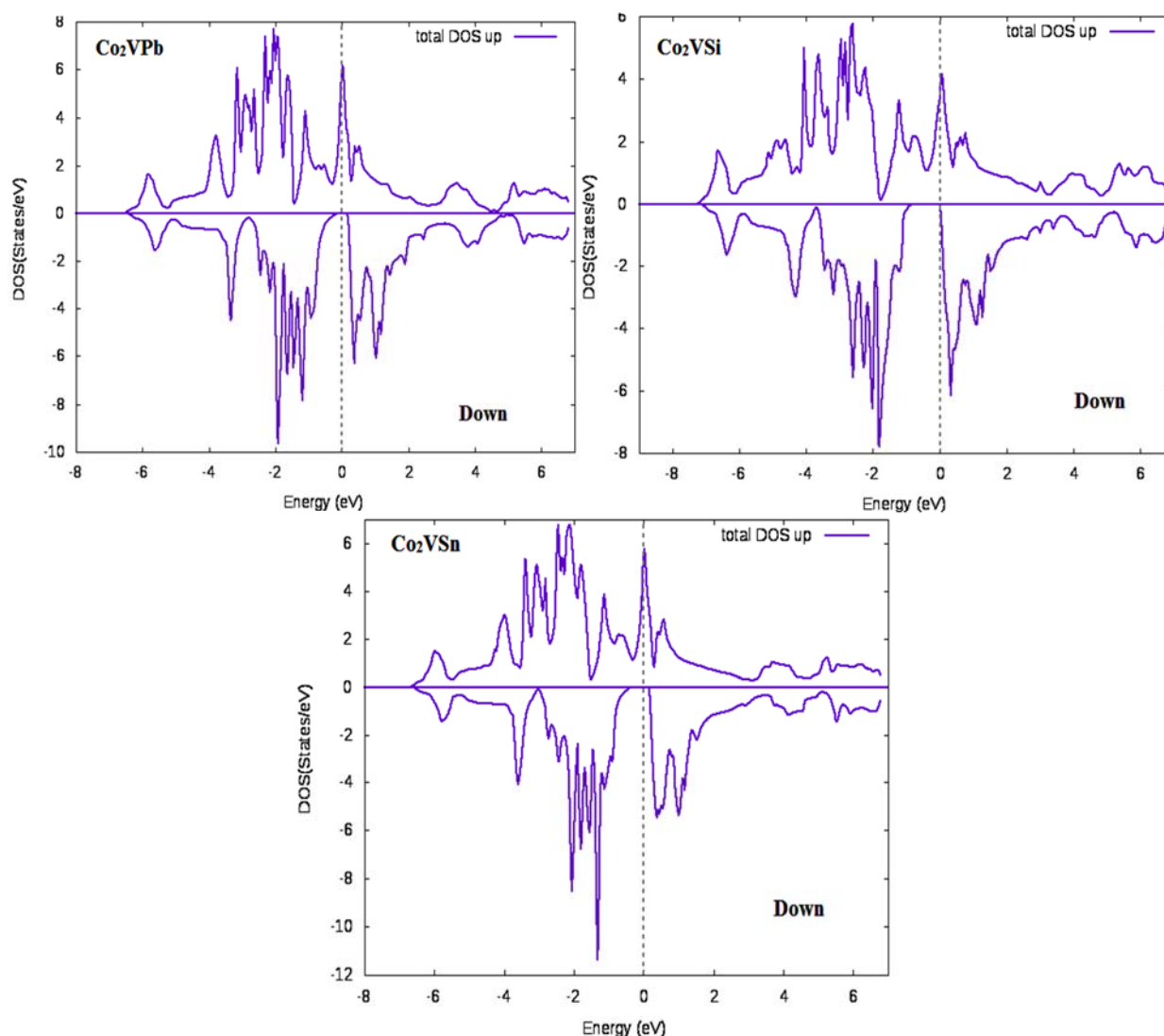
Figure 2. DOS of Co_2VZ (Z= Pb, Si, Sn) using WIEN2K Code
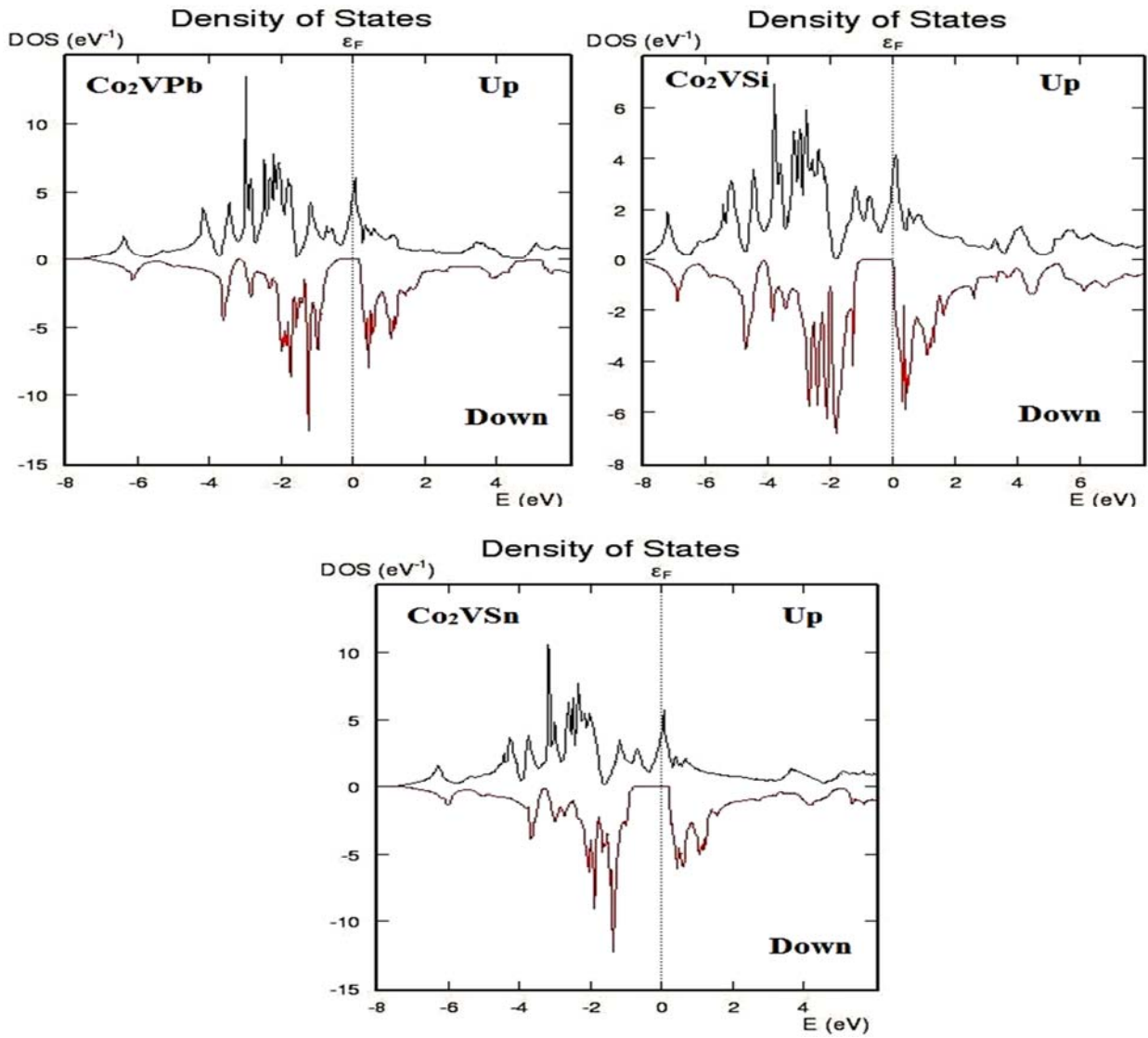
Figure 3. DOS of Co₂VZ (Z= Pb, Si, Sn) using ATK-VNL Code.
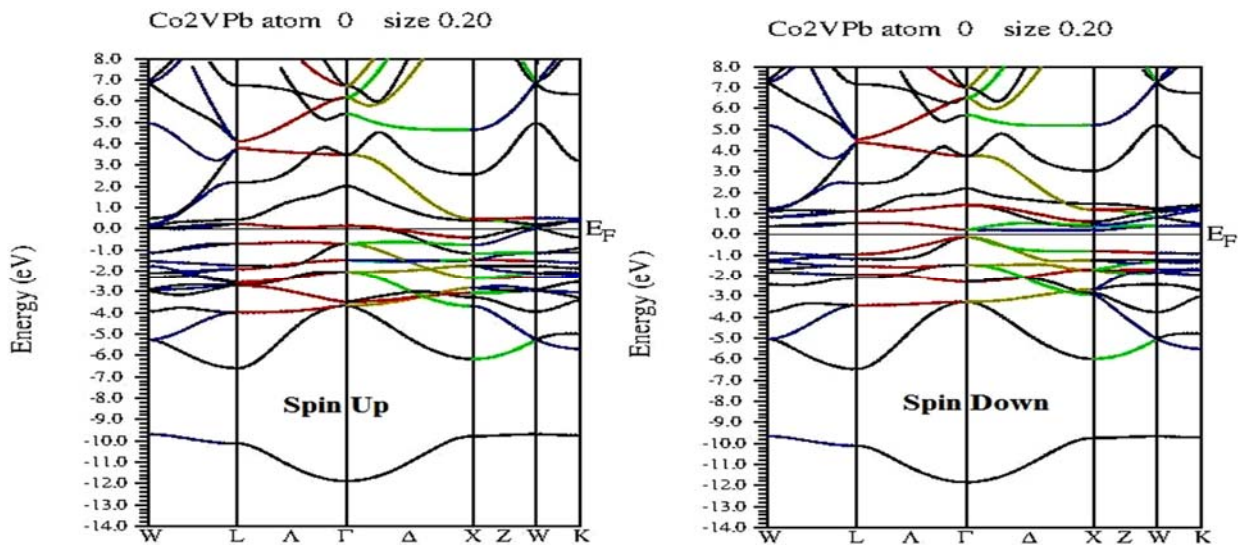
Figure 4. Band Structure of Co₂VZ (Z= Pb, Si, Sn) using WIEN2K Code.
(*Continued on next page*)

Figure 4. Band Structure of Co$_2$VZ (Z= Pb, Si, Sn) using WIEN2K Code.
(*Continuation*)
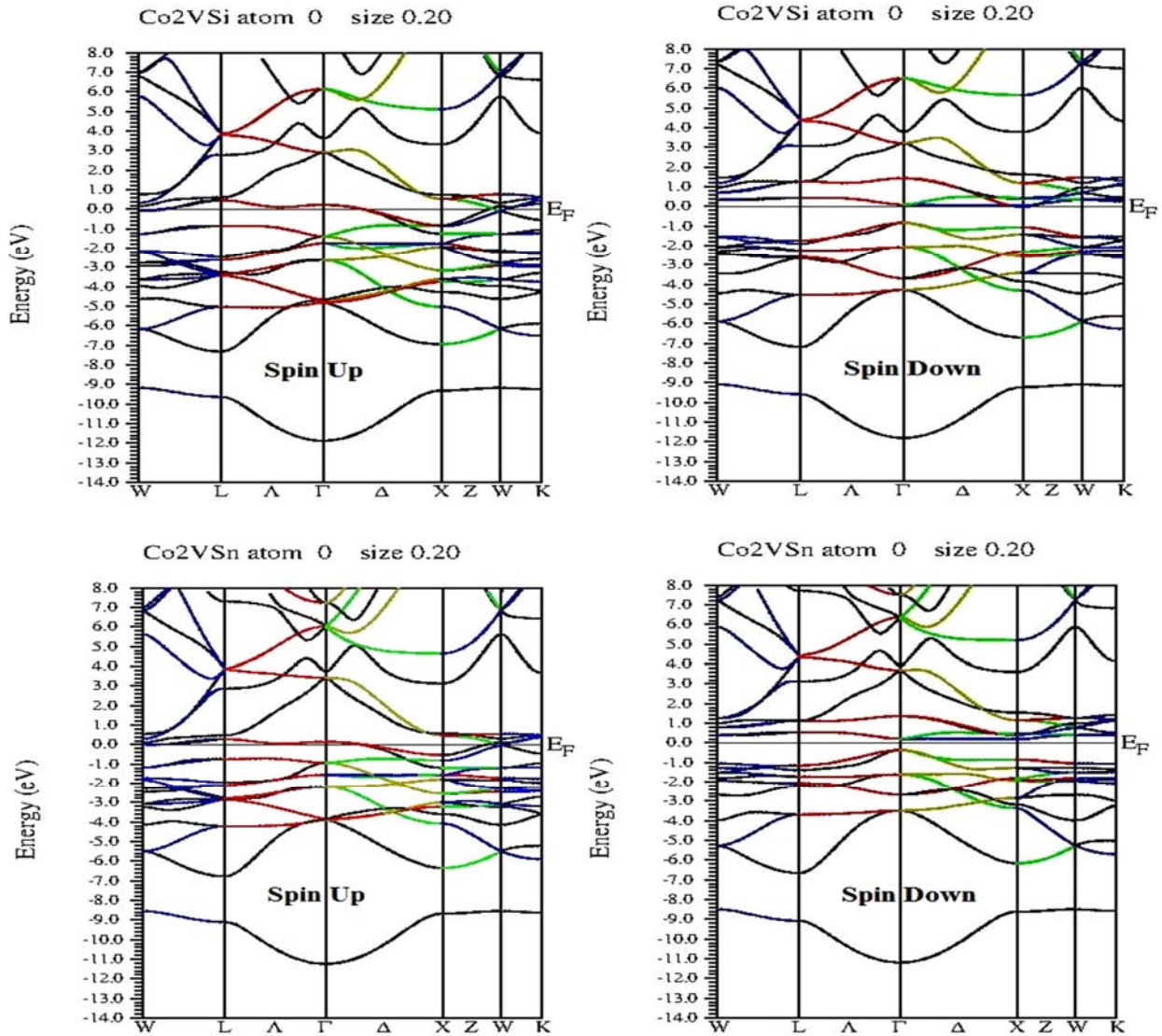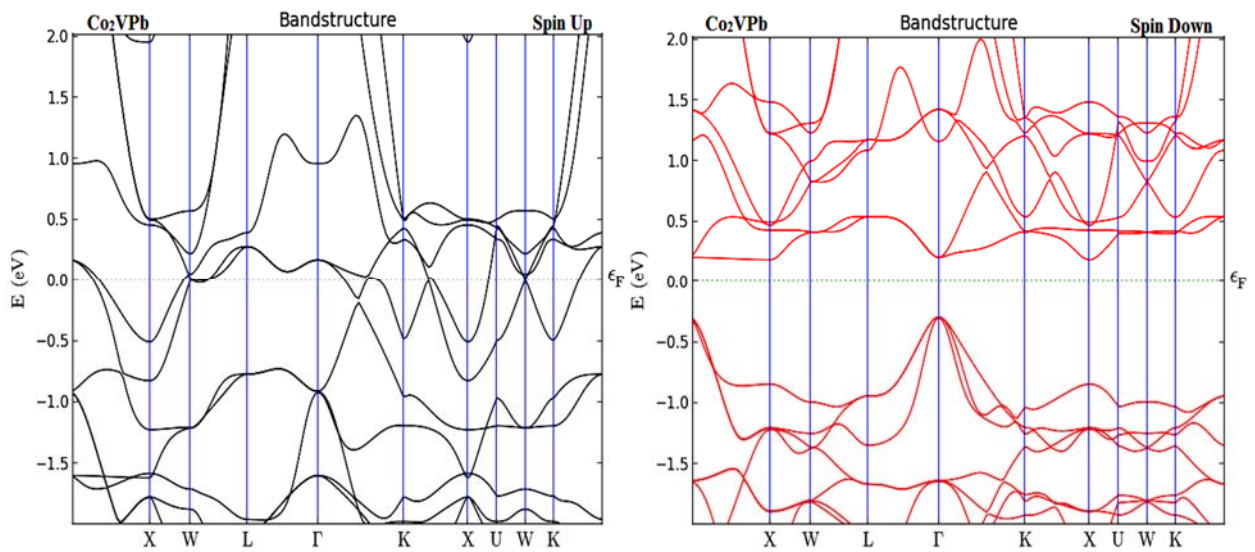

Figure 5. Band Structure of Co$_2$VZ (Z= Pb, Si, Sn) using ATK-VNL Code.
(*Continued on next page*)
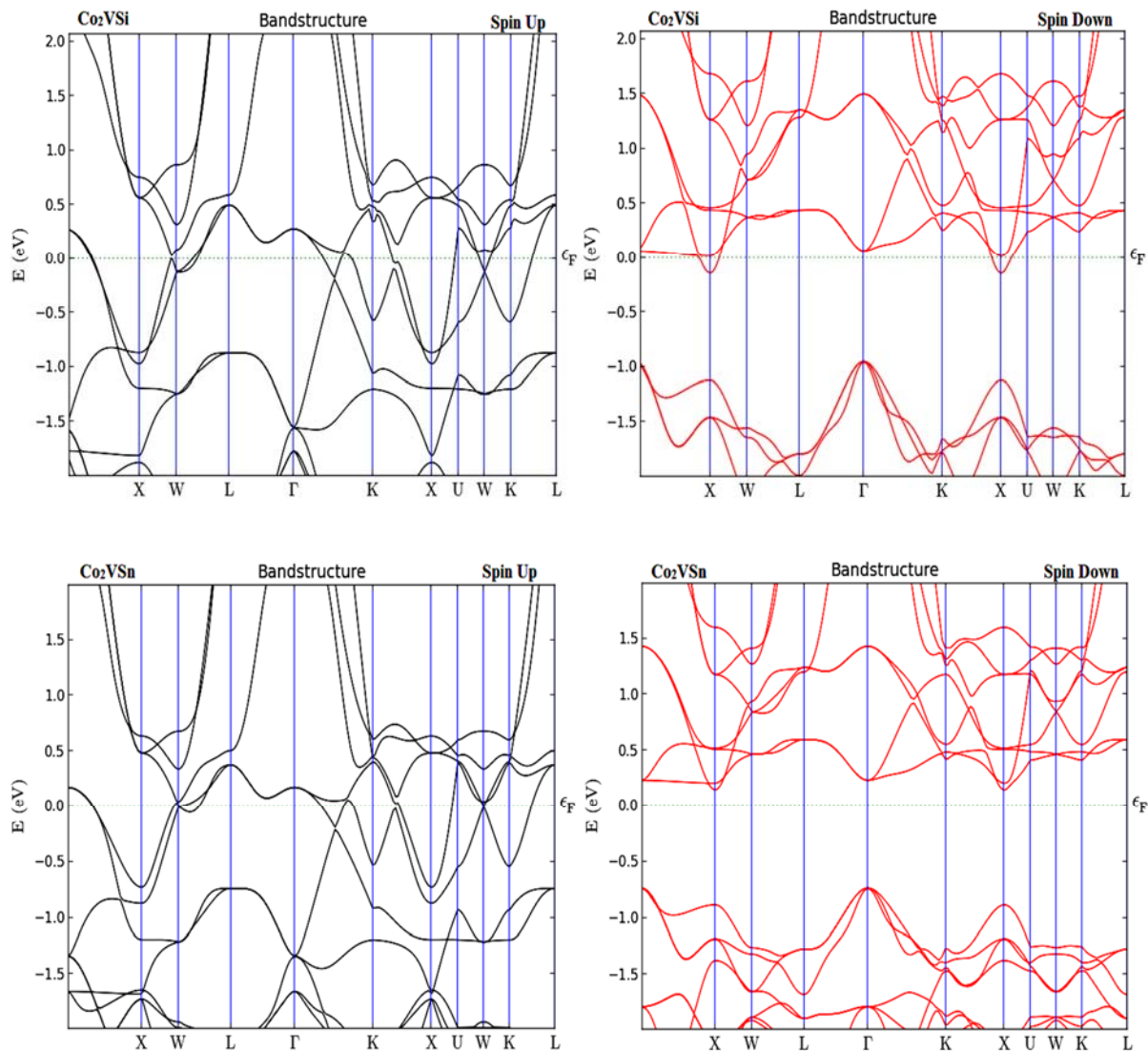
Figure 5. Band Structure of Co$_2$VZ (Z= Pb, Si, Sn) using ATK-VNL Code
(*Continuation*)

There is a linear relationship between numbers of valence electrons and spin magnetic moment. This simple relationship is main clue of Slater-Pauling rule. J. C. Slater [36] and L. Pauling [37] derive a formula for calculating the magnetic moment per unit cell theoretically and that formula is known as Slater-Pauling rule. According to this rule, if count of valence electrons in full Heusler compounds is equal to 24, then that compound shows zero magnetic moment and if, count of valence electron is different to 24, and then difference between the total number of valence electron and 24 represent the net amount of spin magnetic moment per unit cell. This theoretical method of prediction of magnetic moment is provided by Slater-Pauling. Method for Full Heusler compound is given as-

$$M_t = Z_t - 24$$

Where, M_t denotes the total magnetic moment per unit cell and Z_t denotes the total count of valence electron. Full Heusler compounds have a straightforward relationship between Curie temperature and spin magnetic moment i.e. Curie temperature is directly proportional to the spin magnetic moment. For the ferromagnetic half-metallic Heusler compounds, the Curie temperature increases by ~175 K per added electron after 24. Here, the results obtained by the codes WIEN2k and ATK-VNL are compared with results derived from theoretical method Slater-Pauling rule. For analysis the values of magnetic moment from WIEN2k, ATK-VNL code and Slater-Pauling rule, table 4 is very helpful for us. Total number of valence electrons for all the three compounds Co$_2$CrZ (Z= In, Sb, Sn) is 27. So magnetic moments per unit cell for all three compounds from Slater-Pauling rule is 3.0 μ$_B$. Now, the results derived by WIEN2k and ATK-VNL are 3.00 and 3.00, 3.02 and 2.96, 3.00 and 3.00 respectively. These compiled values are equal to the values of theoretical method Slater-Pauling, except slight difference between the values of Co$_2$VSi. So, these listed compounds have nice agreement with Slater-Pauling behavior. Investigation of results revels that Co and Cr position atom contribute major section of magnetic moment and small amount of magnetic moment contribution is due to Z position atom. The

calculated results for magnetic moments for Co_2VZ (Z= Pb, Si, Sn) obtained using full potential linearized augmented plane wave (FP-LAPW) method implemented in WIEN2k and pseudo-potentials method implemented in Atomistic Tool Kit-Virtual NanoLab (ATK-VNL) within Generalized- gradient approximation (GGA) for exchange correlation functions is tabulated in Table 4.

Table 4.

Total magnetic moments of the compounds Co_2VZ (Z= Pb, Si, Sn).

Compounds	Z_t	Magnetic moment (μ_B)		
		WIEN2k	ATK	Slater-Pauling (Z_t - 24)
Co_2VPb	27	3.00	3.00	3.00
Co_2VSi	27	3.02	2.96	3.00
Co_2VSn	27	3.00	3.00	3.00

Optical properties

Before fabrication of optoelectronics devices, it is compulsory to understand the optical properties of a material whether it can be used for it or not. For it, we need to study some optical properties like as dielectric function, optical conductivity, reflectivity, excitation coefficient, absorption coefficient and electron energy loss as a function of photon energy for a given material. Present section describes such optical properties of the compounds Co_2VZ (Z= Pb, Si, Sn). When an electromagnetic radiation is fall on a material then optical response of that material is described by complex dielectric function. This complex dielectric function can be written in the form of as below.

$$\varepsilon\ (m) = \varepsilon_1(m) + i\varepsilon_2(m)$$

Where $\varepsilon_1(m)$ real represents polarization of material when electric field is applied and absorption in a material or loss of energy into the medium is described by ($\varepsilon_2(m)$) imaginary part of complex dielectric function [38, 39]. It is considered that the transitions exist from occupied to unoccupied bands for explain the optical spectra. Inter-band region is chosen for studying the optical properties. The optical spectra for different optical properties are shown in Figure 6(a-h).

Figure 6. Calculated optical parameters (a) real part of dielectric function, (b) imaginary part of dielectric function, (c) optical conductivity, (d) absorption coefficient, (e) electron energy-loss function, (f) reflectivity, (g) refractive index and (h) extinction coefficient for Co_2VZ (Z= Pb, Si, Sn).
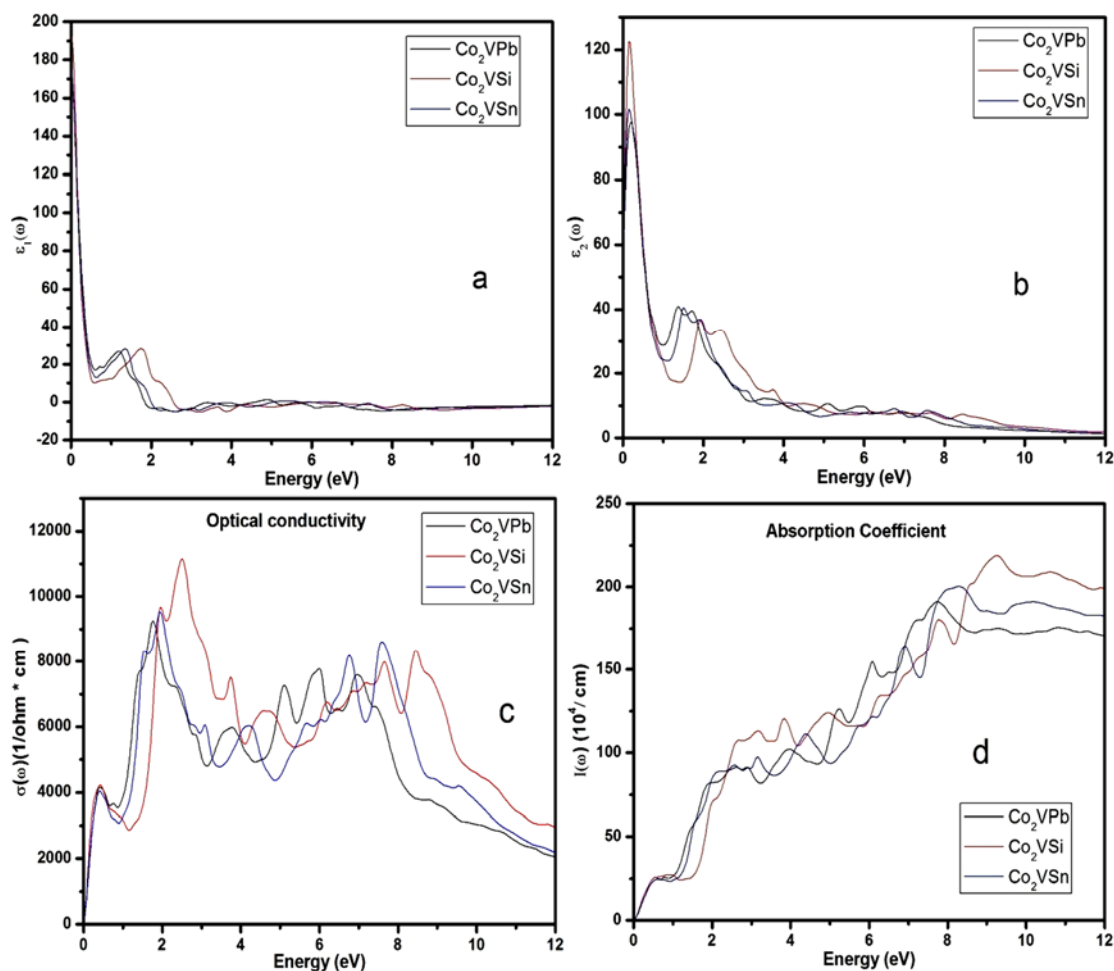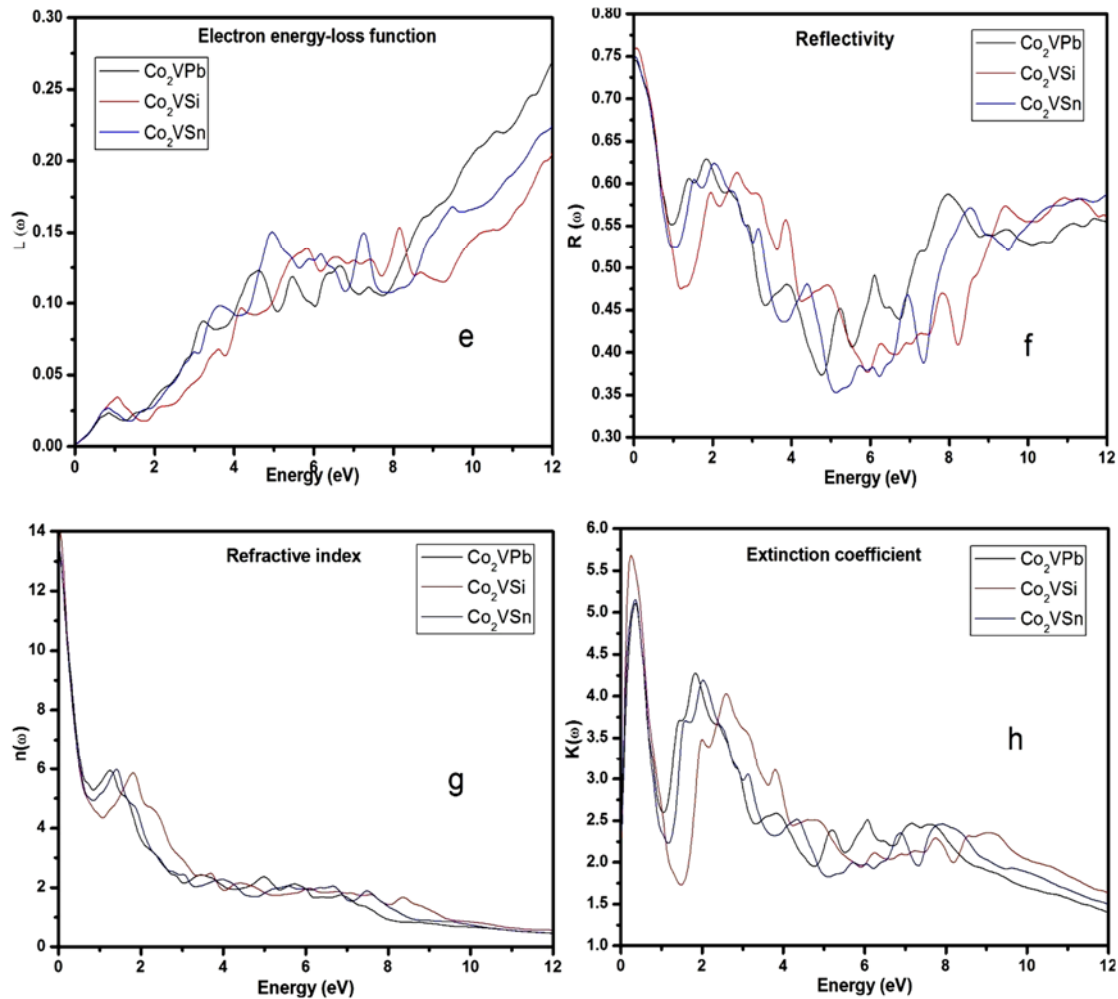
Figure 6. Calculated optical parameters (a) real part of dielectric function, (b) imaginary part of dielectric function, (c) optical conductivity, (d) absorption coefficient, (e) electron energy-loss function, (f) reflectivity, (g) refractive index and (h) extinction coefficient for Co$_2$VZ (Z= Pb, Si, Sn).

(*Continuation*)

The main peaks of imaginary part of dielectric function are obtained in infrared region from 0.08 to 0.30eV. After that, imaginary part of dielectric function decreases rapidly and some small peaks are observed near visible region. The values of zero frequency real (ε_1 (ω)) and imaginary part (ε_2 (ω)) of complex dielectric functions are 170.514 and 58.983, 192.316 and 64.438, 174.193 and 63.898 for the compounds Co$_2$VZ (Z= Pb, Si, Sn) respectively as investigated from the Figure 6 (a) and 6 (b). Due to electromagnetic field, value of conduction of electron is described by optical conductivity. Figure 6(c) gives a graphical representation of optical conductivity. In this graphical view, sharp peaks are shown in visible region and highest sharp peak is obtained at 2.48eV by Co$_2$VSi representing more conduction of electron as compared with other two compound. The value of absorption of photon is described by absorption coefficient means more value of absorption coefficient more photons are absorbed by the material. As we increase the values of energy from infrared region to ultraviolet region then value of absorption coefficient is also increases as shown in the figure 6 (d). Maximum value of photon absorption is found at 9.26eV by Co$_2$VSi showing highest peak out of three compounds. When fast moving electron passes through a medium then there is loss in energy of fast-moving electron. This loss of fast-moving electron can be calculated by electron energy-loss function graph. Like absorption coefficient, value of electron energy – loss function is also increasing as we increase the value of energy as shown in figure 6 (e). From figure 6 (f), we observe the values of zero frequency reflectivity which are 0.745, 0.758 and 0.749 for the compounds Co$_2$VZ (Z= Pb, Si, Sn) respectively. This optical property gives the values of reflection when electromagnetic radiation is fall on the surface of a material. The region in which material substantially absorbs light and it cannot effectively reflect light in the same span. The plasma frequency is the frequency corresponding to plasma resonance at which sharp peaks are associated. As if the frequency is above the plasma frequency then the material showing the dielectric behavior and below which the material shows metallic behavior. Due to wide applications of refractive index, it is most valuable to analyses; because it determines the dispersive power of prisms, focusing power of lenses, light guiding, and critical angle for total internal reflection etc. The values for zero frequency refractive index for the compounds Co$_2$VZ (Z= Pb, Si, Sn) were calculated as 13.246, 14.056 and 13.412 respectively. Figure 6(h) gives the graphical representation of extinction coefficient

spectrum. A notable narrow peak is shown in the infrared region along the range 0.18 to 0.50eV and then value of extinction coefficient is decreases. Near to visible region further a small broad peak is observed between 1.826 – 2.65eV and further value is decreases in the ultraviolet region.

Elastic properties

Elastic properties are the most fundamental properties of the material calculated using first principle method. Cubic crystal elasticity is determined by three reduced elastic constants C_{11}, C_{12} and C_{44}, out of six independent constant. These three reduced elastic constant gives us very important information about structure stability, mechanical properties, bond indexes and anisotropy of material. The crystal must satisfy the traditional mechanical stability condition of elastic constant. The traditional mechanical stability condition for cubic crystal is as below [40, 41].

$$C_{11} - C_{12} > 0,\ C_{11} > 0,\ C_{11} + 2C_{12} > 0,\ C_{44} > 0,\ C_{12} < B < C_{11}$$

Structural stability is obtained by anisotropic factor, which is denoted by 'A' if the value of 'A' is equal to one then material is isotropic and if the value of 'A' deviate from one then material is anisotropic. A property of material which does not depend on the direction is known as isotropic.

$$A = \frac{2C_{44}}{C_{11} - C_{12}}$$

Stiffness and flexibility of a material can be determined by bond index via Cauchy pressure, which is expressed as $C_P = C_{12} - C_{44}$. From this relation if the value is positive, then the material is metallic in nature and if value is negative, then the material is nonmetallic. Further, positive result shows ductile nature material and negative result shows brittle nature of material. If the value of bond index is less than 12 shows soft material and greater than 12 shows hard material [42]. Pugh's ratio B/G is also used for to explain the material is brittle or ductile. If the B/G ratio is less than 1.75 then material is brittle type and if this ratio B/G is greater than 1.75 then it is ductile. Mechanical properties of the compounds are determined by Bulk modulus (B), young modulus (E), Shear modulus (G) and Poisson ratio (v) by Voigt-Reuss-Hill (VRH) averaging method [43-44]. Formulas for B, E, G and v by using elastic constant can be expressed as.

$$B = B_V = B_R = \frac{C_{11} + 2C_{12}}{3}$$

$$G = \frac{G_V + G_R}{2}$$

$$G_V = \frac{C_{11} - C_{12} + 3C_{44}}{5}$$

$$G_R = \frac{5C_{44}\,(C_{11} - C_{12})}{[4C_{44} + 3(C_{11} - C_{12})]}$$

(V = Voigt and R = Reuss)
Young modulus is also used to determine the stiffness of material. This can be obtained in term of B and G.

$$E = \frac{9BG}{3B + G}$$

The value of Poisson ratio can be calculated in term of B and G. The values of Poisson ratio lie between 0 - 0.5 for most of the material.

$$v = \frac{3B - 2G}{2(3B + G)}$$

We use here Atomistic Tool Kit-Virtual NanoLab (ATK-VNL) package using Pseudo-potential method carried out in the framework of density functional theory (DFT). All the results carried out from this code are assembled in table 5.

Table 5.

Elastic constants and bulk modulus B (GPa), shear modulus G (GPa), Young's modulus E (GPa), B/G values, Poisson's ratio (v) and anisotropy factor (A) of Co_2VZ (Z= Pb, Si, Sn) compounds.

Compound	Elastic constants (GPa)			B (GPa)	G (GPa)	E (GPa)	B/G	v	A
	C_{11}	C_{12}	C_{44}						
Co_2VPb	228.51	179.36	85.22	195.74	51.93	70.77	3.77	0.44	3.47
Co_2VSi	271.49	215.17	137.88	233.95	73.94	81.22	3.16	0.44	4.90
Co_2VSn	245.91	186.36	106.81	206.21	64.24	85.22	3.21	0.43	3.59

From the Table 5, we have observed that traditional mechanical stability condition $C_{11} - C_{12} > 0$, $C_{11} > 0$, $C_{11} + 2C_{12} > 0$, $C_{44} > 0$, $C_{12} < B < C_{11}$ for all the compounds Co_2VZ (Z= Pb, Si, Sn) is satisfied. Results of anisotropic

constant 'A' are deviated from one for all three compounds. We have concluded that the compounds Co$_2$VZ (Z= Pb, Si, Sn) are anisotropic in nature. Values of Poisson are lie between zero to 0.5. Table 5 revels that, Pugh's ratio B/G is greater than 1.75 for all compounds recorded in table. These materials are ductile in nature. Values of Cauchy pressure (C$_P$ = C$_{12}$ – C$_{44}$) compiled from the table 5 are positive for these compounds Co$_2$VZ (Z= Pb, Si, Sn) and shows metallic nature.

SUMMARY AND CONCLUSIONS

We have compiled the results for Structural, electronic, optical and magnetic properties of Co2VZ (Z= Pb, Si, Sn) compounds by two simulation codes. From this study, we have analyzed that out of three compounds, two compounds show half metallicity and 100% spin polarization with L2$_1$ ordered stable structures except Co$_2$VSi in full potential linearized augmented plane wave (FP-LAPW) method. But results of pseudo- potentials method revels that all three compounds show half metallicity and 100% spin polarization with L2$_1$ ordered stable structures. Calculated magnetic moments per unit cell have good agreement with the Slater-Pauling behavior. Optical spectra of these compounds named as reflectivity, refractive index, excitation coefficient, absorption coefficient, optical conductivity and electron energy loss have been analyzed. Values of absorption coefficient and electron energy - loss function are increases as we increase the value of energy. The predicted results shows that the compounds Co$_2$VZ (Z= Pb, Sn) are suitable for Spintronics applications. Compilation of elastic properties presented that the above listed compounds are ductile and metallic in nature.

ORCID IDs
Sukhender, https://orcid.org/0000-0002-2149-5669; **Lalit Mohan**, https://orcid.org/0000-0003-3323-8296
Pravesh Pravesh, https://orcid.org/0000-0002-0876-4836; **Ajay Singh Verma**, https://orcid.org/0000-0001-8223-7658

REFERENCES
[1] Y. Ohnuma, M. Matsuo, and S. Maekawa, Phys. Rev. B. **94**, 184405 (2016), https://doi.org/10.1103/PhysRevB.94.184405.
[2] S.M. Griffin, and J.B. Neaton, Prediction of a new class of half-metallic ferromagnets from first principles. Phys. Rev. Mater. **1**, 044401 (2017) https://doi.org/10.1103/PhysRevMaterials.1.044401.
[3] N.I. Kourov, V.V. Marchenkov, K.A. Belozerova, and H.W. Weber, J. Exper. Theor. Phys. **118**, 426-431 (2014), https://doi.org/10.1134/S1063776114020137.
[4] M. Sun, Q. Ren, Y. Zhao, S. Wang, J. Yu, and W. Tang, J. Appl. Phys. **119**, 143904 (2016), https://doi.org/10.1063/1.4945771.
[5] I. Galanakis, K. Özdoğan, and E. Şaşıoğlu, AIP Adv. **6**, 055606 (2016), https://doi.org/10.1063/1.4943761.
[6] Y. Wang, R. Ramaswamy, and H. Yang, J. Phys. D. Appl. Phys. **51**, 273002 (2018), https://doi.org/10.1088/1361-6463/aac7b5.
[7] Y. Feng, Z. Cui, M. S. Wei, and B. Wu, Appl. Surf. Sci. **499**, 78–83 (2019), https://doi.org/10.1016/j.apsusc.2018.09.247.
[8] R.A. de Groot, F.M. Muller, P.G. Van Engen, and K.H.J. Buschow, Phys. Rev. Lett. **50**, 2024-2027 (1983), https://doi.org/10.1103/PhysRevLett.50.2024.
[9] A. Aguayo, and G. Murrieta, J. Magnetism and Magnetic Materials, **323**, 3013-3017 (2011), https://doi.org/10.1016/j.jmmm.2011.06.038.
[10] G. Fiedler, and P. Kratzer, Phys. Rev. B. **94**, 075203 (2016), https://doi.org/10.1103/PhysRevB.94.075203.
[11] C.K. Barman, and A. Alam, Phys. Rev. B. **97**, 075302 (2018), https://doi.org/10.1103/PhysRevB.97.075302.
[12] S. Ishida, S. Akazawa, Y. Kubo, J. Ishida, J. Phys. F: Met. Phys. **12**, 1111 (1982), https://doi.org/10.1088/0305-4608/12/6/012.
[13] J. Kübler, A.R. William, and C.B. Sommers, Phys. Rev. B **28**, 1745-1755 (1983), https://doi.org/10.1103/PhysRevB.28.1745.
[14] Y. Miura, K. Nagao, and M. Shirai, Phys. Rev. B **69**, 144413 (2004), https://doi.org/10.1103/PhysRevB.69.144413.
[15] J. Kübler, G.H. Fecher, and C. Felser, Phys. Rev. B **76**, 024414 (2007), https://doi.org/10.1103/PhysRevB.76.024414.
[16] S.A. Wolf, D.D. Awschalom, R.A. Buhrman, J.M. Daughton, S.V. Molnar, M.L. Roukes, A.Y. Chtchelkanova, and D.M. Treger, Science, **294**, 1488-1495 (2001), https://doi.org/10.1126/science.1065389.
[17] E. Şaşıoğlu, L.M. Sandratskii, P.Bruno, I.Galanakis, Phys. Rev. B. **72**, 184415 (2005), https://doi.org/10.1103/PhysRevB.72.184415.
[18] S. Wurmehl, G.H. Fechel, H.C. Kandpal, V. Ksenofontov, C. Felser, H. Lin, Appl. Phys. Lett. **88**, 032503 (2006), https://doi.org/10.1063/1.2166205.
[19] I. Galanakis, J. Phys.: Condens. Matter, **14**, 6329-6340 (2002), https://doi.org/10.1088/0953-8984/14/25/303.
[20] I. Galanakis, P.H. Dederichs, and N. Papanikolaou, Phys. Rev. B **66**, 134428 (2002), https://doi.org/10.1103/PhysRevB.66.134428.
[21] T. Block, C. Felser, G. Jakob, J. Ensling, B. Muhling, P. Gutlich, V. Beaumont, F. Studer, and R.J. Cava, J. Solid Solid State Chem. **176**, 646-651 (2003), https://doi.org/10.1016/j.jssc.2003.07.002.
[22] E. Wimmer, H. Krakauer, M. Weinert, and A.J. Freeman, Phys. Rev. B, **24**, 864-875 (1981), https://doi.org/10.1103/PhysRevB.24.864.
[23] P. Blaha, K. Schwarz, G.K.H. Madsen, D. Kvasnicka, and J. Luitz, in: *WIEN2k, An Augmented Plane Wave + Local Orbitals Program for Calculating Crystal Properties*, edited by K Schwarz, (Technical Universitatwien, Austria, 2001).
[24] J.P. Perdew, K. Burke, and M. Ernzerhof, Phys. Rev. Lett. **77**, 3865-3868 (1996), https://doi.org/10.1103/PhysRevLett.77.3865.
[25] J.P. Perdew, K. Burke, and Y. Wang, Phys. Rev. B. **54**, 16533 (1996), https://doi.org/10.1103/PhysRevB.57.14999.
[26] E. Sjostedt, L. Nordstrom and D.J Singh, Solid State Commun. **114**, 15-20 (2000), https://doi.org/10.1016/S0038-1098(99)00577-3.
[27] *Atomistix ToolKit-Virtual Nanolab (ATK-VNL), QuantumWise Simulator, Version. 2014.3*, http://quantumwise.com/
[28] Y.J. Lee, M. Brandbyge, J. Puska, J. Taylor, K. Stokbro, and M. Nieminen, Phys. Rev. B, **69**, 125409 (2004), https://doi.org/10.1103/PhysRevB.69.125409.
[29] K. Schwarz, J. Solid State Chem. **176**, 319–328 (2003), https://doi.org/10.1016/S0022-4596(03)00213-5.
[30] P. Pulay, J. Comput. Chem. **3**, 556–560 (1982), https://doi.org/10.1002/jcc.540030413.
[31] H.J. Monkhorst, and J.D. Pack, Phys. Rev. B, **13**, 5188-5192 (1976), https://doi.org/10.1103/PhysRevB.13.5188.
[32] P.J. Webster, J. Phys. Chem. Sol. **32**, 1221-1231 (1971), https://doi.org/10.1016/S0022-3697(71)80180-4.

[33] Fr. Heusler, Ueber magnetische Manganlegierungen. Verh. Dtsch. Phys. Ges. **5**, 219 (1903).

[34] F.D. Murnaghan, Proc. Natl. Acad. Sci. U.S.A. **30**, 244-247 (1944), https://dx.doi.org/10.1073%2Fpnas.30.9.244.

[35] R.J. Soulen Jr., J.M. Byers, M.S. Osofsky, B. Nadgorny, T. Ambrose, S.F. Cheng, P.R. Broussard, C.T. Tanaka, J. Nowak, J.S. Moodera, A. Barry, and J.M.D. Coey, Science **282**, 85-88 (1998), https://doi.org/10.1126/science.282.5386.85.

[36] J. C. Slater, Phys. Rev. **49**, 537-545 (1936), https://doi.org/10.1103/PhysRev.49.537.

[37] L. Pauling, Phys. Rev. **54**, 899-904 (1938), https://doi.org/10.1103/PhysRev.54.899.

[38] Y.V. Kudryavtsev, N.V. Uvarov, V.N. Iermolenko, and J. Dubowik, J. Appl. Phys. **108**, 113708 (2010), https://doi.org/10.1063/1.3511433.

[39] N.V. Uvarov, Y.V. Kudryavtsev, A.F. Kravets, A.Ya. Vovk, R.P. Borges, M. Godinho, and V. Korenivski, J. Appl. Phys. **112**, 063909 (2012), https://doi.org/10.1063/1.4752870.

[40] M. Born, and K. Huang, *Dynamical Theory of Crystal Lattices*, (Oxford, Clarendon, 1956), pp. 420.

[41] A. Akriche, H. Bouafia, S. Hiadsi, B. Abidri, B. Sahli, M. Elchikh, M.A. Timaoui, B. Djebour, J. Magnetism and Magnetic Materials. **422**, 13-19 (2017), https://doi.org/10.1016/j.jmmm.2016.08.059.

[42] D.G. Pettifor, J. Mater. Sci. Technol. **8**, 345-349 (1992), https://doi.org/10.1179/mst.1992.8.4.345.

[43] R. Hill, Proc. Phys. Soc., A **65**, 349-354 (1952), https://doi.org/10.1088/0370-1298/65/5/307.

[44] A. Hamidani, B. Bennecer, B. Boutarfa, Materials Chemistry and Physics. **114**, 732-735 (2009), https://doi.org/10.1016/j.matchemphys.2008.10.038.

ПЛАСТИЧНА І МЕТАЛЕВА ПРИРОДА КОМПАУНДІВ ХЕЙСЛЕРА Co₂VZ (Z = Pb, Si, Sn): БАЗОВІ ПРИНЦИПИ ДОСЛІДЖЕННЯ

Сухендер[a], Правеш Правеш[b], Лаліт Мохан[a], Аджай Сінгх Верма[a]
[a]Фізичний факультет, Банастхалі Відьяпіт, Банастхалі 304022, Індія
[b]Факультет електроніки і техніки зв'язку, група установ KIET
Газіабад, Уттар-Прадеш (Індія) 201206

У цій роботі оптоелектронні, пружні і магнітні властивості L2₁ структурованих сполук Хейслера Co₂VZ (Z = Pb, Si, Sn) були досліджені двома методами. Одним з них є метод повнопотенціальної лінеаризованої розширеної пласкої хвилі (FP-LAPW), реалізований в WIEN2k, а другим - метод псевдопотенціалу, реалізований в Atomistic Tool Kit-Virtual NanoLab (ATK-VNL). Всі ці сполуки показують нульову ширину забороненої зони в основному спіновому каналі в обох кодах моделювання, і кінцева заборонена зона становить 0,33 і 0,54 еВ в сплавах Co₂VZ (Z = Pb, Sn) (напівпровідникових) відповідно. Причина в невеликому спіновому каналі поблизу рівня Фермі, що реалізовано в коді WIEN2k зі 100% спінової поляризацією, за винятком Co₂VSi (металік) з нульовою шириною забороненої зони. Ці сполуки виявилися ідеально напівметалевими феромагнетиками (HMF). Однак вищезгадані сполуки показують кінцеві заборонені зони в коді ATK-VNL. Розрахований магнітний момент цих з'єднань Co₂VZ (Z = Pb, Si, Sn) становить 3,00 і 3,00, 3,02 і 2,96, 3,00 і 3,00 μв в кодах WIEN2k і ATK-VNL відповідно. Таким чином, ми спостерігали, що обчислені значення за цими кодами моделювання і правилом Слейтера-Полінга добре налаштовуються. Були проаналізовані оптичні властивості цих сполук, такі як відбивна здатність, показник заломлення, коефіцієнт збудження, коефіцієнт поглинання, оптична провідність і енергетичні втрати електронів. Коефіцієнт поглинання і значення функції енергетичних втрат електронів збільшуються у міру збільшення енергії. Співвідношення П'ю B/G перевищує 1,75 для всіх з'єднань і показує пластичну природу з позитивним значенням тиску Коші (CP = C12 - C44) і показує металеву поведінку сполук Co₂VZ (Z = Pb, Si, Sn).

КЛЮЧОВІ СЛОВА: напівметалевий феромагнетик, заборонена зона, спінтроніка, магнітний момент, пружні постійні

ПЛАСТИЧНАЯ И МЕТАЛЛИЧЕСКАЯ ПРИРОДА КОМПАУНДА ХЕЙСЛЕРА Co₂VZ (Z = Pb, Si, Sn): БАЗОВЫЕ ПРИНЦИПЫ ИССЛЕДОВАНИЯ

Сухендер[a], Правеш Правеш[b], Лалит Мохан[a], Аджай Сингх Верма[a]
[a]Физический факультет, Банастхали Відьяпит, Банастхали, 304022, Индия
[b]Факультет электроники и техники связи, группа учреждений KIET
Газиабад, Уттар-Прадеш (Индия) 201206

В этой работе оптоэлектронные, упругие и магнитные свойства L2₁ структурированных соединений Хейслера Co2VZ (Z = Pb, Si, Sn) были исследованы двумя методами. Одним из них является метод полнопотенциальной линеаризованной расширенной плоской волны (FP-LAPW), реализованный в WIEN2k, а вторым - метод псевдопотенциала, реализованный в Atomistic Tool Kit-Virtual NanoLab (ATK-VNL). Все эти соединения показывают нулевую ширину запрещенной зоны в основном канале спина в обоих кодах моделирования, и конечная запрещенная зона составляет 0,33 и 0,54 эВ в сплавах Co₂VZ (Z = Pb, Sn) (полупроводниковых) соответственно. Причина в небольшом спиновом канале около уровня Ферми, что реализовано в коде WIEN2k со 100% спиновой поляризацией, за исключением Co₂VSi (металлик) с нулевой шириной запрещенной зоны. Эти соединения оказались идеально полуметаллическими ферромагнетиками (HMF). Однако вышеупомянутые соединения показывают конечные запрещенные зоны в коде ATK-VNL. Рассчитанный магнитный момент этих соединений Co₂VZ (Z = Pb, Si, Sn) составляет 3,00 и 3,00, 3,02 и 2,96, 3,00 и 3,00 μв в кодах WIEN2k и ATK-VNL соответственно. Таким образом, мы наблюдали, что вычисленные значения по этим кодам моделирования и правилу Слейтера-Полинга имеют хорошо настраиваются. Были проанализированы оптические свойства этих соединений, такие как отражательная способность, показатель преломления, коэффициент возбуждения, коэффициент поглощения, оптическая проводимость и энергетические потери электронов. Коэффициент поглощения и значения функции энергетических потерь электронов увеличиваются по мере увеличения энергии. Соотношение Пью B/G превышает 1,75 для всех соединений и показывает пластическую природу с положительным значением давления Коши (CP = C12 - C44) и показывает металлическое поведение соединений Co₂VZ (Z = Pb, Si, Sn).

КЛЮЧЕВЫЕ СЛОВА: полуметаллический ферромагнетик, запрещенная зона, спинтроника, магнитный момент, упругие постоянные

FIRST PRINCIPLES CALCULATIONS FOR ELECTRONIC, OPTICAL AND MAGNETIC PROPERTIES OF FULL HEUSLER COMPOUNDS

Sukhender[a], Pravesh Pravesh[b], Lalit Mohan[a], Ajay Singh Verma*,[a]

[a]Department of Physics, Banasthali Vidyapith
Banasthali 304022, India
[b]Department of Electronics and Communication Engineering, KIET Group of Institutions
Ghaziabad, Uttar Pradesh (India) 201206
*Corresponding Author: ajay_phy@rediffmail.com
Received April 20, 2020; accepted May 30, 2020

For the investigation of structural, electronic, optical and magnetic properties of Co_2CrZ (Z= In, Sb, Sn) compounds, we have used two different methods. One is based on full potential linearized augmented plane wave (FP-LAPW) method as implemented in WIEN2k and second is pseudo potential method as implemented in Atomistic Tool Kit-Virtual NanoLab (ATK-VNL). These compounds show zero band gap in their majority-spin and minority-spin representing metallic behavior except the compound Co_2CrSb, which is showing the band gap 0.54 eV in their minority-spin near the Fermi level and viewing 100% spin polarization; which is implemented in WIEN2k code. Further, the compound Co_2CrSb has been found to be perfectly half-metallic ferromagnetic (HMF). However, above mentioned compounds show zero band gap in ATK-VNL code. Calculations performed using WIEN2k code shows the magnetic moment of these compounds Co_2CrZ (Z= In, Sb, Sn) 3.11, 5.00 and 4.00μ_B respectively. However, the respective magnetic moment of these compounds is found to be 3.14, 5.05 and 4.12μ_B in ATK-VNL code. Calculated magnetic moments have good agreement with the Slater-Pauling behavior. Optical properties play an important role to understand the nature of material for optical phenomenon and optoelectronics devices. Value of absorption coefficient and optical conductivity of Co_2CrSb is greatest than other two compounds. From the absorption and reflection spectra relation, observations indicate that absorption and reflectivity are inversely proportional to each other.
KEYWORDS: Half-metallic ferromagnetic, band gap, density of state, Spintronics

The history of Heusler compounds started in the year 1903 to 1912, when a German mining engineer and chemist Friedrich Heusler discovered a ferromagnetic material at room temperature. In those days that is major finding of Heusler. This ferromagnetic material is shaped by non magnetic element Cu, Mn and Al at room temperature [1, 2, 3]. After that ferromagnetism is found in the materials, which are framed by Cu and Mn with Z position like Sb, Bi and Sn. But in the recent years, there are number of Heusler compounds framed, after the ideas of Louis Neel in the year 1930-1940s of antiferromagnetism and ferrimagnetism [4, 5]. In this paper we discuss the some properties of full Heusler compounds. These compounds are ternary compounds showing $L2_1$ structure formed by three interpenetrating FCC-lattices. Chemical formula for Full Heusler compound is X_2YZ and their composition is representing by 2:1:1 [6-9]. Half metallic ferromagnetic behavior of Heusler alloys was firstly predicted by de Groot in 1983 in semi-Heusler compound NiMnSb [10-11]. Along the passage of time half metallicity turns on more curiosity due to its precious spintronic application. Compounds exhibit 100% spin polarization, if either one spin channel shows band gap and other shows zero band gap at Fermi level [12-15]. Ishida et al. [16] have also put their results represent that the compounds Co_2MnZ (Z= Ge, Sn) are semi metals and showing 100% spin polarization. Galanakis et al. [17] have presented that in Full Heusler compounds X_2YZ band gap occur due to the interaction in d orbital of X and Y, which generate bonding and anti bonding state by a vent. Umetsu et al. [18] have investigated that Co_2CrGa compound has a stable magnetic moment 3.01 μ_B at 4.2 k and follow the Slater-Pauling rule $Zt – 24$ = total magnetic moment. Miura et al. [19] also studied that Co – based Full Heusler compounds shows the behavior of half – metallic ferromagnets. Seema et al. [20] shows by their investigation of electronic, magnetic and optical properties of Co_2CrZ (Z= Al, Ga, Ge, Si) that there are three types of disorders, namely DO_3, A2 and B2. In these disorders DO3 and A2 disorder leads decrease in the spin polarization and B2 disorder retains the spin polarization at Fermi level.

In this paper, we have investigated the structural, electronic, optical and magnetic properties of Co_2CrZ (Z= In, Sb, Sn) compounds, by using WIEN2k code and Atomistic Tool Kit-Virtual NanoLab (ATK-VNL) code within Generalized-gradient approximation (GGA) for exchange correlation functions.

COMPUTATION DETAILS

An investigation of structural, electronic, optical and magnetic properties have been performed by full-potential linearized augmented plane wave (FP-LAPW) [21] method incorporated in Wien2k code [22]. For the calculation of lattice parameter and total energy, Generalized-gradient approximation (GGA) [23] of Perdew, Burke and Ernzerhof (PBE) [24] was approved as the exchange-correlation function. Spin orbit coupling effect was considered to perform all the calculations. Wien2k is one of the most accurate methods for performing electronic structure calculations for solids. Core states are considered relativistically and valence states are considered as semi-relativistic way and energy between these two states was set -6.0Ry. In first Brillouin zone, we have used 1000 k-points for this code. But for the calculation of optical properties we need to increase the number of k-points and this increased value of k-points used are 10000. The

size of the basis sets are controlled by convergence or cutoff parameter, whose value is $R_{mt} K_{max}$ set to 7.0. Here plane wave radius is denoted by R_{mt} and maximum modulus for reciprocal lattice vector is denoted by K_{max}. The energy convergence criterion was taken as 0.0001Ry. To expand the spherical harmonics in the atomic sphere the value of angular momentum maximum (l_{max}) is taken as 10. In the central region the charge density and potential were elaborated as a cheerier series with wave vector up to G_{max}=10. For the each atom muffin tin sphere radii (R_{MT}) are tabulated in Table 1.

Table 1

Muffin tin radius (R_{MT}) for Co_2CrZ (Z= In, Sb, Sn).

R_{MT} (a.u.)	Compounds		
	Co_2CrIn	Co_2CrSb	Co_2CrSn
Co	2.35	2.37	2.43
Cr	2.29	2.31	2.37
Z	2.35	2.37	2.43

Above mentioned properties are also investigated with the help of commercially licensed Atomistic Tool Kit-Virtual NanoLab (ATK-VNL) package [25]. Which is a Pseudo-potential method carried out in the framework of density functional theory (DFT) [26, 27]. First-principles calculations have been applied to investigate electronic and magnetic properties of Co2CrZ (Z= In, Sb, Sn) using Pulay Mixer algorithm [28]. For investigations, we have used double-zeta (ζ) polarized basis set for electron wave function expanding and GGA for exchange-correlation functional. The structures are permitted to optimize until each atom achieve force convergence criteria 0.05 eV/Å and maximum stress is 0.05 eV/Å^3. Optimization is performed in 200 maximum number of step and during this process maximum step size is also fixed i.e. 0.2 Å. Convergence is achieved by deciding mesh cutoff energy on the ground of convergence principle and for this computation 150 Ryd has been projected all over calculation as the most favorable after several convergence test. For spin polarization, up and down initial state have been selected for the atoms. We used 10 x 10 x 10 Monkhorst-Pack k-mesh [29] for brillouin zone sampling to maintain balance between computational time and results accuracy. Further, all constrain in x, y and z directions are removed for optimization of structures.

RESULTS AND DISCUSSIONS
Structural parameters

Space group of full Heusler compound is 225 Fm-3m. The chemical formula for full Heusler is X_2YZ showing their composition 2:1:1. Its structure is formed by three penetrating FCC-lattices with atomic positions at X_1 (1/4, 1/4, 1/4), X_2 (3/4, 3/4, 3/4), Y (1/2, 1/2, 1/2) and Z (0, 0, 0). Where X and Y atoms are transition metal and Z is main group metal or semimetal [30, 31]. The equation of state given by Murnaghan [32] gives the value of total energy & pressure as a function of volume is stated as:

$$E(V) = E_O + \left[\frac{BV}{B_P}\left(\frac{1}{(B_P - 1)}\left(\frac{V_O}{V}\right)^{B_P} + 1\right) - \frac{BV_O}{(B_P - 1)}\right]$$

$$P(V) = \frac{B}{B_P}\left\{\left(\frac{V_O}{V}\right)^{B_P} - 1\right\},$$

where, Pressure $(P) = -\frac{dE}{dV}$, $B_P = -V\frac{dP}{dV} = V\frac{d^2E}{dV^2}$

In the above equations E_0 is the minimum energy at T = 0K, B is the bulk modulus, B_P is the pressure derivative of the bulk modulus and V_o is the equilibrium volume. For structure optimization we have used volume optimization and their results are shown in Figure 1. There are slight differences between the optimized lattice parameter of WIEN2k and ATK lattice parameters. Optimized lattice parameters in WIEN2k for Co_2CrIn and Co_2CrSn are slightly greater than the lattice parameters optimized in ATK-VNL, where Co_2CrSb has slightly less value in WIEN2k. If we compare the values of bulk modulus by WIEN2k and ATK-VNL then results obtained by WIEN2k are greater to the ATK-VNL. The compound Co_2CrSn has showing largest value of bulk modulus in comparison to the others. Calculated values of the optimized lattice parameter, equilibrium energy and pressure derivative have been representing in Table 2.

Table 2.

Lattice parameter, Bulk modulus, Equilibrium energy and Pressure derivative for Co_2CrZ (Z= In, Sb, Sn)

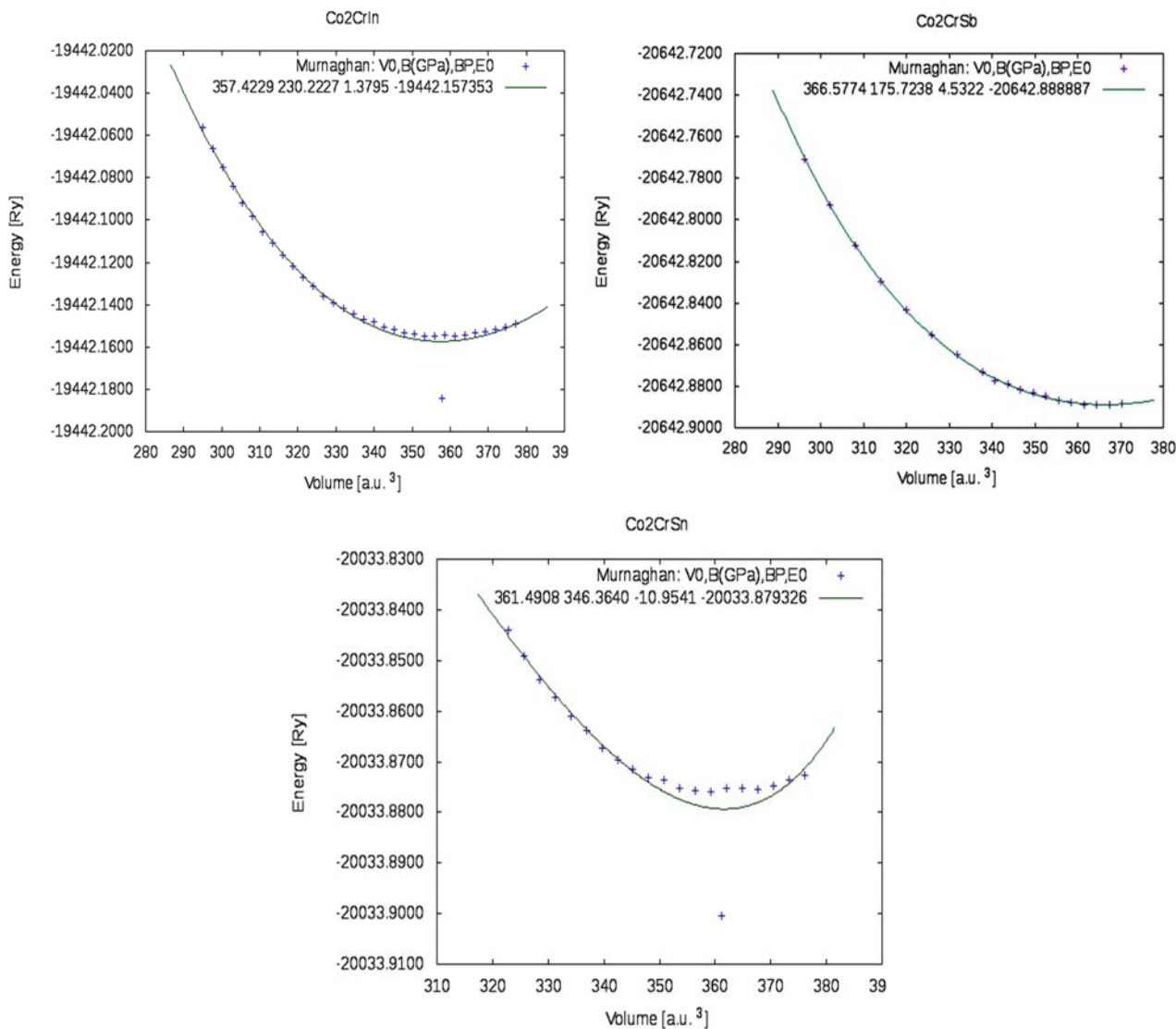| Compound	Lattice Constants a_0 (Å)		Bulk modulus (GPa)		Equilibrium Energy (Ry)	Pressure derivative (GPa)
	Calculated		Calculated			
	WIEN2k	ATK	WIEN2k	ATK		
Co_2CrIn	5.962	5.957	229.40	167.16	-19442.157	1.399
Co_2CrSb	6.014	6.044	180.15	178.43	-20642.889	3.956
Co_2CrSn	5.984	5.957	348.57	208.84	-20033.879	-12.017

Figure 1. Volume optimization for the lattice parameters

Electronic and magnetic properties

In the present era Spintronics is very useful ground work, which is very innovative for future technology. The advantages of Spintronics devices are nonvolatile memory and high processing speed of data. These devices consume less electric power and their heat dissipation is also decrease. Half-metallic ferromagnets having 100% spin-polarized can optimize the accomplishment of these devices. Spin polarized calculations of Co_2CrZ (Z= In, Sb, Sn) compounds within Generalized-gradient approximation (GGA) full Heusler have been carried out at the optimized lattice parameters. If band structure shows zero band gaps in majority spin channel and a band gap in minority spin channel then the compound shows 100% spin polarization at Fermi level. Intrinsic spin of electron is also responsible for magnetic moment. Theoretical calculations of spin polarization can be done using the formula as given below.

$$P_n = \frac{n\uparrow - n\downarrow}{n\uparrow + n\downarrow}.$$

If either $n_\uparrow = 0$ or $n_\downarrow = 0$, then $P_n = 1$ or -1. It means, if either only one spin channel is existing then the spin polarization is 100%. These types of materials are known as half metals ferromagnetic. If the value of P_n is vanishes then the materials are paramagnetic or anti-ferromagnetic even below the magnetic transition temperature [33]. After studying the energy gag from DOS and band structure of the compounds Co_2CrZ (Z= In, Sb, Sn), we have concluded that out of three compounds only Co_2CrSb show a band gap in minority spin with value 0.54 eV in WIEN2k code, showing 100% spin polarization. Other two listed compounds show zero band gaps, showing metallic behavior. Outcome of ATK-VNL code revels that all three compounds show metallic behavior. Obtained energy gap and spin polarization for the above approximation is summarized as under in Table 3. The detailed results of band structures and density of states are shown in Figures 2-5.

Table 3.

Energy gap and spin polarization for Co_2CrZ (Z= In, Sb, Sn).

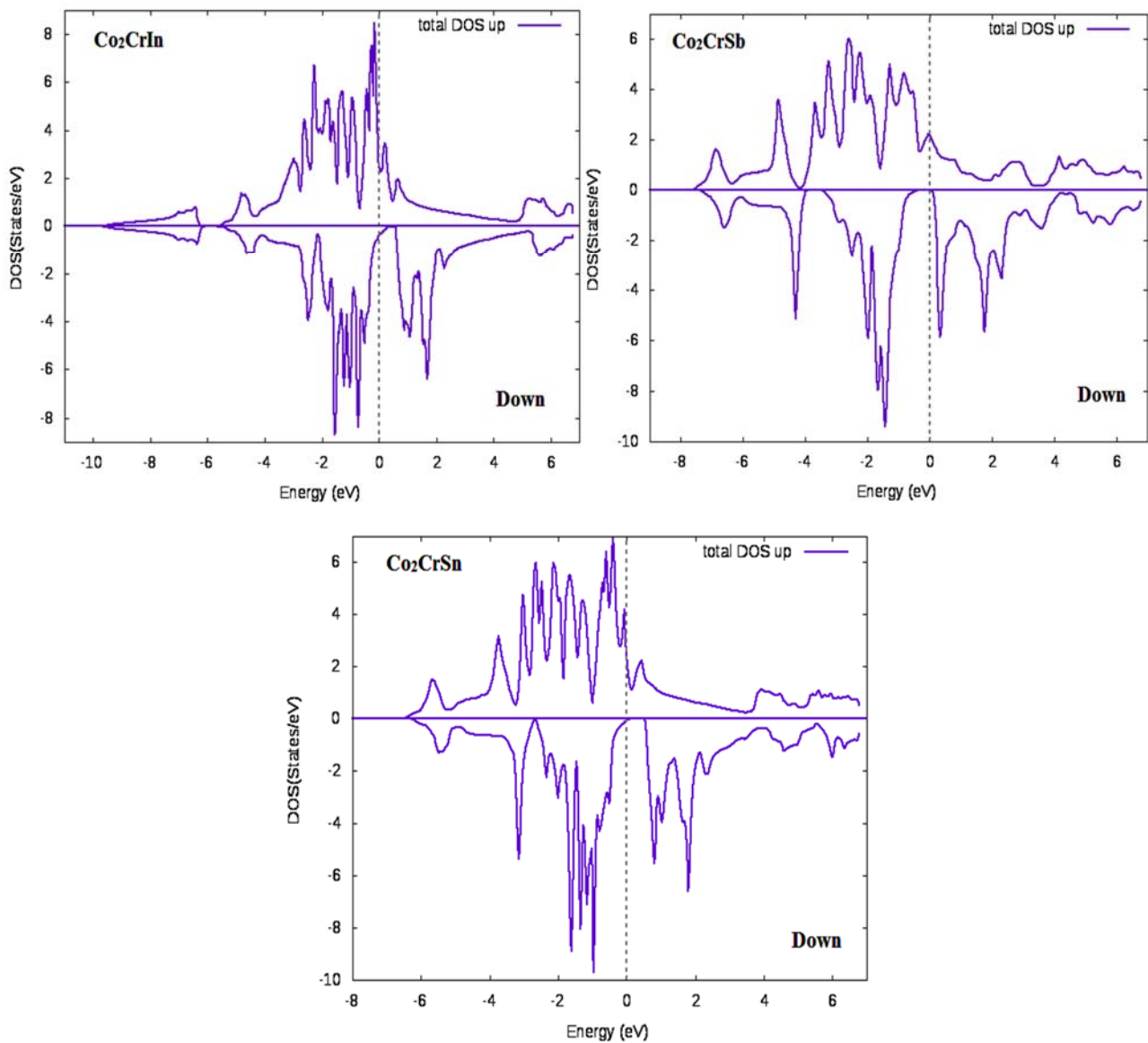| Compound	Energy gap E_g (eV)				Spin polarization	
	WIEN2k		ATK		WIEN2k	ATK
	Up spin	Down spin	Up spin	Down spin		
Co2CrIn	0.0	0.0	0.0	0.0	P_n vanishing	P_n vanishing
Co2CrSb	0.0	0.54	0.0	0.0	100%	P_n vanishing
Co2CrSn	0.0	0.0	0.0	0.0	P_n vanishing	P_n vanishing

Figure 2. DOS of Co_2CrZ (Z= In, Sb, Sn) using WIEN2K Code

Total valence electron count can propose the result of magnetic moment per unit cell of Heusler compounds. This theoretical method of prediction of magnetic moment is provided by Slater-Pauling. Method for Full Heusler compound is as given by

$$M_t = Z_t - 24,$$

where, M_t denotes the total magnetic moment per unit cell and Z_t denotes the total count of valence electron [33,34].
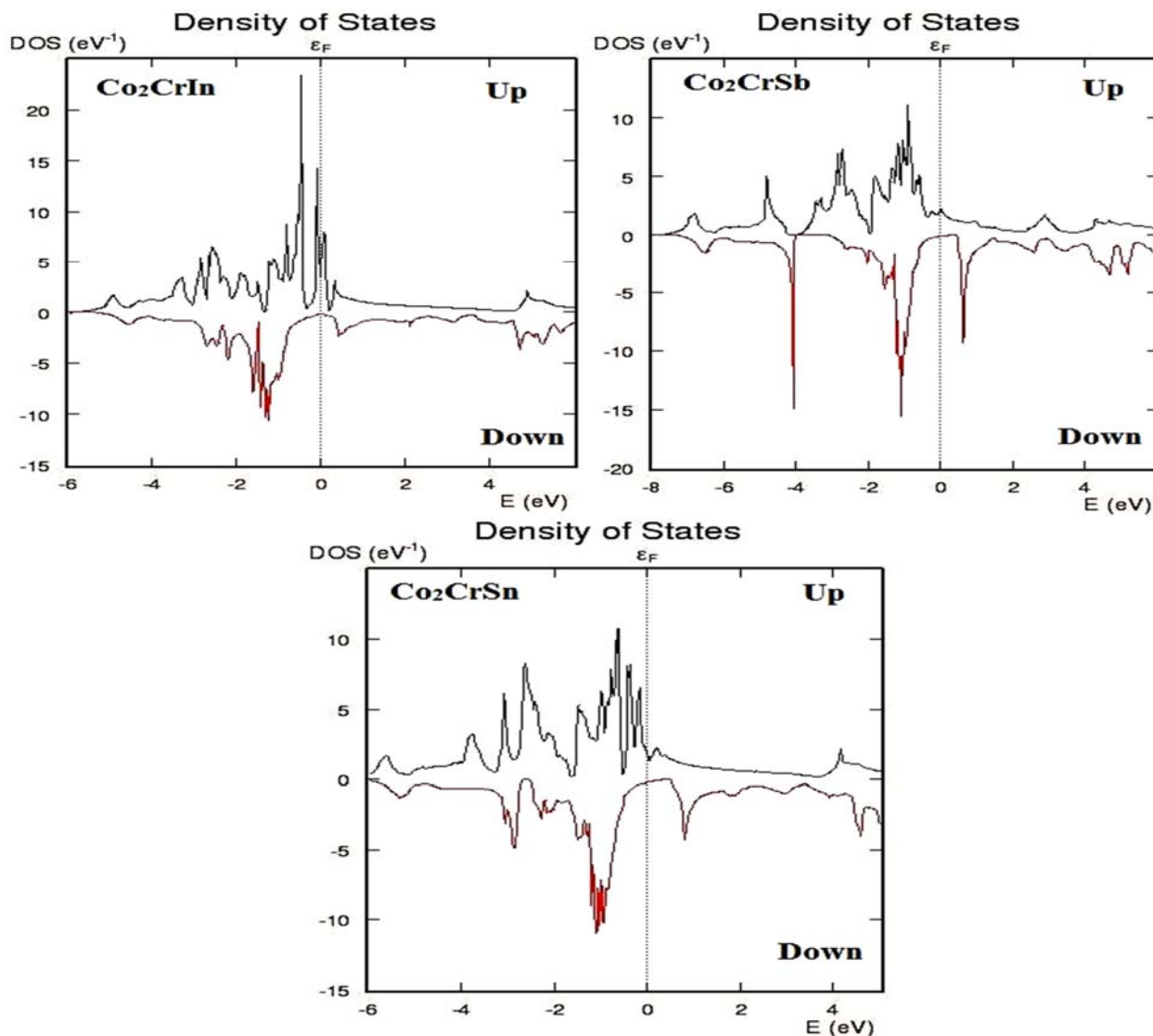
Figure 3. DOS of Co₂CrZ (Z= In, Sb, Sn) using ATK-VNL Code
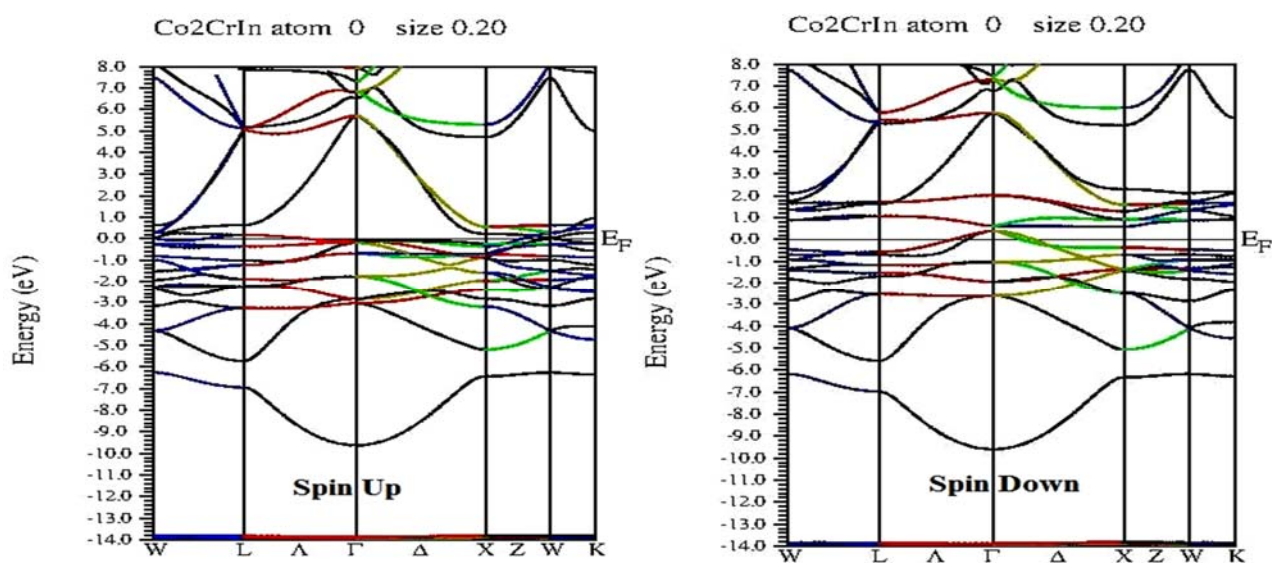

Figure 4. Band Structure of Co₂CrZ (Z= In, Sb, Sn) using WIEN2K Code
(*Continued on next page*)
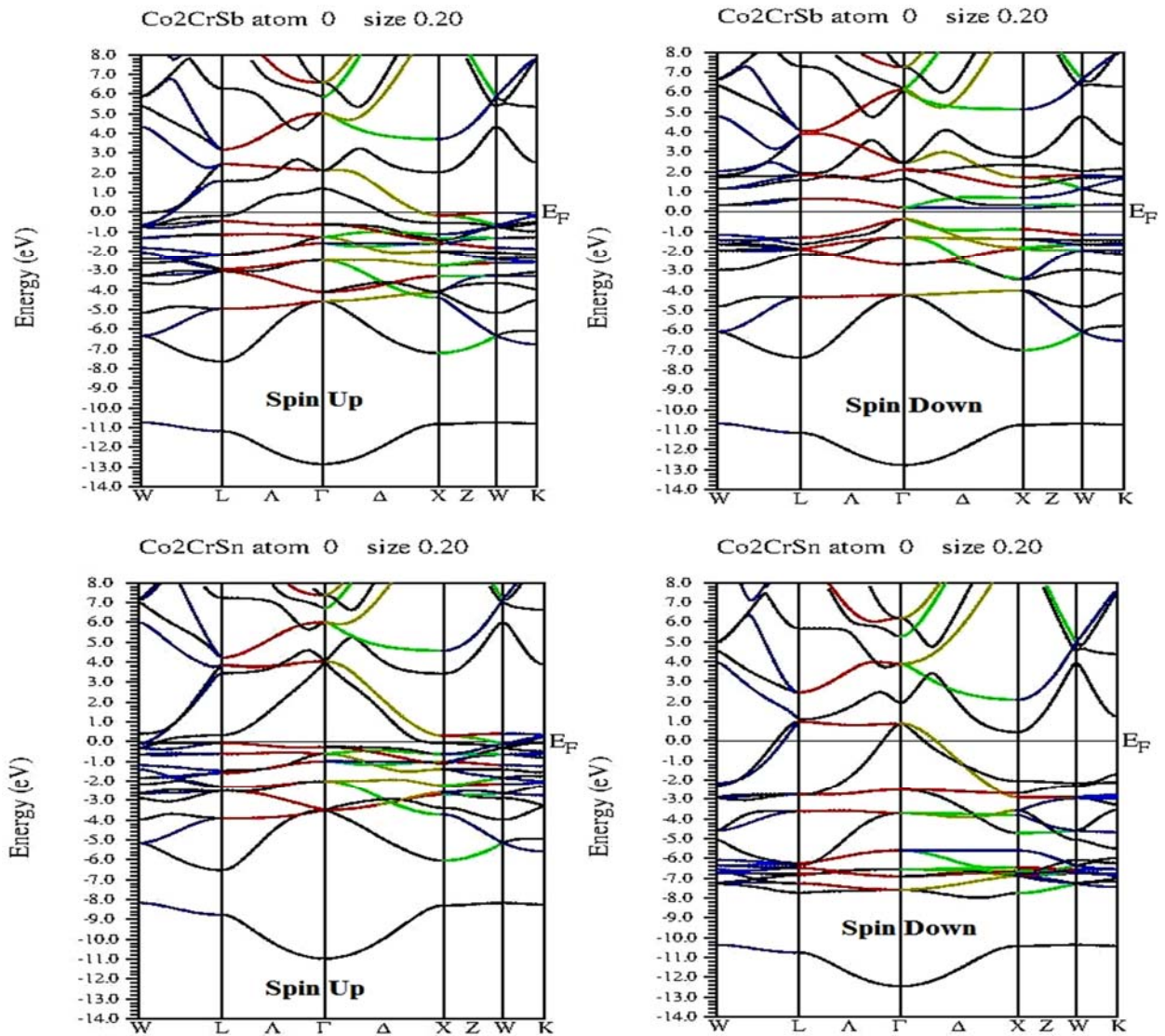
Figure 4. Band Structure of Co₂CrZ (Z= In, Sb, Sn) using WIEN2K Code
(*Continiation*)

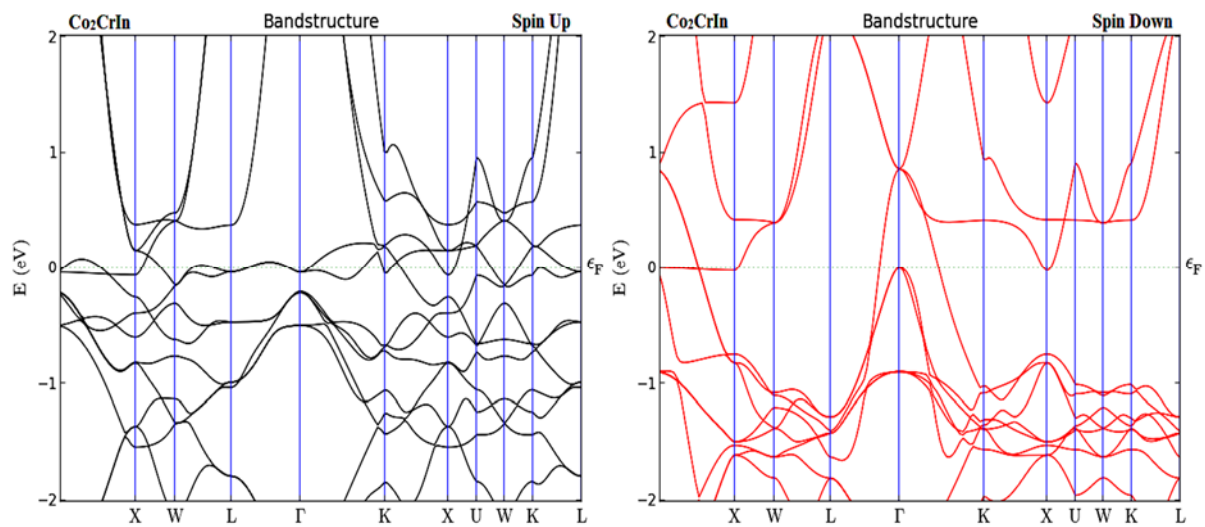
Figure 5. Band Structure of Co₂CrZ (Z= In, Sb, Sn) using ATK-VNL Code
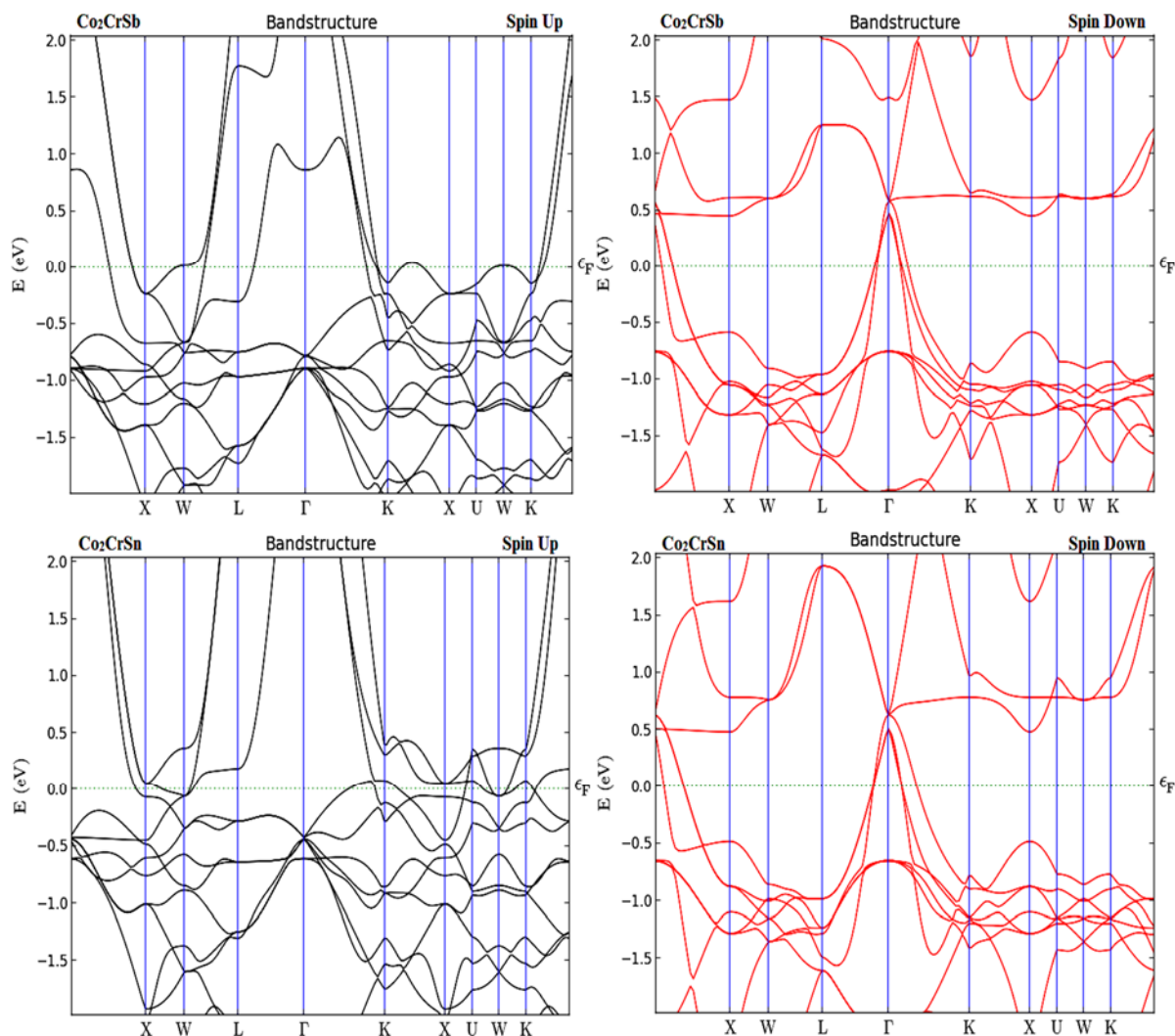(*Continied on next page*)

Figure 5. Band Structure of Co$_2$CrZ (Z= In, Sb, Sn) using ATK-VNL Code
(*Continiation*)

Here, we have compared the values by the codes WIEN2k and ATK-VNL with derived from theoretical method Slater-Pauling. If obtained results are equivalent to Slater-Pauling result then we can say that it follow the Slater-Pauling behavior. From the Table 4, we can easily analysis the values of WIEN2k, ATK-VNL code and Slater-Pauling rule. Total number of valence electron of Co$_2$CrZ (Z= In, Sb, Sn) alloys are 27, 29 and 28 respectively. So there magnetic moments per unit cell are 3.0, 5.0 and 4.0μ_B respectively from Slater-Pauling rule. Now, the results compiled by WIEN2k and ATK-VNL are 3.11 and 3.14, 5.00 and 5.05, 4.00 and 4.12 respectively. These compiled values are equivalent to values of theoretical method Slater-Pauling. So, these listed compounds have nice agreement with Slater-Pauling behavior. Investigation of results revels that Co and Cr position atom contribute major section of magnetic moment and small amount of magnetic moment contribution is due to Z position atom. It was also observed that more amount of magnetic moment at sites Co and Cr are induces as Z atom have more valence electron. The calculated results for magnetic moments for Co2CrZ (Z= In, Sb, Sn) obtained using full potential linearized augmented plane wave (FP-LAPW) method implemented in WIEN2k and pseudo-potentials method implemented in Atomistic Tool Kit-Virtual NanoLab (ATK-VNL) within Generalized- gradient approximation (GGA) for exchange correlation functions is tabulated in Table 4.

Table 4.

Total magnetic moments of the compounds Co$_2$CrZ (Z= In, Sb, Sn).

Compounds	Z$_t$	Magnetic moment (μ_B)		
		WIEN2k	ATK	Slater-Pauling (Z$_t$ - 24)
Co$_2$CrIn	27	3.11	3.14	3.00
Co$_2$CrSb	29	5.00	5.05	5.00
Co$_2$CrSn	28	4.00	4.12	4.00

Optical properties

Optical properties play an important role to understand the nature of material; whether it can be used as optoelectronics device. The present section describes the optical properties of the compounds Co_2CrZ (Z= In, Sb, Sn). For the optical properties, we calculate the dielectric function, optical conductivity, reflectivity, excitation coefficient, absorption coefficient and electron energy loss as a function of photon energy for the above compounds. The complex dielectric function describes the optical response of a material on incident electromagnetic radiation.

$$\varepsilon\,(m) = \varepsilon_1(m) + i\varepsilon_2(m)$$

Where $\varepsilon_1(m)$ real represents polarization and anomalous dispersion of medium and $i\varepsilon_2(m)$ corresponds imaginary part represents the absorption or loss of energy into the medium [35, 36]. It is considered that the transitions exists from occupied to unoccupied bands for explain the optical spectra. Inter-band region is chosen for studying the optical properties. The different optical spectra are shown in Figure 6.

Figure 6. Calculated optical parameters (a) real part of dielectric function, (b) imaginary part of dielectric function, (c) optical conductivity, (d) absorption coefficient, (e) electron energy-loss function, (f) reflectivity, (g) refractive index and (h) extinction coefficient for Co_2CrZ (Z= In, Sb, Sn).
(*Continued on next page*)

The imaginary part of dielectric function for all three compounds shows the main peak in infrared region from 0.08 to 0.31eV. After that, imaginary part of dielectric function decreases continuously and some small peaks are observed in infrared region, near visible region between 1.13 - 1.86eV. The zero frequency real ($\varepsilon_1\,(\omega)$) and imaginary part of complex dielectric functions values are 283.54 and 112.766, 297.748 and 120.002, 265.679 and 86.053for the compounds Co2CrZ

(Z= In, Sb, Sn) respectively as observed from the Figure 6 (a) and 6 (b). Optical conductivity is an important optical parameter for conduction of electron due to an applied electromagnetic field. In the optical conductivity spectrum, sharp peaks are observed at 0.18 to 0.50eV, 1.38 to 1.88eV in infrared region and in ultraviolet region between 3.97 - 8.37eV. A sharp peak is observed at 7.39eV by Co_2CrSb showing largest conduction of electron. High absorption coefficient means that the material absorbs more photon, which excite electron from valence band to conduction band. The values of absorption coefficient are an increase along the values of energy is increases towards visible region to ultraviolet region as shown in the Figure 6(d).
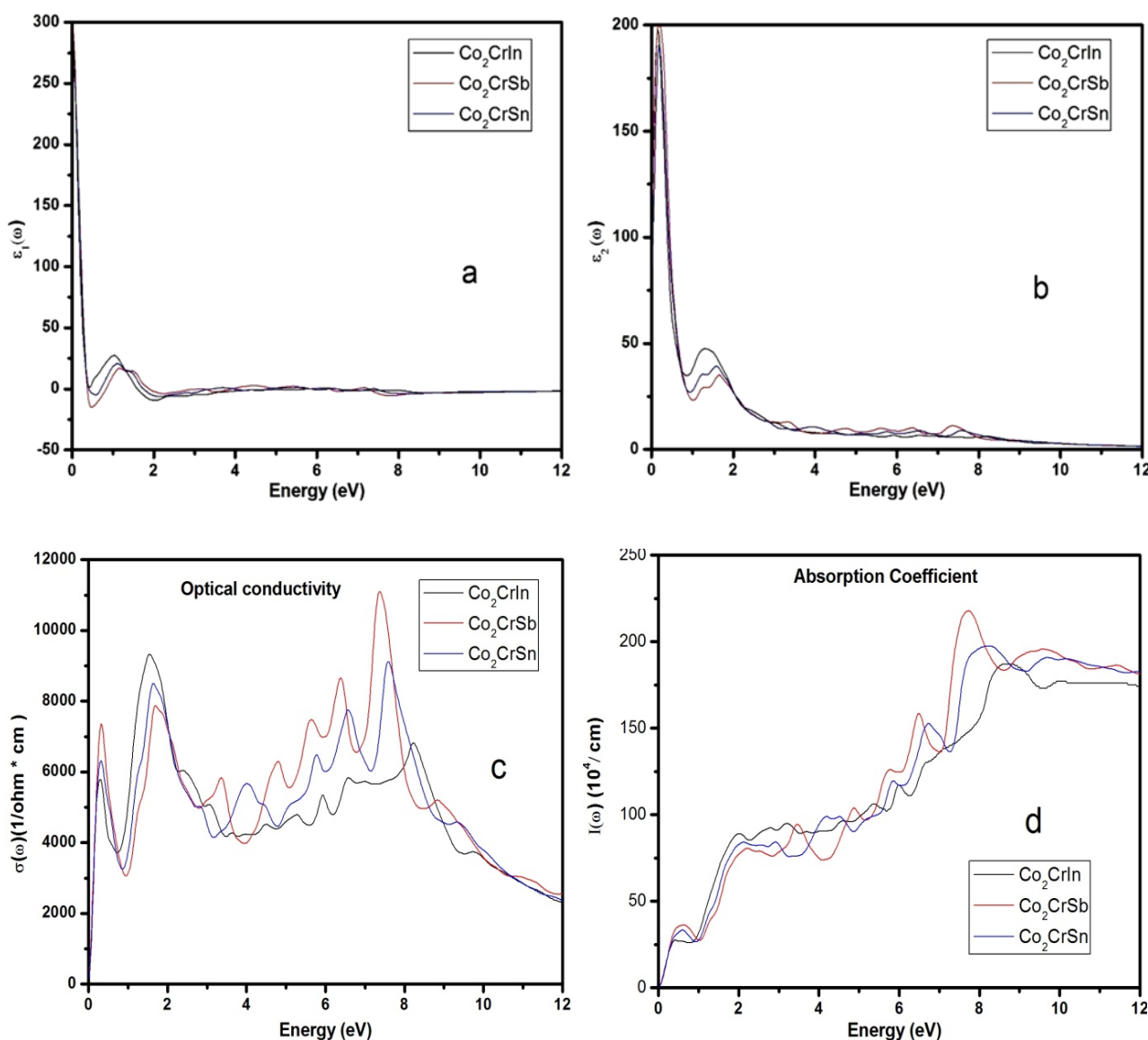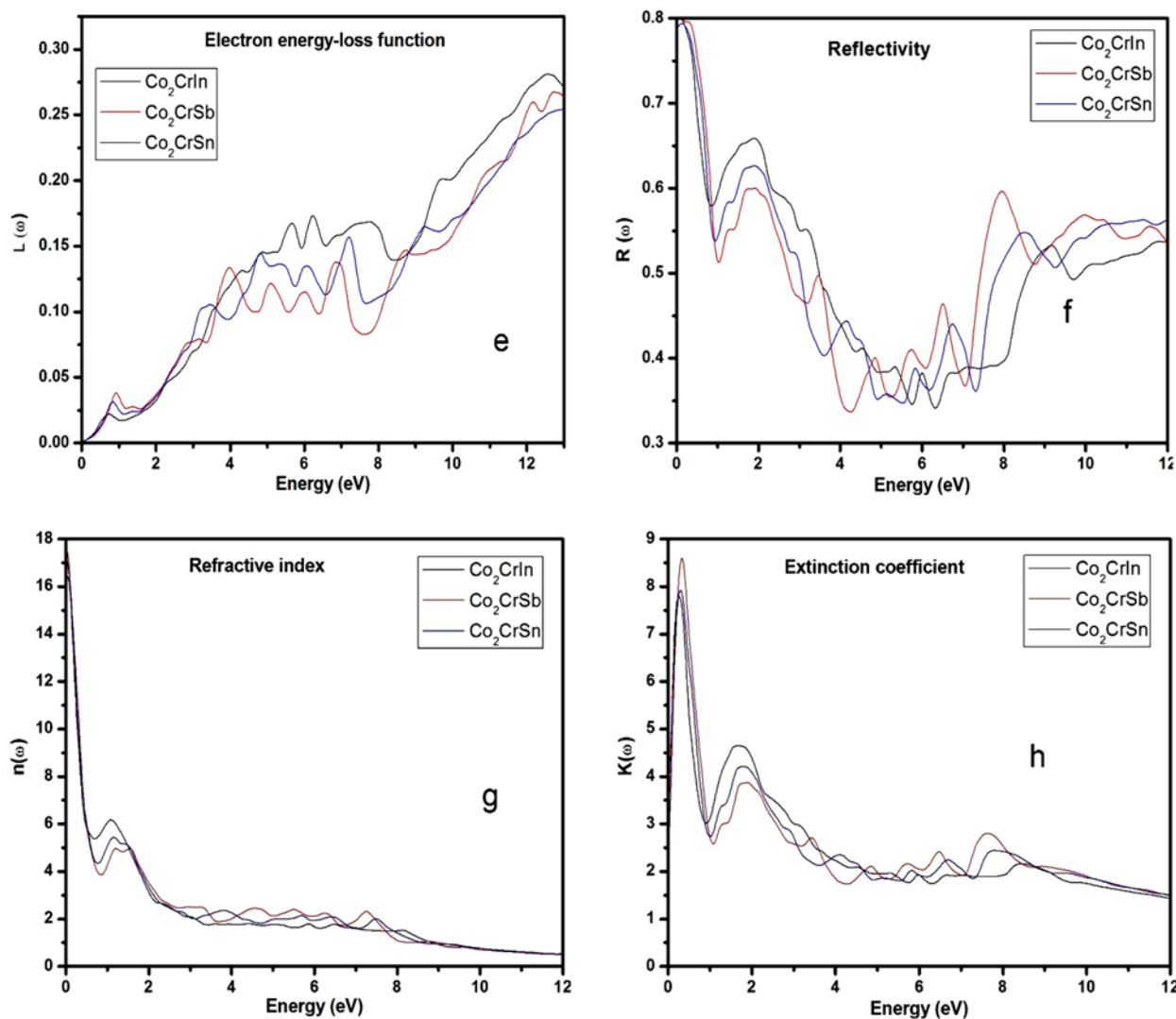

Figure 6. Calculated optical parameters (a) real part of dielectric function, (b) imaginary part of dielectric function, (c) optical conductivity, (d) absorption coefficient, (e) electron energy-loss function, (f) reflectivity, (g) refractive index and (h) extinction coefficient for Co_2CrZ (Z= In, Sb, Sn).
(*Continuation*)

Highest peaks are observed between 7.50 - 8.75eV by all above compounds. At 7.74eV Co_2CrSb showing highest peak out of three compounds representing maximum absorption of photons. Electron energy-loss function gives the energy loss of a fast moving electron when passing through the medium. The plasma frequency is the frequency corresponding to plasma resonance at which sharp peaks are associated. As if the frequency is above the plasma frequency then the material showing the dielectric behavior and below which the material shows metallic behavior. Value energy loss of fast moving electron is increases as move from infrared to ultraviolet region. The maximum energy loss is observed between 12 to 13eV for above these compounds as shown in Figure 6(e). An extinction coefficient spectrum is displayed in Figure 6 (h). A prominent narrow peak is shown in the infrared region along the range 0.20 to 0.46eV and then value of extinction coefficient is decreases. Near to visible region further a small peak is observed between 1.16 – 2.17eV and further value is decreases in the ultraviolet region with small peak near 8eV. The values of zero frequency reflectivity are 0.798, 0.803 and 0.789 for the compounds Co_2CrZ (Z= In, Sb, Sn) respectively as observed from Figure 6 (f). From the absorption and reflection spectra relation, observations indicate that absorption and reflectivity are inversely proportional to each other. Value of reflectivity first decreases showing small peak near 2eV with the increase of energy up to 5.5eV

and after that increases up to 8.3eV in the ultraviolet region. The region in which material substantially absorbs light and it cannot effectively reflect light in the same span. The refractive index is the important optical property due to wide applications because it determines the dispersive power of prisms, focusing power of lenses, light guiding, and critical angle for total internal reflection etc. How fast light is traveling through the materials is described by refractive index. The values for zero frequency refractive index for the compounds Co_2CrZ (Z= In, Sb, Sn) are observed as 17.156, 17.589 and 16.507 respectively.

SUMMARY AND CONCLUSIONS

Here, we have investigated structural, electronic, optical and magnetic properties of Co_2CrZ (Z= In, Sb, Sn). These properties have been studied by using full potential linearized augmented plane wave (FP-LAPW) method implemented in WIEN2k and pseudo- potentials method implemented in Atomistic Tool Kit-Virtual NanoLab (ATK-VNL) within Generalized-gradient approximation (GGA) for exchange-correlation functional. From study of DOS and band structure, we have clearly mentioned that the compound Co_2CrSb is half metallic and 100% spin polarization with $L2_1$ ordered stable structures in WIEN2k code. Other two compounds show the metallic behavior with zero band gaps at Fermi level. Calculated magnetic moments have good agreement with the Slater-Pauling behavior. For above listed compounds, the optical properties named as reflectivity, refractive index, excitation coefficient, absorption coefficient, optical conductivity and electron energy loss have been calculated. Also, we have analyzed their optical spectra and Inter-band region is chosen for studying the optical properties. Value of absorption coefficient and optical conductivity of Co_2CrSb is greatest than other two compounds.

ORCID IDs
Sukhender, https://orcid.org/0000-0002-2149-5669; **Lalit Mohan**, https://orcid.org/0000-0003-3323-8296
Pravesh Pravesh, https://orcid.org/0000-0002-0876-4836; **Ajay Singh Verma**, https://orcid.org/0000-0001-8223-7658

REFERENCES
[1]   Fr. Heusler, Ueber magnetische Manganlegierungen. Verh. Dtsch. Phys. Ges. **5**, 219 (1903).
[2]   Fr. Heusler, W. Starck, and E. Haupt, Magnetisch-Chemische Studien. Verh. Dtsch. Phys. Ges. **5**, 220 (1903)
[3]   Fr. Heusler, and E. Take, The nature of the Heusler alloys, Trans. Faraday Soc. **8**, 169-184 (1912).
[4]   L. Néel, Ann. de Phys. **5**, 232–279 (1936), https://doi.org/10.1051/anphys/193611050232.
[5]   L. Néel, Rev. Mod. Phys. **25** 58–63 (1953), https://doi.org/10.1103/RevModPhys.25.58.
[6]   I. Galanakis, in: *Heusler Alloys. Properties, Growth, Applications*, edited by C. Felser, and A. Hirohata (Springer International Publishing, Switzerland, 2016), pp. 3-36, https://doi.org/10.1007/978-3-319-21449-8.
[7]   C.J. Palmstrom, Prog. Crys. Growth. Char. Mater. **62**, 371-397 (2016), https://doi.org/10.1016/j.pcrysgrow.2016.04.020.
[8]   A.O. Oliynyk, E. Antono, T.D. Sparks, L. Ghadbeigi, M.W. Gaultois, B. Meredig, and A. Mar, Chem. Mater. **28**, 7324-7331 2016), https://doi.org/10.1021/acs.chemmater.6b02724.
[9]   Arash Anjami, Arash Boochani, Seyed Moahammad Elahi, Hossein Akbari, Results Phys. **7**, 3522–3529 (2017), https://doi.org/10.1016/j.rinp.2017.09.008.
[10] R.A. de Groot, F.M. Muller, P.G. van Engen, and K.H.J. Buschow, New class of materials: half-metallic ferrowmagnets, Phys. Rev. Lett. **50**, 2024-2027 (1983), https://doi.org/10.1103/PhysRevLett.50.2024.
[11] J. Kübler, A.R. William, C.B. Sommers, Phys. Rev. B, **28**, 1745-1755 (1983), https://doi.org/10.1103/PhysRevB.28.1745.
[12] M.I. Katsnelson, V.Yu. Irkhin, L. Chioncel, A.I. Lichtenstein, and R.A. de Groot, Rev. Mod. Phys. **80**, 315-378 (2008), https://doi.org/10.1103/RevModPhys.80.315.
[13] Igor Žutić, J. Fabian, and S. Das Sarma, Rev. Mod. Phys. **76**, 323-410 (2004), https://doi.org/10.1103/RevModPhys.76.323.
[14] H. Ohno, Science, **281**, 951-956 (1998), https://doi.org/10.1126/science.281.5379.951.
[15] J.D. Boeck, W.V. Roy, J. Das, V. Motsnyi, Z. Liu, L. Lagae, H. Boeve, K. Dessein, and G. Borghs, Semicond. Sci. Technol. **17**, 342 (2002), https://doi.org/10.1088/0268-1242/17/4/307.
[16] S. Ishida, S. Akazawa, Y. Kubo, and J. Ishida, J. Phys. F: Met. Phys. **12**, 1111 (1982), https://doi.org/10.1088/0305-4608/12/6/012.
[17] I. Galanakis, K. Özdoğan, E. Şaşıoğlu, and B. Aktaş, Phys. Rev. B, **75**, 092407 (2007), https://doi.org/10.1103/PhysRevB.75.092407.
[18] R.Y. Umetsu, K. Kobayashi, R. Kainuma, A. Fujita, K. Fukamichi, K. Ishida, and A. Sakuma, Appl. Phys. Lett. **85**, 2011-2013 (2004), https://doi.org/10.1063/1.1790029.
[19] Y. Miura, K. Nagao, and M. Shirai, Phys. Rev. B, **69**, 144413 (2004), https://doi.org/10.1103/PhysRevB.69.144413.
[20] K. Seema, N.M. Umran, and R. Kumar, J. Supercond. Nov. Magn. **29**, 401-408 (2016), https://doi.org/10.1007/s10948-015-3271-7.
[21] E. Wimmer, H. Krakauer, M. Weinert, and A.J. Freeman, Phys. Rev. B, **24**, 864-875 (1981), https://doi.org/10.1103/PhysRevB.24.864.
[22] P. Blaha, K. Schwarz, G.K.H. Madsen, D. Kvasnicka, and J. Luitz in: *WIEN2k: An Augmented Plane Wave + Local Orbitals Program for Calculating Crystal Properties*, edited by K Schwarz (Technical Universitatwien, Austria, 2001), pp. 287.
[23] E. Sjöstedt, L. Nordström, and D.J. Singh, Solid State Commun. **114**, 15-20 (2000), https://doi.org/10.1016/S0038-1098(99)00577-3.
[24] J.P. Perdew, K. Burke, and M. Ernzerhof, Phys. Rev. Lett. **77**, 3865-3868 (1996), https://doi.org/10.1103/PhysRevLett.77.3865.
[25] *Atomistix ToolKit-Virtual Nanolab (ATK-VNL), QuantumWise Simulator, Version. 2014.3*. Available: http://quantumwise.com/
[26] Y.J. Lee, M. Brandbyge, J. Puska, J. Taylor, K. Stokbro, and M. Nieminen, Phys. Rev. B, **69**, 125409 (2004), https://doi.org/10.1103/PhysRevB.69.125409.
[27] K. Schwarz, J. Solid State Chem. **176**, 319–328 (2003), https://doi.org/10.1016/S0022-4596(03)00213-5.
[28] P. Pulay, J. Comput. Chem. **3**, 556–560 (1982), https://doi.org/10.1002/jcc.540030413.
[29] H.J. Monkhorst, and J.D. Pack, Phys. Rev. B, **13**, 5188-5192 (1976), https://doi.org/10.1103/PhysRevB.13.5188.

[30] T. Hahn, A. Looijenga-Vos, M.I. Aroyo, H.D. Flack, K. Momma, and P. Konstantinov, edited by M. Aroyo, in: International Tables for Crystal-lography Volume A: Space-group Symmetry, (Springer Netherlands, Dordrecht, 2016), pp. 193-687, http://dx.doi.org/10.1107/97809553602060000114.

[31] M.J. Mehl, D. Hicks, C. Toher, O. Levy, R.M. Hanson, G.L.W. Hart, and S. Curtarolo, Comput. Mater. Sci. **136**, S1-S828 (2017), https://doi.org/10.1016/j.commatsci.2017.01.017.

[32] F.D. Murnaghan, Proc. Natl. Acad. Sci. U.S.A, **30**, 244-247 (1944), https://dx.doi.org/10.1073%2Fpnas.30.9.244.

[33] I. Galanakis, P.H. Dederichs, and N. Papanikolaou, Phys. Rev. B, **66**, 134428 (2002), https://doi.org/10.1103/PhysRevB.66.134428.

[34] C.M. Fang, G.A. de Wijs, and R.A. de Groot, J. Appl. Phys. **91**, 8340 (2002), https://doi.org/10.1063/1.1452238.

[35] R. Jain, N. lakshmi, V. K. Jain, V. Jain, A.R. Chandra, and K. Venugopalan, J. Magn. Magn. Mater. **448**, 278-286 (2018), https://doi.org/10.1016/j.jmmm.2017.06.074.

[36] S. Sharma, A.S. Verma, and V.K. Jindal, Mat. Res. Bull. **53**, 218-233 (2014), https://doi.org/10.1016/j.materresbull.2014.02.021.

ПЕРШООСНОВИ РОЗРАХУНКУ ЕЛЕКТРОННИХ, ОПТИЧНИХ І МАГНІТНИХ ВЛАСТИВОСТЕЙ ПОВНИХ СПОЛУК ХЕЙСЛЕРА

Сукхендер[a], Правеш[b], Лаліт Мохан[a], Аджай Сінгх Верма[a]
[a]Кафедра фізики, Банастхалі Відьяпітх
Банастхалі 304022, Індія
[b]Кафедра електроніки і техніки звязку, група установ KIET
Газіабад, Уттар-Прадеш, Індія, 201206

Для дослідження структурних, електронних, оптичних і магнітних властивостей сполук Co_2CrZ (Z = In, Sb, Sn) ми використовували два різних методи. Один з них базується на методі повної потенційної лінеарізованої розширеної плоскої хвилі (FP-LAPW), який є реалізованим у коді WIEN2k, а другий – на псевдопотенційному методі, реалізованому в Atomistic Tool Kit-Virtual NanoLab (ATK-VNL). Для цих сполук є характерною нульова ширина енергетичної щілини як для основної так і протилежної орієнтації спіну, що представляють металічні характеристики, за винятком сполуки Co_2CrSb, яка показує ширину енергетичної щілини 0,54 еВ для протилежної орієнтації спіну поблизу рівня Фермі, і спостерігається 100%-на спінова поляризація; всі ці дані отримані з використанням коду WIEN2k. Крім того, було виявлено, що сполука Co_2CrSb є ідеальним напівметалевим феромагнетиком (HMF). У той же час, при використанні коду ATK-VNL для вищезазначених сполук має місце нульова енергетична щілина. Розрахунки, що були виконані з використанням коду WIEN2k, показують магнітний момент цих сполук Co_2CrZ (Z = In, Sb, Sn) 3,11, 5,00 і 4,00 μ_B, відповідно. Однак, відповідний магнітний момент цих сполук у коді ATK-VNL становить 3,14, 5,05 і 4,12 μ_B. Розраховані магнітні моменти добре узгоджуються з властивостями по Слейтер-Полінгу. Оптичні властивості відіграють важливу роль у розумінні природи матеріалу, що використовується для вивчення оптичних явищ, а також використовуються в пристроях оптоелектроніки. Значення коефіцієнта поглинання та оптичної провідності для Co_2CrSb є більшим, ніж для двох інших сполук. Зі співвідношення спектрів поглинання і відбиття видно, що поглинання і відбивна здатність є обернено пропорційними один одному.
КЛЮЧОВІ СЛОВА: напівметалевий феромагнетик, ширина енергетичної щілини, щільність стану, спінова електроніка

ПЕРВООСНОВЫ РАСЧЕТА ЭЛЕКТРОННЫХ, ОПТИЧЕСКИХ И МАГНИТНЫХ СВОЙСТВ ПОЛНЫХ СОЕДИНЕНИЙ ХЕЙСЛЕРА

Сукхендер[a], Правеш[b], Лалит Мохан[a], Аджай Сингх Верма[a]
[a]Кафедра физики, Банастхали Видьяпитх
Банастхали 304022, Индия
[b]Кафедра электроники и техники связи, Группа учреждений KIET
Газиабад, Уттар-Прадеш (Индия) 201206

Для исследования структурных, электронных, оптических и магнитных свойств соединений Co_2CrZ (Z = In, Sb, Sn) мы использовали два разных метода. Один из них основан на методе полной потенциальной линеаризованной расширенной плоской волны (FP-LAPW), реализованном в коде WIEN2k, а второй – на псевдопотенциальном методе, реализованном в Atomistic Tool Kit-Virtual NanoLab (ATK-VNL). Для этих соединений характерна нулевая ширина энергетической щели как для основной так и противоположной ориентации спина, представляющих металлические характеристики, за исключением соединения Co_2CrSb, которое показывает ширину энергетической щели 0,54 эВ с противоположной ориентации спина вблизи уровня Ферми, и наблюдается 100%-ная спиновая поляризация; все эти данные получены с использованием кода WIEN2k. Кроме того, было обнаружено, что соединение Co_2CrSb является идеальным полуметаллическим ферромагнетиком (HMF). В то же время, при использовании кода ATK-VNL для вышеупомянутых соединений имеет место нулевая энергетическая щель. Расчеты, выполненные с использованием кода WIEN2k, показывают магнитный момент этих соединений Co_2CrZ (Z = In, Sb, Sn) 3,11, 5,00 и 4,00 μ_B, соответственно. Однако соответствующий магнитный момент этих соединений в коде ATK-VNL составляет 3,14, 5,05 и 4,12 μ_B. Рассчитанные магнитные моменты хорошо согласуются со свойствами по Слейтер-Полингу. Оптические свойства играют важную роль в понимании природы материала, используемого для изучения оптических явлений, а также используемых в устройствах оптоэлектроники. Значение коэффициента поглощения и оптической проводимости для Co_2CrSb больше, чем для двух других соединений. Из соотношения спектров поглощения и отражения видно, что поглощение и отражательная способность обратно пропорциональны друг другу.
КЛЮЧЕВЫЕ СЛОВА: полуметаллический ферромагнетик, ширина энергетической щели, плотность состояния, спиновая электроника

FIRST PRINCIPLES CALCULATION OF MANGANESE BASED HALF HEUSLER COMPOUNDS

Lalit Mohan[a], Sukhender[a], Sudesh Kumar[b], Deepak Sharma[c], Ajay Singh Verma*,[a]

[a]Department of Physics, Banasthali Vidyapith, Banasthali 304022, India
[b]Department of Chemistry, Banasthali Vidyapith, Banasthali 304022, India
[c]Department of Physics, IIMT College of Engineering, Greater Noida, 201306, India
Corresponding Author: ajay_phy@rediffmail.com
Received March 30, 2020; accepted May 27, 2020

The Half-Heusler compounds exhibit a diverse range of tuneable properties including half-metallic ferromagnetism topological insulator, solar cells and thermoelectric converters. We have studied four half-Heusler compounds MnFeIn, MnFeGa, MnNiAs and MnNiSb. The nature and properties of half-heusler compounds can be studied on the bases of their valance electron count. In this paper, Fe based compounds have 18 valence electrons; whereas 22 valence electrons in Ni based. The Density Functional Theory (DFT) has been performed with WIEN2k code. Ni based compounds with Mn located at octahedral sites are half-metals as revealed from the Density of States (DoS) and band structure calculations. In all of them, spin-up channels are conducting; whereas in MnNiAs and MnNiSb spin-down channels have the small band gaps. MnNiAs and MnNiSb exhibit half-metallic property with integer magnetic moments of 4 μB per formula unit and half-metallic gaps of 0.15 and 0.17 eV at their equilibrium volume respectively.
KEYWORDS: Half-heusler, Spin polarisation, Optimization, Half- metallic

INTRODUCTION

The Heusler compounds were named after its discoverer Fritz Heusler. Surprisingly, the compound is ferromagnetic although none of its constituent elements is magnetic by itself. Half-Heusler compound is an impressive group of unconventional semiconductors being comprised of metal and containing at least one transition metal. Based on their properties they can be used in many applications [1-5]. The structure of Manganese based Half-Heusler compounds is a combination of rock salt and Zinc blend type lattices. This class of compounds with a 1:1:1 stoichiometric composition and can be represented as XYZ type structure with space group F-43 m [6, 7]. The main group elements such as As, Ga, In and Sb represents Z in our study. These compounds can be viewed as Mn and Z form zinc blend sub lattice arranged in a primitive cell at Wyckoff positions (0,0,0) and $\left(\frac{1}{2},\frac{1}{2},\frac{1}{2}\right)$ whereas [8,9]. We can also mention the ordering by interchanging above said Wyckoff positions, but the preferred atomic arrangements have dependency on size of involved atoms and the inter-atomic interaction between them. But in our case the size dependency on arrangement of transition metal is dominating factor over inter-atomic interaction configured by electro negativity of atoms. So, Manganese is most electropositive atom in our series of interest occupies position (0,0,0) whereas p-block elements are most electronegative element arranged at (0.5,0.5,0.5) for such set of configuration the transition elements having intermediate electronegativity acts like a bridge to pass on valence electrons from electropositive to most electronegative atom. This bridge type consideration forwarded by electronegativity difference plays important role for determination of bonding nature of materials. Also, half Heusler compounds considered as ternary relatives of binary semiconductors with vacant tetrahedral structures [10, 11]. The properties of these compounds depend strongly on number of valance electron in the primitive cell which determine the band structure & physical properties of the compound. Generally, it has been observed that half Heusler compounds with 18 valence electron having closed shell configuration shows tuneable band gap apart from this phase compounds will show magnetic behaviour but manganese-based compounds show tuneable band gap with 22 valence electrons instead of 18 [12,13]. Such behaviour can also be seen in rare earth metal based half Heusler compounds [14, 15].

COMPUTATIONAL DETAILS

The first principles calculations are done by using full potential Linearized Aungumated Plane Wave method (FP-LAPW) implemented in WIEN2k simulation package to describe the interaction between atomic core and valence electrons [16]. Considering the valance electrons, the electronic wave function is expanded. Generalized gradient approximation (GGA) in Perdew-Burke-Ernzerhof (PBE) is used to describe the exchange correlation energy [17]. For the geometry optimization of electronic structure; we have used the FP-LAPW method which lies within the framework of spin-polarized Density Functional Theory (SDFT). The cut-off energy separation between core and band states is kept -0.6 Ry for plane wave basis set in all studied materials. The energy convergence criterion was set to 0.00001 Ry and for charge to 0.001 e⁻. Total numbers of K - point are kept 1000 for irreducible Brillouin zones in Wien2k.

RESULT AND DISCUSSION

In the first step, the lattice constants were determined. The total energies for mentioned compounds with half-Heusler structure as a function of the lattice constant are calculated. The equilibrium lattice constants were derived by minimizing the total energy.

Structural properties

For all compounds volume optimization was done based on the Murnaghan equation of state [18]. The volume vs. energy curves are shown in Fig. 1. The optimized volume, pressure, pressure derivative and the minimum ground state energy is calculated and tabulated in Table 1. The optimized value of the lattice constant was used for the DOS, band structures and magnetic moment calculations to predict the electronic and magnetic properties of compounds.

Table 1.

The calculated values of the equilibrium lattice constant a_o, equilibrium volume, the bulk modulus B (GPa), the pressure derivative of bulk modulus B_P and minimum energy during optimization.

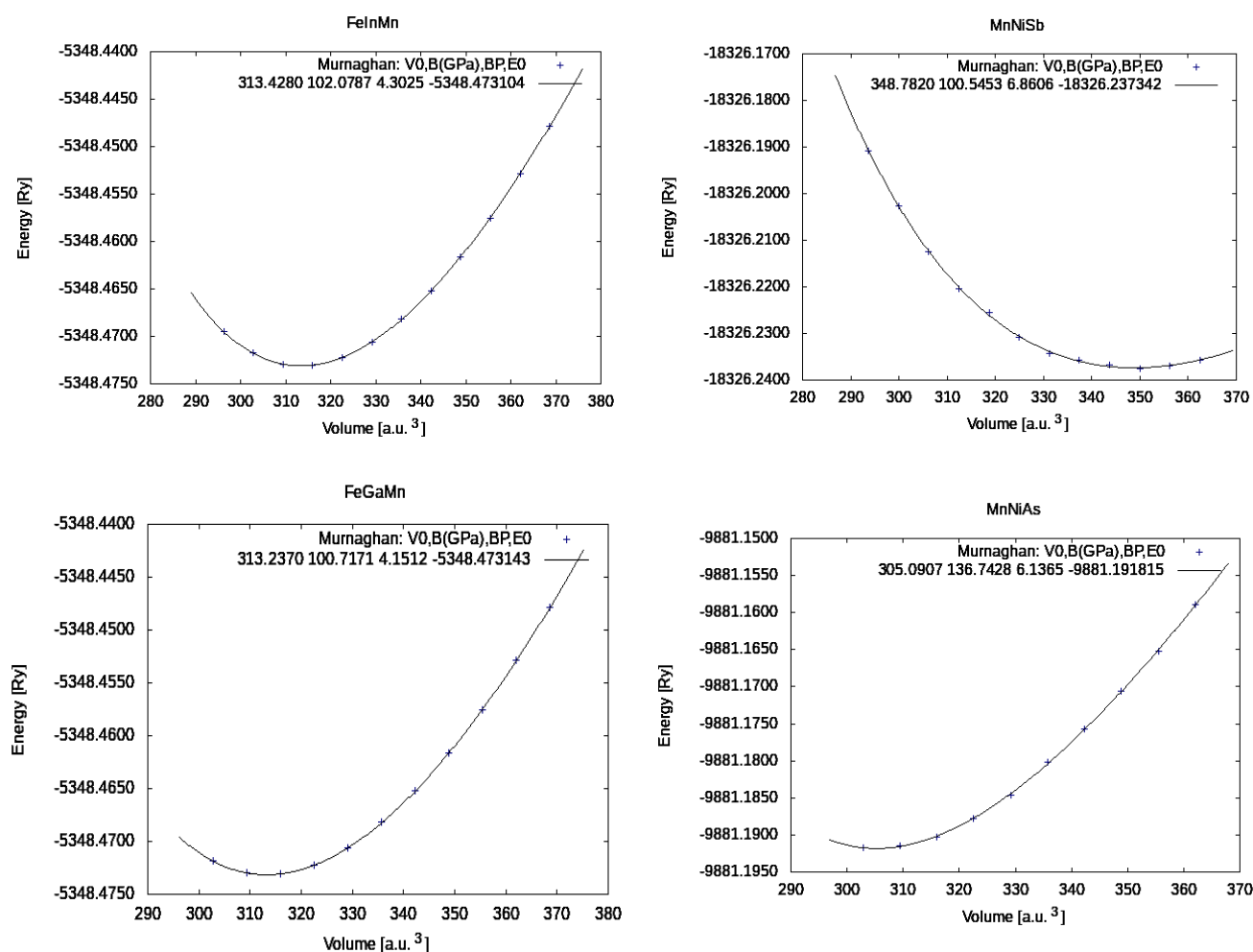| Compound	Optimized Lattice Parameter (A^0)	Equilibrium Volume (V_0)	Bulk Modulus (GPa)	B_P	Energy
MnFeIn	5.7057	341.56	140.90	3.34	-16629.13
MnFeGa	5.7048	313.22	101.56	4.58	-5348.47
MnNiAs	5.7048	305.23	141.97	7.40	-9881.19
MnNiSb	5.9128	348.81	102.37	6.02	-18326.23

Figure 1. Total energy as a function of volume per formula unit corresponding to MnFeIn, MnFeGa, MnNiSb & MnNiAs alloys

Electronic and Magnetic Properties

The electronic structure plays an important role in determining the half-metallic properties of half-Heusler compounds, so in order to understand the electronic structure of compounds; we have calculated the total density of states (DOS) and shown in Fig. 2.
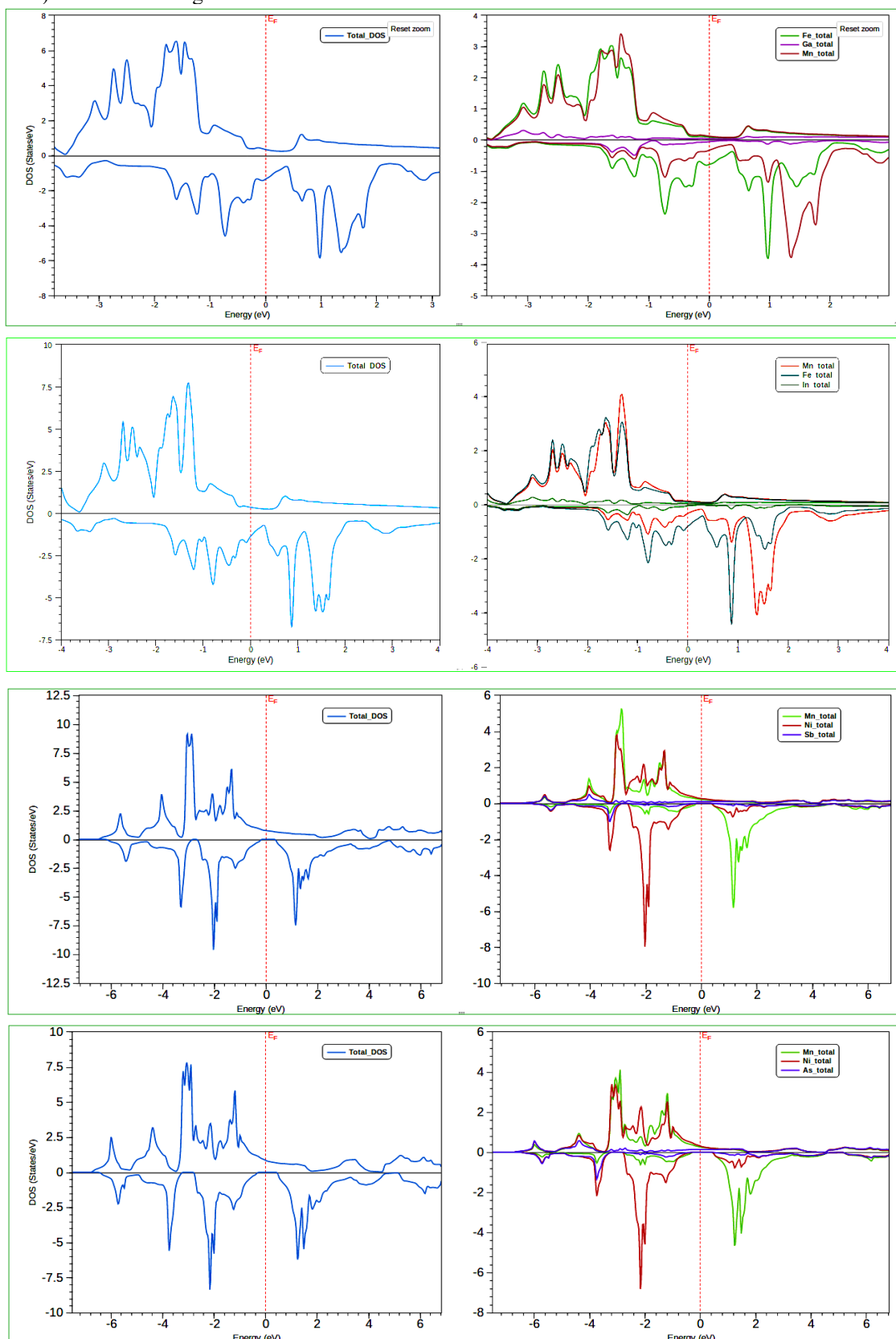

Figure 2. Total and atomic spin- density of states of all studied metallic (MnFeIn, MnFeGa) and half metallic ferromagnetic (MnNiSb, MnNiAs) compounds at their equilibrium lattice constant. Negative of DOS axis represents the minority spin

It is clear from the figure for both MnFeGa and MnFeIn both the majority and minority spin electrons exhibits metallic character. For MnNiAs and MnNiSb compounds, the electronic states in the majority-spin band are metallic and there is an energy gap at the Fermi level in minority-spin state confirms the half-metallic characteristics at their equilibrium lattice constants. We have focused on the calculations of MnNiAs and MnNiSb compounds, and the origin of half-metallic band gaps for these compounds has investigated. The partial DOS are also shown in the Fig. 2 for all the four compounds. Because the half-metallic band gap is an important factor in these materials, the atomic-projected DOSs of MnNiAs and MnNiSb compound. The states around -4.4 eV to -0.8 eV are essentially composed of Ni-d states with some admixture of As/Sb-p and Mn-d states. The states above 0.2 eV are mainly composed of Ni and Mn-d states. The Ni-d states are mainly located below the Fermi level, while the majority Mn-d states are mainly found around Fermi level. The ferromagnetism in MnNiAs and MnNiSb is attributed to the strong tendency of the d electrons of Mn^{3+} (d^4) to localize. The s and p states of Arsenic and Antimony are fully occupied and hybridize with unoccupied p and s state of Nickel, forming a set of low energy bonding a_1 and triple degenerated t_2 orbital, as well as a set of high energy anti-bonding and unoccupied orbital forming. The coupling of sublattices [NiAs] $^{3-}$ and [NiSb] $^{3-}$ with Mn^{3+} atom leads to the formation of bonding orbital doubly occupied and filled with 18 valance electrons. The anti-bonding hybrid orbital occupies four valance electrons. Mn^{3+} with d^4 configuration giving rise to a magnetic moment of approximately 4 μ_B.

To determine the band gap, we have also calculated the band structures of Half-Heusler compounds as shown in the Fig. 3. Both the panels for spin-up (black) channels and for the spin-down (blue) are given. Spin-down states have the band gaps and are, therefore, semiconducting. In the minority-spin band structure of MnNiSb and MnNiAs, the valence band maximum (VBM) is at the Γ-point and the conduction band minimum (CBM) at the X-point. Thus, the minority-spin band structure shows half-metallic behaviour with an indirect energy gap. The origin of the gap is mainly attributed to the covalent hybridization between the d-states of the Mn and Ni atoms, leading to the formation of bonding and anti-bonding bands with a gap in between [19]. The bonding hybrids are localized mainly at the Ni atoms whereas the anti-bonding states are mainly at the Mn sites.

Figure 3. Spin resolved structure of compounds in majority spin channel (left) and minority spin channel (right),
at the equilibrium lattice constant
(*Continued on next page*)
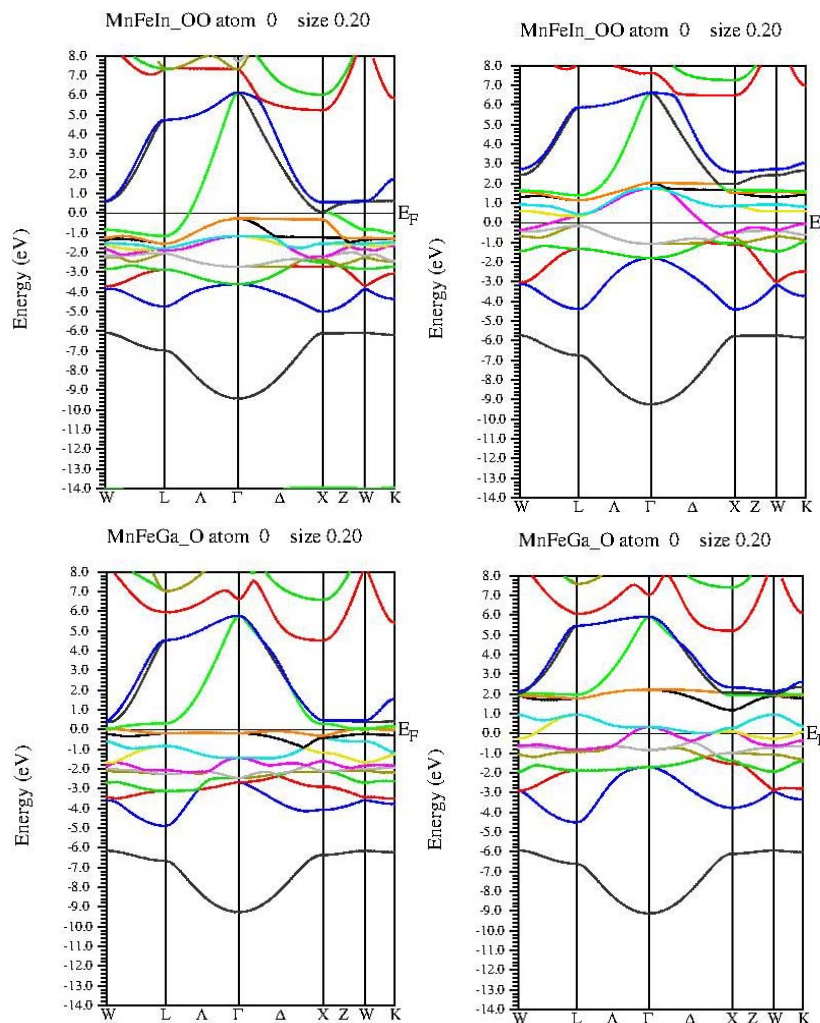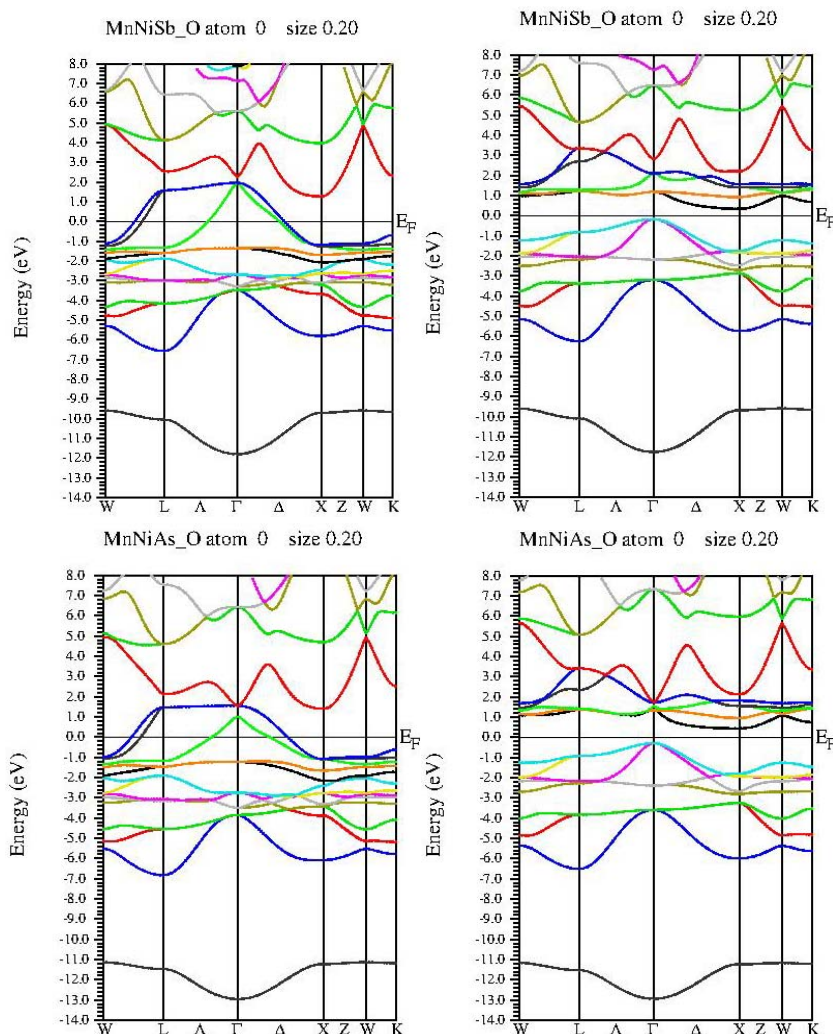
Figure 3. Spin resolved structure of compounds in majority spin channel (left) and minority spin channel (right),
at the equilibrium lattice constant
(*Continuation*)

Here, we come to the magnetic properties of these Half-Heusler compounds. The Galanakis model describes the spin magnetic moment of half-Heusler compounds using the difference between spin-up and spin-down states [20,21]. The integral total magnetic moment, which is a typical characteristic of half metallic ferromagnetism, obeys the Slater-Pauling rule for the half-Heusler alloys $M_t = Z_t - 18$; where M_t is the total magnetic moment per formula unit and Z_t is the total number of valence electrons [22,23]. For example, Mn, Fe, Ni, In, Ga, Sb and As atoms have 7,8,10,3,3,5 and 5 valence electrons, respectively. The total magnetic moments per formula unit for these four compounds are integral and shown in table 2.

Table 2.
Calculated values of total magnetic moments of the compounds

μ_B	Mn	Fe/Ni	X(In, Ga, Sb, As)	Total
MnFeIn	3.291	2.367	-0.338	5.32
MnFeGa	3.21	2.342	-0.42	5.132
MnNiSb	3.883	0.298	-0.181	4
MnNiAs	3.812	0.332	-0.145	3.999

For example, Mn, Fe, Ni, In, Ga, Sb and As atoms have 7,8,10,3,3,5 and 5 valence electrons, respectively. Also, the spin polarization P is defined by the total number of valence electrons and total magnetic moment per formula unit is shown in Table 3. It is clear that the compounds with 22 valance electrons are 100% spin polarized. The calculated result has good agreement with theoretical value of magnetic moment.

Table 3.

Compound parameters

Compound	Z_t	$M_t (\mu_B)$	Spin Polarization
MnFeIn	18	Zero	Unpolarized
MnFeGa	18	Zero	Unpolarized
MnNiAs	22	4	100%
MnNiSb	22	4	100%

SUMMARY AND CONCLUSIONS

Half-metallic behaviour of materials has been found and the applications in different aspects of the emerging field of spintronics, e.g. half-metallicity produces 100% spin polarization at the Fermi level; which generates a fully spin-polarized current. Furthermore, due to conduction of only one type of electrons, i.e. spin-up or down, they can be used as electrical switches. These properties make half-metals suitable for applications in Spintronics. We have been observed from theoretical calculations that Fe based half-Heusler compounds containing Mn at octahedral lattice have metallic behaviour inspite of they having 18 valance electron, whereas Ni based 22 valance electron alloys have band gap in their minority spin state.

ORCID IDs
Lalit Mohan, https://orcid.org/0000-0003-3323-8296; **Sukhender**, https://orcid.org/0000-0002-2149-5669
Sudesh Kumar, https://orcid.org/0000-0002-7507-4712; **Deepak Sharma**, https://orcid.org/0000-0001-9163-9050
Ajay Singh Verma, https://orcid.org/0000-0001-8223-7658

REFERENCES

[1] K. Yang, W. Setyawan, S. Wang, M.B. Nardelli and S. Curtarolo, Nature Mater. **11**, 614–619 (2012), https://doi.org/10.1038/nmat3332.
[2] S. Wang, Z. Wang, W. Setyawan, N. Mingo and S. Curtarolo, Phys. Rev. X, **1**, 021012 (2011), https://doi.org/10.1103/PhysRevX.1.021012.
[3] T. Gruhn, Phys. Rev. B, **82**, 125210 (2010), https://doi.org/10.1103/PhysRevB.82.125210.
[4] A. Roy, J.M. Bennett, K.M. Rabe, and D. Vanderbilt, Phys. Rev. Lett. 109 037602 (2012), https://doi.org/10.1103/PhysRevLett.109.037602.
[5] Jiong Yang, Huanming Li, Ting Wu, Wenqing Zhang, Lidong Chen, and Jihui Yang, Adv. Funct. Mater. **18**, 2880–2888 (2008), https://doi.org/10.1002/adfm.200701369.
[6] B.R.K. Nanda, and I. Dasgupta, J. Physics: Condensed Matter, **15**, 7307 (2003), https://doi.org/10.1088/0953-8984/15/43/014.
[7] H.C. Kandpal, C. Felser, and R. Seshadri, J. Phys. D: Appl. Phys. **39**(5), 776 (2006), https://doi.org/10.1088/0022-3727/39/5/S02.
[8] R. Allmann, and R. Hinek, Acta Cryst. A, **63**, 412-417 (2007), https://doi.org/10.1107/S0108767307038081.
[9] P. Villars, and L.D. Calvert. *Pearson's handbook of crystallographic data for intermetallic phases*. (American Society for Metals, 1986).
[10] Zhang Xiuwen, Chinese Physics B, **27**(12), 127101 (2018), https://doi.org/10.1088/1674-1056/27/12/127101.
[11] Feng Yan, Xiuwen Zhang, Yonggang G. Yu, Liping Yu, Arpun Nagaraja, Thomas O. Mason, and Alex Zunger, Nat. Commun. **6**, 7308 (2015), https://doi.org/10.1038/ncomms8308.
[12] J. Tobola, and J. Pierre, J. All. Comp. **296**, 243-252 (2000), https://doi.org/10.1016/S0925-8388(99)00549-6.
[13] T. Graf, C. Felser, and S.S.P. Parkin, Progress in Solid State Chemistry. **39**(1), 1-50 (2011), https://doi.org/10.1016/j.progsolidstchem.2011.02.001.
[14] L. Zhang, X. Wang, and Z. Cheng, J. Alloys and Compounds, **7**, 16183 (2017), https://doi.org/10.1016/j.jallcom.2017.05.116.
[15] K. Gofryk, D. Kaczorowski, T. Plackowski, A. Leithe-Jasper, and Yu. Grin, Phys. Rev. B, **84**, 035208 (2011), https://doi.org/10.1103/PhysRevB.84.035208.
[16] P. Blaha, K. Schwarz, G.K.H. Madsen, D. Kvasnicka, J. Luitz, R. Laskowski, F. Tran, and L.D. Marks, *WIEN2k, An Augmented Plane Wave + Local Orbitals Program for Calculating Crystal Properties*, edited by K. Schwarz (Technical Universitatwien, Austria, 2001), http://susi.theochem.tuwien.ac.at/reg_user/textbooks/usersguide.pdf.
[17] J.P. Perdew, K. Burke, and M. Ernzerhof, Phys. Rev. Lett. **77**, 3865 (1996), https://doi.org/10.1103/PhysRevLett.77.3865.
[18] S. Ouardi, G.H. Fecher, B. Balke, X. Kozina, G. Stryganyuk, C. Felser, S. Lowitzer, D. Ködderitzsch, H. Ebert, and E. Ikenaga, Phys. Rev. B, **82**, 085108 (2010), https://doi.org/10.1103/PhysRevB.82.085108.
[19] I. Galanakis, P.H. Dederichs, and N. Papanikolaou, Phys. Rev. B, **66**, 134428 (2002), https://doi.org/10.1103/PhysRevB.66.134428.
[20] I. Galankis, and P.H. Dederiches, *Half-metallic Alloys: Fundamentals and Applications*, (Springer, Berlin, 2005), ISBN 10-3540277196.
[21] I. Galanakis, P.H. Dederichs, and N. Papanikolaou, Phys. Rev. B, **66**, 174429 (2002), https://doi.org/10.1103/PhysRevB.66.174429.
[22] I. Galanakis, P. Mavropoulos, and P.H. Dederichs, J. Physics D: Applied Physics, **39**, 765 (2006), https://doi.org/10.1088/0022-3727/39/5/S01.
[23] C. Felser, G.H. Fecher, and B. Balke, Angewandte Chemie International Edition, **46**, 668 (2007), https://doi.org/10.1002/anie.200601815.

ПЕРШООСНОВИ РОЗРАХУНКІВ НАПІВХЕЙСЛЕРОВИХ СПОЛУК НА ОСНОВІ МАРГАНЦЮ

Лаліт Мохан[a], Сухендер[a], Судеш Кумар[b], Діпак Шарма[c], Аджай Сінгх Верма[a]
[a]Кафедра фізики, Банастхалі Від'япіт, Банастхалі, 304022, Індія
[b]Кафедра хімії, Банасталі Відяпіт, Банастхалі 304022, Індія
[c]Кафедра фізики, інженерний коледж ІІМТ, Велика Нойда, 201306, Індія

Напівхейслерові сполуки мають різноманітні властивості застосування включаючи напівферомагнітні топологічні ізолятори, сонячні елементи і термоелектричні перетворювачі. Ми досліджували чотири напівхейслерові сполуки: MnFeIn, MnFeGa, MnNiAs і MnNiSb. Природа і властивості напівхейслерових сполук може бути вивчена на основі розрахунку їх валентних електронів. У цій статті сполуки на основі Fe містять 18 валентних електронів; тоді як сполуки на основі Ni містять 22 валентних електрона. Функціональна теорія щільності (DFT) була розроблена з використанням коду WIEN2k. Сполуки на основі Ni з Mn, що розташовані в октаедричних зонах, є напівметалами, як це випливає з розрахунків густини станів і зонної структури. У всіх них канали з орієнтацією спіну вгору є такими, що проводять, тоді як в MnNiAs і MnNiSb канали з орієнтацією спіну вниз мають малу енергетичну щілину. MnNiAs і MnNiSb проявляють напівметалеві властивості з цілочисельними магнітними моментами в 4 μ_B на формульну одиницю і відповідно мають напівметалеві проміжки 0,15 і 0,17 еВ, при їх рівноважному об'ємі.
КЛЮЧОВІ СЛОВА: напівхейслерові сполуки, спінова поляризація, оптимізація, напівметалевий

ПЕРВООСНОВЫ РАСЧЕТА ПОЛУХЕЙСЛЕРОВЫХ СОЕДИНЕНИЙ НА ОСНОВЕ МАРГАНЦА

Лалит Мохан[a], Сухендер[a], Судеш Кумар[b], Дипак Шарма[c], Аджай Сингх Верма[a]
[a]Кафедра физики, Банастхали Видьяпит, Банастхали, 304022, Индия
[b]Кафедра химии, Банастали Видяпит, Банастхали 304022, Индия
[c]Кафедра физики, инженерный колледж ИИМТ, Большая Нойда, 201306, Индия

Полухейслеровы соединения имеют различные свойства применения включая полуферомагнитные топологические изоляторы, солнечные элементы и термоэлектрические преобразователи. Мы исследовали четыре полухейслеровы соединения: MnFeIn, MnFeGa, MnNiAs и MnNiSb. Природа и свойства полухейслеровых соединений может быть изучена на основе расчета их валентных электронов. В этой статье соединения на основе Fe содержат 18 валентных электронов; тогда как соединения на основе Ni содержат 22 валентных электрона. Функциональная теория плотности (DFT) была разработана с использованием кода WIEN2k. Соединения на основе Ni с Mn, расположенных в октаэдрических зонах, являются полуметаллами, как это следует из расчетов плотности состояний и зонной структуры. Во всех них каналы с ориентацией спина вверх являются проводящими, тогда как в MnNiAs и MnNiSb каналы с ориентацией спина вниз имеют малую энергетическую щель. MnNiAs и MnNiSb проявляют полуметаллические свойства с целочисленными магнитными моментами в 4 μ_B на формульную единицу и соответственно имеют полуметаллические промежутки 0,15 и 0,17 эВ, при их равновесном объеме.
КЛЮЧЕВЫЕ СЛОВА: полухейслеровые соединения, спиновая поляризация, оптимизация, полуметаллический

SYNTHESIS AND CHARACTERIZATION OF TIO₂ THIN FILM ELECTRODE BASED DYE SENSITIZED SOLAR CELL

Varsha Yadav, Swati Chaudhary, Saral Kumar Gupta, Ajay Singh Verma*
Department of Physics, Banasthali Vidyapith, Rajasthan, 304022 (India)
*Corresponding Author: ajay_phy@rediffmail.com
Received April 4, 2020; accepted May 26, 2020

Dye-Sensitized Solar Cells (DSSCs) are prominent alternative devices to conventional p-n junction silicon based solar cells because of their low fabrication cost and high-power conversion efficiency, good cost/efficiency ratio. In the present work, DSSC devices were made-up with fluorine doped tin oxide (FTO) glass substrate, a TiO_2 compact layer was deposited on FTO, Ruthenium (II) dye (N_{719}), an iodide - triiodide electrolyte and a platinum (Pt) counter electrode. Photo anode with thin film layers of TiO_2 and Pt counter electrode (photo-cathode) were prepared. Field emission electron microscope (FESEM) was employed to investigate the surface morphology of TiO_2 layers. The DSSC device efficiency was evaluated by J-V characteristics. Fabricated devices were exhibited high power conversion efficiencies. The electrochemical impedance characteristics were analyzed by fitting the experimental results to the corresponding electrical equivalent circuit simulated data.
KEYWORDS: Solar cell, Nanocrystalline TiO_2, Surface Morphology, Performance Parameters, Ruthenium Dye, impedance spectroscopy

State-of-the-art, the existing solar technologies are based on materials such as crystalline silicon, cadmium telluride materials. All of these materials have different problems and issues associated with the current technology. At present over 90% of the photovoltaic's (PVs) are silicon-based solar cells [1]. Which offer relatively high power conversion efficiencies (about 27%) and about of 15-20 years operational lifetime. However, none of these approaches can address the key issue facing the PV market-the "cost to electricity output ratio" of solar generated electricity [2]. Also, the high energy cost to produce some of these PV negates the environmental benefits that can be gained. This clearly leaves the door ajar for a more economically viable material system to be produced to deliver the necessary infrastructure to harvest solar energy [3].We believe that an ideal system suited to deliver such a solution is TiO_2 based dye-sensitized solar cells. The combination of very low material cost, combined with solution-processable cheap production facilities lends itself to easy fabrication methods and low environmental costs on both energy for production and green materials, hugely support the claim that PVs offer the ideal material system to deliver a suitable mechanism for large area solar harvesting [4,5].

DSSCs are often regarded as a third generation photovoltaic (PV) technology or an "emerging technology", that are promising alternative energy conversion devices for low cost energy conversion. Substantial progress has been made in fundamental research and technological application of DSSCs during the last two decades [6]. The combination of very low material cost, combined with solution-processable cheap production facilities lends itself to easy fabrication methods and low environmental costs on both energy for production and green materials, hugely support the claim that PVs offer the ideal material system to deliver a suitable mechanism for large area solar harvesting. The long term reliability parameters can be achieved by the incorporation of suitable Nanomaterial which provide enough mechanical strength and flexibility for roll-to-roll process of flexible device [7].

The concept of DSSCs originated from the photosynthesis phenomenon in the plants, where chlorophyll, an organic compound, absorbs the sunlight and initiates photosynthesis process. The photovoltaic effect in DSSCs was first demonstrated in the early 1970s, but instability was their biggest problem. Though the efficiency improved in subsequent years but poor stability remained a big problem [8,9]. In 1991, O'Regan and Gratzel presented the modern version of is composed of porous layer of titanium dioxide nanoparticles, covered with a molecular dye that absorbs sunlight, like the chlorophyll in green leaves. The titanium dioxide is immersed under an electrolyte solution, above which is a platinum- based catalyst [10]. As in a conventional alkaline battery an anode (the titanium dioxide) and a cathode (the platinum) are placed on either side of a liquid conductor (the electrolyte). The sunlight passes through the transparent electrode into the dye layer, where it can stimulate the electrons floating in titanium dioxide. The electrons flow toward the transparent electrode, where they are collected to give the power to the load [11]. After flowing through the outer circuit, they are presented again in the cell on the metal electrode on the back flowing in electrolyte [12,13]. The electrolyte then transports the electrons back to the dye molecules [14].

In this work, DSSCs were fabricated using TiO_2 electrode as a photoanode and Pt electrode as a Photocathode, here photoanode was used with the TiO_2 paste and solar cell performance was analyzed. We have examined the development of the device performance like short circuit current density (Jsc), open circuit voltage (Voc) and solar energy to conversion efficiency (η). We also excluded TiO2 film morphology with the help of FESEM technique and some electrical parameters by impedance technique.

EXPERIMENTAL SECTION

Titanium dioxide (TiO_2), Fluorine –doped tin oxide (FTO) coated glass substrate (sheet resistance ~ 8-12 Ω/cm^2), Dye (N719), Platinum paste, Lithium iodide (LiI), Iodine (I_2), 1butyle-3methyle inidazolium iodide (BMIT), 4-tert butyl pyridine, Acetonitrile and valeronitrile . All chemicals purchased from sigma Aldrich and used without any purification.

Synthesis of Dye precursor solution. Dye solution was prepared by dissolving 36 mg N_{719} dye in 100 ml absolute ethanol. Shake well until the solution dissolved properly.

Synthesis of Electrolyte precursor solution. Electrolyte solution was prepared by dissolving 0.1M LiI, 0.05M iodine, 0.6 BMIT, 0.5 4-tert butyl pyridine in (17:3) ml ratio of Acetonitrile – Valeronitrile by stirring at room temperature until obtain uniform solution.

Device Fabrication and characterization. A Systematic DSSCs consists of several majors parts like Photoanode, Dye, Electrolyte, and Photocathode which is mentioned in the diagrammatic structure of DSSC shown below as Figure 1. Firstly, for the synthesis of photoanode, FTO glass substrate was cleaned with DI water acetone and iso-propanol by ultrasonic bath process [15]. A scotch tape was paste on the conducting side of FTO then, TiO_2 films were applied with the help of Doctor Blade technique.
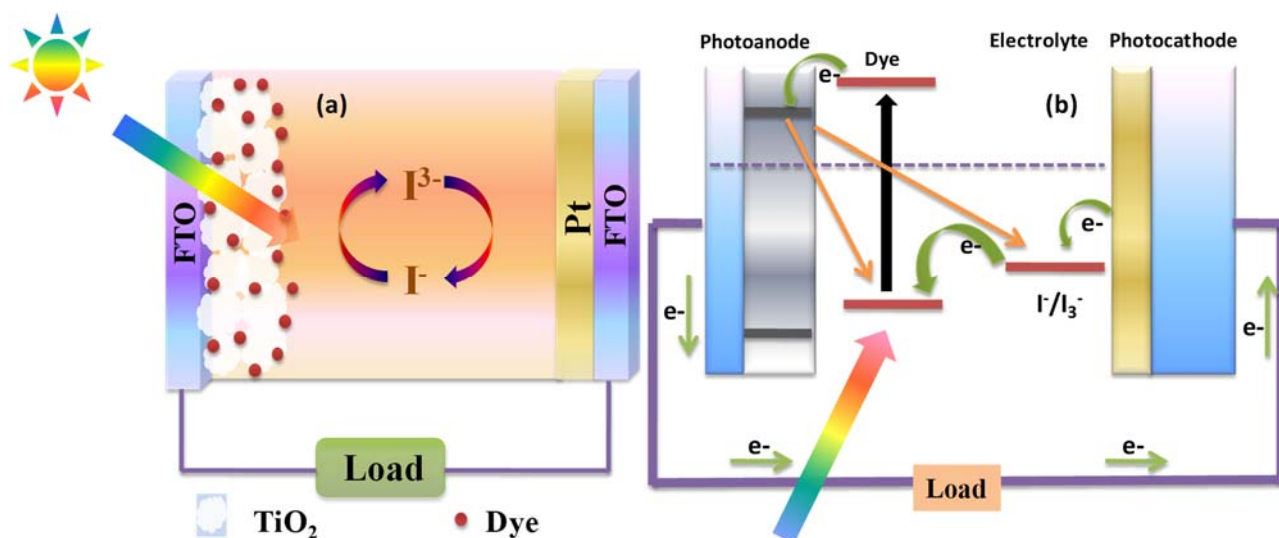

Figure 1. (a) Reveals the structure of device and (b) associated energy level diagram.

The deposited films were annealed at 470°C for 45 minutes in high temperature furnace. The TiO_2 films were deposited immersed in a dye solution for 24 hours in dark. The Pt also deposited on FTO substrate by using doctor blade method as a counter electrode and for 30 minutes annealed at 500°C. The TiO_2 films were formed as dye loaded photoanode and counter electrode as Pt deposited substrate [16,17]. Each sandwich cell was held in place with the help of two heavy duty clips on both opposites' sides of electrode. Liquid electrolyte was introduced between both [18]. Along with basic electron transfer processes in DSSC prospects of a state-of-art device based on dye adsorbed on TiO_2 and I^-/I^{3-} in the form of redox pairs electrolyte is shown in Figure 1(a). On illumination, an electron photo generated by dye molecules as like in photosynthesis [19]. By photon (hυ) absorption a dye molecule is excited whereas electron is excited from HOMO into LUMO subsequently, the free electron is injected into the TiO_2 conduction band and left the oxidized dye molecule. Then, the electron reach the Pt catalyst layer where redox reactions occur by the recombination with holes with in the electrolyte by reducing tri iodide (I^{3-}) to iodide ion (I^-). However, the negative charge of I, in the final step, diffuses back to the dye molecules and it will react with the oxidized molecule. Thus, it completes the electrical cycle and repeats again. Besides this process some recombination happened like recombination of injected electron in the TiO_2 with either acceptors or oxidized dyes, which degrade the performance of the cell [20,21].

RESULTS AND DISCUSSION

The surface microstructure features of the film were characterized using Field Emission Scanning Electron Microscope (FESEM) as shown in the Figure 2. FESEM image of the TiO_2 film sample annealed at 470° C for 45 min. The image reveals a film that was crack-free, uniform and smooth on the surface. It also shows that the TiO_2 thin film possesses a nanocrystalline and nonporous structure which consists of nanoparticles.

The photovoltaic performance of the DSSCs based on Titanium Dioxide thin film photoanode were investigate under a simulated solar irradiation of 100mW cm^{-2} (AM 1.5G) [22,23]. Figure 3(a) display the measured J-V characteristics of solar cell based on TiO_2 films and 3(b) shows different efficiencies of DSSC based on wavelength. The corresponding photovoltaic parameters short circuit current (J_{sc}), fill factor (FF), open circuit voltage (V_{oc}), and conversion efficiency (η) for DSSCs for the TiO_2 films has been calculated. We have found the values of cell parameters such as; V_{oc}, J_{sc}, FF,

I_{max}, V_{max}, P_{max} and efficiency are of 0.60V, 3.337mA/cm^2, 56.13%, 0.00289A, 0.4704V, 1.36 and 1.13%. The performance of cell is considerable at low cost DSSC technology available today [24]. On other hand we have found different values of efficiency at different range of wave length as mentioned in figure 3(b), and are continuously increase. From all the parameters we have measured overall highest efficiency of fabricated cell is 1.5% at 900-1100 nm range of wavelength. Photovoltaic performances are influenced by the dye adsorption solvent [25].
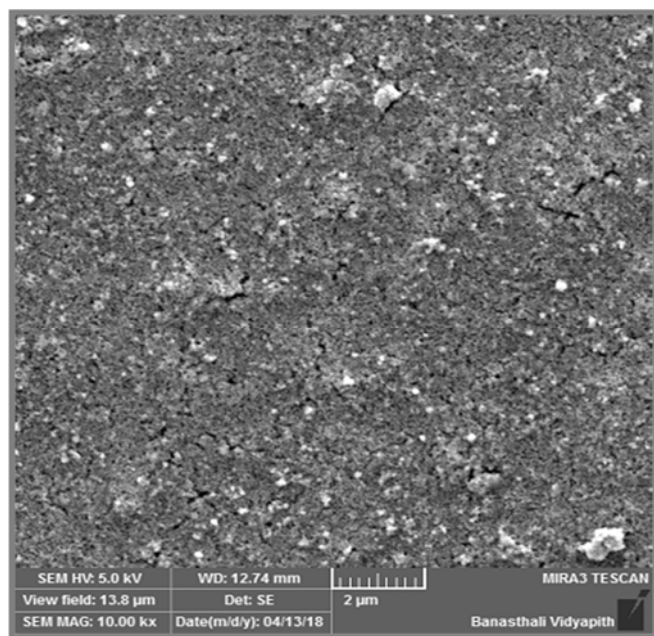

Figure 2. FESEM image of TiO$_2$ thin film deposited on glass substrate

The adsorption behavior of dye is significant at this wavelength. Electrochemical impedance spectroscopy (EIS) is a beneficial technique to investigate the internal impedance of photovoltaic device [26], such as DSSC. Electrochemical interface of split in three parallel circuits, additionally the equivalent circuit of DSSC is related to the experimental result of the Nyquist plot as display in Figure 4(a).
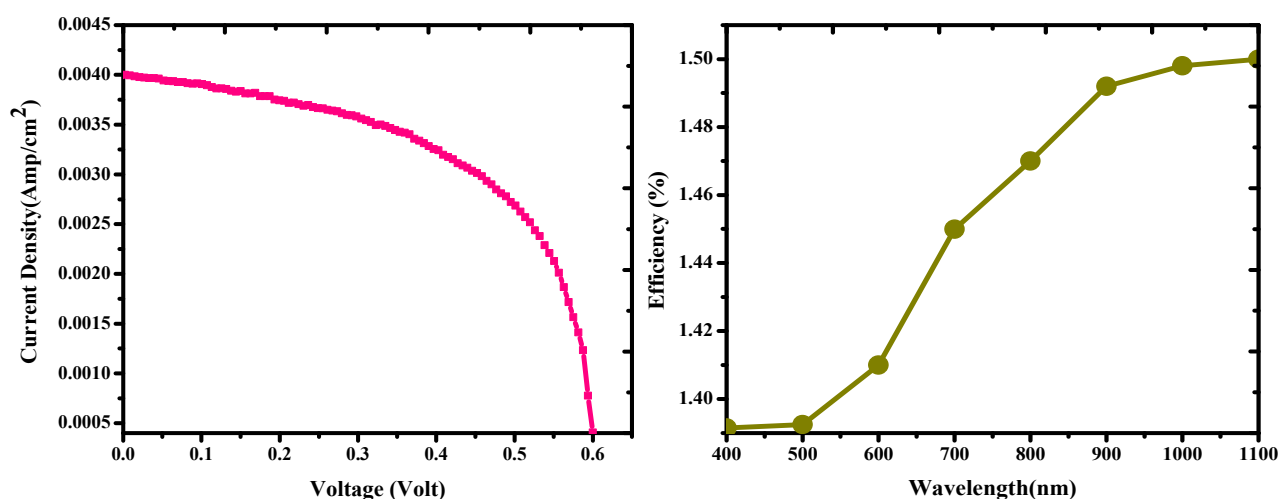
Figure 3. (a) – The J-V curve under illumination of DSSC based on TiO$_2$ film. (b) – Efficiency performance based on different range of wavelength.

In Nyquist plot equivalent circuit in the horizontal axis represent the serial resistance (R_1) between wire and substrate, from the impedance spectra represent resistance (R_2) and (R_3) at interface between electrolyte and Pt counter electrode and as well as between electrolyte and TiO$_2$ film. On the other side at the interface C_1 shows the double layer capacitance between electrolyte and Pt counter electrode and as well as between electrolyte and TiO$_2$ film [27,28]. The values of all the parameters of Nyquist plots of DSSC based on TiO$_2$ photoanode with the equivalent circuit are summarized in Table.
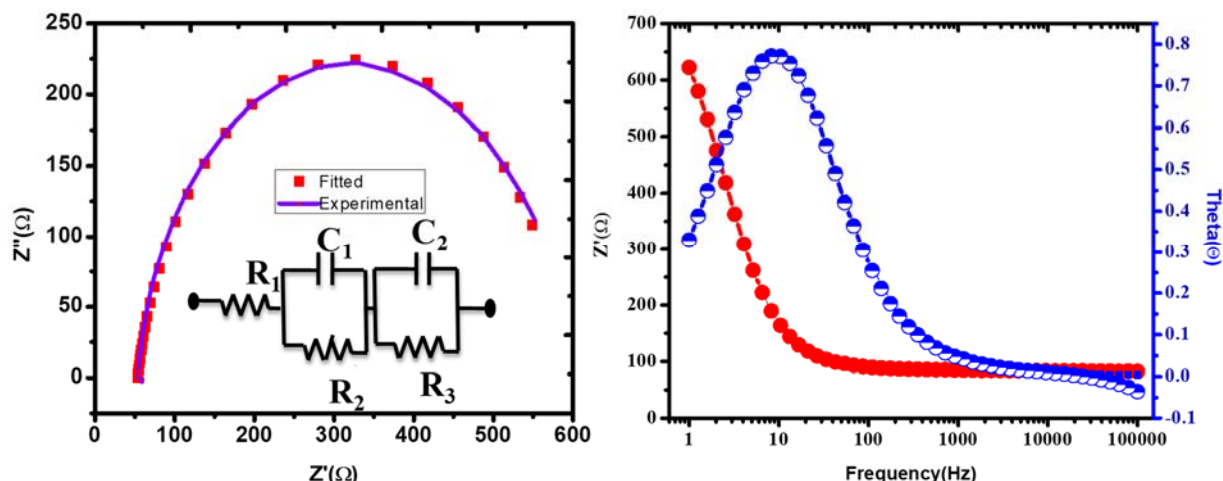
Figure 4. (a): The Nyquist plots of DSSC based on TiO_2 photoanode with the equivalent circuit of DSSC; **(b)** Bode plot of DSSC based on TiO_2 photoanode.

Table

The resistance and capacitance values of equivalent circuit for DSSC based on TiO_2 photoanode

Sample	$R_1(\Omega)$	$C_1(mF)$	$C_2(mF)$	$R_2(\Omega)$	$R_3(\Omega)$
TiO_2	85.91	0.125	0.149	132.32	494.62

In the bode plot of cell based on photoanode TiO_2 under the solar irradiation, the frequency was shifted in higher frequency region with the TiO_2 photoanode as shows in figure 4(b). According to curve recombination charge transfer processes at the TiO_2/dye/electrolyte interface is low and enhance the electron transmission [29,30]. On the other hand illumination condition f_{max} is inversely proportional to the electron transport time as $\tau_s =1/ (2\pi f_{max})$, increment in f_{max} shows the increased rate of charge transport process in DSSC [24]. Hence, with the reduced value τ_s of indicates that the electrons reaches at FTO electrode at a faster rate, so that we can improve the performance of DSSC by further modification.

SUMMARY AND CONCLUSIONS

We have successfully fabricated and characterized Dye sensitized solar cell based on TiO_2 photoactive layer. Which shows the PCE of 1.13%, J_{sc} of 3.337mA/cm^2, V_{oc} of 0.60V and FF of 56.13%, and overall highest PCE is 1.5% on 900 to 1100 nm wavelength ranges. The performance of cell is good at simple laboratory condition, but we can improve photovoltaic performance by using this methodology. The EIS analysis observes that the resistance between electrolyte and TiO_2 film increase, which indicates that a larger resistance at the interface between TiO_2 film and electrolyte is beneficial for suppression of charge recombination. Hence, we can achieve enhancement in performance of DSSC by modification in TiO_2 (like doping and annealing etc) and Dye and electrolyte (natural sources achieved by immediate environment).

ORCID IDs

Varsha Yadav https://orcid.org/0000-0003-1990-5910; **Swati Chaudhary** https://orcid.org/0000-0002-8504-3602,

Saral Kumar Gupta https://orcid.org/0000-0002-0446-8984; **Ajay Singh Verma** https://orcid.org/0000-0001-8223-7658

REFERENCES

[1] O. K. Simya, M. Selvam, A. Karthik, V. Rajendran, Synth. Met. **188**, 124–129 (2014), https://doi.org/10.1016/j.synthmet.2013.12.005.
[2] S. Battersby, Proc. Natl. Acad. Sci. **116**, 7-10 (2019), https://doi.org/10.1073/pnas.1820406116.
[3] M. Grätzel, J. Photochem. Photobiol. C Photochem. Rev. **4**, 145–153 (2003), https://doi.org/10.1016/S1389-5567(03)00026-1.
[4] K. Ebrahim, Sol. Cells - Dye. Devices, InTech. 171-204 (2012), https://doi.org/10.5772/19749.
[5] W. Jarernboon, S. Pimanpang, S. Maensiri, E. Swatsitang, and V. Amornkitbamrung, Thin Solid Films. 517, 4663–4667 (2009), https://doi.org/10.1016/j.tsf.2009.02.129.
[6] D. Wei, Int. J. Mol. Sci. **11**, 1103–13 (2010), https://doi.org/10.3390/ijms11031103.
[7] S. Bose, V. Soni, and K.R. Genwa, Int. J. Sci. Res. Publ. **5**, 2250–3153 (2015), http://www.ijsrp.org/research-paper-0415.php?rp=P403882.
[8] B.O. Regan, and M. Gratzel, Nature, **353**, 737–740 (1991), https://doi.org/10.1038/353737a0.
[9] C. Cavallo, F. Di Pascasio, A. Latini, M. Bonomo, and D. Dini, J. Nanomater. **2017**, 1–31 (2017), https://doi.org/10.1155/2017/5323164.
[10] J. Gong, K. Sumathy, Q. Qiao, and Z. Zhou, Renew. Sustain. Energy Rev. **68**, 234–246 (2017), https://doi.org/10.1016/j.rser.2016.09.097.

[11] S. Yun, J.N. Freitas, A.F. Nogueira, Y. Wang, S. Ahmad, and Z.S. Wang, Prog. Polym. Sci. **59**, 1–40 (2016), https://doi.org/10.1016/j.progpolymsci.2015.10.004.

[12] M. Eslamian, and J. Newton, Coatings. **4**, 85–97 (2014), https://doi.org/10.3390/coatings4010085.

[13] A. Jena, S.P. Mohanty, P. Kumar, J. Naduvath, V. Gondane, P. Lekha, J. Das, H.K. Narula, S. Mallick, and P. Bhargava, Trans. Indian Ceram. Soc. **71**, 1–16 (2012), https://doi.org/10.1080/0371750X.2012.689503.

[14] K. Miettunen, J. Vapaavuori, A. Tiihonen, A. Poskela, P. Lahtinen, J. Halme, and P. Lund, Nano Energy. **8**, 95–102 (2014), https://doi.org/10.1016/j.nanoen.2014.05.013.

[15] B. Siwach, D. Mohan, S. Sharma, and D. Jyoti, Bull. Mater. Sci. **40**, 1371–1377 (2017), https://doi.org/10.1007/s12034-017-1492-z.

[16] T. Phonkhokkong, T. Thongtem, S. Thongtem, A. Phuruangrat, and W. Promnopas, Dig. J. Nanomater. Biostructures. **11**, 81–90 (2016), http://www.chalcogen.ro/81_Phonkhokkong.pdf.

[17] T.V. Nguyen, H.C. Lee, and O.B. Yang, Sol. Energy Mater. Sol. Cells. **90**, 967–981 (2006), https://doi.org/10.1016/j.solmat.2005.06.001.

[18] S. Xuhui, C. Xinglan, T. Wanquan, W. Dong, and L. Kefei, AIP Adv. **4**, 031304 (2014), https://doi.org/10.1063/1.4863295.

[19] S. Widodo, G. Wiranto, and M.N. Hidayat, Energy Procedia. **68**, 37–44 (2015), https://doi.org/10.1016/j.egypro.2015.03.230.

[20] A. Karmakar, and J. Ruparelia, in *International Conference on Current Trends in Technology, NUiCONE,* (IEEE, Piscataway, 2011), pp. 1-6.

[21] D.L. Domtau, J. Simiyu, E.O. Ayieta, L.O. Nyakiti, B. Muthoka, and J.M. Mwabora, Surf. Rev. Lett. **24**, 1750065 (2017), https://doi.org/10.1142/S0218625X17500652.

[22] B. Alfa, M.T. Tsepav, R.L. Njinga, and I. Abdulrauf, Appl. Phys. Res. **4**, 48-56 (2012), https://doi.org/10.5539/apr.v4n1p48.

[23] A.F. Ole, G.N.C. Santos, and R.V Quiroga, Int. JSER, **3**, 1-7 (2012).

[24] L. Wei, P. Wang, Y. Yang, Z. Zhan, Y. Dong, W. Song, and R. Fan, Inorg. Chem. Front. **5**, 54–62 (2018), https://doi.org/10.1039/C7QI00503B.

[25] Z.A. Shah, K. Zaib, and A. Khan, J. Fundam Renewable Energy Appl. **7**, 4-6 (2017).

[26] H. Yu, S. Zhang, H. Zhao, G. Will, and P. Liu, Electrochim. Acta. **54**, 1319-1324 (2009), https://doi.org/10.1016/j.electacta.2008.09.025.

[27] J.C. Chou, C.M. Chu, Y.H. Liao, C.H. Lai, Y.J. Lin, P.H. You, W.Y. Hsu, C.C. Lu, and Y.H. Nien, IEEE J. Electron Devices Soc. **5**, 32-39 (2017).

[28] A. Upadhyaya, C.M. Singh Negi, A. Yadav, S.K. Gupta, and A.S. Verma, Superlattices Microstruct. **122**, 410-418 (2018).

[29] N. Sharma, C.M.S. Negi, A.S. Verma, and S.K. Gupta, J. Electron. Mater. **47**, 7023-7033 (2018), https://doi.org/10.1007/s11664-018-6629-3.

[30] A.S. Verma, A. Upadhyaya, S.K. Gupta, A. Yadav, and C.M.S. Negi, Semicond. Sci. Technol. **33**, 065012 (2018), https://doi.org/10.1088/1361-6641/aac066.

СИНТЕЗ І ХАРАКТЕРИСТИКИ СОНЯЧНОГО ЕЛЕМЕНТУ З ТОНКОПЛІВКОВИМ TiO₂ ЕЛЕКТРОДОМ СЕНСИБІЛІЗОВАНОГО БАРВНИКОМ
Варша Ядав, Сваті Чаддхарі, Сарал Кумар Гупта, Аджай Сінгх Верма*
Кафедра фізики, 304022 Раджастан, Банасталі Відяпіт, Індія

Сенсибілізовані барвником сонячні елементи (DSSC) є значною альтернативою звичайним сонячним елементам на основі кремнію з p-n-переходом через їх низьку вартість виготовлення і високу ефективність перетворення енергії, гарного співвідношення ціна/ефективність. У цій роботі пристрої DSSC були виготовлені зі скляної підкладки, яка містить оксид олова легованого фтором (FTO), компактного шару TiO₂ нанесеного на FTO, рутенієвого (II) барвника (N₇₁₉), йодид-трійодідного електроліту і платинового (Pt) протиструминного електрода. Були підготовлені фотоанод з тонкоплівковими шарами з TiO₂ і платиновий протиструминний електрод (фотокатод). Польовий емісійний електронний мікроскоп (FESEM) використовувався для дослідження морфології поверхні шарів з TiO₂. Ефективність пристроїв DSSC (сенсибілізовані барвником сонячні елементи) оцінювалася за характеристиками J-V. Виготовлені пристрої показали високу ефективність перетворення енергії. Характеристики електрохімічного імпедансу були проаналізовані шляхом приведення експериментальних результатів до відповідних даних, змодельованих на основі еквівалентної електричної схеми.

КЛЮЧОВІ СЛОВА: сонячний елемент, нанокристалічний TiO2, морфологія поверхні, робочі характеристики, рутенієвий барвник, імпедансна спектроскопія

СИНТЕЗ И ХАРАКТЕРИСТИКИ СОЛНЕЧНЫХ ЭЛЕМЕНТОВ С ТОНКОПЛЕНОЧНЫМ TiO₂ ЭЛЕКТРОДОМ СЕНСИБИЛИЗИРОВАННОГО КРАСИТЕЛЕМ
Варша Ядав, Свати Чаддхари, Сарал Кумар Гупта, Аджай Сингх Верма *
Кафедра физики, 304022 Раджастан, Банастали Видяпит, Индия

Сенсибилизированные красителем солнечные элементы (DSSC) являются существенной альтернативой обычным солнечным элементам на основе кремния с p-n-переходом из-за их низкой стоимости изготовления и высокой эффективности преобразования энергии, хорошего соотношения цена/эффективность. В настоящей работе устройства DSSC были изготовлены из стеклянной подложки содержащей оксид олова легированного фтором (FTO), компактного слоя TiO₂ нанесенного на FTO, рутениевого (II) красителя (N₇₁₉), йодид-трийодидного электролита и платинового (Pt) противоточного электрода. Подготовлены фотоанод с тонкопленочными слоями из TiO₂ и платиновый противоточный электрод (фотокатод). Полевой эмиссионный электронный микроскоп (FESEM) использовался для исследования морфологии поверхности слоев из TiO₂. Эффективность устройств DSSC оценивалась по характеристикам J-V. Изготовленные устройства показали высокую эффективность преобразования энергии. Характеристики электрохимического импеданса были проанализированы путем приведения экспериментальных результатов к соответствующим данным, смоделированным на основе эквивалентной электрической схемы.

КЛЮЧЕВЫЕ СЛОВА: солнечный элемент, нанокристаллический TiO₂, морфология поверхности, рабочие характеристики, рутениевый краситель, импедансная спектроскопия.

MOLECULAR DYNAMICS SIMULATION OF THE INTERACTION BETWEEN BENZANTHRONE DYE AND MODEL LIPID MEMBRANES

Olga Zhytniakivska

Department of Medical Physics and Biomedical Nanotechnologies, V.N. Karazin Kharkiv National University
4 Svobody Sq., Kharkiv, 61022, Ukraine
*Corresponding Author: olya_zhitniakivska@yahoo.com
Received 15 June 2020, revised June 28, 2020; accepted June 30, 2020

The benzanthrone fluorescent dyes are known as environmentally-sensitive reporters for exploring the physicochemical properties and structural alterations of lipid membranes. In the present work the 100-ns molecular dynamics simulation (MD) was used to characterize the bilayer location and the nature of interactions between the benzanthrone fluorescent dye ABM and the model lipid membranes composed of the zwitterionic lipid phosphatidylcholine (PC) and its mixtures with the anionic lipid phosphatidylglycerol (PG20) and sterol cholesterol (Chol30). The MD simulations were performed in the CHARMM36m force field using the GROMACS package. The ABM molecule, which was initially placed at a distance of 30 Å from the midplane of the lipid bilayer, after 10 ns of simulation was found to be completely incorporated into the membrane interior and remained within the lipid bilayer for the rest of the simulation time. The analysis of the MD simulation results showed that the lipid bilayer location of the benzanthrone dye ABM depends on the membrane composition, with the distance from bilayer center being gradually shifted from 0.78 nm in the neat PC bilayer to 0.95 nm and 1.5 nm in the PG- and Chol-containing membranes, respectively. In addition, the partitioning of the ABM into the neat PC bilayer was followed by the probe translocation from the outer membrane leaflet to the inner one. A separate series of MD simulations was aimed at examining the ABM influence on the lipid bilayer structure. It was found that ABM partitioning into the lipid bilayers of various composition has no significant effect on the orientation of the fatty acid chains and leads only to a small increase of the deuterium order parameter for the carbon atoms 5-to-8 in the *sn-2* acyl chains of the neat PC membranes. In addition, the interaction of the ABM with the model lipid membranes caused the slight decrease of the surface area per lipid pointing to the slight increase of the packing density of lipid molecules in the presence of ABM. The results obtained provide a basis for deeper understanding of the membrane interactions of benzanthrone dyes and may be useful for the design of the novel fluorescent probes for membrane studies.
KEYWORDS: ABM, benzanthrone dye, lipid bilayer, molecular dynamics simulation.

The benzanthrone dyes, a well-known class of fluorescent probes that emit in the spectral region from yellow–green to red–purple (depending on the dye structure), have found diverse applications in biomedical research and diagnostics due to their favorable spectral characteristics, such as a large extinction coefficient, a marked Stokes shift; negligible fluorescence in an aqueous phase, etc [1-10]. Specifically, it has been shown that the benzanthrone dye in combination with the thin polylactic acid film is capable of displaying the antimicrobial activity against Gram-positive and Gram-negative bacteria [11]. Staneva et al. also demonstrated a good antimicrobial activity against the Gram-positive *B. cereus* and the yeasts *C. lipolytica* bacteria for the dendrimers modified with eight fluorescent benzanthrone chromophore units [12]. A good deal of studies indicate that benzanthrone dyes can be used as effective microenvironmental sensors for monitoring structural changes in biological systems [2-14]. In particular, the benzanthrone derivatives were employed in DNA [8], protein [4-6] and membrane studies [7,9,10,13]. Notably, Dobretsov and Vladimirov demonstrated that one representative of the benzanthrone class, 3-methoxybenzanthrone can be effectively used to monitor the membrane structural changes caused by the alterations in cholesterol (Chol) level, temperature, pH, etc. [3]. Likewise, the high lipid-associating ability was also observed for other amino- and amidinobenzanthrones [7,13]. Moreover, the spectral responses of some benzanthrone dyes in different lipid systems have been shown to correlate with the degree of lipid bilayer hydration [9], rendering these probes highly suitable for examining the membrane-related processes, especially those coupled with the changes in membrane polarity [7]. The applicability of the novel benzanthrones is not limited to the membrane studies since these dyes are extensively used in the protein research field, for instance, in the studies of a particular class of protein aggregates, amyloid fibrils [4-7]. Specifically, it has been shown previously that aminobenzanthrones are capable of distinguishing between the native monomeric and fibrillar protein states, surpassing the classical amyloid marker ThT in the sensitivity to the lysozyme amyloid fibrils [3,4,6]. Moreover, it has been shown that the benzanthrone dyes are sensitive to the distinctions in fibril morphology [4] and can be effectively used to characterize amyloid fibrils in terms of their fractal-like dimensions [6].

Increasing evidence indicates that one representative of aminobenzanthrones, ABM, may be especially useful for exploring the alterations of the structural and functional properties of cells during different pathologies such as lung tuberculosis [14], gastrointestinal tract cancer [15], rheumatoid arthritis [16], chronic myeloid and B-cells lymphoid leukemia [14], as well as for the check-up of the Chernobyl clean-up workers [17]. Specifically, it was found that spectral characteristics of the benzanthrone dye ABM correlate with a number of parameters of cellular and artificial membranes such as physicochemical properties of a ipid bilayer, microviscosity, proliferating and lipid metabolic activities of cells, distribution of lymphoid subsets, etc [14-17]. Despite numerous applications of ABM in the membrane studies, the molecular details of the dye-membrane complexation, its distribution across the membrane and the depth of location in a lipid bilayer are still unknown. To fill this gap, in the present investigation the molecular dynamics technique was used

to gain deeper insights into the nature of ABM interactions with a lipid bilayer. More specifically, the aim of our study was twofold: i) to uncover the molecular level details of ABM partitioning in the homogenous phosphatidylcholine bilayer and the bilayers from PC mixtures with anionic lipid phosphatidylglycerol and sterol cholesterol; ii) to examine how the membrane location of the probe depends on the lipid bilayer composition.

EXPERIMENTAL SECTION

The molecular dynamics simulations and analysis of the trajectories were performed using the GROMACS software (version 5.1) with the CHARMM36m force field. The calculations were performed at a temperature of 310 K. The input files for MD calculations were prepared using the web-based graphical interface CHARMM-GUI [18]. The .pdb-file of ABM was created in OpenBabelGUI 2.4.1, using the structure drawn in MarvinSketch (.mrv format). The partial charges of AMB were corrected using the RESP ESP charge Derive Server. The topology of the ABM was generated using the CHARMM-GUI Ligand Reader and Modeler [19]. The obtained files were further used to generate the dye-lipid systems using the Membrane Builder option [20]. The three different ABM-membrane systems were created for the simulation with a nearly identical number of lipids. One system was composed of ABM and a lipid bilayer containing 94 PC (palmitoyl-oleyl-phosphatidylcholine) molecules in each monolayer. The second and the third systems were represented by the ABM and heterogeneous lipid bilayers composed of PC and PG (paimitoyl-oleyl-phosphatidylglycerol) or cholesterol (Chol), respectively. The molar ratios PC/PG and PC/Chol were 4:1 and 7:3, respectively. In order to examine the effects of ABM on the lipid bilayer properties, the ABM-free PC, PC/PG (4:1) and PC/Chol (7:3) bilayers were also simulated. Hereafter, the systems containing 20 mol% of PG and 30 mol% of Chol are referred to as PG20 and Chol30, respectively. The MD simulations of ABM-lipid systems were carried out in the NPT ensemble. The ABM molecule was translated to a distance of 30 Å from the membrane midplane along the bilayer normal. The TIP3P water model was used. To obtain a neutral total charge of the system a necessary number of counterions was added. For correct treatment of the long-range electrostatic interactions, the Particle Mesh Ewald algorithm was utilized [21]. The bond lengths were constrained using the LINC algorithm [22]. The pressure and temperature controls were carried out using the Berendsen thermostat [23]. The minimization and equilibration of the system were performed during 50000 and 5000000 steps, respectively. The time step for MD simulations was 2 fs. The whole time interval for MD calculations was 100 ns. The GROMACS commands gmx density and gmx order, were used to calculate the mass density distribution for various components of the lipid bilayer, density distribution of ABM across a lipid bilayer and deuterium order parameter profiles, respectively. The analysis of the membrane thickness, membrane area and area per lipid were performed using the FATSLiM package [24]. The molecular graphics and visualization were performed using the VMD software.

RESULTS AND DISCUSSION

During the last decades the molecular dynamics simulation has become a powerful tool in characterizing the atomic-level details of the interaction between peptides [25,26], proteins [27], organic solvents [28,29] and drugs [30] with lipid membranes. Moreover, MD simulation appeared to be especially useful in studying the behavior of fluorescent membrane probes [31-34]. The increasing use of the MD techniques in the dye-membrane studies is dictated mainly by the difficulties in the determination of the probe location by the experimental methods [*]. To exemplify, the molecular dynamics simulation was used to characterize the partitioning and disposition of the diphenylhexatriene probes [32], ESIPT fluorophores [31], coumarin derivatives [33], membrane polarity probes Prodan and Laurdan [34,35], to name only a few. In the present study the 100-ns molecular dynamics simulation was used to investigate the lipid bilayer location and interactions between the fluorescent probe ABM and the model lipid membranes composed of zwitterionic lipid PC and its mixtures with anionic lipid PG and sterol Chol. Fig. 1 illustrates the disposition of the benzanthrone dye with respect to the lipid/water interface at different simulation times. From a simple visual inspection of simulation snapshots, it is apparent that ABM molecule, which was initially placed at a distance of 30 Å from the bilayer midplane, after ~10 ns of simulation was found to be fully incorporated into the membrane and remained within the lipid bilayer for the rest of simulation time. Specifically, the probe moved to the bilayer polar region and is positioned at the level of glycerol moiety of the upper leaflet of PC and PG20 membranes (the distance from bilayer center ~ 1.5 nm) and at the level of PC choline nitrogen of the Chol30 lipid bilayer (the distance from bilayer center ~ 2.0 nm). During the further time of simulation, the deeper penetration of ABM in the membrane interior was observed coupled with the slowdown of the dye movement. The right panel of the Fig.1 demonstrates location of ABM at the 100 ns of simulations. The snapshots demonstrate that lipid bilayer partitioning of ABM strongly depends on the membrane composition. Accordingly, ABM is localized mainly in the hydrophobic part of the PC and PG20 lipid bilayers. In turn, in the Chol30 bilayer ABM prefers the binding sites which are closer to the membrane surface.

Fig.2 shows the time evolution of the separation of ABM center of mass from the bilayer center for the neat PC (black line) and the mixed PG20 (blue line) and Cho30 (red line) lipid bilayers. The bilayer center is defined as the average position of the C316 and C218 carbons on the termini of PC tails. The analysis of the positions occupied by ABM molecule during the molecular dynamics simulation (Fig.2.) indicates that this probe prefers the region separated by a distance *ca.* 0.8 nm from the PC bilayer center. Remarkably, the obtained results are in good agreement with the experimental measurements [7,10]. More specifically, based on the quantitative parameters of the dye-membrane binding derived from the fluorimetric titration data and the red-edge excitation shift of the membrane-bound dyes it

was hypothesized previously that ABM is localized in the nonpolar bilayer region near the lipid carbonyl groups [7]. Interestingly, these findings are consistent with those obtained for other benzanthrone dyes [10]. Specifically, the study of the Förster resonance energy transfer between the anthrylvinyl-labeled phosphatidylcholine as a donor and the newly synthesized benzanthrones as acceptors showed that benzanthrone dyes tend to penetrate into the hydrophobic region of PC bilayer, with limiting separations from the membrane center falling in the range 0.5-1.3 nm [10]. Notably, the diphenylhexatriene membrane probes DPH and TMA-DPH which are commonly used for the measurements of membrane fluidity are located also at the non-polar membrane region (with the distance from bilayer center ~ 0.7 nm and 0.9 nm for DPH and TMA-DPH, respectively) [32].

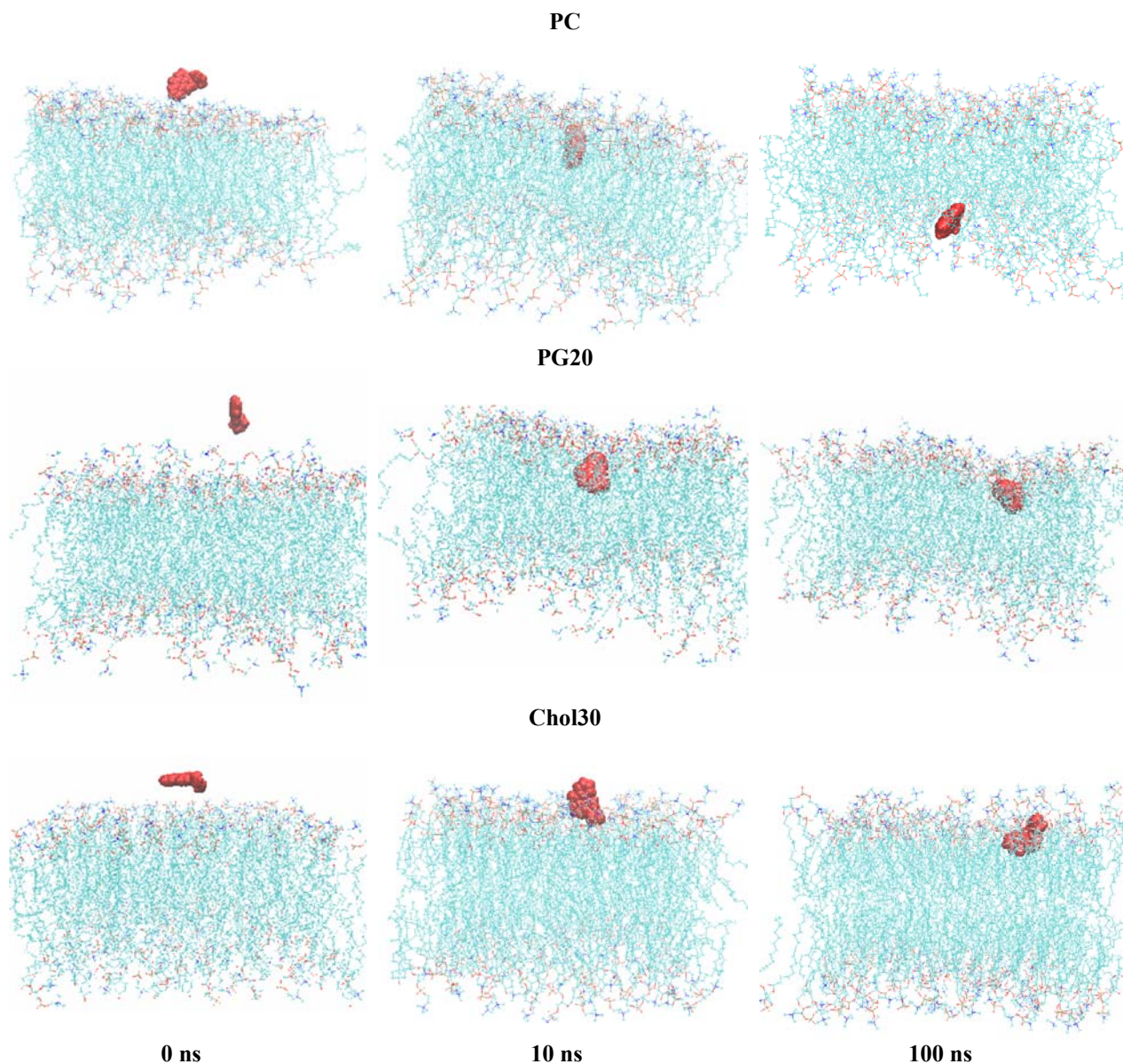**PC**

PG20

Chol30

| 0 ns | 10 ns | 100 ns |

Figure 1. The snapshots of the partitioning of ABM into PC, PG20 and Chol30 bilayers at different simulation time points. The ABM is depicted in red using the VDW drawing method. The lipid tails are represented as sticks in cyan, the phosphorus and nitrogen atoms of the lipid headgroups are shown by orange and blue, respectively. For clarity, water molecules and ions are not shown. (For the interpretation of the references to color in this figure legend, the reader is referred to the web version of this article).

It should be noted that in the PG20 and Chol30 lipid bilayers the benzanthrone dye under study tends to occupy more polar membrane binding sites since ABM center of mass was localized at the distances ~ 0.95 nm and 1.5 nm from the membrane midplane, respectively. The obtained results are in good agreement with the recent studies indicating that inclusion of anionic lipids into PC bilayer induces a relocation of the benzanthrone dyes from the hydrophobic membrane core to the lipid-water interface [10]. Moreover, taken into account the ability of cholesterol to alter the lipid packing density of the PC bilayer [36] and a well-known Chol condensing effect [37], it seems energetically unfavorable to ABM to penetrate deeply in the Chol30 bilayer hydrophobic region and the probe tends to locate at the level of glycerol backbone.
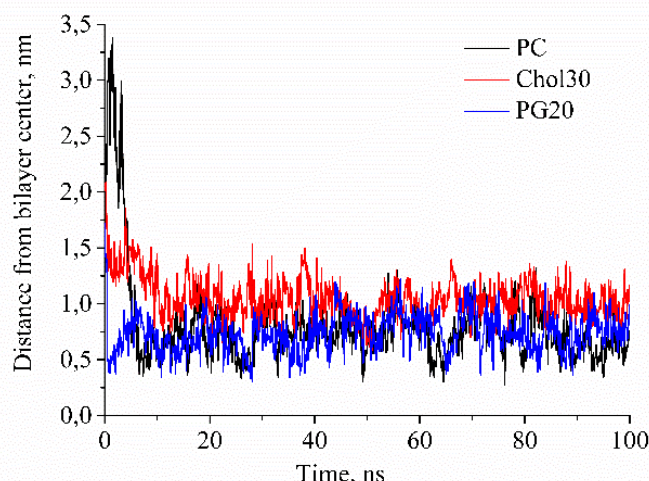
Figure 2. Time evolution of the ABM distance from the bilayer center

Another interesting observation is the translocation of the ABM molecule from the upper leaflet to the lower one of the PC bilayer (Fig. 1, right column). Therefore, at the next step of study the ABM distribution across the lipid bilayer was studied. Fig. 3 represents the mass density distribution of the ABM probe, the molecular groups of lipids (polar heads, glycerols and acyl chains) and water. The position of the selected groups was averaged with respect to the bilayer normal for all atoms over the 100 ns of the MD sampling trajectories. As can be seen, the peak of the ABM mass distribution in the PG20 (Fig.3 B) and Chol30 (Fig. 3C) bilayers is observed at the distances 0.95 and 1.5 nm from the bilayer center.
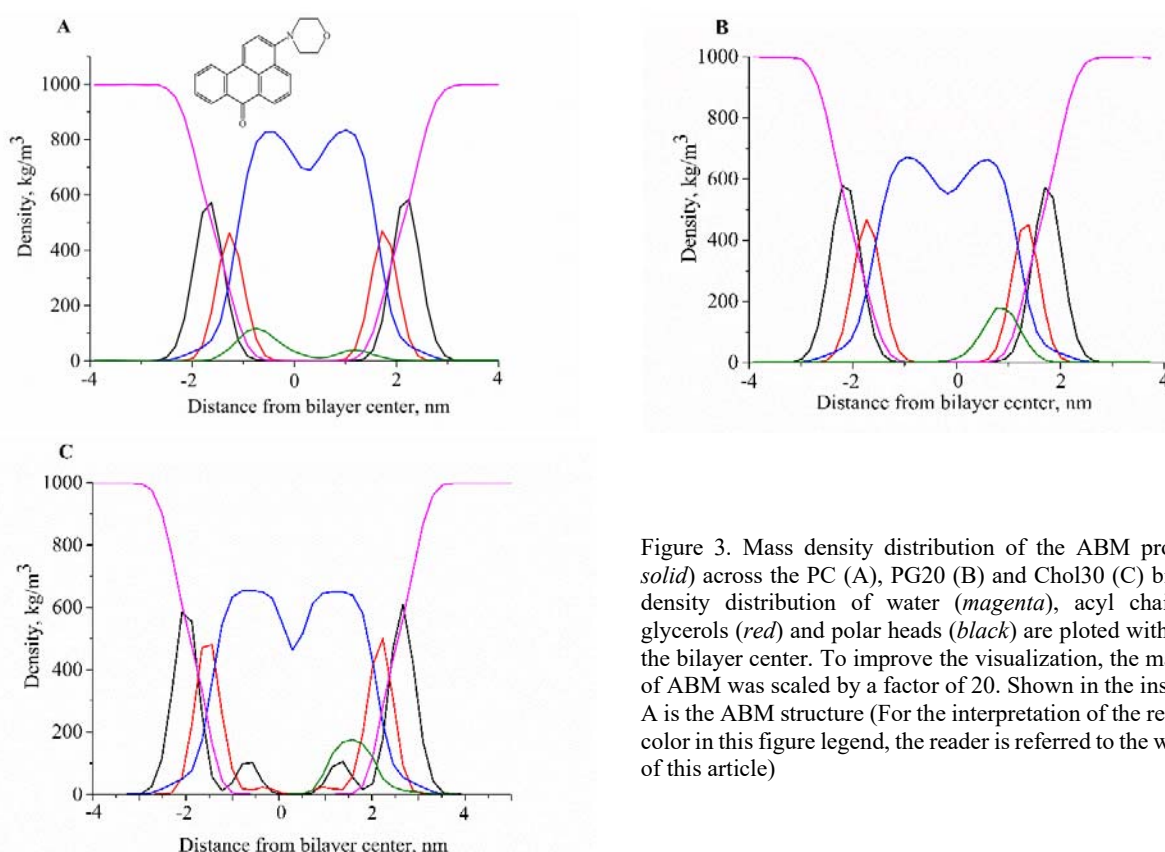

Figure 3. Mass density distribution of the ABM probe(*green solid*) across the PC (A), PG20 (B) and Chol30 (C) bilayer. The density distribution of water (*magenta*), acyl chains (*blue*), glycerols (*red*) and polar heads (*black*) are ploted with respect to the bilayer center. To improve the visualization, the mass density of ABM was scaled by a factor of 20. Shown in the inset of panel A is the ABM structure (For the interpretation of the references to color in this figure legend, the reader is referred to the web version of this article)

In turn, the ABM mass density profile in the PC bilayer is characterized by two peaks. The first low-intensive peak is placed at 1.2 nm from the bilayer center (the region of carbonyl groups) at the outer membrane leaflet, while the second one at ~0.75 nm is attributed to the probe location in the acyl chain region. As seen from Fig. 1., A, the ABM is able to change its bilayer leaflet within the timescale of the simulation. It is noteworthy that the possibility of the probe translocation between the bilayer leaflets was previously observed for DPH [32,36]. Specifically, Repakova et al. observed the four leaflet changes for DPH in the fluid 1,2-dipalmitoyl-phosphatidylcholine bilayer during 400 ns MD simulation [36]. The translocation of DPH was described also for the palmitoyl-oleyl-phosphatidylcholine (POPC)

bilayers and Chol-containing membranes, with the magnitude of this effect being significantly higher for a less ordered POPC bilayer [32].

Next, to ascertain the ABM influence on the lipid bilayer structure, the deuterium order parameter profiles characterizing the average orientation of the fatty acid chains with respect to the bilayer normal were calculated (Fig. 4).
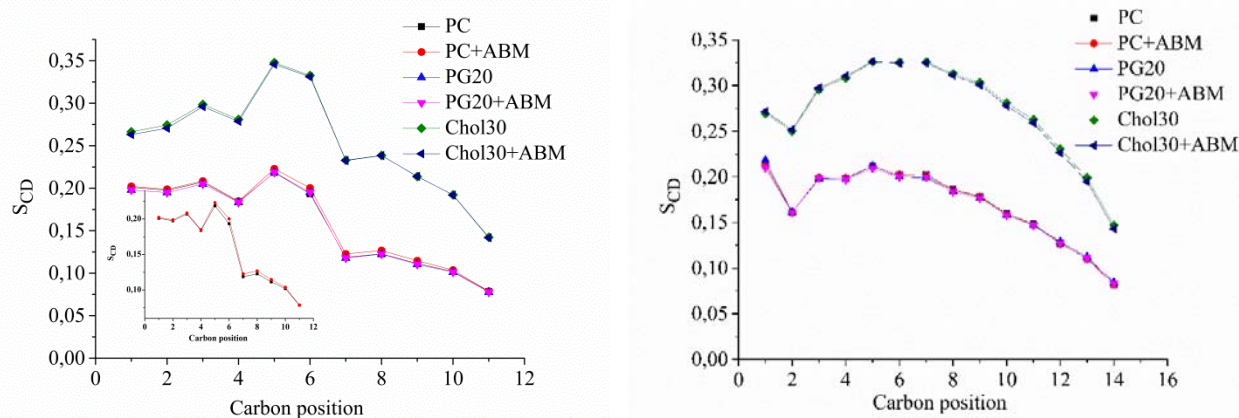

Figure 4. The calculated deuterium order parameter v*ersus* carbon position for *sn-1* (right panel) and *sn-2* (left panel) chain for PC, PG20 and Chol30 bilayers in the absence and presence of the ABM. Shown in the inset are lipid order parameters for the neat PC bilayer.

The chain order parameter S_{CD} is defined through the order parameter tensor:

$$S_{CD} = 1/2(3\langle\cos^2\theta_{CD}\rangle - 1)$$

where θ_{CD} is the angle between the CD bond and the membrane normal. As seen in Fig.4, the ABM partitioning in the PC, PG20 and Chol30 lipid bilayers does not affect the order of *sn-1* and *sn-2* acyl chains, except the *sn-2* acyl chains of PC membranes (the inset in Fig.4) for which a small increase of the S_{CD} value was observed for the carbon atoms 5-to-8. These results correlate well with the previously reported observations that the low and moderate concentrations of the probe molecules have no essential influence on the structure of lipid bilayers [31,35].

One of the macroscopic parameters describing the ordering and packing of lipid molecules is the surface area per lipid molecule. The average values of the surface area per lipid calculated in MD simulations were equal to 63.4 ± 1.0 Å^2, 66.3 ± 1.0 Å^2, 55.2 ± 0.9 Å^2, for the PC, PG20 and Chol30 lipid bilayers, respectively. These values are in good agreement with the results from previous simulations and experiments [37,38, 39]. The ABM partitioning into the lipid membranes caused the slight decrease of this parameter to 62.9 ± 0.9 Å^2, 65.5 ± 1.0 Å^2, 54.6 ± 0.9 Å^2, for the PC, PG20 and Chol30 lipid bilayers, respectively. The obtained results are in harmony with the previously reported findings that the binding of some fluorescent dyes and drugs could lead to the decrease in the surface area per lipid.

CONCLUSIONS

In the present study the behavior of the benzanthrone dye ABM as a membrane probe was investigated using the 100 ns molecular dynamics simulation of this compound in the neat phosphatidylcholine and the mixed phospatidylcholine/phosphatidylglycerol or phosphatidylcholine/cholesterol lipid bilayers. The MD simulation results showed that the ABM molecule, which was initially placed at a distance of 30 Å from the bilayer midplane, after ~10 ns of simulation became incorporated into the membrane and remained within the lipid bilayer for the rest of the simulation time. The analysis of the positions occupied by the ABM in the lipid bilayers of various composition revealed that this reporter molecule enters into the depth of the neat PC membrane preferring the region separated by a distance *ca.* 0.8 nm from the PC bilayer center. In turn, in the PG20 and Chol30 lipid bilayers the examined benzanthrone dye tends to occupy more polar membrane binding sites distributing at the distances ~ 0.95 nm and 1.5 nm from the membrane midplane, respectively. It was found that ABM does not significantly perturb the lipid bilayer structure. Overall, the outcomes of this study may prove of importance for the structural design of the novel fluorescent probes for membrane studies.

ORCID IDs

Olga Zhytniakivska, https://orcid.org/0000-0001-9554-0090

REFERENCES

[1]. I. Grabchev, V. Bojinov, I. Moneva, Dyes Pigm. **48**, 143-150 (2001), https://doi.org/10.1016/S0143-7208(00)00098-X.

[2]. E. M. Kirilova, I. Kalina, G. Kirilov, et al., Nature J. Fluoresc. **18**, 645-648 (2008), https://doi.org/10.1038/78948.

[3]. G. Dobretsov, V. Dmitriev, L. Pirogova, V. Petrov, Yu Vladimirov, Stud. Biophys. **71**, 189-196 (1978).

[4]. K. Vus, V. Trusova, G. Gorbenko, R. Sood, E. Kirilova, G. Kirilov, et al., J. Fluoresc. **24**, 193-202 (2014), https://doi.org/10.1007/s10895-013-1318-3.

[5]. K. Vus, V. Trusova, G. Gorbenko, E. Kirilova, G. Kirilov, I. Kalnina, P. Kinnunen, Chem. Phys. Lett. **532**, 110-115 (2012), https://doi.org/10.1016/j.cplett.2012.02.061.

[6]. G. Gorbenko, V. Trusova, E. Kirilova, G. Kirilov, I. Kalnina, A. Vasilev, et al., Chem. Phys. Lett. **495**, 275-279 (2010), https://doi.org/10.1016/j.cplett.2010.07.005.

[7]. O. Ryzhova, K. Vus, V. Trusova, E. Kirilova, G. Kirilov, G. Gorbenko, P. Kinnunen, Methods. Appl. Fluoresc. **4**, 034007 (2016), https://doi.org/10.1088/2050-6120/4/3/034007.

[8]. X. Yang, W.-H. Liu, W.-J. Jin, G.-L. Shen, R.-Q. Yu, Spectrochim. Acta. **A55**, 2719-2727 (1999), https://doi.org/10.1016/S1386-1425(99)00161-4.

[9]. V. Trusova, E. Kirilova, I. Kalnina, G. Kirilov, O. Zhytniakivska, P. Fedorov, G. Gorbenko, J. Fluoresc. **22**, 953-959 (2011), https://doi.org/10.1007/s10895-011-1035-8.

[10]. O. Zhytniakivska, V. Trusova, G. Gorbenko, E. Kirilova, I. Kalnina, G. Kirilov, et al., J. Fluoresc. **24**, 899-907 (2014), https://doi.org/10.1007/s10895-014-1370-7.

[11]. D. Staneva, E. Vasileva-Tonkova, T.R. Sobahi, R.H. Abdel-Rahman, A.M. Asiri, I. Grabchev. J. Photochem. Photobiol. B: Biology. **143**, 44-51 (2015), https://doi.org/10.1016/j.jphotobiol.2014.12.024.

[12]. D. Staneva, E. Vasileva-Tonkova, I. Grabchev. J. Photochem. Photobiol. A: Chemistry. **375**, 24-29 (2019), https://doi.org/10.1016/j.jphotochem.2019.02.004.

[13]. O. Zhytniakivska, V. Trusova, G. Gorbenko, E. Kirilova, I. Kalnina, G. Kirilov, et al., J. Luminescsc. **146**, 307-313 (2014), https://doi.org/10.1016/j.jlumin.2013.10.015.

[14]. I. Kalnina, R. Bruvere, T. Zvagule, N. Gabruseva, L. Klimkane, E. Kirilova, et al., J. Fluoresc. **20**, 9-17 (2010), https://doi.org/10.1007/s10895-009-0515-6.

[15]. I. Kalnina, L. Klimkane, E. Kirilova, M. Toma, G. Kizane, I. Meirovics, J. Fluoresc., **17**, 619-625 (2007), https://doi.org/10.1007/s10895-007-0249-2.

[16]. I. Kalnina, T. Zvagule, R. Bruvere, I. Meirovics, J. Fluoresc., **15**, 105-110 (2005), https://doi.org/10.1007/s10895-005-2516-4.

[17]. I. Kalnina, T. Zvagule, N. Gabruseva, et al., J. Fluoresc., 17, 633-638 (2007), https://doi.org/10.1007/s10895-007-0256-3.

[18]. S. Jo, T. Kim, V. G. Iyer, W. Im. J. Comp. Chem. **29**, 1859-1865 (2008), https://doi.org/10.1002/jcc.20945.

[19]. .S. Kim, J. Lee, S. Jo, C.L. Brooks, H.S. Lee, W. Im, J. Comp. Chem. **38**, 1879-1886 (2017), https://doi.org/10.1002/jcc.24829.

[20]. J. Lee, D.S. Patel, J. Ståhle, S-J. Park, N.R. Kern, S. Kim, et al., J. Chem. Theory Comp. **15**, 775-786 (2017), https://doi.org/10.1021/acs.jctc.8b01066.

[21]. T. Darden, D. Yolk, L. Pedersen, J. Chem. Phys. **98**, 10089-10092 (1993), https://doi.org/10.1063/1.464397.

[22]. B. Hess, H. Bekker, H.J.C. Berendsen, J.G.E.M. Fraaije, J. Comp. Chem. **18**, 1463-1472 (1997), https://doi.org/10.1002/(SICI)1096-987X(199709)18:12<1463::AID-JCC4>3.0.CO;2-H.

[23]. H. Berendsen, J. Postma, W. van Gunsteren, A. DINola, J. Haak, J.Chem. Phys. **81**, 3684-3690 (1984), https://doi.org/10.1063/1.448118.

[24]. S. Buchoux, FATSLiM/fatslim: FATSLiM v 0.2.1 (2016), https://doi.org/10.5281/zenodo.158942.

[25]. Yi. Wang, D.E. Schalamadinger, J.D. Kim, J.A. McCammon, Biochim. Biophys. Acta, **1818**, 1402-1409 (2012), https://doi.org/10.1016/j.bbamem.2012.02.017.

[26]. H. Jang, B. Ma, T.Woolf, R. Nussinov, Biophys. J., **91**, 2848-2859 (2006), https://doi.org/10.1529/biophysj.106.084046.

[27]. V. Trusova, G. Gorbenko, U. Tarabara, K. Vus, O Ryzhova, East Europian Journal of Physics, **4**, 54-62 (2017), https://doi.org/10.26565/2312-4334-2017-3-08.

[28]. A. Kyrychenko, T. Dyubko, Biophys. Chem. **136**, 23-31 (2008), https://doi.org/10.1021/jp0102567.

[29]. Y.O. Posokhov, A. Kyrychenko, Comput. Biol. Chem. **46**, 23-31 (2013), https://doi.org/10.1016/j.compbiolchem.2013.04.005.

[30]. T.J, Yacoub, A.S. Reddy, I. Szleifer, Biophys J. **101**, 378-385 (2011), https://doi.org/10.1016/j.bpj.2011.06.015.

[31]. Y.O. Posokhov, A. Kyrychenko, Biophys. Chem. **235**, 9-18 (2018), https://doi.org/10.1016/j.bpc.2018.01.005.

[32]. A.M.T.M. do Canto, J.R. Robalo, P.D. Santos, et al., Biochim. Biophys. Acta, **1858**, 2647-2661 (2016), https://doi.org/10.1016/j.bbamem.2016.07.013.

[33]. O. Garcia-Beltran, N. Mena, O. Yanez, J. Caballero, V. Vargas, M. Tunes, et al., Eur. J. Med. Chem. **67**, 60-63 (2013), https://doi.org/10.1016/j.ejmech.2013.06.022.

[34]. M.W. Baig, M. Pederzoli, P. Jurkiewicz, L. Cwiklik, J. Pittner, Molecules, **23**, 1707 (2018), https://doi.org/10.3390/molecules23071707.

[35]. J. Barucha-Kraszewska, S. Kraszewski, P. Jurkiewicz, C. Ramseyer, M. Hof, Biochim. Biophys. Acta, **1798**, 1724-1734 (2010), https://doi.org/10.1016/j.bbamem.2010.05.020.

[36]. J. Repakova, P. Capcova, J. Holopainen, I. Vattulainen, J. Phys. Chem. B, **108**, 13438-13448 (2004), https://dx.doi.org/10.1021/jp048381g.

[37]. M. Pasenkiewicz-Gierula, T. Rog, K. Kitamura, A. Kusumi, Biophys J. **78**, 1376-1389 (2000), https://doi.org/10.1016/S0006-3495(01)75867-5.

[38]. T. Rog, M. Pasenkiewicz-Gierula, FEBS Letters, **502**, 68-71 (2000), https://doi.org/10.1016/S0014-5793(01)02668-0.

[39]. L. Janosi, A.A. Gorfe, J. Chem. Theory Comput. **6**, 3267-3273 (2010), https://doi.org/10.1021/ct100381g.

МОЛЕКУЛЯРНО-ДИНАМІЧНЕ ДОСЛІДЖЕННЯ ВЗАЄМОДІЇ БЕНЗАНТРОНОВОГО ЗОНДУ З МОДЕЛЬНИМИ ЛІПІДНИМИ МЕМБРАНАМИ

О. Житняківська

Кафедра медичної фізики та біомедичних нанотехнологій, Харківський національний університет імені В.Н. Каразіна
м. Свободи 4, Харків, 61022, Україна

Бензантронові зонди широко відомі як чутливі до змін їх мікрооточення сенсори для дослідження фізико-хімічних властивостей та структурних змін ліпідних мембран. В даній роботі методом молекулярно-динамічного моделювання досліджено локалізацію в ліпідному бішарі та природу взаємодій між бензантроновим флуоресцентним зондом АВМ і модельними мембранами, що складалися із цвіттеріонного ліпіду фосфатидилхоліну (ФХ) і його сумішей з аніонним ліпідом фосфатидилгліцерином (ФГ) і холестерином (Хол). Молекулярно-динамічне дослідження проводили з використанням CHARMM36m силового поля в програмному пакеті GROMACS. Продемонстровано, що молекула АВМ, яка спочатку була розташована на відстані 30 Å від центру бішару, проникала в мембрану протягом перших 10 нс моделювання, залишаючись в ліпідному бішарі на протязі решти часу симуляції. Результати молекулярно-динамічного дослідження свідчать про те, що локалізація бензантронового зонду АВМ в ліпідному бішарі в значній мірі залежить від складу мембрани, та варіюється від 0,78 нм в чистому ФХ бішарі до 0,95 нм і 1,5 нм в ліпідних бішарах , що містили ФГ та Хол, відповідно. Виявлено, що при взаємодії АВМ з чистим ФХ бішаром відбувається перехід зонду з зовнішнього моношару ліпідного бішару на внутрішній. Досліджено вплив зонду на структуру ліпідних бішарів. Було виявлено, що розподіл АВМ в ліпідну фазу не має суттєвого впливу на орієнтацію ланцюгів жирних кислот та викликає збільшення дейтерієвого параметру порядку для атомів вуглецю 5-8 в sn- 2 ацильних ланцюгах ФХ ліпідного бішару. Крім того, взаємодія АБМ з модельними ліпідними мембранами супроводжувалась незначним зменшенням площі поверхні на ліпід, що вказує на незначне збільшення щільності упаковки ліпідних молекул у присутності АБМ. Отримані результати створюють основу для більш глибокого розуміння взаємодії бензантронових зондів з мембранами та можуть бути корисні для розробки нових флуоресцентних зондів для мембранних досліджень.

КЛЮЧОВІ СЛОВА: АБМ, бензантроновий зонд, ліпідний біслой, молекулярно-динамічне моделювання

МОЛЕКУЛЯРНО-ДИНАМИЧЕСКОЕ ИССЛЕДОВАНИЕ ВЗАИМОДЕЙСТВИЯ БЕНЗАНТРОНОВОГО ЗОНДА С МОДЕЛЬНЫМИ ЛИПИДНЫМИ МЕМБРАНАМИ

О. Житняковская

Кафедра медицинской физики и биомедицинских нанотехнологий,
Харьковский национальный университет имени В.Н. Каразина
пл. Свободы 4, Харьков, 61022, Украина

Бензантроновые флуоресцентные красители широко известны как чувствительные к окружающей среде сенсоры для мониторинга физико-химических свойств и структурных изменений липидных мембран. В данной работе методом молекулярно-динамического моделирования исследована локализация зонда в липидном бислое и природа взаимодействия между бензантроновым флуоресцентным зондом АВМ и модельными липидными мембранами, состоящими из цвиттерионного липида фосфатидилхолина (ФХ) и его смесей с анионным липидом фосфатидилглицерином (ФГ) и холестерином (Хол). Моделирование МД проводилось в силовом поле CHARMM36m с использованием пакета GROMACS. Показано, что молекула АВМ, которая была первоначально размещена на расстоянии 30 Å от центра бислоя, встраивалась в мембрану в течение первых 10 нс моделирования, оставаясь в липидном бислое на продолжении остального времени симуляции. Результаты молекулярно-динамического моделирования свидетельствуют о том, что локализация бензантронового зонда АВМ в липидном бислое в значительной степени зависит от состава мембраны, сдвигаясь от 0,78 нм в чистом ФХ бислое до 0,95 нм и 1,5 нм в ФГ- и Хол-содержащих мембранах, соответственно. Обнаружено, что взаимодействие АВМ с чистым ФХ бислоем сопровождалось переходом зонда из внешнего шара липидного бислоя во внутренний. Отдельная серия симуляций MD была направлена на изучение влияния АВМ на структуру липидного бислоя. Было обнаружено, что встраивание АБМ в липидные бислои различного состава не оказывает существенного влияния на ориентацию цепей жирных кислот и приводит лишь к небольшому увеличению дейтериевого параметра порядка для атомов углерода 5-8 sn- 2 ацильных цепей ФХ мембран. Кроме того, обнаружено, что взаимодействие АБМ с модельными липидными мембранами вызывает небольшое уменьшение площади поверхности на липид, что указывает на незначительное увеличение плотности упаковки молекул липидов в присутствии АБМ. Полученные результаты создают основу для более глубокого понимания взаимодействия бензантроновых красителей с мембранами и могут быть полезны для разработки новых флуоресцентных зондов для исследования мембран.

КЛЮЧЕВЫЕ СЛОВА: АБМ, бензантроновый зонд, липидный бислой, молекулярно-динамическое моделирование

BINDING OF BENZANTHRONE DYE ABM TO INSULIN AMYLOID FIBRILS: MOLECULAR DOCKING AND MOLECULAR DYNAMICS SIMULATION STUDIES

Kateryna Vus

Department of Medical Physics and Biomedical Nanotechnologies, V.N. Karazin Kharkiv National University
4 Svobody Sq., Kharkiv, 61022, Ukraine
Corresponding Author: kateryna.vus@karazin.ua

The binding of the benzanthrone dye ABM to the model amyloid fibrils of human insulin, referred to here as vealyl (12-VEALYL-17, insulin B-chain)), lyqlen (13-LYQLEN-18, insulin A-chain) and Insf (11-LVEALYL-17, B-chain) + 12-SLYQLENY-19, A-chain) was studied by the molecular docking and molecular dynamics simulations. To obtain the relaxed structures with the enhanced conformational stability, the model fibril structures were solvated and equilibrated in water at 300-310 K using the Gromacs simulation package, with backbone position restraints being applied to prevent the beta-sheet disruption. It appeared that the vealyl fibril relaxation resulted in the twisting of the two β-sheets, and only the vealyl fibril remained stable during 20 ns MD simulations of the relaxed structures. Next, Insf, vealyl, lyqlen, and vealyl (relaxed) fibrils were used for the molecular docking studies (by SwissDock), revealing the binding modes of ABM and standard amyloid marker Thioflavin T (ThT) to the examined fibril structures. Specifically, in the most energetically stable complex the vealyl (relaxed) fibril binding site for ABM was located on the dry steric zipper interface, although the dye was associated with only one twisted β-sheet. During the 20 ns MD simulation the ABM fibril location was changed to a deeper position in the dry interface between the two β-sheets, with the dye-interacting residues being represented by 6 LEU, 3 VAL, 2 ALA, 1 TYR and 1 GLU. The binging free energy ($\Delta G_{binding}$) for ABM complexation with vealyl (relaxed) fibril evaluated with the GMXPBSA GROMACS tool was found to be −31.4±1.8 kJ/mol, that is in accordance with our estimates derived from the fluorescence studies for ABM binding to the bovine insulin amyloid fibrils ($\Delta G_{binding}$ = −30.2 kJ/mol). The Lennard-Jones component appeared to dominate the dye-fibril interactions, with much smaller contributions of Coulombic and nonpolar solvation terms to the total $\Delta G_{binding}$ value, and unfavorable effect of the polar solvation term. These findings indicate that a high specificity of ABM to the insulin amyloid fibrils may arise predominantly from the dye-protein hydrophobic interactions, followed by the formation of van der Waals contacts, thus providing additional evidence for sensitivity of the dye spectral properties to environmental polarity, suggested in our previous studies. Overall, the obtained results provided further insights into the atomistic mechanism of the ABM binding to insulin amyloid fibrils and can be used for development of the novel fluorescent reporters possessing high sensitivity to the amyloid assemblies.

KEYWORDS: ABM, insulin amyloid fibrils, binding free energy, molecular docking, molecular dynamics simulations, Thioflavin T.

The formation of specific protein aggregates, amyloid fibrils, is currently associated with the development of severe human disorders, viz. Alzheimer's and Parkinson's diseases, systemic amyloidosis, etc. In view of this, detection and characterization of amyloid fibrils is very important for early medical diagnostics and testing the potential anti-amyloid drugs. Over the past decades, a great deal of effort has been invested in exploring the amyloid fibril formation at the atomistic level using the molecular dynamics simulations [1,2]. Along with elucidating the role of environmental factors (pH, temperature, ionic strength, etc.), increasing attention is paid to the interactions of amyloid fibrils with potential small molecule markers and inhibitors [3,4]. Insulin is a hormone, involved in the regulation of sugar level in blood, that contains 51 amino acids forming two polypeptide chains – A and B, connected by the disulfide bonds. Insulin pathological aggregation may result in the development of injection-localized amyloidosis in diabetic patients. Furthermore, the protein easily forms amyloid fibrils under acidic pH, increased temperature and ionic strength, resulting in the problems with the long-term storage of insulin pharmaceutical formulations. In our previous studies, we reported the applicability of the benzanthrone fluorescent dye, referred to here as ABM, to detection and characterization of the bovine insulin amyloid fibrils, with the advantages such as high quantum yield (*ca.* 0.52) and association constant (*ca.* 0.2 µM⁻¹) for the dye-protein complex, and a large shift (*ca.* 74 nm) of the dye emission maximum to the shorter wavelengths in the presence of fibrillized protein [5]. The aim of the present study is to obtain an atomistically detailed picture of the ABM binding to insulin amyloid species, using the molecular docking and MD simulations techniques, and to compare the ABM binding mode with that of the classical amyloid marker Thioflavin T [6]. Specifically, our goals were: i) to select from the database and to relax insulin amyloid fibril models (to enhance their stability) using the MD equilibration and the position restraints for the protein backbone and side chains; ii) to optimize the ABM/Thioflavin T structures and to calculate the atomic charges of the dye molecules (by RESP ESP charge Derive server) [7]; iii) to determine the ABM and ThT fibril binding modes by molecular docking (via SwissDock server [8,9]), using the unrelaxed and relaxed fibril structures; iv) to perform 20 ns MD simulations of the most energetically favorable dye-protein complexes and free proteins, in order to refine the stability of these complexes; v) to analyze the ABM-protein distances, protein RMSD, radius of gyration, position of the protein binding site for ABM/ThT, the dye effect on the fibril structure during MD simulations; vi) to estimate the binding free energy $\Delta G_{binding}$ of ABM/ThT to the fibrils and the impact of the Coulombic, Lennard-Jones, polar and nonpolar

solvation components on the final $\Delta G_{binding}$ value using GMXPBSA GROMACS tool [10,11]; viii) to compare the theoretically predicted $\Delta G_{binding}$ values with those derived from the fluorescence studies and to reveal the predominant types of ABM interactions with the insulin fibrils.

MATERIALS AND METHODS
Preparation of the dye and insulin amyloid chemical structures

Four human insulin amyloid fibril models, referred to here as Insf, lyqlen, vealyl were used in this study. Insf, lyqlen and vealyl pdb structures were downloaded from the database provided by Sawaya M.R. [12–14]. Insf fibril is composed of 12 β-strands 11-LVEALYL-17 (insulin B-chain) and 12 β-strands 12-SLYQLENY-19 (insulin A-chain), forming two parallel in-register β-sheets. Lyqlen and vealyl fibril structures are composed of 12 β-strands 13-LYQLEN-18 (insulin A-chain) and 12-VEALYL-17 (insulin B-chain), respectively, forming two anti-parallel β-strands.

The relaxation of the amyloid fibrils was performed using the GROMACS software (version 2020.2) and CHARMM36-m force field, in order to enhance the conformational stability of the protein assemblies [15]. The input files for MD minimization and equilibration were prepared using the web-based platform CHARMM-GUI. The energy minimization (40 ps) of the lyqlen, vealyl, Insf structures was carried out in water (0.15 M NaCl for lyqlen, vealyl and neutralizing ions for Insf) using h-bond constraints (LINCS algorithm, lincs-order = 8) and the backbone restraints of 6 kcal/mol/Å^2 (5 kcal/mol/Å^2 for the Insf fibril).

MD equilibration of the lyqlen and vealyl amyloid species was performed in water, at 310 K, 0.15 M NaCl, using h-bond constraints (LINCS algorithm, lincs-order = 8). Simultaneously, position restraints for the side chains (0.1 kcal/mol/Å^2) coupled with backbone distance restraints of 6, 3.5, 2, 1.5, 1 kcal/mol/Å^2 descending steps with a total of 25 ns MD equilibration, followed by 10 ns equilibration without any restraints, were used. The resulting fibril structures are referred to here as vealyl (relaxed) and lyqlen (relaxed). The same h-bond constraints were employed for Insf MD equilibration in water, although it was carried out at 300 K in the presence of neutralizing ions, and using backbone distance restraints of 5, 2.5, 1, 0.5 kcal/mol/Å^2 descending steps with a total of 20 ns MD equilibration. The resulting Insf structure is referred to here as Insf (relaxed).

The .mol2 files of ABM and ThT were built in OpenBabelGUI, using the ligand structures drawn in MarvinSketch and optimized in Avogadro (.mrv files).

Molecular docking studies

The insulin fibril models (.pdb files): Insf, lyqlen, vealyl, vealyl (relaxed), and ABM, ThT (.mol2 files) structures were used for docking studies of the dye binding modes to the protein aggregates, performed by SwissDock web server [8,9]. SwissDock is based on EADock DSS software, that generates a huge number of ligand binding modes in the vicinity of all protein cavities (blind docking), followed by estimation the free energies of dye-protein binding in CHARMM22 force field. Next, ligand-protein complexes with the lowest binding energies are ranked, taking into account the solvent effect (implicit solvent model), clustered, and the most favorable clusters are included in the output-files of the docking studies. The performance of EADock DSS is good for the small and relatively rigid ligands, and for the cross-docking studies (when the protein structure does not present a perfect fit for the ligand) performance was about 40%, so the validation of the results is needed via, e.g. adding the flexibility to the protein [8,9].

The most energetically favorable dye-protein complexes were analyzed and visualized in the UCSF Chimera molecular viewer.

Molecular dynamics simulations of the insulin fibrils and the dye-fibril complexes

The 20 ns MD simulations were performed using the GROMACS package (version 2020.2) and the CHARMM36m force field. The input files for MD run of Insf (relaxed), lyqlen (relaxed) and vealyl (relaxed) fibril structures, as well as for the best energetically favorable ABM- and ThT-vealyl (relaxed) fibril complexes were prepared in CHARMM-GUI. The .itp files of ABM and ThT were constructed from the dye .mol2 files, using the CHARMM General Force Field, followed by replacing the ABM/ThT partial charges with those assigned by RESP ESP charge Derive Server [7]. The fibrils and dye-fibril complexes were solvated in a rectangular box with a minimum distance of 10 Å from the protein to the box edges and 0.15 M NaCl (neutralizing ions for Insf (relaxed) fibril) were added to the systems. The temperature was set at 310 K (300 K for the Insf (relaxed) fibril). The MD simulations were performed in the NPT ensemble. The minimization and equilibration of the dye-protein complexes were carried out during 5000 (10 ps) and 125000 (0.5 ns) steps, respectively. The constant temperature conditions were provided by the V-rescale thermostat. H-bonds were constrained using LINCS algorithm (lincs-order = 8). The molecular dynamics trajectories were corrected after the MD run, using the gmx trjconv GROMACS command and –pbc nojump option [10,11]. The commands gmx rms, gmx gyrate, gmx distance, gmx angle, and gmx make_ndx, included in GROMACS, were employed to calculate the protein backbone root-mean-square deviation ($RMSD$), protein radius of gyration (R_g), distances between the dye and protein centers of geometry, dihedral angles between benzanthrone and morpholine groups of ABM or between phenyl and benzothiazole

moieties of ThT, and to generate the index groups. Visualization of the snapshots of the MD runs and analysis of the protein secondary structures were performed in VMD.

Binding free energy calculations

The GMXPBSA 2.1 GROMACS tool allowing to post-process a series of representative snapshots from MD trajectories by combining explicit molecular mechanical energies and continuum (implicit) solvation models by MM/PBSA method, was used to calculate the binding free energies of a ABM-vealyl (relaxed) fibril complex [10,11]. This approach enables a rapid estimation of the free energy of binding ($\Delta G_{binding}$), exhibits a good correlation with experiment, although generally does not reproduce the absolute binding free energy values. The MM/PBSA method expresses the free energy of binding as the difference between the free energy of the complex ($G_{complex}$) and the sum of free energies of the protein ($G_{protein}$) and ligand (G_{ligand}):

$$\Delta G_{binding} = G_{complex} - \left(G_{protein} + G_{ligand} \right), \tag{1}$$

where $G_{complex}, G_{protein}, G_{ligand}$ are free energies of the ligand-protein complex, protein and ligand, respectively. The obtained difference is averaged over a number of trajectory snapshots.

The free energy terms for a ligand-protein complex, protein and ligand are calculated as averages of the thermodynamically weighted ensembles of structures obtained in MD simulations:

$$< G > = < E_{MM} > + < G_{solv} > - T < S_{MM} >, \tag{2}$$

$$E_{MM} = E_{int} + E_{coul} + E_{LJ}, \tag{3}$$

$$G_{solv} = G_{polar} + G_{nonpolar}, \tag{4}$$

where E_{int} comprises bond, angle and torsional angle energies; T is temperature (K); $< S_{MM} >$ is the entropic contribution of the solute; E_{coul}, E_{LJ} are the intramolecular Coulombic (electrostatic) and Lennard-Jones (van der Waals) energies, respectively; G_{solv} is the solvation free energy term, referring to the energy required to transfer the molecule from a continuum medium with a low dielectric constant (ε=1) to a continuum medium with the dielectric constant of water (ε=80); $G_{polar}, G_{nonpolar}$ are polar and nonpolar contributions to G_{solv}, respectively. The value of G_{polar} (the electrostatic contribution to the free energy of solvation, i.e. electrostatic free energy of the solute charge density optimized in electrolyte solution) was calculated using the linearized Poisson Boltzmann equation, and $G_{nonpolar}$ was considered to be proportional to the solvent accessible surface area ($SASA$) [16,17].

The binding free energy for ABM-vealyl (relaxed) fibril complex was calculated at every 100 ps from the 20 ns MD trajectory. Vealyl (relaxed) fibril and ABM topologies (.itp files) used for MD simulations were employed for the $\Delta G_{binding}$ calculations [10]. The term G_{solv} was calculated at 310 K, 0.15 NaCl using the APBS 1.4.1 suite. The E_{coul} and E_{LJ} contributions were determined using the GROMACS 2020.2 tools.

RESULTS AND DISCUSSION

The relaxation of amyloid fibrils with distance restraints has been suggested in previous MD simulation studies, because the available model structures of insulin fibrils appeared to be rather unstable in solution, that greatly complicates MD studies of the small-molecule-protein binding [15,18]. Insf, non-relaxed Insf, lyqlen and vealyl fibril structures are shown in Fig. 1A–C, while the relaxed ones are depicted in Fig.1D–F. The twisting of vealyl (relaxed) fibril (Fig. 1E) with respect to the long axis, made it different from the flattened pattern of the non-relaxed configuration (Fig. 1C). The increase in the vealyl (relaxed) curvature may be due to fibril tendency to minimize the electrostatic repulsion between the E13 residues of the β-sheets, as well as the unfavorable contacts of nonpolar amino acid residues with the solvent. Indeed, our previous studies of lysozyme, apolipoprotein A-I and Aβ amyloid fibrils in water under varying twisting angles, revealed the lowest fibril free energies for the angles *ca.* 15–20°, suggesting that the fibrils relaxed in solution are likely to prefer twisted configuration [19]. Further studies showed that 10 ns MD simulations of the solvated flattened lysozyme fibril configuration at 310 K did induce the increase of the fibril curvature [20].

It appeared that Insf (relaxed) and lyqlen (relaxed) structures were significantly destabilized (Fig. 1G,H), while the two β-sheets of the vealyl (relaxed) fibril remained twisted with respect to the fibril long axis, after 20 ns MD simulations

(Fig. 1I). Interestingly, high curvature of the vealyl (relaxed) fibril (Fig.1F) may enhance the fibril stability upon MD simulation (Fig.I), as compared to that of Insf and lyqlen (Fig.G,H). In turn, strong electrostatic repulsion within Insf, comprising the charged E13 (B-chain) and E17 (A-chain) residues, located closer to each other, than in lyqlen and vealyl, due to the parallel in-register β-strand orientation, may explain significant structural transformations of Inf upon relaxation (Fig.1D) and subsequent MD simulation (Fig.1G). Finally, lyqlen fibril tended to be planar after relaxation (Fig.1E) and MD simulation (Fig.1H) steps, presumably due to the higher elastic rigidity, as compared to that of vealyl [19]. However, some β-strands were detached from the lyqlen (relaxed) configuration (Fig.1H), suggesting that fibril stability may be increased upon restraining terminal β-strands during the MD simulations [18].
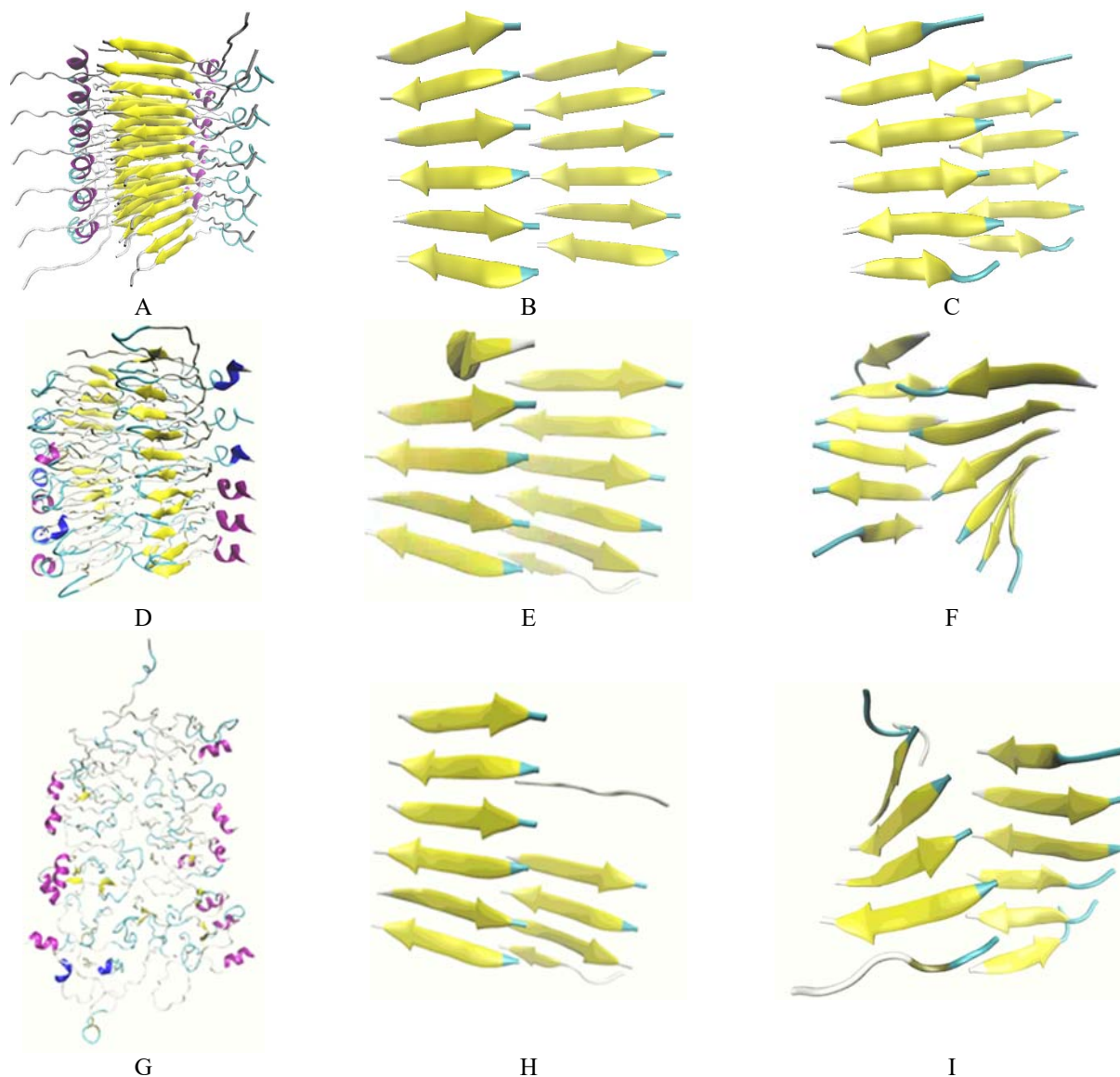

Figure 1. Insf (A), lyqlen (B) and vealyl (C) fibril structures downloaded from the websites: https://people.mbi.ucla.edu/sawaya/jmol/fibrilmodels; https://people.mbi.ucla.edu/sawaya/jmol/xtalpept/index.html. Snapshots of the 20 ns MD simulation of the insf (relaxed, D,G), lyqlen (relaxed, E,H), and vealyl (relaxed, F,I) fibrils relaxed in water. D,E,F – 0 ns, G,H,I – 20 ns. Protein structure is represented as NewCartoon. Protein is colored according to the secondary structure: yellow – extended β-sheets, cyan – β-turns, white – coil, magenta and blue – 310- and α-helices, respectively.

In view of the above, only the vealyl (relaxed) was used for further docking studies of the dye-protein binding, along with the non-relaxed Insf, lyqlen and vealyl fibrils. Shown in Figs. 2–6 are the most energetically favorable protein-ligand complexes (docking solutions), revealing the prevalent binding modes of ABM and ThT to the fibrils. For example, Fig. 2A represents all the ABM poses from the best 32 clusters, the most populated of which are located on the wet surface of the β-sheets almost perpendicular to the fibril long axis.

In the most stable ABM-Insf complex (Fig.2B) ABM interacts with 3 GLN residues of the A-chain β-sheet, as well as with 2 GLN, 1 PHE, 1 VAL and 1 HIS residues of the B-chain coil structure (these residues are located within the distance from the ABM molecule of ca. <5 Å). The free energy of the dye-protein binding ($\Delta G_{binding}$) calculated by

Swissdock was *ca.* –28.9 kJ/mol. Thus, ABM did not prefer to locate along the fibril channels, running parallel to the fibril long axis, as was suggested previously for lysozyme and insulin protein aggregates [5, 21,22]. However, docking results require further verification using the MD simulation of the complex combined with weak position restraints applied to all protein atoms [18].

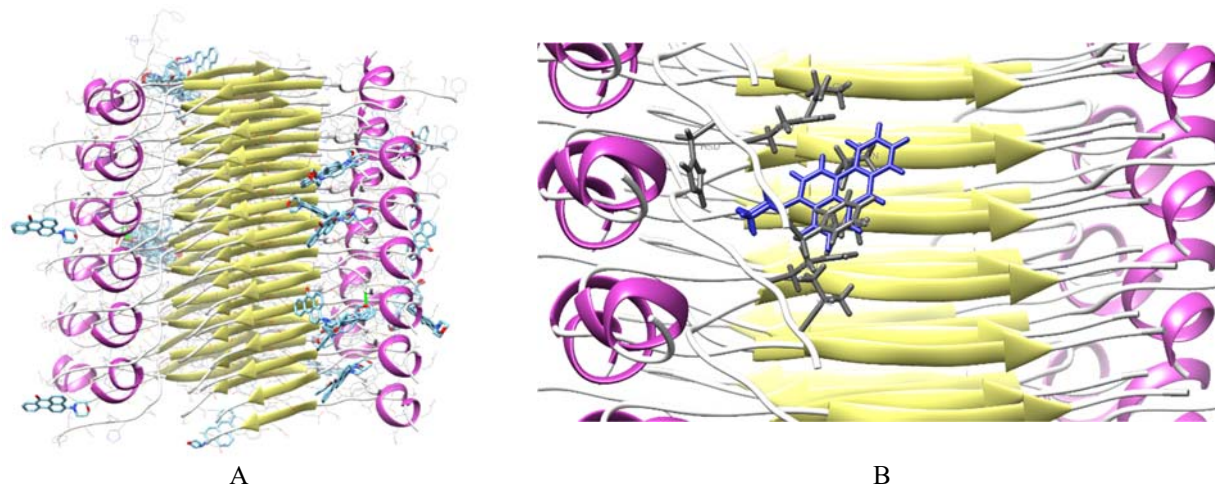A   B

Figure 2. The best docking (SwissDock) complexes between ABM and Insf amyloid fibril. A – All the dyes from 32 dye clusters, B – representative of the dye cluster (0.0) with the lowest $\Delta G_{binding}$ value (–28.9 kJ/mol). Protein and ABM structures are represented as NewCartoon/lines and sticks, respectively. The protein is colored according to the secondary structure: yellow – extended β-sheets, light grey – β-turns, white – coil. Dye molecules are colored by atom Name (C – cyan, O – red, N – blue), and the dye-protein hydrogen bonds are shown as green sticks (A). Insf residues, interacting with ABM, are represented as sticks and colored in dim grey (B).

Next, the best docking solutions for ABM-lyqlen and ABM-vealyl systems revealed the preferred dye location in the grooves L13_Q15/L16_ N18 (Fig. 3A) and L15_L17/ V12_A14 (Fig. 3B). Specifically, 5 LEU, 2 ASN, 1 GLN and 1 TYR16 lyqlen residues, or 2 ALA, 2 VAL, 4 LEU and 1 TYR16 vealyl residues were located in close vicinity of the fluorophore. ABM binds almost parallel to the lyqlen and vealyl long axes, although the clusters with the second largest population also revealed the dye association with the β-sheet edges (data not shown). Notably, $\Delta G_{binding}$ values for ABM complexation with lyqlen (–24.4 kJ/mol) and vealyl (–24.7 kJ/mol) were ~4 kcal/mol lower than that for ABM-Insf binding, most likely due to the greater separations of the dye from the fibril cores, resulting in the weaker van der Waals interactions.
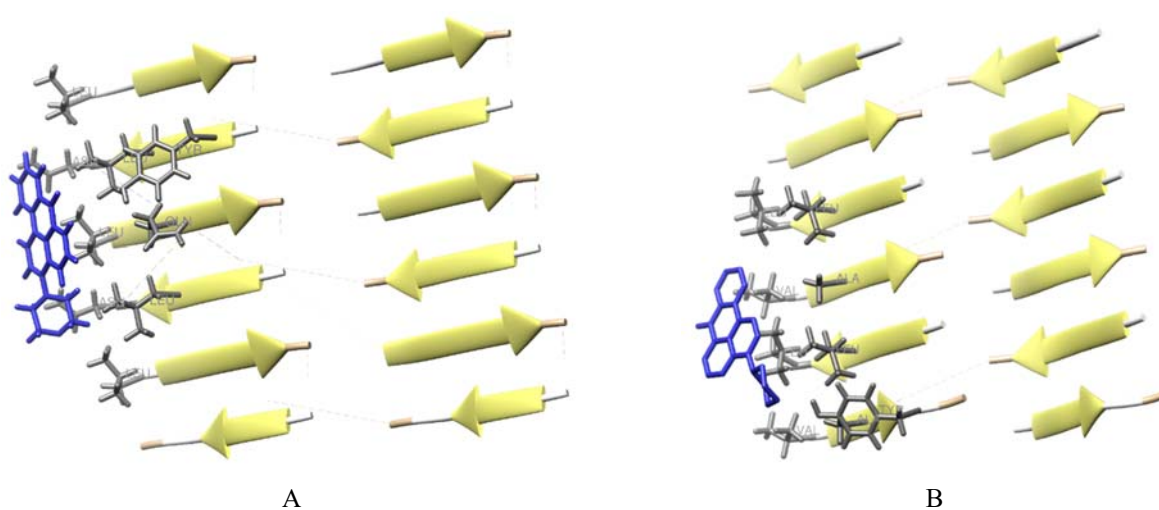

A   B

Figure 3. The best docking (SwissDock) complexes between ABM and lyqlen (A) and vealyl (B) model fibrils. The lowest $\Delta G_{binding}$ values are –24.4 (A) and –24.7 (B) kJ/mol. The protein and ABM structures are represented as NewCartoon and sticks, respectively. Protein is colored according to the secondary structure: yellow – extended β-sheets, peach – β-turns, white – coil. Lyqlen/vealyl residues, interacting with ABM, are represented as sticks and colored in dim grey.

Fig. 4A represents the most stable ThT-Insf docking complex, possessing the lowest $\Delta G_{binding}$ value *ca.* –35.2 kJ/mol. ThT is attached parallel to the fibril long axis, to the groove L13_Q15 (4 LEU, 4 GLN residues of the A-chain), although the clusters in which the dye molecule binds to the β-sheet edges perpendicular to the fibril axis are largely populated (data not shown). In the most favorable binding mode (Fig. 4A), S-atom of ThT also forms intermolecular H-bond with the H-atom of the amide group of Q15, that may explain much greater $\Delta G_{binding}$ value as compared to that of ABM.

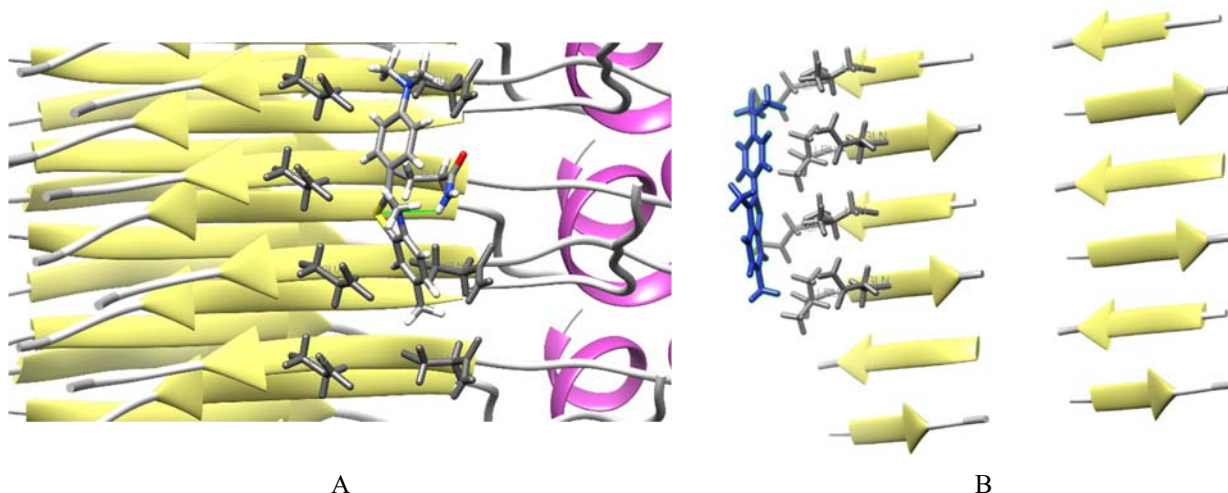A   B

Figure 4. The best docking (SwissDock) complexes between ThT and Insf (A) and lyqlen (B) amyloid fibrils. The lowest $\Delta G_{binding}$ values are –35.2 (A) and –25.5 (B) kJ/mol. The protein and ThT structures are represented as NewCartoon and sticks, respectively. The protein is colored according to the secondary structure: yellow – extended β-sheets, light grey – β-turns, white – coil. Dye molecules are colored by the atom name (C – dim grey, N – blue, S – yellow). Insf residues, interacting with ThT, are represented as sticks and colored in dim grey. The dye-protein hydrogen bond is shown as a green stick (A).

ThT also associated with the grooves L13_Q15/L16_N18 (4 LEU, 2 ASN, 2 GLN residues) of lyqlen (Fig. 4B) and L15_L17/V12_A14 (2 ALA, 2 VAL, 6 LEU residues forming the groove + 2 TYR16 residues outside of the groove) of vealyl (Fig. 5A) fibrils, although in several large clusters the dye also binds to the β-sheet edges perpendicular to the fibril axis (data not shown).

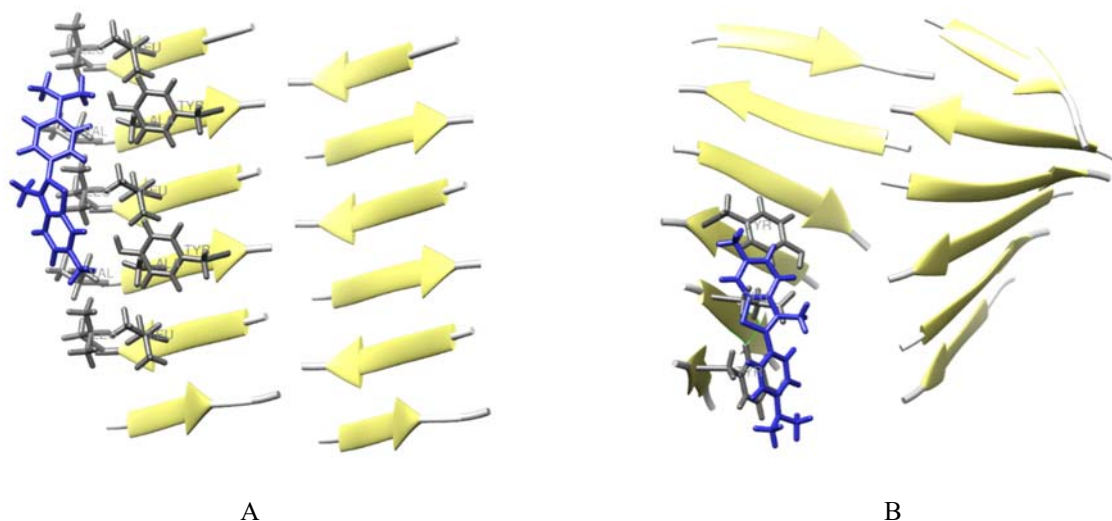A   B

Figure 5. The best docking (SwissDock) complexes between ThT and vealyl (A) and vealyl (relaxed) (B) amyloid fibrils. $\Delta G_{binding}$ values are –25.3 (A) and –28.2 (B) kJ/mol. The protein and ThT structures are represented as NewCartoon and sticks, respectively. The protein is colored according to the secondary structure: yellow – extended β-sheets, light grey – β-turns, white – coil. Vealyl residues, interacting with ThT, are represented as sticks and colored in dim grey.

In the latter case, S atom of ThT forms the H-bonds with C_a atoms of LEU16/ASN18 lyqlen and with the N-termini of LEU15/TYR16/LEU17 vealyl residues, while N2 atom of ThT forms the H-bonds with GLN15/GLU17 lyqlen and with the N-terminus of ALA14 vealyl residues. The $\Delta G_{binding}$ values for ThT-lyqlen and ThT-vealyl complexation were estimated to be *ca.* –25.5 and –25.3 kJ/mol, respectively, that is about 10 kJ/mol lower than the corresponding value for

ThT-InsF binding, presumably due to the absence of the dye-protein H-bonds and a more remote ThT location relative to the lyqlen and vealyl fibril cores. The above data validated the commonly recognized ThT-fibril binding mode for the studied insulin fibril structures [6]. Furthermore, half of the protein residues representing Insf, lyqlen and vealyl binding sites for the dye were represented by LEU, that is in good agreement with the studies of Biancalana and coworkers, who revealed a high affinity of ThT for TYR/LEU cross-strand ladders [23].

By analogy with the approach of Amdursky et al., who studied the interactions of photoacids with insulin amyloid fibril surfaces, using the Insf fibril model, the docking of ThT and ABM was also performed with vealyl (relaxed) fibril model. The best ThT-vealyl (relaxed) complex was characterized by the dye binding to the part of the β-sheet (2 TYR16, 1 GLU13 residues) parallel to the fibril axis (Figs. 5B,6A).

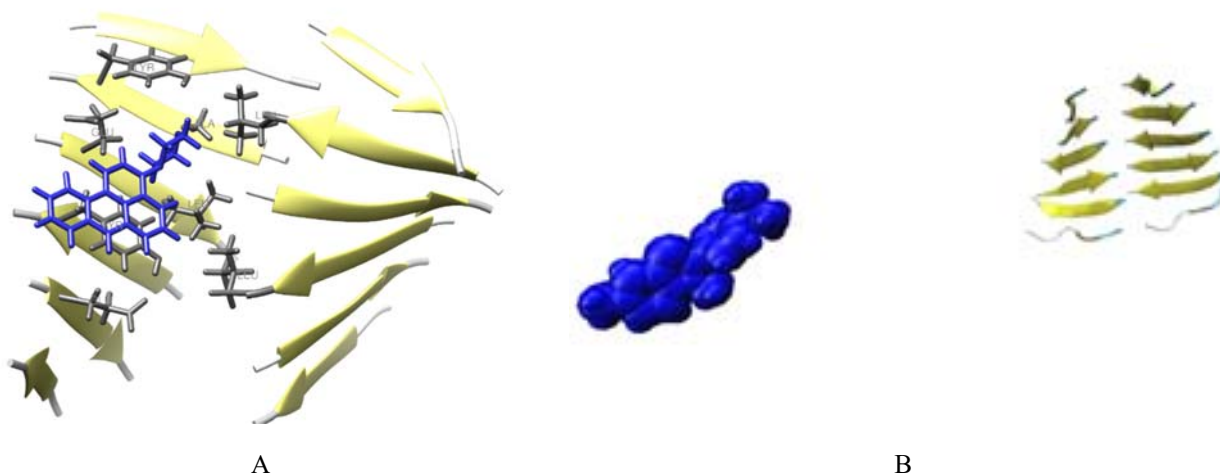A   B

Figure 6. A – The best docking (SwissDock) complex between ABM and vealyl (relaxed) amyloid fibril with $\Delta G_{binding}$ value –27.2 kJ/mol. The protein and ABM structures are represented as NewCartoon and sticks, respectively. The protein is colored according to the secondary structure: yellow – extended β-sheets, light grey – β-turns, white – coil. The vealyl residues interacting with ABM are represented as sticks and colored in dim grey. B – the last frame (20 ns) of the MD simulation of the best docking complex between ThT and vealyl (relaxed) amyloid fibril. The protein and ThT structures are represented as NewCartoon and VDW, respectively. The protein is colored according to the secondary structure: yellow – extended β-sheets, cyan – β-turns, white – coil.

The ThT formed few contacts with vealyl (relaxed), in contrast to vealyl, most likely due to the low affinity for the twisted fibril structures. Indeed, the dye did not bind to the highly twisted β-sheets of globular proteins [3]. Furthermore, in our previous molecular docking studies of the ThT interactions with the model twisted lysozyme fibrils, ThT preferred to locate in the central channels of the fibrillar assemblies, where the twisting angles are minimal, and the binding free energy values decreased with increasing the curvature of fibrillar aggregates [20]. Notably, 10 ns MD simulation of the solvated ThT-flattened lysozyme fibril complex at 310 K resulted in the fibril twisting, accompanied by the dye moving from the specific binding site (fibril channel) to the β-sheet edge [20].

Surprisingly, the most stable ThT-vealyl (relaxed) complex had $\Delta G_{binding}$ value *ca.* –28.2 kJ/mol, that is about 3 kJ/mol greater than that for the ThT-vealyl complex, where more amino acid residues are located in close vicinity of the dye. Such discrepancies may occur due to the smaller ThT distance from the vealyl (relaxed) core, resulting in the stronger van der Waals intermolecular interactions.

Fig.6A represents the best docking solution for ABM-vealyl (relaxed) binding, revealing that the dye is attached along the twisted fibril axis and interacts with 2 TYR, 3 LEU, 2 GLU, 1 ALA residues of the dry "steric zipper interface", although the ligand molecule may also be aligned perpendicular to the fibril axis and attached to the β-sheet surface and to the β-sheet edges (data not shown). $\Delta G_{binding}$ value for the ABM-vealyl (relaxed) complex was equal to –27.2 kJ/mol, that is about 2 kJ/mol greater than that for the ABM-vealyl one (Fig.3B), presumably due to stronger van der Waals contacts formed between the dye and the residues of the two β-sheets (Fig.6A).

In order to validate the stability of the docked ABM-vealyl (relaxed) and ThT-vealyl (relaxed) complexes, the 20 ns molecular dynamics simulations were performed at 310 K, 0.15 M NaCl, which is long enough for the binding site residues to relax, followed by the calculations of the ABM-fibril binding affinity [18]. It appeared that ThT was completely detached from the vealyl (relaxed) binding site (Fig. 6B), similar to the ThT-lysozyme fibril complex [20]. Thus, investigation of the ThT-fibril interactions should be performed using the flattened insulin amyloid fibril models, and position restraints could be applied to the terminal β-strands in order to increase stability of the fibril structures [18]. Notably, more dynamically stable molecular docking solutions for the ThT-vealyl (relaxed) complex can be obtained through using the ThT .mol2 file with the corrected charges on atoms calculated by RESP ESP charge Derive server.

In contrast to ThT, ABM showed a higher affinity for vealyl (relaxed) fibril, because it remained attached to the protein during 20 ns MD simulation (Fig.7), although the dye molecule was relocated from the initial fibril binding site

and was buried deeper into the dry interface between the two β-sheets (Fig.7D,E). Additional evidence for the change of ABM binding mode is provided by the time evolution of the dye-protein distance (Fig.8A): first, the distance increased from ~0.85 to ~1.15 nm, followed by a significant drop to a final value of *ca.* 0.55 nm, starting from about 6 ns of the MD simulation. The last frame (20 ns, Fig.7D,E) revealed that in the novel fibril binding site ABM axis is almost perpendicular to the fibril axis, and 6 LEU, 3 VAL, 2 ALA, 1 TYR and 1 GLU residues are located in close vicinity of the dye. The increased number of contacts formed between ABM molecule and vealyl (relaxed) confirms the stabilization of the final ABM-fibril complex (Fig. 7D,E).

A   B   C

D   E
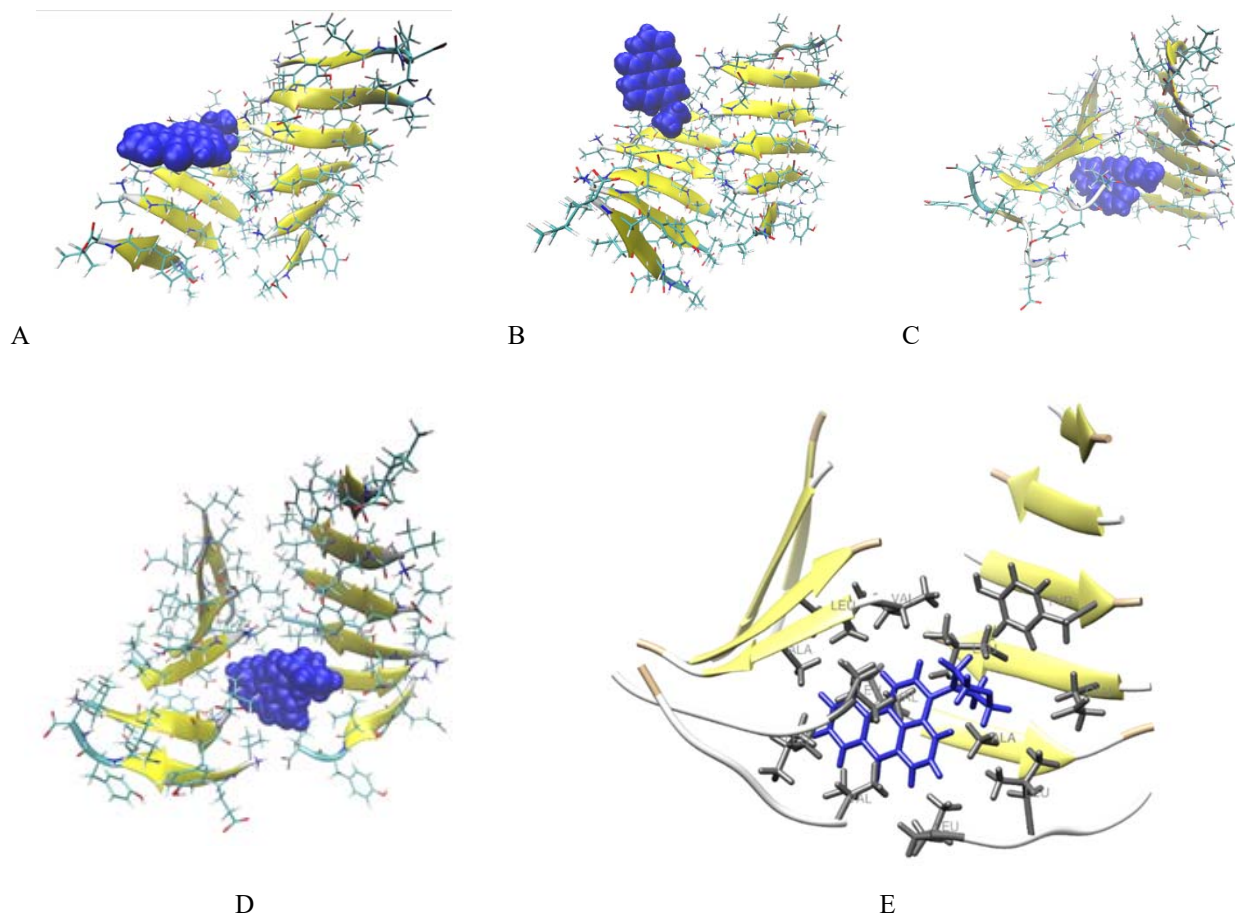
Figure 7. The snapshots of the 20 ns MD simulation of the best docking complex between ABM and vealyl (relaxed) amyloid fibril. A – 0 ns, B – 5 ns, C – 10 ns, D,E – 20 ns. The protein and ABM structures are represented as NewCartoon/Bonds and VDW/Sticks, respectively. The protein is colored according to the secondary structure: yellow – extended β-sheets, cyan/peach – β-turns, white – coil. Vealyl residues, interacting with ABM, are represented as sticks and colored in dim grey (E).

Furthermore, a deeper penetration of ABM into the dry interface between the β-sheets, as well as the increased number of LEU and VAL residues surrounding the dye after 20 ns MD simulations, as compared to that for the ABM-vealyl (relaxed) complex (Figs. 6A,7A), indicate that strong ABM-protein hydrophobic interactions are involved in the complex formation and stabilization. Interestingly, the change of the ABM binding mode may be due to the fact, that the dye molecule with the corrected charges on atoms was used for MD simulations. Notably, the dye orientation with respect to the fibril long axis significantly differed from that of ThT (Fig. 5B), suggesting the different physico-chemical determinants behind the ABM and ThT sensitivity to the amyloid structures. Indeed, ThT belongs to the class of molecular rotors and parallel orientation of the dye to the fibril axis is a necessary prerequisite for the stable ThT- fibril complex, followed by the increase of the dye planarity and significant fluorescence enhancement [23,24]. Such an orientation allows ThT to be entrapped into the fibril grooves and to form π-stacking and hydrophobic interactions with the amino acid side chains [6,23]. In contrast, ABM showed the increased quantum yield and ca. 77 nm shift of the fluorescence spectrum to the shorter wavelengths upon the dye transfer from polar ethanol to nonpolar benzene [25]. Notably, ABM (0.3 μM) binding to the insulin fibrils (12 μM) formed at pH 2, 37 °C induced the 3-fold fluorescence increase and about 70 nm blue shift of the emission maximum, as compared to that in buffer solution (Fig. 8A). Furthermore, ABM was also reported to possess high quantum yields in the presence of phospholipid membranes [22], suggesting that its sensitivity to insulin amyloid structures may result from the decrease of the environmental polarity [5]. Notably, dihedral angle between ABM benzanthrone and morpholine groups, which may rotate relative to each other, varied drastically from 0 to 150° during MD simulations, and the average torsion angle was about 90° (data not shown). Thus, unlike ThT, ABM

molecule remains non-planar in the dynamically stable dye-fibril complex, suggesting that a high fluorescence response of the dye to the insulin amyloid assemblies can hardly be explained by the decreased ABM torsion angle. Notably, our quantum-chemical calculations revealed that ABM molecular volume and width were about 12% and 40% greater, respectively, than those of ThT, and the neutral dye molecule was characterized by significantly greater lipophilicity as compared to the positively charged ThT counterpart (Table 1) [22,24,26]. These data provide additional evidence for the ability of ABM to form stronger hydrophobic and van der Waals contacts with biomolecules, as compared to that of ThT.
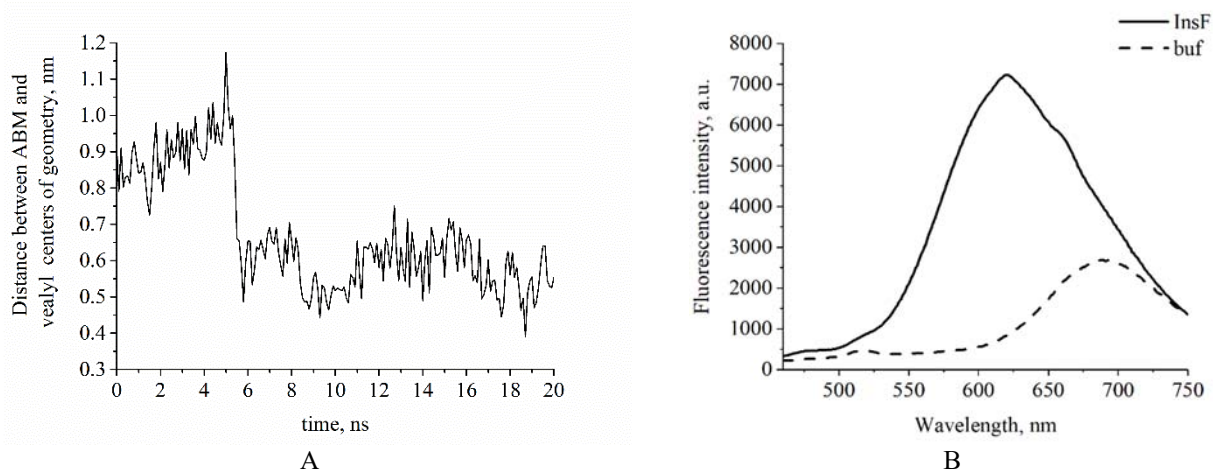

A   B

Figure 8. A – Distance between ABM and vealyl (relaxed) fibril centers of geometry during MD simulation. B – Fluorescence spectra of ABM (0.3 µM) in Tris-HCl buffer (10 mM, pH 7.4) and in the presence of bovine insulin (InsF) amyloid fibrils (12 µM), formed at pH 2, 37 °C and continuous shaking for 2 days. ABM was excited at 440 nm and fluorescence spectra were recorded by Shimadzu RF-6000 spectrofluorimeter.

Table 1.

Quantum-chemical characteristics of ABM and ThT after geometry optimization*

Quantum-chemical parameter	Dye	
	ABM	ThT
Length, Å	11.8	14.3
Width, Å	7.9	5.7
Height, Å	3.4	3.7
Molecular volume, Å³	359	318
Lipophilicity (LogP)	4.52	-0.14

*these data were reported in our previous papers

Thus, MD simulations showed that ABM lacks specificity to the insulin amyloid fibrils structures, because only the binding parallel the fibril long axis is a characteristic feature of the fluorescent amyloid markers. However, in contrast to ThT, ABM is capable of associating with the twisted amyloid assemblies.

Our previous fluorescence studies revealed that ThT had stronger association constant with the insulin amyloid fibrils (*ca.* 0.5 µM^{-1}), than ABM (*ca.* 0.2 µM^{-1}) [5]. Furthermore, Kuznetsova et al. reported ~40 times greater affinity of the ThT binding to the insulin fibrils of different morphology, revealing high specificity of the dye to the fibrillar assemblies [27]. Such disagreement between the experimental results and MD simulations can be explained by the fact that crystal structures of the insulin fibrillar fragments obtained by X-ray structural analysis, are flattened, allowing the formation of the specific fibril binding sites for the dyes with high affinity [13]. In turn, the vealyl (relaxed) fibril is twisted, so the stable ThT complexes with the vealyl fibril may be obtained if the non-relaxed (flattened) vealyl structure is used in MD simulations in combination with weak position restraints applied to the protein atoms (that should prevent twisting of the fibril).

The backbone $RMSD$ value for the free vealyl (relaxed) fibril, as well as for the ABM-vealyl (relaxed) complex, did not increase significantly during the MD simulation, and attained equilibrium value ~0.25 nm in ~10 ns, suggesting the dynamic stability of the protein structure in the last 10 ns of the simulation (Fig. 9A). It should be noted that the fibril compactness remained unchanged for 20 ns of the simulation, because the R_g value was ~1.3 nm for both the free vealyl (relaxed) and its complex with ABM (Fig. 9B). Thus, the ABM molecule did not induce noticeable alterations in the fibril structure, and the dye binding mode to the vealyl (relaxed) revealed by the MD simulation should be reliable due to the dynamic stability of the fibrillar assembly.

To further characterize the ABM binding to the vealyl (relaxed) fibril, we calculated the binding free energy $\left(\Delta G_{binding} \right)$ and its components by analyzing the MD trajectory obtained for the most stable ABM-vealyl (relaxed) docked complex

(Fig. 10) using the GMXPBSA GROMACS tool. The $\Delta G_{binding}$ value was equal to -31.4 ± 1.8 kJ/mol, that is in good agreement with the results obtained for ABM association with bovine insulin amyloid fibrils at 25°C, pH 7.4 $\left(\Delta G_{binding} = -30.2 \text{ kJ/mol}\right)$ [5]. Furthermore, the Lennard-Jones component showing the strongest favorable contribution was increased, while the Coulombic and nonpolar solvation terms showing the weak favorable contributions remained unchanged during the 20 ns MD simulation, and the polar solvation term that strongly unfavored the ABM-vealyl complex formation was decreased (Fig. 10A).
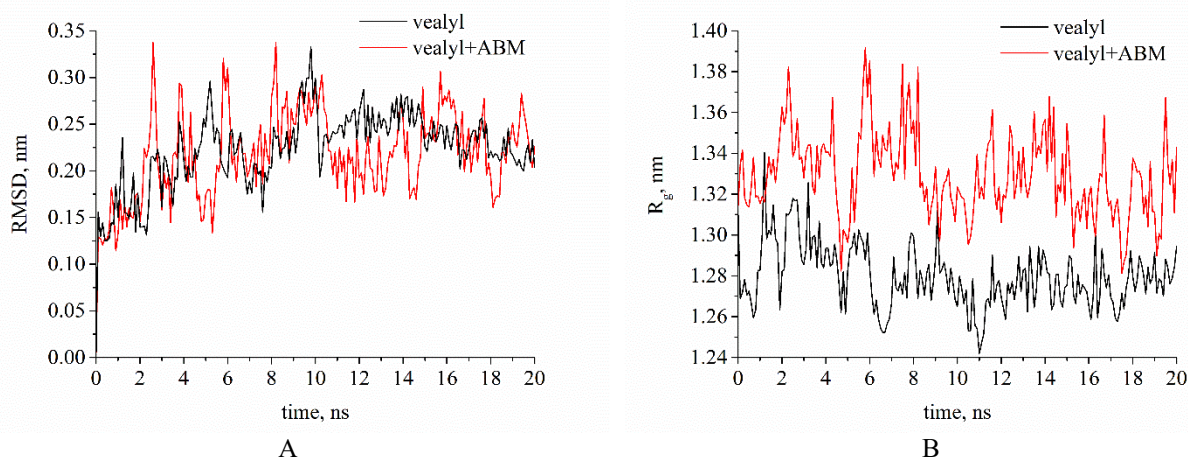

Figure 9. A – Time evolution of vealyl (relaxed) fibril *RMSD* (backbone) (A) and radius of gyration (R_g) (B) at 310.15 K during MD simulation in the absence and in the presence of ABM.
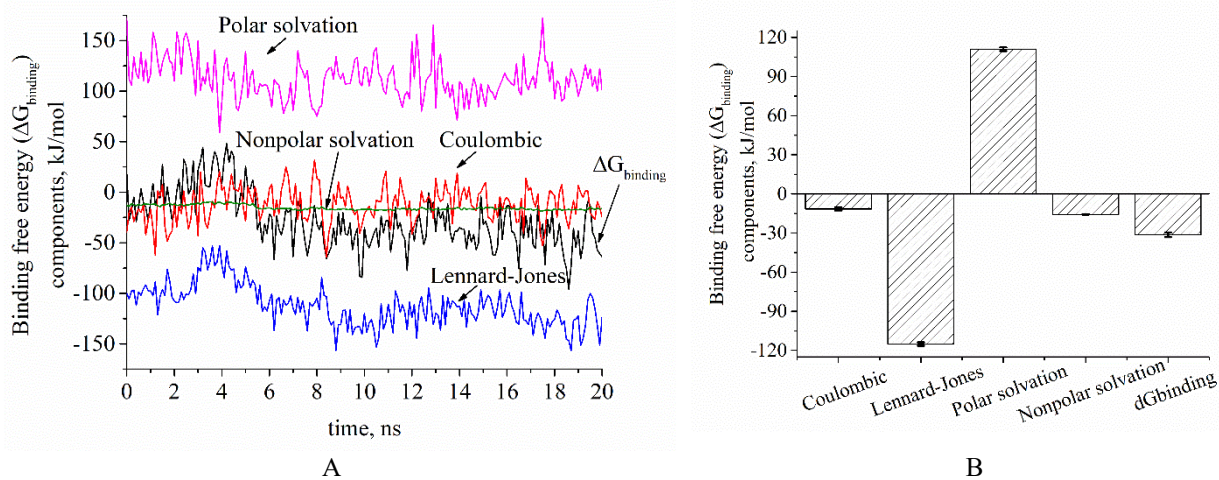

Figure 10. A – Free energy terms for the ABM-vealyl fibril (relaxed in water) during MD simulation, determined using the GMXPBSA program (v 2.1.2), the Gromacs tool for calculating the binding free energies of a protein-ligand complex by MM/PBSA method [10]. $\Delta G_{binding}$ – binding free energy. Nonpolar solvation energy component is reduced during the simulation, and the Lennard-Jones energy is increased (by module). $\Delta G_{binding}$ calculations were performed at 310.15 K, 0.15 M NaCl, using the protein dielectric constant of *ca.* 2, cutoff-scheme Verlet and constraints for H-bonds. The Coulombic energy terms were calculated in Gromacs 2020.2. The polar and nonpolar solvation energy values were determined using the APBS suite 1.4.1. B – Final values of the ABM- fibril (relaxed in water) binding energy and its components, averaged over 20 ns MD trajectory.

The obtained energy contributions are the quantitative characteristics of the processes occurring during the MD simulations: i) the decrease of ABM-vealyl distance (Fig.8A), indicating the strengthening of the van der Waals dye-protein interactions; ii) ABM penetration in the dry interface between the two β-sheets, resulting in the weakening of destabilizing dye-solvent interactions; iii) reduced number of GLU residues in close vicinity of the uncharged dye, leading to the decrease of the unfavorable dye-protein electrostatic interactions. The values of $\Delta G_{binding}$ and its constituents are presented in Fig. 10B and Table 2.

Interestingly, the obtained overall $\Delta G_{binding}$ value was about 3.5 times lower than that for the binding of the Morin hydrate to the native insulin molecule [28], similar to that reported for the Tacrine, flavonoid quercetin hybride inhibitor

of Aβ pathogenic aggregation [29], and about 2.5 times greater than that for ThT complexation with the amyloid-β(1−42) fibril [18], revealed by GMXPBSA. Remarkably, in the latter study ThT was located on the dry steric zipper interface between the two β-sheets of the amyloid-β(1−42) fibrillar assembly, and associated with the groove formed by LEU and PHE residues.

Table 2.

Free energy of ABM binding to vealyl (relaxed) fibril averaged over 20 ns MD trajectory, calculated by GMXPBSA GROMACS tool

Binding free energy terms	$\Delta G_{binding}$, kJ/mol
Coulombic (E_{coul})	−11.5±1.3
Lennard-Jones (E_{LJ})	−115.1±1.4
Polar solvation (G_{polar})	111.0±1.5
Nonpolar solvation ($G_{nonpolar}$)	−15.8±0.2
Polar contribution ($G_{polar} + E_{coul}$)	99.5
Non-polar contribution ($G_{nonpolar} + E_{LJ}$)	−130.8
Binding free energy ($\Delta G_{binding}$)	−31.4±1.8
Binding free energy revealed by fluorescence studies ($\Delta G_{binding}^{experimental}$)*	−30.2

* ABM association constant (K_a) with insulin fibrils at pH 7.4, 25 °C determined previously from the fluorescence studies is equal to 0.2 μM^{-1} ($\Delta G_{binding}^{experimental} = -RT \ln K_a$) [5]

CONCLUSIONS

In conclusion, the molecular docking and molecular dynamics simulations studies revealed two typical binding modes of the benzanthrone dye ABM and the standard amyloid marker Thioflavin T to the model insulin amyloid fibrils, i.e. the binding to the β-sheet surface and to the β-sheet edges. The former was predominant for both dyes, forming hydrophobic and van der Waals contacts with the neutral amino acids LEU, VAL, TYR, ALA, ASN and GLN, although ABM and ThT were oriented perpendicular and parallel to the fibril long axis, respectively. The binding free energy of ABM to the fibrillar insulin was similar to that derived from the fluorescence studies. The Lennard-Jones, Coulombic and nonpolar solvation terms contributed positively to the overall binding free energy, revealing that high affinity of the ABM molecule to the amyloid fibrils results from the dye binding to the hydrophobic interface between the insulin β-sheets. Overall, the ABM sensitivity to the environmental polarity is likely to be the key factor in the dye fluorescence response to the presence of insulin fibrillar assemblies. Further studies should be carried out for the insulin fibrillar structures with the enhanced dynamic stability, in order to keep the protein binding sites for the small ligands intact during the MD simulation and thus, to provide greater accuracy for the atomistic mechanism of the dye-protein interactions, that is important for sensible design of the novel amyloid markers and anti-amyloid agents.

ACKNOWLEDGEMENTS

ORCID IDs

Kateryna Vus, http://orcid.org/0000-0003-4738-4016

REFERENCES

[1]   L. Tran, and T. Ha-Duong, Peptides. **69**, 86-91 (2015), https://doi.org/10.1016/j.peptides.2015.04.009.
[2]   W.M. Berhanu, and A.E. Masunov, J. Mol. Model. **18**, 1129-1142 (2012), https://doi.org/10.1007/s00894-011-1123-3.
[3]   M. Biancalana, and S. Koide, Biochim. Biophys. Acta. **1804**, 1405-1412 (2010), https://doi.org/10.1016/j.bbapap.2010.04.001.
[4]   C. Wu, J. Scott, and J.E. Shea, Biophys. J. **103**, 550-557 (2012), https://doi.org/10.1016/j.bpj.2012.07.008.
[5]   K.O. Vus, *Fluorescence detection of amyloid fibrils, PhD Thesis:* 03.00.02. Kharkiv, 2016, P. 94, http://rbecs.karazin.ua/wp-content/uploads/2015/dis/dis_Vus.pdf.
[6]   M.R. Krebs, E.H. Bromley, and A.M. Donald, J. Struct. Biol. **149**, 30-37 (2005), https://doi.org/10.1016/j.jsb.2004.08.002.

[7] E. Vanquelef, S. Simon, G. Marquant, E. Garcia, G. Klimerak, J.C. Delepine, P. Cieplak, and F.Y. Dupradeau, Nucleic Acids Res. **39**, W511-W517 (2011), https://doi.org/10.1093/nar/gkr288.

[8] A. Grosdidier, V. Zoete, and O. Michielin, Nucleic Acids Res. **39**, W270-W277 (2011), https://doi.org/10.1093/nar/gkr366.

[9] A. Grosdidier, V. Zoete, and O. Michielin, J. Computational Chem. **32**, 2149-2159 (2011), https://doi.org/10.1002/jcc.21797.

[10] C. Paissoni, D. Spiliotopoulos, G. Musco, and A. Spitaleri, Computer Physics Communications. **186**, 105-107 (2015), https://doi.org/10.1016/j.cpc.2014.09.010.

[11] I. Massova, and P.A. Kollman, J. Am. Chem. Soc. **121**, 8133-8143 (1999), https://doi.org/10.1021/ja990935j.

[12] UCLA-DOE Institute, 611 Young Drive East, Los Angeles, CA 90095, https://people.mbi.ucla.edu/sawaya/jmol.

[13] M.R. Sawaya, S. Sambashivan, R. Nelson R, M.I. Ivanova, S.A. Sievers, M.I. Apostol, M.J. Thompson, M. Balbirnie, J.J.W. Wiltzius, H.T. McFarlane, A.O. Madsen, C. Riekel, and D.Eisenberg, Nature, **447**, 453-457 (2007), https://doi.org/10.1038/nature05695.

[14] M.I. Ivanova, S.A. Sievers, M.R. Sawaya, J.S. Wall, and D. Eisenberg, PNAS. 106, 18990-18995 (2009), https://doi.org/10.1073/pnas.0910080106.

[15] N Amdursky, M.H. Rashid, M.M. Stevens, and I. Yarovsky, Sci. Rep. **7**, 6245 (2017), https://doi.org/10.1038/s41598-017-06030-4.

[16] C.J. Stein, J.M. Herbert, and M. Head-Gordon, J. Chem. Phys. **151**, 224111 (2019), https://doi.org/10.1063/1.5131020.

[17] J. Dzubiella, J.M.J. Swanson and J.A. McCammon, J. Chem. Phys. **124**, 084905 (2006), https://doi.org/10.1063/1.2171192.

[18] G. Kuang, N.A. Murugan, Y. Tu, A. Nordberg, and H. Ågren, J. Phys. Chem. B, **119**, 11560-11567 (2015), https://doi.org/10.1021/acs.jpcb.5b05964.

[19] V. Trusova, East European Journal of Physics. **2**, 51-58 (2015), https://doi.org/10.26565/2312-4334-2015-2-06.

[20] A. Kokorev, V. Trusova, K. Vus, U. Tarabara, and G. Gorbenko, East European Journal of Physics. **4**, 30-36 (2017), https://doi.org/10.26565/2312-4334-2017-4-04.

[21] G. Gorbenko, V. Trusova, E. Kirilova, G. Kirilov, I. Kalnina, A. Vasilev, S. Kaloyanova, and T. Deligeorgiev, Chem. Phys. Lett. **495**, 275-279 (2010), https://doi.org/10.1016/j.cplett.2010.07.005.

[22] O. Ryzhova, K. Vus, V. Trusova, E. Kirilova, G. Kirilov, G. Gorbenko ,and P. Kinnunen, Methods Appl. Fluoresc. **4**, 034007 (2016), https://doi.org/10.1088/2050-6120/4/3/034007.

[23] M. Biancalana, K. Makabe, A. Koide and S. Koide, J. Mol. Biol. **385**,1052-1063 (2009), https://doi.org/10.1016/j.jmb.2008.11.006.

[24] V.I. Stsiapura, A.A. Maskevich, V.A. Kuzmitsky, K.K. Turoverov, and I.M. Kuznetsova, J. Phys. Chem. A. **111**, 4829-4835 (2007), https://doi.org/10.1021/jp070590o.

[25] E.M. Kirilova, I. Kalnina, G.K. Kirilov and I. Meirovics, J. Fluoresc. **18**, 645-648 (2008), https://doi.org/10.1007/s10895-008-0340-3.

[26] U. Tarabara, M. Shchuka, K. Vus, O. Zhytniakivska, V. Trusova, G. Gorbenko, N. Gadjev, and T. Deligeorgiev, East European Journal of Physics. **4**, 58-69 (2019), https://doi.org/10.26565/2312-4334-2019-4-06.

[27] I.M. Kuznetsova, A.I. Sulatskaya, V.N. Uversky, and K.K. Turoverov, PloS ONE. **7**, e30724 (2012), https://doi.org/10.1371/journal.pone.0030724.

[28] P. Patel, K. Parmar, and M. Das, Int. J. Biol. Macromol. **108**, 225-239 (2018), https://doi.org/10.1016/j.ijbiomac.2017.11.168.

[29] R.H. Gharacheh, M. Eslami, P. Amani, and S.B. Novir, Phys. Chem. Res. **7**, 561-579 (2019), https://doi.org/10.22036/PCR.2019.183077.1624.

ДОСЛІДЖЕННЯ ЗВ'ЯЗУВАННЯ БЕНЗАНТРОНОВОГО ЗОНДА АБМ З АМІЛОЇДНИМИ ФІБРИЛАМИ ІНСУЛІНУ МЕТОДАМИ МОЛЕКУЛЯРНОГО ДОКІНГУ ТА МОЛЕКУЛЯРНО-ДИНАМІЧНОГО МОДЕЛЮВАННЯ

К. Вус

Кафедра медичної фізики та біомедичних нанотехнологій, Харківський національний університет імені В.Н. Каразіна
м. Свободи 4, Харків, 61022, Україна

За допомогою молекулярного докінгу та молекулярно-динамічного моделювання (MD) досліджено зв'язування бензантронового зонда АБМ з амілоїдними фібрилами інсуліну людини, які позначено тут як vealyl, lyqlen та Insf, що складалися із амінокислотних залишків 12-VEALYL-17 (В-ланцюг інсуліну), 13-LYQLEN-18 (А-ланцюг інсуліну), 11-LVEALYL-17 (В-ланцюг інсуліну) + 12-SLYQLENY-19 (А-ланцюг інсуліну), відповідно. На першому етапі роботи амілоїдні структури інсуліну було сольватовано та проведено MD еквілібрацію при температурах 300–310 К (у пакеті ГРОМАКС) з використанням позиційних обмежень руху атомів білкового остова, для попередження руйнування β-листів. Виявлено, що релаксація фібрил vealyl призвела до закручення двох β-листів відносно довгої осі фібрили, причому тільки цей тип фібрил залишився стабільним упродовж 20 нс MD-симуляції релаксованих структур. На наступному етапі роботи, фібрили Insf, vealyl, lyqlen, та vealyl (релаксована) було використано для молекулярного докінгу (за допомогою SwissDock), що дозволило визначити типи сайтів зв'язування АБМ та стандартного амілоїдного маркеру тіофлавіну Т (ThT) з досліджуваними амілоїдними структурами. Зокрема, у найбільш енергетично вигідному комплексі фібрили vealyl (релаксована) сайт зв'язування для АБМ був розташований на гідрофобній поверхні одного з двох β-листів. MD-симуляція протягом 20 нс призвела до зміни положення АБМ на фібрилі інсуліну – зонд став глибше зануреним у гідрофобну область між двома β-листами, що супроводжувалося взаємодією з такими амінокислотними залишками: 6 LEU, 3 VAL, 2 ALA, 1 TYR та 1 GLU. Значення вільної енергії зв'язування ($\Delta G_{binding}$) АБМ з фібрилою vealyl (релаксована), що отримано за допомогою GROMACS інструменту GMXPBSA, складало –31.4±1.8 кДж/моль, що узгоджується з оцінкою, отриманою за допомогою флуоресцентних досліджень асоціації АБМ з амілоїдними фібрилами інсуліну при температурі 25°C, pH 7.4 ($\Delta G_{binding}$= - 30.2 кДж/моль). Компонента Леннарда-Джонса домінувала у взаємодії між зондом та фібрилою, кулонівський компонент та компонент неполярної сольватації мали слабкі вклади у сумарне значення $\Delta G_{binding}$, а компонент полярної сольватації мав несприятливий ефект на формування комплексу між АБМ та фібрилою vealyl (релаксована). Отримані результати свідчать про те, що значна специфічність АБМ до амілоїдних фібрил інсуліну, спостерігається, переважно, завдяки сильним гідрофобним взаємодіям між зондом та білком, що супроводжується формуванням підвищеної кількості ван-дер-

Ваальсових зв'язків, і також додатково підтверджує спостережувану раніше чутливість спектральних властивостей АБМ до полярності оточення. Таким чином, отримані результати дають більш детальну картину зв'язування бензантронового зонда АБМ з аміллоїдними фібрилами інсуліну на атомному рівні, та можуть бути використані у розробці нових флуоресцентних репортерів, що мають високу специфічність до аміллоїдних ансамблів інсуліну.

КЛЮЧОВІ СЛОВА: АБМ, аміллоїдні фібрили інсуліну, вільна енергія зв'язування, молекулярний докінг, молекулярно-динамічне моделювання, тіофлавін Т.

ИЗУЧЕНИЕ СВЯЗЫВАНИЯ БЕНЗАНТРОНОВОГО ЗОНДА АБМ С АМИЛОИДНЫМИ ФИБРИЛЛАМИ ИНСУЛИНА МЕТОДАМИ МОЛЕКУЛЯРНОГО ДОКИНГА И МОЛЕКУЛЯРНО-ДИНАМИЧЕСКОГО МОДЕЛИРОВАНИЯ

К. Вус

Кафедра медицинской физики и биомедицинских нанотехнологий
Харьковский национальный университет имени В.Н. Каразина
пл. Свободы 4, Харьков, 61022, Украина

При помощи молекулярного докинга и молекулярно-динамического моделирования (MD) исследовано связывание бензантронового зонда АБМ с амилоидными фибриллами инсулина человека, обозначенными здесь как vealyl, lyqlen и Insf, которые состояли из аминокислотных остатков 12-VEALYL-17 (В-цепь инсулина), 13-LYQLEN-18 (А-цепь инсулина), 11-LVEALYL-17 (В-цепь инсулина) + 12-SLYQLENY-19 (А-цепь инсулина), соответственно. На первом этапе работы амилоидные структуры инсулина были сольватированы и была проведена MD-эквилибрация при температурах 300–310 К (в пакете ГРОМАКС) с применением позиционных ограничений движения атомов белкового остова, для предотвращения разрушения β-листов. Обнаружено, релаксация фибрилл vealyl привела к закручиванию двух β-листов относительно длинной оси фибриллы, причем только этот тип фибрилл оставался стабильным в течение 20 нс MD-симуляции релаксированных структур. На следующем этапе работы, фибриллы Insf, vealyl, lyqlen, и vealyl (релаксированная) были использованы для молекулярного докинга (при помощи SwissDock), что позволило определить типы сайтов связывания АБМ и стандартного амилоидного маркера тиофлавина Т (ThT) с исследуемыми амилоидными структурами. В частности, в наиболее энергетически выгодном комплексе фибриллы vealyl (релаксированная) сайт связывания для АБМ был расположен на гидрофобной поверхности одного из двух β-листов. MD-симуляция в течение 20 нс привела к изменению положения АБМ на фибрилле инсулина – зонд глубже погрузился в гидрофобную область между двумя β-листами, что сопровождалось взаимодействием с такими аминокислотными остатками: 6 LEU, 3 VAL, 2 ALA, 1 TYR и 1 GLU. Значения свободной энергии связывания ($\Delta G_{binding}$) АБМ с фибриллой vealyl (релаксированная), полученное при помощи GROMACS инструмента GMXPBSA, составило –31.4±1.8 кДж/моль, что согласуется с оценкой, полученной при помощи флуоресцентных исследований ассоциации АБМ с амилоидными фибриллами инсулина при температуре 25 °C, pH 7.4 ($\Delta G_{binding}$= - 30.2 кДж/моль). Компонента Леннарда-Джонса доминировала во взаимодействии между зондом и фибриллой, кулоновская компонента и компонента неполярной сольватации имели слабые вклады в суммарное значение $\Delta G_{binding}$, а компонента полярной сольватации имела неблагоприятное влияние на образование комплекса между АБМ и фибриллой vealyl (релаксированная). Полученные результаты свидетельствуют о том, что значительная специфичность АБМ к амилоидным фибриллам инсулина, наблюдается, преимущественно, благодаря сильным гидрофобным взаимодействиям между зондом и белком, сопровождаемым формированием повешенного числа ван-дер-Ваальсовых контактов, что также дополнительно подтверждает наблюдаемую ранее чувствительность спектральных свойств АБМ к полярности окружения. Таким образом, полученные результаты дают более детальную картину связывания бензантронового зонда АБМ с амилоидными фибриллами инсулина на атомном уровне, и могут быть использованы при разработке новых флуоресцентных репортеров, которые имеют высокую специфичность к амилоидным ансамблям инсулина.

КЛЮЧЕВЫЕ СЛОВА: АБМ, амилоидные фибриллы инсулина, свободная энергия связывания, молекулярный докинг, молекулярно-динамическое моделирование, тиофлавин Т.

INSTRUCTIONS FOR PREPARING MANUSCRIPT IN EAST EUROPEAN JOURNAL OF PHYSICS

N.N. Author[a,*], N.N. Co-author(s)[b,†]

[a]Affiliation of first author
[b]Affiliation of second author (if different from first Authors)
*Corresponding Author: corresponding_authors@mail.com, [a]ORCID ID
[†]E-mail: co_authors@mail.com, [b]ORCID ID

Each paper must begin with an abstract. The abstract should be typed in the same manner as the body text (see below). Please note that these Instructions are typed just like the manuscripts should be. The abstract must have at least **1800 phonetic symbols**, supplying general information about the achievements, and objectives of the paper, experimental technique, methods applied, significant results and conclusions. Page layout: the text should be printed on the paper **A4** format, at least **5 pages**, with margins of: **Top - 3, Bottom, Left and Right - 2 cm**. The abstract should be presented in English (only for foreign authors), Ukraine and Russian.

KEYWORDS: there, must, be, at least, 5 keywords

This is introduction section. This paper contains instructions for preparing the manuscripts. The text should be prepared in "**doc" or "docx"** format.

INSTRUCTIONS

The text should be typed as follows:
• **title**: Times New Roman, 12 pt, ALL CAPS, bold, 1 spacing, centred;
• **authors**: name, initials and family names; Times New Roman, 12 pt, bold, 1 spacing, centred;
• **affiliation(s)**: Times New Roman, 9 pt, italic, 1 spacing, centred;
• **abstract**: Times New Roman, 9 pt, 1 spacing, justified;
• **body text**: Times New Roman, 10 pt, 1 spacing, justified; paragraphs in sections should be indented right (tabulated) for 0.75 cm;
• **section titles**: Times New Roman, 10 pt, bold, 1 spacing, centred, without numbering, one line should be left, blank above section title;
• **subsection titles**: Times New Roman, 10 pt, bold, 1 spacing, centred, without numbering in accordance to the section (see below), one line should be left blank above subsection title;
• **figure captions**: width of the figure should be 85 or 170 mm, figures should be numbered (Fig. 1) and titled below figures using sentence format, Times New Roman, 9 pt, 1 spacing, centred (if one line) or justified (if more than one line); one line should be left blank below figure captions;
• **table captions**: width of the table should be 85 or 170 mm, tables should be numbered (Table 1.) and titled above tables using sentence format, Times New Roman, 10 pt, 1 spacing, centred (if one line) or justified (if more than one line), tables should be formatted with a single-line box around the outside border and single ruling lines between rows and columns; one line should be left blank below tables;
• **equations**: place equations centred, numbered in Arabic (1), flush right, equations should be specially prepared in "**Math Type"**, or "**Microsoft Equation"**; one line should be left blank below and above equation.

Additional instructions

Numerated figures and tables should be embedded in your text and placed after they are cited. Only sharp photographs and drawings are acceptable. Letters in the figures should be 3 mm high. The figures should be presented in one of the following graphic formats: jpg, gif, pcx, bmp, tif.

REFERENCES

Cite references in AIP style (https://guides.lib.monash.edu/citing-referencing/aip). Numbering in the order of referring in the text, e.g. [1], [2-5], etc. References should be listed in numerical order of citation in the text at the end of the paper (justified), Times New Roman, 9 pt, 1 spacing.

Journal Articles
[1] T. Mikolajick, C. Dehm, W. Hartner, I. Kasko, M. J. Kastner, N. Nagel, M. Moert, and C. Mazure, Microelectron. Reliab. **41**, 947-950 (2001), https://doi.org/10.1016/S0026-2714(01)00049-X.
[2] S. Bushkova, B.K. Ostafiychuk, and O.V. Copaiev, Physics and Chemistry of Solid State. **15**(1), 182-185 (2014), http://page.if.ua/uploads/pcss/vol15/!1501-27.pdf. (in Ukrainian)
[3] M. Yoshimura, E. Nakai, K. Tomioka and T. Fukui, Appl. Phys. Lett. **103**, 243111 (2013), http://dx.doi.org/10.7567/APEX.6.052301.

E-print Resourses with Collaboration Research
[4] M. Aaboud et al. (ATLAS Collaboration), Eur. Phys. J. C, **77**, 531 (2017), http://dx.doi.org/10.1140/epjc/s10052-017-5061-9
[5] Sjöstrand et al., *Comput. Phys. Commun.* **191,** 159-177 (2015), http://arxiv.org/abs/1410.3012.
[6] Boudreau, C. Escobar, J. Mueller, K. Sapp, and J. Su, (2013), http://arxiv.org/abs/1304.5639.

Books
[7] S. Inoue, and K.R. Spring, *Video Microscopy*: *The fundamentals*, 2nd ed. (Plenum, New York, 1997), pp. 19-24.
[8] I. Gonsky, T.P. Maksymchuk, and M.I. Kalinsky, *Біохімія Людини [Biochemistry of Man],* (Ukrmedknyga, Ternopil, 2002), p. 16. (in Ukrainian)

Edited Books
[9] Z.C. Feng, editor, *Handbook of Zinc Oxide and Related Materials: Devices and Nano Engineering, vol. 2*, (CRC Press/Taylor & Francis, Boca Raton, FL, 2012)

Book Chapters
[10] P. Blaha, K. Schwarz, G.K.H. Madsen, D. Kvasnicka, and J. Luitz, in: *WIEN2K, An Augmented Plane Wave Plus Local Orbitals Program for Calculating Crystal Properties,* edited by K. Schwarz (Techn. Universität Wien, Austria, 2001).
[11] M. Gonzalez-Leal, P. Krecmer, J. Prokop and S.R. Elliot, in: *Photo-Induced Metastability in Amorphous Semiconductors*, edited by A.V. Kolobov (Wiley-VCH, Weinheim, 2003), pp. 338-340.
[12] A. Kochelap and S.I. Pekar, in: *Теория Спонтанной и Стимулированной Хемилюминесценции Газов [Theory of Spontaneous and Stimulated Gas Chemiluminescence]* (Naukova dumka, Kyiv, 1986), pp. 16-29. (in Russian)

Conference or Symposium Proceedings
[13] C. Yaakov, and R. Huque, in: *Second International Telecommunications Energy Symposium Proceedings*, edited by E. Yow (IEEE, New York, 1996), pp. 17-27.
[14] V. Nikolsky, A.K. Sandler and M.S. Stetsenko, in: *Автоматика-2004: Матеріали 11 Міжнародної Конференції по Автоматичному Управлінню [Automation-2004: Materials of the 11th International Conference on Automated Management]* (NUHT, Kyiv, 2004), pp. 46-48. (in Ukrainian)

Patent
[15] I.M. Vikulin, V.I. Irha and M.I. Panfilov, Patent Ukraine No. 26020 (27 August 2007). (in Ukrainian)

Thesis / Dissertation
[16] R.E. Teodorescu, Ph.D. dissertation, The George Washington University, 2009.

Special Notes
1. Use International System of Units (SI system). 2. It is undesirable to use acronyms in the titles. Please define the acronym on its first use in the paper. 3. Refer to isotopes as ^{14}C, ^{3}H, ^{60}Co, etc.

Наукове видання

СХІДНО-ЄВРОПЕЙСЬКИЙ ФІЗИЧНИЙ ЖУРНАЛ
Номер 3, 2020

EAST EUROPEAN JOURNAL OF PHYSICS
No 3, 2020

Збірник наукових праць
англійською, українською, російською мовами